ÇUKUROVA UNIVERSITY
INSTITUTE OF NATURAL AND APPLIED SCIENCES

PhD. THESIS

Aytül ADIGÜZEL

SEARCH FOR A W′ GAUGE BOSON DECAYING TO WZ IN PROTON-PROTON COLLISIONS AT $\sqrt{s} = 7$ TeV

DEPARTMENT OF PHYSICS

ADANA, 2014

ÇUKUROVA UNIVERSITY
INSTITUTE OF NATURAL AND APPLIED SCIENCES

SEARCH FOR A W′ GAUGE BOSON DECAYING TO WZ IN PROTON-PROTON COLLISIONS AT $\sqrt{s}$ = 7 TeV

Aytül ADIGÜZEL

PhD THESIS

DEPARTMENT OF PHYSICS

We certify that the thesis titled above was reviewed and approved for the award of degree of the Doctor of Philosophy by the board of jury on …/…/2014.

……………….................	…………………………………..	……...............................
Prof. Dr. Ayşe POLATÖZ	Assoc. Prof. Dr. Samim ERHAN	Prof. Dr. Gülsen ÖNENGÜT
SUPERVISOR	CO-SUPERVISOR	MEMBER

………………...............	……………………....
Prof. Dr. Sefa ERTÜRK	Prof. Dr. Eda EŞKUT
MEMBER	MEMBER

This PhD Thesis is performed in Department of Physics of Institute of Natural And Applied Sciences of Çukurova University.
Registration Number:

Prof. Dr. Mustafa GÖK
Director
Institute of Natural and Applied Sciences

This Study was supported by Çukurova University Scientific Research Fund.
Project Number:FEF2011D5

to my parents.

ABSTRACT

PhD. THESIS

SEARCH FOR A W¢GAUGE BOSON DECAYING TO WZ IN PROTON-PROTON COLLISIONS AT √s = 7 TeV

Aytül ADIGÜZEL

UNIVERSITY OF ÇUKUROVA
INSTITUTE OF NATURAL AND APPLIED SCIENCES
DEPARTMENT OF PHYSICS

Supervisor	:Prof. Dr. Ayşe POLATÖZ
Co-Supervisor	:Assoc. Prof. Dr. Samim ERHAN
	Year: 2014, Pages: 200
Jury	:Prof. Dr. Ayşe POLATÖZ
	:Assoc. Prof. Dr. Samim ERHAN
	:Prof. Dr. Gülsen ÖNENGÜT
	:Prof. Dr. Sefa ERTÜRK
	:Prof. Dr. Eda EŞKUT

This thesis presents a measurement of the WZ invariant mass spectrum and search for new exotic particles decaying to the WZ final state with electrons and muons using an integrated luminosity of 4.8 fb^{-1} of 7 TeV data collected by the CMS experiment at the LHC in 2011. No significant excess is observed in the mass distribution of the WZ candidates compared to the background expectation from Standard Model processes. Since there is no evidence for WZ resonances, lower bounds at %95 Confidence Level (C.L.) are set on the mass of hypothetical particles decaying to the WZ final state in Sequential Standard Model (SSM).

Assuming the SSM, W¢ bosons with masses below 800 GeV have been excluded at %95 C.L.

Key Words: CMS, Muons, Electrons, LHC, Exotic particles

ÖZ

DOKTORA TEZİ

√s = 7 TeV'deki PROTON-PROTON ÇARPIŞMALARINDA WZ'e BOZUNAN W¢AYAR BOZONUNUN ARANMASI

Aytül ADIGÜZEL

ÇUKUROVA ÜNİVERSİTESİ
FEN BİLİMLERİ ENSTİTÜSÜ
FİZİK ANABİLİM DALI

Danışman :Prof. Dr. Ayşe POLATÖZ
İkinci Danışman :Assoc. Prof. Dr. Samim ERHAN
Yıl: 2014, Sayfa: 200
Jüri :Prof. Dr. Ayşe POLATÖZ
:Assoc. Prof. Dr. Samim ERHAN
:Prof. Dr. Gülsen ÖNENGÜT
:Prof. Dr. Sefa ERTÜRK
:Prof. Dr. Eda EŞKUT

Bu tezde 2011'de BHÇ'de CMS tarafından toplanan 7 TeV'lik 4.8 fb^{-1} toplam ışıklılık verisi kullanılarak WZ değişmez kütle spektrum ölçümü ve elektron ve muonlu WZ son durumlarına bozunan yeni egzotik parçacıkları arama sonuçları sunulmuştur. Standart Model proseslerinden beklenen fonlarla karşılaştırıldığında WZ adaylarının kütle dağılımında anlamlı bir fazlalık gözlenmemiştir. WZ resonanslarının varlığına dair anlamlı bir kanıt olmadığı için, Sequential Standart Model de WZ son durumuna bozunan kuramsal parçacıkların kütlesinde %95'lik güvenilirlik seviyesinde daha düşük sınırlar hesaplanmştır.

Sequential Standart Model göz önüne alındığında %95'lik güvenilirlik seviyesinde 800 GeV'nin aşağısındaki W¢bozonu kütleleri dışarlanmıştır.

Anahtar Kelimeler: CMS, Muonlar, Elektronlar, BHÇ, Egzotik parçacıklar

ACKNOWLEDGMENTS

I would like to thank my dear supervisor Prof. Dr. Ayşe POLATÖZ for her great guidance, encouragement and support during my MSc and PhD degrees. It was a pleasure for me to work with her. I am thankful for her patience and confidence in my work through the years of my study. I very much appreciate that she has found time for detailed proofreading of this thesis.

I owe a great debt of gratitude to Assoc. Prof. Dr. Samim ERHAN for his extraordinary support and guidance throughout the thesis work. I am grateful for his enormous enthusiasm and incredible patience in teaching and discussions since I have started to work within the CMS. It was a great opportunity for me to work with him and his help and encouragement was of great value throughout this analysis. He always showed me the best ways for my carrier. It was a great chance for me to have him as an advisor. He has been not only a mentor to me but also a model scientist to imitate.

I special thank Srecko MOROVIC for his help, valuable comments, suggestions and support during my studies. I wish to thank my Turkish team leader Prof. Dr. Gülsen ÖNENGÜT for her encouragement during my graduate studies. I am especially grateful for her critical reading of the thesis. I thank also Prof. Dr. Sefa ERTÜRK and Prof. Dr. Eda EŞKUT for their kindly reading and evaluating my thesis. I would like to thank to our high energy physics group members, Prof. Dr. Eda EŞKUT, Prof. Dr. Aysel KAYIŞ TOPAKSU and Prof. Dr. İsa DUMANOĞLU for their moral support and encouragement during my studies. I would like to thank to Prof. Dr. Pawel DE BARBARO for his support and his great guidance during I have been working on HCAL.

Special thanks are due to my dear friends Tülin VAROL, Sertaç ÖZTÜRK and Alaettin Serhan METE for sharing their optimistic attitude and encouragement even at my hard times and valuable comments, suggestions and support during working on this thesis.

I wish to thank to my dear friends and colleagues Kadri ÖZDEMİR, İlknur HOŞ, Çağlar ZORBİLMEZ, Semiray GİRGİS, Özlem ÖZKAN, Gülşah GÖLOĞLU and Güray ERTEĞİ for their support and contributions to keep my moral and motivation high.

A special thank you goes to my family: mother, father and my brother for their enormous love, understanding and support I have been getting through all my life.

Special thanks are to TAEK (project code: 2012K120260) who sponsored me during the time I have spent at CERN.

CONTENTS **PAGE**

LIST OF TABLES **PAGE**

LIST OF FIGURES **PAGE**

LIST OF ABBREVIATIONS

ALICE : A Large Ion Collider Experiment
ATLAS : A Toroidal LHC Apparatus
CDF : Collider Detector at Fermilab
CERN : Conceil Europeenne pour la Recherche Nucleaire
CL : Confidence Level
CTEQ : Coordinated Theoretical-Experimental Project on QCD
DAQ : Data AcQusition
ECAL : Electromagnetic CALorimeter
HCAL : Hadronic CALorimeter
HB : Hadronic Barrel
HE : Hadronic Endcap
HO : Hadronic Outer
HF : Hadronic Forward
LEP : Large Electron Positron Collider
LHC : Large Hadron Collider
LHCb : Large Hadron Collider Beauty Experiment
EWSB : ElectroWeak Symmetry Breaking
MC : Monte Carlo
PDF : Parton Density Function
QCD : Quantum Chromo Dynamics
QED : Quantum Electro Dynamics
SM : Standard Model
SSM : Sequential Standard Model
HLT : High Level Trigger

1. INTRODUCTION

In particle physics, a large amount of theoretical and experimental work has been carried out in order to understand the fundamental components of matter and establish description of their interactions for the last fifty years. These studies have led to a fundamental theory. This theory is called the *Standard Model* (SM). This model has been successfully tested over the past thirty years. Its predictions are consistent with all experimental data. On the other hand, the SM cannot answer some of the observed features of universe, such as the origin of the dark matter and the predominance of matter over antimatter.

The Large Hadron Collider (LHC) has been built to find the answers for this kind of unsolved questions. The LHC is expected to explore up to TeV energy scale. The existence of new pyhsics phenoma are predicted mostly as the extensions of the SM. This new energy scale will lead to the discovery of new particles and interactions to overcome the limitations of the SM.

After twenty years of designing, building and commissioning, the LHC delivered its first proton-proton collisions at the centre-of-mass energies of 0.9 TeV and successively at 2.36 TeV in November 2009. Then its performance is optimized and the first proton-proton collisions at the centre-of-mass energy of 7 TeV took place in March 2010. The Compact Muon Solenoid (CMS) experiment collected data up to November 2010 then a heavy ion (PbPb) run took place and was analysed. LHC delivered ~5fb^{-1} of integrated luminosity in 2011 at $\sqrt{s}$ = 7 TeV.

Understanding the nature of the electroweak symmetry breaking (EWSB) is one of the important challenges of particle physics today. The Higgs Mechanism is assumed to be the origin of the particle masses. Besides Higgs Mechanism, many extensions of the Standard Model (SM) try to explain the mechanism of EWSB. They are predicting as a consequence the existence of new gauge bosons in the TeV range, W' and Z'. This thesis describes an experimental search for such new physics using Compact Muon Solenoid (CMS).

In this thesis, the W' gauge bosons (as exotic WZ rezonances) in *pp* collisions at a centre-of-mass energy of 7 TeV has been searched via the trilepton signal in the CMS experiment. The main process is given as following:

$$pp \to W' \to W(\to \ell_1 \nu_{\ell_1}) Z(\to \ell_2^+ \ell_2^-)$$

where ℓ_1 and ℓ_2 can belong to identical or distinct families of leptons. The missing energy is carried away by the neutrinos. In the scattering process above ν_{ℓ_1} represents missing energy in the experiment. The background comes from the W and Z bosons and it is expected to be small.

Chapter 2 gives detailed information on theoretical context and presents the physics motivation to study the W' gauge boson. First of all, it gives a brief summary of the historical background. Then the most fundamental contemporary model in this field, the SM is given and finally possible models beyond the SM that might give rise to new particles are presented. The experimental context is described and brief overviews of the LHC and CMS detector are presented with respect to the studies in this analysis described in Chapter 3. Chapter 4 is dedicated to physics objects. The reconstruction algorithms are introduced to qualify the final candidates performances in this Chapter. The event selection procedure is described and the measurement of WZ mass spectrum in this analysis is covered in Chapter 5. It is dedicated to the analysis of the WZ decay channels looking only for muons and electrons final states. Then searches for new exotic particles are given in Chapter 6. Finally, the stability of response of Hadronic Forward (HF) and Hadronic Barrel (HB) detectors of HCAL Calorimeter will be introduced in Chapter 7.

2. THEORETICAL MOTIVATION

In this chapter theoretical motivation behind this study will be presented. At first, the historical background will be briefly given and then the Standard Model (SM) is introduced with the focus on the electroweak interaction. After the WZ production mechanism is described and motivations for its study are given, the properties of the W' models will be discussed in short. Finally, the goal of this work will be explained.

2.1. Historical Background

Elementary particle physics researches the smallest constituents of matter and their interactions. Great progress have been accomplished in this field since last 60 years. Discovery of the electron in cathode rays by J.J Thomson in 1897 is known to start the particle physics. In 1900s Planck started the quantum era and then in 1905 Albert Einstein started the relativistic era at 1905 (Novaes, 2000). Later, in 1916, his theory of general relativity which is relativistic generalization of Newton's earlier findings, is published.

Later in the 1940s, Richard P. Feynman, Julian Schwinger and Sin-Itiro Tomonaga perfected the quantum theory of electrodymanics, QED. It won them the Nobel Prize in 1965. Going back to the 1890s, the first observation of β^- decay puzzled the scientists. Since this phenomenon wouldn't fit into classical physics, it remained unexplained until the 1930s. The first theory which explains this observation is introduced by Enrico Fermi in 1934 (Novaes, 2000).

Later in the 1950s the first theory for the weak force was refined by Tsung-Dao Lee and Chen N. Yang. In the 1960s a model of particles physics, currently known as the SM which predicted many quantities, is proposed by Sheldon Glasgow, Steven Weinberg and Abdus Salam (Glashow, 1961; Salam, 1967; Weinberg 1967; Glashow 1970). In 1967 Abdus Salam and Steven Weinberg independently revised Glashow's theory which allows for the masses for the W and Z particles that arise through spontaneous symmetry breaking with the Higgs mechanism (Weinberg, 1967). Salam, Glashow and Weinberg won the Nobel Prize in Physics in 1979 for their work. The other remarkable phenomena in particle physics are the discoveries of the electroweak bosons W and Z in 1983, and the observation of the heaviest quark, the top quark in 1995 and the τ neutriono in 2000.

2.2. Standard Model

The forces in the Standard Model (SM) are mediated by gauge bosons associated with the symmetry groups

$$SU(3)_{Color} \times SU(2)_L \times U(1)_Y \tag{2.1}$$

The $SU(3)_{Color}$ term describes the gluonic force of the strong interactions (Wilczek, 1982). Because the $SU(3)_{Color}$ gauge invariance is unbroken, the eight associated gluons remain massless. The theory of quarks interacting by exchange of massless gluons is called Quantum Chromodynamics (QCD). It is parallel with quantum electrodynamics (QED) and also has unbroken gauge invariance and an associated massless gauge boson- the photon.

The $SU(2)_L \times U(1)_Y$ factors describe the unified electroweak interactions (Glashow, 1961). The subscript L indicates coupling to left-handed fermions. The subscript Y refers to the "weak hypercharge" and it is determined from the electric charge and 3rd component of isospin. The relation among them is given by

$$Q = T_{3L} + \frac{Y}{2} \tag{2.2}$$

Unlike the $SU(3)_{Color}$ term, the $SU(2)_L \times U(1)_Y$ invariance is broken (Weinberg, 1967; Salam, 1968) down to the $U(1)_{EM}$ subgroup, the unbroken gauge invariance of electromagnetism. As a result, three of the four gauge bosons, W^+,

W^-, and Z of $SU(2)_L \times U(1)_Y$ are massive while the fourth, the photon, γ, remains massless (Chanowitz, 1988).

SM describes the properties of all elementary particles and their interactions (Nakamura, 2010; Novaes, 2000). The SM particle content is split into two parts: *fermions* with spin ½ which constitute matter and *bosons* with spin 1 which carry forces. According to their properties, fermions are divided into *quarks* and *leptons* and organized into families of identical structure and differing only for the particle mass.

There are six types of leptons and six types of quarks. The leptons are called electron (e), electron-neutrino (ν_e), muon (μ), muon-neutrino (ν_μ), tau (τ) and tau-neutrino (ν_τ). The quarks are called up (u), down (d), charm (c), strange (s), top (t) and bottom (b). They can be grouped into three families or generations. Each generation contains two leptons and two quarks. Each extra generation is an exact copy of the first one. But it has increasing particle mass. An overview of all fermions, leptons and quarks is given in Table 2.1. The up quark carries an electric charge of +2/3, while down quark has -1/3. A proton consists of two up quarks and one down quark with an electric charge of +1. A neutron consists of two down quarks with one up quark with neutral charge. The hydrojen atom which is known as the most bacis atom consists of only one proton and one electron. The first generation of massive fermions (u, d, e) build all stable matter. They were the first ones to be discovered. Besides electric charge, the quarks have also three color charges: *red*, *green* and *blue*. This is relevant to their interaction. They interact via strong nuclear force which binds them together inside mesons and baryons (hadrons) as known nuclear particles. Every quark appears in three different color states, belonging to a $SU(3)_C$ triplet, while the leptons are colorless $SU(3)_C$ singlets. The leptons don't carry color charge, but carry electric charge.

Fermions interact through the exchange of the gauge bosons. For each fermion, there exists a corresponding anti-particle which has exactly same quantum number as the fermions but it's charge reverted.

Among the bosons with spin 1, the photon (γ) is mediator of the electromagnetic force, the W and Z are mediators of the weak force and the gluon (g) is mediator of the strong force.

Table 2.1. Fundamental fermions of the Standard Model (Nakamura, 2010).

Fermion Generations	Q_{EM}	Y	T^3	Interaction
Leptons				
$\begin{pmatrix} \nu_{eL} \\ e_L \end{pmatrix}$ $\begin{pmatrix} \nu_{\mu L} \\ \mu_L \end{pmatrix}$ $\begin{pmatrix} \nu_{\tau L} \\ \tau_L \end{pmatrix}$ e_R μ_R τ_R	0 -1 -1	-1 -1 -2	+1/2 -1/2 0	weak weak, EM weak, EM
Quarks				
$\begin{pmatrix} u_L \\ d'_L \end{pmatrix}$ $\begin{pmatrix} c_L \\ s'_L \end{pmatrix}$ $\begin{pmatrix} t_L \\ b'_L \end{pmatrix}$ u_R c_R t_R d_R s_R b_R	+2/3 -1/3 +2/3 -1/3	+1/3 +1/3 +4/3 -2/3	+1/2 -1/2 0 0	weak, EM, strong weak, EM, strong weak, EM, strong weak, EM, strong

Even though the photon is the mediator of the electromagnetic force, it doesn't carry electric charge, however gluons carry color charge and there are a total of eight of them. All force carriers are massless, except the W and Z bosons in the SM. All fundamental gauge bosons of SM are listed in Table 2.2. Although the graviton which is the mediator of the gravitational interaction is not included in the SM, it is listed in Table 2.2. In addition, a scalar boson, the Higgs (H^0) which was predicted by SM to account for the masses of the fermions and the vector bosons, is also included in the Table 2.2.

So in total, at least 61 "elementary particles", 36 quarks and anti-quarks, 12 leptons and anti-leptons, 12 force carriers and the Higgs boson are predicted by SM.

Although the SM describes with high precision almost all known phenoma in high energy physics, there are several unresolved problems. The following questions remain problematic in the SM:

- The reason why there are only three fermions families is unknown.

- It doesn't include the *gravitational interaction*, so the theory isn't complete.

Table 2.2. Fundamental gauge bosons of the Standard Model. The table also includes the predicted Higgs boson and the Graviton (not included by the SM).

Interaction	boson	spin	mass(GeV/c^2)	charge(q_e)
Electromagnetic	Photon, γ	1	0	0
Weak	$W^{\pm}$ Z	1 1	80.4 91.2	± 1 0
Strong	Gluon, g	1	91.2	0
	Higgs, H	0	> 114 (?)	0
Gravity	Graviton, G	2	0	0

- The neutrinos are massless in the SM. But recent experiments (Fukuda et al., 2000; Ambrosio, 2001) have provided evidence that they have very small but non-zero neutrino masses. The nature of them is unknown as well as the mechanism of mass generation and the reason why the masses are so small compared with the charged leptons.
- It has a large number of free parameters which includes coupling constants and particle masses. But those can not be calculated using model itself.
- The large gap between the energy scale ($\approx$ 100 GeV, EW scale) at which electroweak forces are unified and the energy scale ($\approx 10^{19}$ GeV, the Planck scale) where quantum gravity is called as the *hierarchy problem*. The SM doesn't explain the problem.
- It doesn't explain the origin of the Charge-Parity violation, responsible for the matter-antimatter asymmetry in the universe. However, the existence of non-relativistic, neutral, non-baryonic dark matter is observed at many astrophysical observations. Since neutrinos are not massive enough to explain the observations, a new candidate for this cold dark matter is needed.

- It doesn't explain the reason why the coupling strengths of the weak, strong and electromagnetic interactions don't unify at the some energy scale.

2.2.1. Right- and Left-Handed Fermions

When we discuss some properties of the fermionic helicity states, the Dirac spinors are given as following at high energies (i.e. for $E >> m$),

$$u(p,s), \quad \text{and} \quad v(p,s) \equiv C\ \bar{u}^T(p,s) = i\gamma_2 u^*(p,s),$$

are eigenstates of the γ_5 matrix.

The helicity $+1/2$ (right-handed, R) and the helicity $-1/2$ (left-handed, L) states satisfy

$$u_{\substack{R\\L}} = \frac{1}{2}(1 \pm \gamma_5)u \quad \text{and} \quad v_{\substack{R\\L}} = \frac{1}{2}(1 \pm \gamma_5)v$$

It is convenient to define the *helicity projectors*:

$$L \equiv \frac{1}{2}(1-\gamma_5), \qquad R \equiv \frac{1}{2}(1+\gamma_5) \tag{2.3}$$

which satisfy the usual properties of projection operators,

$$L+R = 1,$$
$$RL = LR = 0,$$
$$L^2 = L,$$
$$R^2 = R.$$

For the conjugate spinors we have,

$$\bar{\psi}_L = (L\psi)^\dagger \gamma_0 = \psi^\dagger L^\dagger \gamma_0 = \psi^\dagger L \gamma_0 = \psi^\dagger \gamma_0 R = \bar{\psi} R$$
$$\bar{\psi}_R = \bar{\psi} L\,.$$

Fermion mass term mixes right- and left-handed fermion components, *i.e.*

$$\bar{\psi}\psi = \bar{\psi}_R \psi_L + \bar{\psi}_L \psi_R\,. \tag{2.4}$$

On the other hand, the electromagnetic (vector) current, does not mix those components, *i.e.*

$$\bar{\psi}\gamma^\mu \psi = \bar{\psi}_R \psi_L + \bar{\psi}_L \psi_R\,, \tag{2.5}$$

Finally, the $(V - A)$ fermionic weak current can be written in terms of the helicity states as,

$$\bar{\psi}_L \gamma^\mu \psi_L = \bar{\psi} R \gamma^\mu L \psi = \bar{\psi}\gamma^\mu L^2 \psi = \bar{\psi}\gamma^\mu L \psi = \frac{1}{2}\bar{\psi}\gamma^\mu (1 - \gamma_5)\psi\,, \tag{2.6}$$

it shows that only the left-handed fermions play a role in weak interactions (Novaes, 2000).

2.2.2. The Gauge Principle, Gauge Invariance and Lagrangians

As it is well known, symmetry has always played a very important role in the improvement of physics. From the spacetime symmetry of special relativity up to the internal and gauge invariances, the symmetries have mapped out the route to most of the physical theories in this last century.

The Noether's theorem provides an important result for field theory and particle physics. If an action is invariant under some group of transformations (symmetry), there exist one or more conserved quantities (constants of motion) which are associated to these transformations. In this sense, symmetries which are established, by Noether's theorem imply conservation laws.

The following natural question would be asked: upon imposing to a given Lagrangian the invariance under a certain symmetry, would it be possible to determine the form of the interaction among the particles? In other words, could symmetry also imply dynamics?

It happens in the best theory ever built to describe Nature known as Quantum Electrodynamics (QED). It has become a prototype of a successful quantum field theory. The existence and some of the properties of the gauge field (the photon) follow from a principle of invariance under *local gauge transformations* of the $U(1)$ group in QED.

The idea that this principle be generalized to other interactions was a possible dream for Salam and Ward who invented the gauge principle as the basis to construct the quantum field theory of interacting fields.

In fact, after some new and important ingredients were introduced to describe weak and strong interactions, those ideas could be just accomplished. The existence of very heavy weak gauge bosons require the new concept of spontaneous breakdown of the gauge symmetry and the Higgs Mechanism (Higgs, 1964; Englert, 1964; Guralnik, 1964) for weak interactions.

The gauge principle and the concept of gauge invariance are presented in quantum mechanics of a particle in the presence of an electromagnetic field (Aitchison and Hey, 1990). The Classical Hamiltonian that gives rise to Lorentz force ($\vec{F} = q\vec{E} + q\vec{v}\vec{B}$) is defined as:

$$H = \frac{1}{2m}\left(\vec{p} - q\vec{A}\right)^2 + q\phi, \tag{2.7}$$

where the electric and magnetic fields can be described in terms of the potentials $A^{\mu} = (\phi, \vec{A})$,

$$\vec{E} = -\vec{\nabla}\phi - \frac{\partial \vec{A}}{\partial t}, \qquad \vec{B} = \vec{\nabla} \times \vec{A}. \tag{2.8}$$

These fields remain exactly the same when we apply the *gauge transformation* (G) to the potentials:

$$\phi \to \phi' = \phi - \frac{\partial \chi}{\partial t}, \qquad \vec{A} \to \vec{A}' = \vec{A} + \vec{\nabla}\chi \tag{2.9}$$

When the Hamiltonian (2.7) is quantized by applying the usual prescription $\vec{p} \to -i\vec{\nabla}$, we get the Schrödinger equation for a particle in an electromagnetic field,

$$\left[\frac{1}{2m}\left(-i\vec{\nabla} - q\vec{A}\right)^2 + q\phi\right]\psi(x,t) = i\frac{\partial \psi(x,t)}{\partial t} \tag{2.10}$$

which can be written in a compact form as

$$\frac{1}{2m}(-i\vec{D})^2\psi = iD_0\psi \tag{2.11}$$

The equation (2.11) is equivalent to make the substitution

$$\vec{\nabla} \to \vec{D} = \vec{\nabla} - iq\vec{A}, \qquad \frac{\partial}{\partial t} \to D_0 = \frac{\partial}{\partial t} + iq\phi \tag{2.12}$$

in the free Schrödinger equation.

If the gauge transformation is made, $(\phi, \vec{A}) \xrightarrow{G} (\phi', \vec{A}')$, given by (2.9), the new field ψ' which is the solution of

$$\frac{1}{2m}(-i\vec{D}')^2\psi' = iD_0'\psi,$$

doesn't describe the same physics. However, we can recover the invariance of our theory by making, at the same time, the phase transformation in the matter field

$$\psi' = \exp(iq\chi)\psi \tag{2.13}$$

with the same function $\chi = \chi(x,t)$ used in the transformation of electromagnetic fields (2.9). The derivative of ψ' transforms as,

$$\begin{aligned}\vec{D}'\psi' &= \left[\vec{\nabla} - iq(\vec{A} + \vec{\nabla}\chi)\right] \exp\ (iq\chi)\ \psi \\ &= \exp\ (iq\chi)\ (\vec{\nabla}\psi) + iq(\vec{\nabla}\chi)\ \exp\ (iq\chi)\ \psi \\ &\quad -iq\vec{A}\exp\ (iq\chi)\ \psi - iq(\vec{\nabla}\chi)\exp\ (iq\chi)\ \psi \\ &= \exp\ (iq\chi)\ \vec{D}\psi,\end{aligned} \tag{2.14}$$

and the same way, we have for D_0,

$$D_0'\psi' = \exp\ (iq\chi)\ D_0\psi \tag{2.15}$$

Now the field ψ (2.13) and its derivaties $\vec{D}\psi$ (2.14), and $D_0\psi$ (2.15), all transform exactly in the same way: they are all multiplied by the same phase factor.

Therefore, the Schrödinger equation (2.11) for ψ' becomes

$$\begin{aligned}\frac{1}{2m}(-i\vec{D}')^2\psi' &= \frac{1}{2m}(-i\vec{D}')(-i\vec{D}'\psi') \\ &= \frac{1}{2m}(-i\vec{D}')\left[-i\exp\ (iq\chi)\ \vec{D}\psi\right] \\ &= \exp\ (iq\chi)\frac{1}{2m}(-i\vec{D})^2\ \psi \\ &= \exp\ (iq\chi)\ (iD_0)\ \psi = iD_0 = iD_0'\psi'.\end{aligned}$$

and now both ψ and ψ' describe the same physics, since $|\psi|^2 = |\psi'|^2$. In order to get invariance for all observables, it should be assured that the following substitution is made:

$$\vec{\nabla} \to \vec{D}, \qquad \frac{\partial}{\partial t} \to D_0,$$

For instance, the current

$$\vec{J} \;\alpha\; \psi^*(\vec{\nabla}\psi) - (\vec{\nabla}\psi)^*\psi,$$

becomes also gauge invariant with this substitution since

$$\psi^{*\prime}(\vec{D}'\psi') = \psi^* \exp\,(-iq\chi)\,\exp\,(iq\chi)\,(\vec{D}\psi) = \psi^*(\vec{D}\psi)$$

After it is shown how to obtain a gauge invariant quantum description of a particle in an electromagnetic field, could the argument be reversed? That is: when we demand that a theory is invariant under a spacetime dependent phase transformation, can this procedure impose the specific form of the interaction with the gauge field? In other saying, can the *symmetry imply dynamics*?

The Standard Model is a *relativistic quantum field theory*. It means that it respects special relativity and free fermions (bosons) can be described by the Dirac (Klein-Gordon) equation. The equations of motions for fermions can be derived from the Dirac free Lagrangian

$$L_\psi = \overline{\psi}(i\partial - m)\psi,$$

that is not invariant under the *local gauge transformation*,

$$\psi \to \psi' = \exp\,[-i\alpha(x)]\,\psi,$$

since

$$L_\psi \to L'_\psi = L_\psi + \overline{\psi}\gamma_\mu \psi(\partial^\mu \alpha),$$

However, if the *gauge filed* A_μ is introduced through the *minimal coupling*

$$D_\mu \equiv \partial_\mu + ieA_\mu,$$

and the same time, require that A_μ transforms like

$$A_\mu \to A'_\mu = A_\mu + \frac{1}{e}\partial_\mu \alpha. \tag{2.16}$$

We have

$$\begin{aligned} L_\psi \to L'_\psi &= \overline{\psi}' \left[(i\partial - eA') - m \right] \psi' \\ &= \overline{\psi} \exp(+i\alpha) \left[i\partial - e\left(A + \frac{1}{e}\partial\alpha \right) - m \right] \exp(-i\alpha)\psi \\ &= L_\psi - e\overline{\psi}\gamma_\mu \psi A^\mu. \end{aligned} \tag{2.17}$$

The coupling between ψ (*e.g.* electrons) and the gauge field A_μ (photon) arises naturally when the invariance is required under local gauge transformations of the kinetic-energy terms in the free fermion Lagrangian.

Since, the electromagnetic strength tensor

$$F_{\mu\nu} \equiv \partial_\mu A_\nu - \partial_\nu A_\mu, \tag{2.18}$$

is invariant under the gauge transformation (2.16), so is the Lagrangian for free gauge field,

$$L_A = -\frac{1}{4} F_{\mu\nu} F^{\mu\nu}, \tag{2.19}$$

This Lagrangian together with (2.17) describes the Quantum Electrodynamics.

It should be point out that a hypothetical mass term for the gauge field,

$$L_A^m = -\frac{1}{2} A_\mu A^\mu,$$

is not invariant under the transformation (2.16). Therefore, something else should be necessary to describe massive vector bosons in a gauge invariant way, preserving the renormalizability of the theory.

2.2.3. Gauge Invariance for Non-Abelian Groups

As suggested by Heisenberg (Heisenberg, 1932) in 1932, proton and neutron can be regarded as degenerate under nuclear interactions since their mass are quite similar and electromagnetic interaction is negligible.

Therefore any arbitrary combination of their wave function would be equivalent,

$$\psi \equiv \begin{pmatrix} \psi_p \\ \psi_n \end{pmatrix} \rightarrow \psi' = U\psi,$$

where U is a unitary transformation ($U^+U = UU^+ = 1$) to preserve normalization (probability). Morever, if $\det|U| = 1$, U represents the Lie group *SU(2)*:

$$U = \exp\left(-i\frac{\boldsymbol{\tau}^a}{2}\alpha^a\right) \cong 1 - i\frac{\boldsymbol{\tau}^a}{2}\alpha^a,$$

where $\boldsymbol{\tau}^a$, $a = 1,2,3$ are the Pauli matrices.

Yang and Mills (Yang and Mills, 1954) introduced the idea of local gauge isotopic invariance in quantum field theory in 1954 as following: "*The differentiation between a neutron and a proton is then a purely arbitrary process. As usually conceived, however, this arbitrariness is subject to the following limitation: once one chooses what to call a proton, what a neutron, at one space-time point, one is then not free to make any choices at the other space points. It seems that this is not consistent with the localized field concept that underlies the usual physical theories.*"

Following their arguments, we should preserve our freedom to choose what to call a proton or a neutron *no matter when or where we are*. This can be implemented by requiring that the gauge paramaters depend on the spacetime points, *i.e.* $\alpha^a \to \alpha^a(x)$.

This idea was generalized by Utiyama (Utiyama, 1956) in 1956 for any non-Abelian group G with generators t_a satisfying the Lie algebra (Abers and Lee, 1973),

$$\left[t_a, t_b\right] = iC_{abc}t_c,$$

with C_{abc} being the structure constant of the group.

The Lagrangian L_ψ should be invariant under *the matter field transformation*

$$\psi \to \psi' = \Omega\psi,$$

with

$$\Omega \equiv \exp\,[-iT^a\alpha^a(x)],$$

where T^a is a convenient representation (*i.e.* according to the fields ψ) of the generators t^a.

When introducing one gauge field for each generator, the *covariant derivative* is defined as

$$D_\mu \equiv \partial_\mu - igT^a A_\mu^a \ .$$

Since the covariant derivative transforms just like the matter field, *i.e.* $D_\mu\psi \rightarrow \Omega(D_\mu\psi)$, this will ensure the invariance under the local non-Abelian gauge transformation for the terms containing the fields and its gradients as long as the *gauge field transformation* is

$$T^a A_\mu^a \rightarrow \Omega \left(T^a A_\mu^a + \frac{i}{g}\partial_\mu \right) \Omega^{-1}$$

or, in infinitesimal form, *i.e.* for $\Omega \approx 1 - iT^a \alpha^a(x)$,

$$A_\mu^{a'} = A_\mu^a - \frac{1}{g}\partial_\mu \alpha^a + C_{abc}\alpha^b A_\mu^c \ .$$

Finally, the *strength tensor* (2.18) is generalized for a non-abelian Lie group,

$$F_{\mu\nu}^a \equiv \partial_\mu A_\nu^a - \partial_\nu A_\mu^a + gC_{abc}A_\mu^b A_\nu^c \ , \tag{2.20}$$

which transforms like $F_{\mu\nu}^{a\,'} \rightarrow F_{\mu\nu}^a + C_{abc}\alpha^b F_{\mu\nu}^c$. Therefore, the invariant kinetic term for the gauge bosons, can be written as

$$L_A = -\frac{1}{4} F_{\mu\nu}^a F^{a\mu\nu} \ , \tag{2.21}$$

and is invariant under the local gauge transformation, However, a mass term for the gauge bosons like

$$A_\mu^a A^{a\mu} \rightarrow \left(A_\mu^a - \frac{1}{g}\partial_\mu \alpha^a + C_{abc}\alpha^b A_\mu^c \right)\left(A^{a\mu} - \frac{1}{g}\partial_\mu \alpha^a + C_{ade}\alpha^d A^{e\mu} \right),$$

is still not gauge invariant.

It is noted that since

$$F \;\alpha\; (\partial A - \partial A) + gAA\,,$$

unlike the Abelian case, there is a new feature: the gauge fields have triple and quadratic self-couplings,

$$L_A \;\alpha\; (\partial A - \partial A)^2 + g(\partial A - \partial A)AA + gAAAA\,.$$

In this equation, first, second and third terms respectively show propagator, triple and quartic (Novaes, 2000).

The Gauge theories are in the heart of particle physics. As it is mentioned before the SM is a non-abelian gauge theory with the symmetry group $SU(3)\times SU(2)\times U(1)$ and it has a total of twelve gauge bosons as the photon, three weak bosons and eight gluons which are introduced as force carriers in Table 2.1 and mediators in Table 2.2. But here there is an interesting point. The principle of local gauge invariance works very properly for the strong and electromagnetic forces because the mass term in the lagrangian had to be set zero which is the case for their carriers. But it is not the case for the weak carriers. This brings the discussion to *spontaneous symmetry breaking* and the *Higgs Mechanism.*

2.2.4. Spontaneous Symmetry Breaking

The SM can not account for massive fermions and bosons as observed in Nature, *i.e* all fermions and bosons must be massless. From (2.4), where a non-zero mass would mix up the left- and right-handed fermions and from (2.17), where adding a $\frac{1}{2}mA_\mu A^\mu$ term for the bosons would break the gauge invariance. In order to allow massive particles, one needs to break the electroweak symmetry in such way that all successful symmetry predictions are still preserved. In addition, the $W^\pm$ and Z bosons must acquire large masses while the photon must remain massless in the gauge boson sector. This can be achieved through a mechanism which is called *spontaneous symmetry breaking* (Englert and Brout, 1964; Higgs, 1964; Guralnik et al., 1964).

In general exact symmetries give rise to exact conservation laws. In this case both the Lagrangian and the vacuum (the ground state of the theory) are invariant. However, there are some conservation laws which are not exact, *e.g.* isospin, strangeness, etc. These situations can be described by adding to the invariant Lagrangian (L_{sym}) a small term that breaks this symmetry (L_{sb}),

$$L = L_{sym} + \varepsilon L_{sb}.$$

Another situation occurs when the system has a Lagrangian that is invariant and a non-invariant vacuum. A classic example of the situation is provided by a ferromagnet where the Lagrangian describing the spin-spin interaction is invariant under tridimensional rotations. For temperatures above the ferromagnetic transition temperature (T_C) the spin system is completely disordered (paramagnetic phase) and therefore the vacumm is also $SO(3)$ invariant (Fig 2.1 (a)).

However, for temperatures below T_C (ferromagnetic phase) a spontaneous magnetisation of the system occurs, aligning the spins in some specific direction (Fig 2.1 (b)). In this case, the vacuum is not invariant under the $SO(3)$ group. This symmetry is broken to $SO(2)$, representing the rotation of the whole system around the spin directions.

When analyzing the simple example of scalar self-interacting real field with Lagrangian,

$$L = \frac{1}{2}\partial_\mu \phi \partial^\mu \phi - V(\phi) \tag{2.22}$$

with

$$V(\phi) = \frac{1}{2}\mu^2\phi^2 + \frac{1}{4}\lambda\phi^4 \tag{2.23}$$

The Gibbs free energy density is analogous to $V(\phi)$ with ϕ playing the role of the average spontaneous magnestism M in the theory of the phase transition of a ferromagnet.

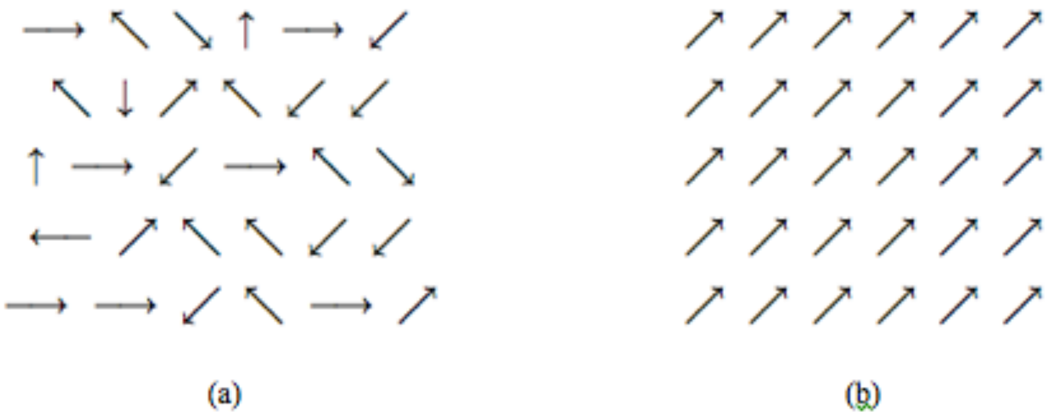

Figure 2.1. Representation of the spin orientation in the paramagnetic (a) and ferromagnetic (b) phases.

The whole Lagrangian (2.22) is invariant under the discrete transformation

$$\phi \rightarrow -\phi \tag{2.24}$$

Is the vacuum also invariant under this transformation? The vacuum (ϕ_0) can be obtained from the Hamiltonian

$$\mathrm{H} = \frac{1}{2}[(\partial_0\phi)^2 + (\nabla\phi)^2] + V(\phi) \tag{2.25}$$

In here ϕ_0 = *constant* corresponds to the minimum of $V(\phi)$ and consequently to the energy:

$$\phi_0(\mu^2 + \lambda\phi_0{}^2) = 0.$$

Since λ should be positive to guarantee that H is bounded, the minimum depends on the sign of μ. For $\mu^2 > 0$, we have just one vacuum at $\phi_0 = 0$ and it is also invariant under 2.24 (see Fig. 2.2 (a)). However, for $\mu^2 < 0$, we have two vacuum states corresponding to $\phi_0^{\pm} = \pm\sqrt{-\mu^2/\lambda}$ (see Fig. 2.2 (b)). This case corresponds to a wrong sign for the mass term.

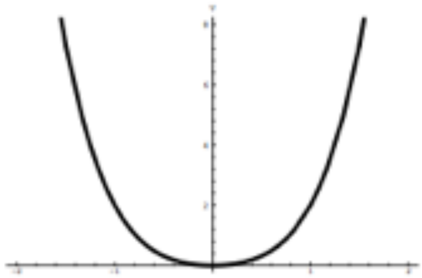

(a)

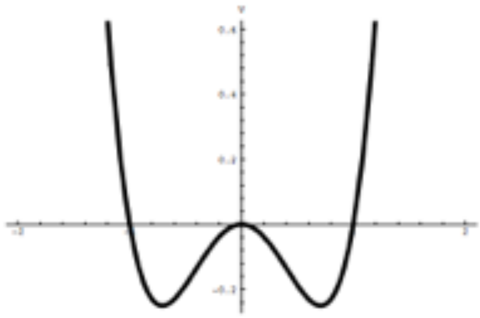

(b)

Figure 2.2. Scalar potential (2.23) for $\mu^2 > 0$ (a) and for $\mu^2 < 0$ (b).

Since the Lagrangian is invariant under (2.24) the choice between ϕ_0^+ or ϕ_0^- is irrelevant. Nevertheless, once one choice is made (*e.g* $v = \phi_0^+$) the symmetry is *spontaneously broken* since L is invariant but the vacumm is not.

Defining a new field ϕ' by shifting the old field by $v = \sqrt{-\mu^2/\lambda}$,

$$\phi' \equiv \phi - v,$$

Making theory suitable for small oscillations around the vacumm state, the vacuum of the new field $\phi_0' = 0$ is verified. The Lagrangian becomes:

$$L = \frac{1}{2}\partial_\mu \phi' \partial^\mu \phi - \frac{1}{2}\left(\sqrt{-2\mu^2}\right)^2 \phi'^2 - \lambda v \phi'^3 - \frac{1}{4}\lambda \phi'^4 .$$

The Lagrangian describes a scalar field ϕ' with real and positive mass, $M_{\phi'} = \sqrt{-2\mu^2}$, but it lost the original symmetry due to the ϕ'^3 term.

A new interesting phenomenon happens when a *continuous* symmetry is spontaneously broken. When analyzing the case of a charged self-interacting scalar field,

$$L = \partial_\mu \phi^* \partial^\mu \phi - V(\phi^* \phi) , \tag{2.26}$$

with a similar potential,

$$V(\phi^* \phi) = \mu^2 (\phi^* \phi) + \lambda (\phi^* \phi)^2 \tag{2.27}$$

it is noticed that the Lagrangian (2.26) is invariant under the *global phase* transformation

$$\phi \rightarrow \exp(-i\theta)\phi .$$

When we redefine the complex field in terms of two real fields by

$$\phi = \frac{(\phi_1 + \phi_2)}{\sqrt{2}}$$

the Lagrangian (2.26) becomes

$$L = \frac{1}{2}(\partial_\mu \phi_1 \partial^\mu \phi_1 + \partial_\mu \phi_2 \partial^\mu \phi_2) - V(\phi_{1,}\phi_2) \tag{2.28}$$

which is invariant under $SO(2)$ rotations,

$$\begin{pmatrix} \phi_1 \\ \phi_2 \end{pmatrix} \rightarrow \begin{pmatrix} \cos\theta & -\sin\theta \\ \sin\theta & \cos\theta \end{pmatrix} \begin{pmatrix} \phi_1 \\ \phi_2 \end{pmatrix}.$$

For $\mu^2 > 0$ the vacuum is at $\phi_1 = \phi_2 = 0$, and for small oscillations,

$$L = \sum_{i=1}^{2} \frac{1}{2}(\partial_\mu \phi_i \partial^\mu \phi_i - \mu^2 \phi_i^2),$$

which means that we have two scalar fields ϕ_1 and ϕ_2 with mass $m^2 = \mu^2 > 0$.

In the case of $\mu^2 < 0$, we have a continuum of distinct vacuum (see Fig. 2.3 (a)) located at

$$\langle |\phi^2| \rangle = \frac{\left(\langle \phi_1 \rangle^2 + \langle \phi_2 \rangle^2 \right)}{2} = \frac{-\mu^2}{2\lambda} \equiv \frac{v^2}{2} \tag{2.29}$$

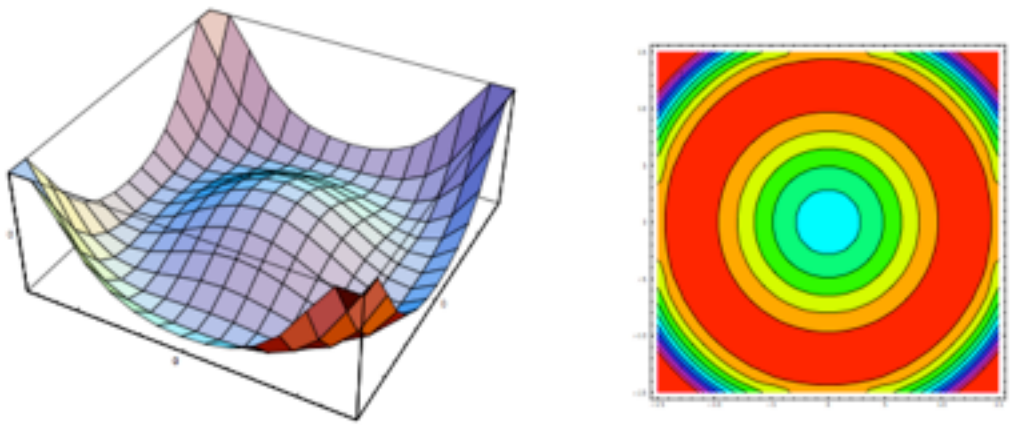

(a) (b)

Figure 2.3. The potential $V(\phi_1,\phi_2)$ (a) and its contour plot (b).

We can see from the contour plot (Fig 2.3 (b)) that the vacuum are also invariant under $SO(2)$. However, this symmetry is spontaneously broken when we choose a particular vacuum. When we choose, for instance, the configuration,

$$\phi_1 = v, \qquad \phi_2 = 0$$

the new fields, suitable for small perturbations, can be defined as,

$$\phi_1' = \phi_1 - v\,,\ \phi_2' = \phi_2 .$$

In terms of these new fields the Lagrangian (2.28) becomes,

$$L = \frac{1}{2}\partial_\mu \phi_1' \partial^\mu \phi_1' - \frac{1}{2}(-2\mu^2)\phi_1'^2 + \frac{1}{2}\partial_\mu \phi_2' \partial^\mu \phi_2' + \text{ interactions terms.}$$

Finally we define in the particle spectrum a scalar field ϕ_1' with real and positive mass and a massless scalar boson (ϕ_2'). This could be seen Fig. 2.3 (b), when we consider the mass matrix in tree approximation,

$$M_{ij}^2 = \frac{\partial^2 V(\phi_1' \phi_2')}{\partial \phi_i' \partial \phi_j'} \Big|_{\phi' = \phi_0'} .$$

The second derivative of $V(\phi_1', \phi_2')$ in the ϕ_2' direction corresponds to the zero eigenvalue of the mass matrix, while for ϕ_1' it is positive (Novaes, 2000).

This is an example of the prediction of the so called Goldstone theorem (Goldstone, 1961; Nambu, 1960) which states that when an exact continuous global symmetry is spontaneously broken, *i.e* it is not a symmetry of the physical vacuum, the theory contains one massless scalar particle for each broken generator of the original symmetry group.

2.2.5. The Electroweak Interaction

The gauge group should be able to unify the electromagnetic and weak interactions. First of all the charged weak current for leptons will be looked for. Since electron-type and muon-type lepton numbers are separately conserved, they must form separate represantations of the gauge group. Therefore ℓ refers to any lepton flavor ($\ell = e,\mu,\tau$), and the final Lagrangian will be given by a sum over all these flavors.

From Eq. (2.6), for a generic lepton, the weak current is given by,

$$J_\mu^+ = \bar{\ell}\partial_\mu(1-\gamma_5\nu) = 2\bar{\ell}_L\gamma_\mu\nu_L \qquad (2.30)$$

The left-handed isospin doublet ($T = 1/2$) is,

$$\mathrm{L} \equiv \begin{pmatrix} \nu \\ \ell \end{pmatrix}_L = \begin{pmatrix} L\nu \\ L\ell \end{pmatrix} = \begin{pmatrix} \nu_L \\ \ell_L \end{pmatrix}, \qquad (2.31)$$

where the $T_3 = +1/2$ and $T_3 = -1/2$ componets are the left-handed parts of the neutrino and of the charged lepton respectively. Since, there is no right-handed components for the neutrino (at the moment, it is considered that the neutrinos are massless), the right-handed part of the charged lepton is accommodated in a weak isospin singlet ($T = 0$)

$$\mathrm{R} = R\ell = l_R . \qquad (2.32)$$

The charged weak current (2.30) can be written in terms of leptonic isospin currents:

$$J_\mu^i = \bar{\mathrm{L}}\gamma_\mu \frac{\tau^i}{2}\mathrm{L},$$

where τ^i are the Pauli matrices. They are given as following in an explicit form,

$$J_\mu^1 = \frac{1}{2}\left(\bar{\nu}_L\,\bar{\ell}_L\right)\gamma_\mu \begin{pmatrix} 0 & 1 \\ 1 & 0 \end{pmatrix}\begin{pmatrix} \nu_L \\ \ell_L \end{pmatrix} = \frac{1}{2}\left(\bar{\ell}_L\gamma_\mu\nu_L + \bar{\nu}_L\gamma_\mu\ell_L\right),$$

$$J_\mu^2 = \frac{1}{2}\left(\bar{\nu}_L\,\bar{\ell}_L\right)\gamma_\mu \begin{pmatrix} 0 & -i \\ i & 0 \end{pmatrix}\begin{pmatrix} \nu_L \\ \ell_L \end{pmatrix} = \frac{i}{2}\left(\bar{\ell}_L\gamma_\mu\nu_L - \bar{\nu}_L\gamma_\mu\ell_L\right),$$

$$J_\mu^3 = \frac{1}{2}\left(\bar{\nu}_L\,\bar{\ell}_L\right)\gamma_\mu \begin{pmatrix} 1 & 0 \\ 0 & -1 \end{pmatrix}\begin{pmatrix} \nu_L \\ \ell_L \end{pmatrix} = \frac{1}{2}\left(\bar{\nu}_L\gamma_\mu\nu_L - \bar{\ell}_L\gamma_\mu\ell_L\right).$$

Therefore, the weak charged current (2.30), that couples with intermediate vector boson W_μ^-, can be written in terms of J^1 and J^2 as,

$$J_\mu^+ = 2(J_\mu^1 - iJ_\mu^2).$$

In order to accommodate the third (neutral) current J^3, the *hypercharge current* can be defined by,

$$J_\mu^Y \equiv -(\bar{\mathsf{L}}\,\gamma_\mu\,\mathsf{L} + 2\,\bar{\mathsf{R}}\,\gamma_\mu\,\mathsf{R}) = -(\bar{\nu}_L\gamma_\mu\nu_L + \bar{\ell}_L\gamma_\mu\ell_L + 2\bar{\ell}_R\gamma_\mu\ell_R)$$

The *electromagnetic current* can be written as

$$J_\mu^{em} = -\bar{\ell}\gamma_\mu\ell = -(\bar{\ell}_L\gamma_\mu\ell_L + \bar{\ell}_R\gamma_\mu\ell_R) = J_\mu^3 + \frac{1}{2}J_\mu^Y.$$

It should be noticed that neither T_3 nor Q commute with $T_{1,2}$. However, the 'charges' associated to the currents J^i and J^Y,

$$T^i = \int d^3x J_0^i \qquad \text{and} \qquad Y = \int d^3x J_0^Y,$$

satisfy the algebra of the $SU(2)\otimes U(1)$ group:

$$[T^i, T^j] = i\varepsilon^{ijk}T^k, \quad \text{and} \quad [T^i, Y] = 0 \qquad ,$$

and the Gell-Mann-Nishijima relation between Q and T_3 emerges in a natural way,

$$Q = T_3 + \frac{1}{2}Y. \tag{2.33}$$

The weak hypercharge of the doublet ($Y_L = -1$) and of the fermion singlet ($Y_R = -2$) can be defined with the aid of (2.33).

When building a general gauge theory, the candidate for the gauge group have just been chosen as $SU(2)\otimes U(1)$. The next step is to introduce the *gauge fields* corresponding to each generator, that is,

$$SU(2)_L \rightarrow W_\mu^1, W_\mu^2, W_\mu^3,$$
$$U(1)_Y \rightarrow B_\mu.$$

Defining the *strength tensors* for the gauge fields according to (2.18) and (2.20),

$$W_{\mu\nu}^i \equiv \partial_\mu W_\nu^i - \partial_\nu W_\mu^i + g\varepsilon^{ijk} W_\mu^j W_\nu^k,$$
$$B_{\mu\nu} \equiv \partial_\mu B_\nu - \partial_\nu B_\mu,$$

the free Lagrangian can be written for the gauge fields following the results (2.19) and (2.21),

$$L_{gauge} = -\frac{1}{4} W_{\mu\nu}^i W^{i\mu\nu} - \frac{1}{4} B_{\mu\nu} B^{\mu\nu}. \tag{2.34}$$

For the leptons, the free Lagrangian is written as,

$$\begin{aligned} L_{leptons} &= \overline{\mathrm{R}} i\partial R + \overline{\mathrm{L}} i\partial \mathrm{L} \\ &= \overline{\ell}_R i\partial \ell_R + \overline{\ell}_L i\partial \ell_L + \overline{\nu}_L i\partial \nu_L \\ &= \overline{\ell} i\partial \ell + \overline{\nu} i\partial \nu. \end{aligned} \tag{2.35}$$

Remember that a mass term for the fermions (2.4) mixes the right- and left-components and would break the gauge invariance of the theory from the very beginning.

The next step is to introduce the fermion-gauge boson coupling via the *covariant derivative*, *i.e.*

$$\mathrm{L}: \quad \partial_\mu + i\frac{g}{2}\tau^i W_\mu^i + \frac{g'}{2}YB_\mu, \tag{2.36}$$

$$\mathrm{R}: \quad \partial_\mu + i\frac{g'}{2}YB_\mu, \tag{2.37}$$

where g and g' are the coupling constant associated with the groups $SU(2)_L$ and $U(1)_Y$ respectively, and

$$Y_{\mathrm{L}_\ell} = -1, \qquad Y_{\mathrm{R}_\ell} = -2 \tag{2.38}$$

Therefore, the fermion Lagrangian (2.35) becomes

$$L_{leptons} \rightarrow L_{leptons} + \bar{\mathrm{L}} i\gamma^\mu \left(i\frac{g}{2}\tau^i W_\mu^i + i\frac{g'}{2}YB_\mu\right)\mathrm{L} + \bar{\mathrm{R}}\, i\gamma_\mu \left(i\frac{g'}{2}YB_\mu\right)\mathrm{R} \tag{2.39}$$

Just the "left" piece of (2.39) is first picked up,

$$L_{leptons}^{\mathrm{L}} = -g\,\bar{\mathrm{L}}\,\gamma^\mu \left(\frac{\tau^1}{2}W_\mu^1 + \frac{\tau^2}{2}W_\mu^2\right)\mathrm{L} - g\,\bar{\mathrm{L}}\,\gamma^\mu \frac{\tau^3}{2}\mathrm{L}W_\mu^3 - \frac{g'}{2}Y\bar{\mathrm{L}}\gamma^\mu\,\mathrm{L}\,B_\mu$$

The first term is *charged* and can be written as

$$L_{leptons}^{\mathrm{L}(\pm)} = -\frac{g}{2}\bar{\mathrm{L}}\,\gamma^\mu \begin{pmatrix} 0 & W_\mu^1 - iW_\mu^2 \\ W_\mu^1 + iW_\mu^2 & 0 \end{pmatrix}\mathrm{L}.$$

This suggests the definition of the *charged gauge bosons* as

$$W_\mu^{\pm} = \frac{1}{\sqrt{2}}(W_\mu^1 \mp W_\mu^2) \tag{2.40}$$

in such a way that

$$L_{leptons}^{L(\pm)} = -\frac{g}{2\sqrt{2}}\,[\bar{\nu}\gamma^\mu(1-\gamma_5)\ell W_\mu^+ + \bar{\ell}\gamma^\mu(1-\gamma_5)\nu W_\mu^-] \tag{2.41}$$

reproduces exactly the $(V - A)$ structure of the weak charged current.

With the introduction of intermediate vector boson (IVB), the Fermi Lagrangian for leptons is given by

$$L_{weak}^{W} = G_W(J^\alpha W_\alpha^+ + J*\alpha W_\alpha^-), \tag{2.42}$$

with a new coupling constant G_W.When we compare the Lagrangian (2.41) with (2.42) and take into account the result from low-energy phenomenology ($G_W^2 = M_W^2 G_F/\sqrt{2}$) we see that $G_W = g/2\sqrt{2}$ and we obtain the relation

$$\frac{g}{2\sqrt{2}} = \left(\frac{M_W^2 G_F}{\sqrt{2}}\right)^{1/2} \tag{2.43}$$

The neutral piece of $L_{leptons}$ (2.39) that contains both left and right fermion components is,

$$\begin{aligned} L_{leptons}^{(L+R)(0)} &= -g\,\bar{L}\left(\gamma^\mu \frac{\tau^3}{2}\right) L W_\mu^3 - \frac{g'}{2}(\bar{L}\gamma^\mu Y L + \bar{R}\gamma^\mu Y R)B_\mu \\ &= -g\,J_3^\mu\, W_\mu^3 - \frac{g'}{2}J_Y^\mu B_\mu, \end{aligned} \tag{2.44}$$

where the currents J_3 and J_Y have been defined before,

$$J_3^\mu = \frac{1}{2}(\bar{\nu}_L\gamma^\mu\nu_L - \bar{\ell}_L\gamma^\mu\ell_L)$$
$$J_Y^\mu = -(\bar{\nu}_L\gamma^\mu\nu_L + \bar{\ell}_L\gamma^\mu\ell_L + 2\bar{\ell}_R\gamma^\mu\ell_R).$$

It is noted that 'charges' respect the Gell-Mann-Nishijima relation (2.33) and currents satisfy,

$$J_{em} = J_3 + \frac{1}{2}J_Y.$$

In order to obtain the right combination of fields that couple to the electromagnetic current, the neutral fields are rotated the new fields A and Z are defined by,

$$\begin{pmatrix} A_\mu \\ Z_\mu \end{pmatrix} = \begin{pmatrix} \cos\theta_W & \sin\theta_W \\ -\sin\theta_W & \cos\theta_W \end{pmatrix} \begin{pmatrix} B_\mu \\ W_\mu^3 \end{pmatrix}, \tag{2.45}$$

or,

$$W_\mu^3 = \sin\theta_W A_\mu + \cos\theta_W Z_\mu,$$
$$B_\mu = \cos\theta_W A_\mu - \sin\theta_W Z_\mu,$$

where θ_W is called the Weinberg angle and the *SU(2)* and *U(1)* coupling constants obey the relations,

$$\sin\theta_W = \frac{g'}{\sqrt{g^2 + g'^2}}, \qquad \cos\theta_W = \frac{g}{\sqrt{g^2 + g'^2}}. \tag{2.46}$$

The neutral part of the fermion Lagrangian (2.44) becomes as following in terms of the new fields,

$$
\begin{aligned}
L^{(\mathrm{L+R})(0)}_{leptons} &= -\,(\mathrm{g}\sin\theta_{\mathrm{W}} J_3^{\mu} + \frac{1}{2}\mathrm{g}'\cos\theta_W J_Y^{\mu})A_\mu \\
&\quad + (-\,\mathrm{g}\cos\theta_W J_3^{\mu} + \frac{1}{2}\mathrm{g}'\sin\theta_W J_Y^{\mu})Z_\mu \\
&= -\,\mathrm{g}\sin\theta_W(\bar{\ell}\gamma^{\mu}\ell)A_\mu - \frac{\mathrm{g}}{2\cos\theta_W}\sum_{\psi_i=\nu,\ell}\overline{\psi}_i\gamma^{\mu}(\mathrm{g}_V^i - \mathrm{g}_A^i\gamma_5)\,\psi_i Z_\mu\,,
\end{aligned}
\tag{2.47}
$$

and the electromagnetic current coupled to the photon field A_μ and the *electromagnetic charge* are easily identified as,

$$
e = \mathrm{g}\sin\theta_W = \mathrm{g}'\cos\theta_W \tag{2.48}
$$

The SM introduces a new component, weak interactions without change of charge, and makes a specific prediction for the vector (V) and axial (A) couplings of the Z to the fermions,

$$
\mathrm{g}_V^i \equiv T_3^i - 2Q_i\sin^2\theta_W\,, \tag{2.49}
$$

$$
\mathrm{g}_A^i \equiv T_3^i \tag{2.50}
$$

Since at that time we had no hint about this kind of weak interaction, this was a very successful prediction of the SM. Up to now we have in the theory:

- 4 massless gauge fields W_μ^i, B_μ or equivalently, $W_\mu^{\pm}$, Z_μ and A_μ;
- 2 massless fermions: ν,ℓ.

The next step will be to add scalar fields in order to break spontaneously the symmetry and use the Higgs mechanism to give mass to three weak intermediate vector bosons, making sure that the photon remains massless.

2.2.6. The Higgs Mechanism and the W and Z Mass

In order to apply the Higgs mechanism to give mass to $W^{\pm}$ and Z^{0}, the following scalar doublet is introduced

$$\Phi \equiv \begin{pmatrix} \phi^{+} \\ \phi^{-} \end{pmatrix}. \tag{2.51}$$

From the relation (2.33), the hypercharge of the Higgs doublet is verified as $Y = 1$. The following Lagrangian is introduced

$$L_{scalar} = \partial_{\mu}\Phi^{*}\partial^{\mu}\Phi - V(\Phi * \Phi),$$

where the potential is given by

$$V(\Phi^{*}\Phi) = \mu^{2}\Phi * \Phi + \lambda(\Phi * \Phi)^{2}. \tag{2.52}$$

In order to maintain the gauge invariance under the $SU(2)_{L} \otimes U(1)_{Y}$, the covariant derivative should be introduced:

$$\partial_{\mu} \rightarrow D_{\mu} = \partial_{\mu} + i\,g\frac{\tau^{i}}{2}W_{\mu}^{i} + i\frac{g'}{2}YB_{\mu}.$$

The vacuum expectation value of the Higgs field can be chosen as,

$$\langle\Phi\rangle_{0} = \begin{pmatrix} 0 \\ v/\sqrt{2} \end{pmatrix},$$

in here

$$v = \sqrt{-\frac{\mu^2}{\lambda}} \tag{2.53}$$

Since we want to preserve the exact electromagnetic symmetry to maintain the electric charge conserved, we must break the original symmetry group as

$$SU(2)_L \otimes U(1)_Y \rightarrow U(1)_{em} \ ,$$

i.e. after the spontaneous symmetry breaking, the sub-group $U(1)_{em}$, of dimension 1, should remain as a symmetry of the vacuum.

In this case the corresponding gauge boson, the photon, will remain massless. It can be verified that our choice let indeed the vacuum invariant under $U(1)_{em}$. This invariance requires that

$$e^{i\alpha Q} \langle\Phi\rangle_0 \cong (1 + i\alpha Q) \langle\Phi\rangle_0 = \langle\Phi\rangle_0,$$

or, the operator Q annihilates the vacuum, $Q \langle\Phi\rangle_0 = 0$. This exactly implies that the electric charge of the vacuum is zero,

$$\begin{aligned} Q \langle\Phi\rangle_0 &= \left(T_3 + \frac{1}{2}Y\right) \langle\Phi\rangle_0 \\ &= \frac{1}{2} \left[\begin{pmatrix} 1 & 0 \\ 0 & -1 \end{pmatrix} + \begin{pmatrix} 1 & 0 \\ 0 & 1 \end{pmatrix} \right] \begin{pmatrix} 0 \\ v/\sqrt{2} \end{pmatrix} = 0. \end{aligned}$$

Corresponding to the *broken generators* T_1, T_2, and $T_3 - Y/2 = 2T_3 - Q$, the other gauge bosons should acquire mass. In order to make this explicit, the Higgs doublet is parametrized as following,

$$\Phi \equiv \exp\left(i\frac{\tau^i}{2}\frac{\chi_i}{v}\right) \begin{pmatrix} 0 \\ (v + H)/\sqrt{2} \end{pmatrix}$$

$$\cong \langle \Phi \rangle_0 + \frac{1}{2\sqrt{2}} \begin{pmatrix} \chi_2 + i\chi_1 \\ 2H - i\chi_3 \end{pmatrix} = \frac{1}{\sqrt{2}} \begin{pmatrix} i\sqrt{2}\omega^+ \\ v + H - iz^0 \end{pmatrix}.$$

where $\omega^{\pm}$ and z^0 are the Goldstone bosons.

Now, if we make a $SU(2)_L$ gauge transformation with $\alpha_i = \chi_i / v$ (unitary gauge) the fields become

$$\Phi \to \Phi' = \exp\left(-i\frac{\tau^i}{2}\frac{\chi_i}{v}\right)\Phi = \frac{(v+H)}{\sqrt{2}}\begin{pmatrix} 0 \\ 1 \end{pmatrix}. \tag{2.54}$$

and the scalar Lagrangian can be written in terms of these new fields as

$$L_{scalar} = \left| \left(\partial_\mu + i\mathrm{g}\frac{\tau^i}{2}W^i_\mu + i\frac{\mathrm{g}'}{2}YB_\mu \right) \frac{(v+H)}{\sqrt{2}} \begin{pmatrix} 0 \\ 1 \end{pmatrix} \right|^2$$

$$-\mu^2\frac{(v+H)^2}{2} - \lambda\frac{(v+H)^4}{4}. \tag{2.55}$$

In terms of the physical fields $W^{\pm}$(2.40) and Z^0 (2.45) the first term of (2.55), that contain the vector bosons, is

$$\left| \begin{pmatrix} 0 \\ \partial_\mu H/\sqrt{2} \end{pmatrix} + i\frac{\mathrm{g}}{2}(v+H) \begin{pmatrix} W^+_\mu \\ (-1/\sqrt{2}c_W)Z_\mu \end{pmatrix} \right|^2$$

$$= \frac{1}{2}\partial_\mu H \partial^\mu H + \frac{\mathrm{g}^2}{4}(v+H)^2\left(W^+_\mu W^{-\mu} + \frac{1}{2c_W^2}Z_\mu Z^\mu \right), \tag{2.56}$$

where the c_W is defined as $c_W \equiv \cos\theta_W$.

The quadratic terms in the vector fields, are,

$$\frac{\mathrm{g}^2 v^2}{4}W^+_\mu W^{-\mu} + \frac{\mathrm{g}^2 v^2}{8\cos^2\theta_W}Z_\mu Z^\mu,$$

When compared with the usual mass terms for a charged and neutral vector bosons,

$$M_W^2 W_\mu^+ W^{-\mu} + \frac{1}{2} M_Z^2 Z_\mu Z^\mu ,$$

and we can easily identify

$$M_W = \frac{gv}{2}, \qquad M_Z = \frac{gv}{2c_W} = \frac{M_W}{c_W} \ . \tag{2.57}$$

It can be seen from (2.56) that no quadratic term in A_μ appears, and therefore, the photon remains massless, as we should expect since the $U(1)_{em}$ remains as a symmetry of the theory.

Taking into account the low-energy phenomology via the relation (2.43), we obtain for the vacuum expectation value

$$v = \left(\sqrt{2} G_F\right)^{1/2} \cong 246 \ \text{GeV}, \tag{2.58}$$

and the SM predictions for the W and Z masses are

$$M_W^2 = \frac{e^2}{4s_W^2} v^2 = \frac{\pi\alpha}{s_W^2} v^2 \cong \left(\frac{37.2}{s_W} \text{GeV}\right)^2 \sim (80 \ \text{GeV})^2 ,$$

$$M_Z^2 \cong \left(\frac{37.2}{s_W c_W} \text{GeV}\right)^2 \sim (90 \ \text{GeV})^2 ,$$

where it is assumed an experimental value for $s_W^2 \equiv \sin^2\theta_W \sim 0.22$.

It can be learned from (2.55) that one scalar boson, out of the four degrees of freedom introduced in (2.51), is remnant of the symmetry breaking. The search for the so called Higgs boson, remains as one of the major challenges of the experimental high energy physics.

The second term of (2.55) gives rise to terms involving exclusively the scalar field H, namely,

$$-\frac{1}{2}(-2\mu^2)H^2 + \frac{1}{4}\mu^2 v^2\left(\frac{4}{v^3}H^3 + \frac{1}{v^4}H^4 - 1\right). \tag{2.59}$$

In (2.59) the Higgs boson mass term can be also identified with

$$M_H = \sqrt{-2\mu^2}, \tag{2.60}$$

and the self-interactions of the H field. In spite of predicting the existence of the Higgs boson, the SM does not give a hint on the value of its mass since μ^2 is a *priori* unknown (Novaes, 2000).

2.2.7. The WZ Diboson Production Mechanism in the Standard Model

The interaction between the W and Z gauge bosons which are the trilinear gauge coupling is the most experimentally accessible. For this part of the electroweak sector, the SM Lagrangian is described by the following terms

$$\begin{aligned} L = &-ie(W_\mu^- W_\nu^+ A^{\mu\nu} + W_\mu^+ W^{-\mu\nu} A_\nu - W^{i\mu\nu} W_\mu^- A_\nu) \\ &-ie\cot\theta_W (W_\mu^- W_\nu^+ Z^{\mu\nu} + W_\nu^+ W^{-\mu\nu} Z_\nu - W^{+\mu\nu} W_\mu^- Z_\mu) \end{aligned} \tag{2.61}$$

In this equation, θ_W is the weak mixing angle, $W^{\pm\mu}$ is the $W^\pm$ field, Z^μ is the Z field, and A^μ is the photon field and $W^{\mu\nu} \equiv \partial^\mu W^\nu - \partial^\nu W^\mu$, $A^{\mu\nu} \equiv \partial^\mu A^\nu - \partial^\nu A^\mu$ and $Z^{\mu\nu} \equiv \partial^\mu Z^\nu - \partial^\nu Z^\mu$. These terms respectively specify the $WW\gamma$ and WWZ vertices. They arise due to non-Abelian gauge structure of the electroweak theory. The Feynman diagrams of the trilinear gauge boson couplings are shown in Figure 2.4. The WZ production at the tree level in the SM is fully described by these terms when combined with the fermion couplings to bosons.

Figure 2.4. Feynman diagrams of the trilinear gauge boson couplings allowed by the SM. The WWZ vertex is shown in (a), the $WW\gamma$ vertex is shown in (b).

Three Feynman diagrams describe tree level WZ production at a hadron collider in the SM. The WZ boson pairs are produced at leading-order (LO). They are shown in Figure 2.5. Figure 2.5 (a) and (b) represent u- and t-channel WZ production. They are fully described by the couplings of the fermions to the W and Z bosons. These couplings have been measured for the production of single W and Z bosons (Arnison et al., 1983a-1983b; Barner et al., 1983; Bagnaia et al., 1983). Figure 2.5 (c) represents s-channel WZ production. It involves the coupling of the W and Z bosons, *i.e.* the WWZ coupling.

Since the tree level Feynman diagrams for WZ production have been known, it is possible to predict observables such as the cross section. In order to calculate the total cross section if u- and t-channel diagrams were only used, the results would be linear rise of the cross section with increasing $\sqrt{\hat{s}}$ which are called the parton center of mass energy. It is indicated that partial wave unitarity will be violated for sufficiently large energies. By including the s-channel diagrams which involves the boson-boson couplings, the cross terms which result from squaring all the summed amplitudes provide the delicate gauge cancellations that are required to restore unitarity. This cancellation will have important results in the search for deviations from the SM predicted values for the boson-boson couplings.

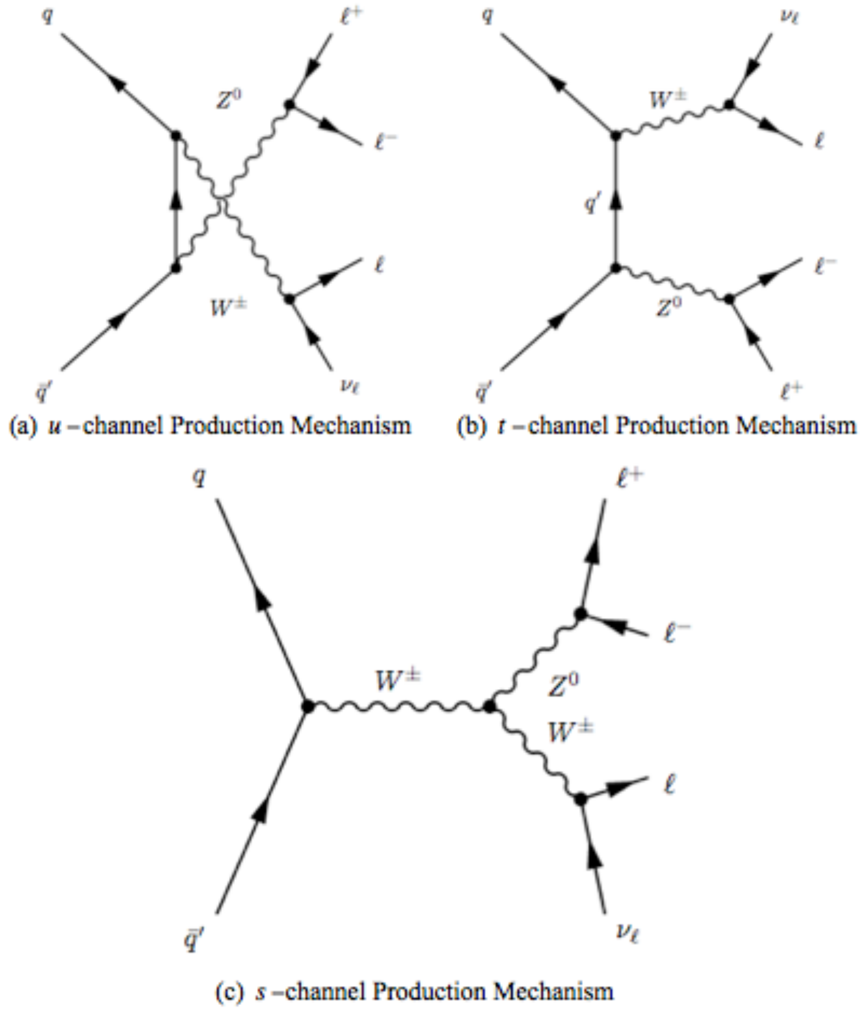

Figure 2.5. Standard Model leading-order (LO) Feynman Diagrams for tree level WZ production with subsequent decay into leptons: (a) u-channel (b) t-channel (c) s-channel.

Because of the composite nature of the proton and antiproton, a numerical result for the *WZ* production cross section can not be produced analytically. But the parton subprocess cross section can be computed. It must be summed over all possible pairs of participating partons in the proton and antiproton and additionally integrated over the parton momentum distributions. This problem can be solved by using a Monte Carlo (MC) approach. Event generators such as PYTHIA which produce numerical results for the cross section can be used to fully model SM *WZ* production. The cross section is corrected with a next-to-leading-order (NLO) for the PYTHIA generator. The initial and final state gluon radiations and one–loop corrections are taken into account by the NLO calculations. The ratio of the NLO MC predictions to the LO MC predictions is defined as k-factor, $k \equiv \frac{\sigma_{NLO}}{\sigma_{LO}}$.

2.2.8. Experimental Signature of the WZ Production

The *WZ* process can be looked in three distinct channels: fully leptonic ($\ell\nu + \ell\ell$), semi-leptonic ($jj + \ell\ell$ or $\ell\nu + jj$) and pure hadronic final state ($jj + jj$).

The purely hadronic final state has a significantly larger branching ratio than all leptonic decays. But it has also disadvantages. First of all, it is nearly impossible to determine from which boson a reconstructed hadronic jet came. The reason for this is the finite energy resolution of hadronic calorimeters and to the difficulty of charge sign determination of jets. Since the limited energy resolution of hadronic calorimeters makes distinguishable *W*'s from *Z*'s difficult at best, *WW* and *WZ* production are indistinguishable in this channel. Due to continuum multijet production as well as the production of single *W* or *Z* bosons in association with jets, this channel suffers from a large background.

The semi-leptonic decay modes have the largest branching ratio, 15% and 4.5%, respectively for $\ell\nu jj$ and $\ell\ell jj$ final states. In here ℓ represents an electron or muon and j is a hadron jet. This channel suffers from large QCD background from both multijet production and W production in association with jets. For $\ell\nu jj$ channel, it is impossible to distinguish *WZ* production from *WW* production. Although the $\ell\ell jj$ final state has the advantage of being identified only with *WZ* production, it is dominated by backgrounds from Z production in association with jets. The relatively large branching fraction and ability to clearly reconstruct the momentum of each boson are the main advantages for this channel. Due to the inability to distinguish signal from background, a cross section measurement is insensitive in the semi-leptonic channel.

The purely leptonic final state has the smallest branching ratio of all, 1.5% when both muons and electrons are counted. τ's are excluded due to the difficulty in identifying them efficiently. This channel has one disadvantage due to relatively small braching ratio. On the other hand, the main advantage of this channel is its unique signature, three charged leptons with high transverse momentum (p_T), and large missing transverse energy (E_T). This signature is unique among diboson final states and it is virtually background free. There is no physics processes which produce a significant background. The only backgrounds are instrumental backgrounds which arise from misidentification of a jet as a lepton (Degenhart, 2007). The Table 2.3 shows the decay braching ratios for the W and Z gauge bosons (Nakamura et al., 2010).

The first observation of $W^{\pm}Z$ production was perfomed by the CDF II detector at the Fermilab Tevatron hadron collider. The production is observed in $p\bar{p}$ collisions at $\sqrt{s} = 1.96$ TeV using 1.1 fb^{-1} of integrated luminosity. The decay channel was considered as $WZ \rightarrow \ell' \nu_{\ell'} \ell \ell$, where ℓ and ℓ' are electrons and muons come directly from W and Z decay, respectively, or from the leptonic decay for τ's when one or both vector bosons decay to τ leptons (Abulencia et al.,2007).

For the WZ pair production the most updated next-to-leading order cross sections at the LHC and Tevatron are listed in Table 2.4. The contributions from singly resonant diagrams are taken into account by this NLO calculation. Renormalisation and factorization scales are set equal to the average mass of the W and Z ($\mu_R = \mu_F = (M_W + M_Z)/2$). By varying the scales around central scale by a factor of two, upper and lower percentage deviations are obtained. The vector boson are kept on-shell, with no decays included.

Table 2.3. Decay branching ratios of the W and Z gauge bosons (Nakamura et al., 2010).

$W^{\pm}$	BR%		Z	BR%
$e^+\nu_e$	10.75 ± 0.13		e^+e^-	3.363 ± 0.004
$\mu^+\nu_\mu$	10.57 ± 0.15		$\mu^+\mu^-$	3.366 ± 0.007
$\tau^+\nu_\tau$	11.25 ± 0.20		$\tau^+\tau^-$	3.370 ± 0.008
hadrons	67.60 ± 0.27		hadrons	69.91 ± 0.06
$\ell^+\nu_\ell$	10.80 ± 0.09		$\ell^+\ell^-$	3.3658 ± 0.0023
			$\nu_\ell\bar{\nu}_\ell$	20.00 ± 0.06

At the Tevatron, the production cross section is expected to be the same for $W^{+}Z$ and $W^{-}Z$. But it is not the case for the LHC in pp collisions. The expected ratio of $\sigma_{NLO}(W^{-}Z)/\sigma_{NLO}(W^{+}Z)$ varies between 0.56 for $\sqrt{s} = 7$ TeV and 0.65 for $\sqrt{s} = 14$ TeV. In fact, the predominance of u quarks enhances the $W^{+}Z$ production through $u\overline{d'}$ type interactions, with anti-quarks taken among sea-quarks.

The first WZ event by the CMS detector at the LHC was observed with ~30 pb^{-1} of integrated luminosity. It was looked for the only leptonic decays in to electrons and muons ($\sigma(WZ) \times BR \approx 0.07$ pb per single channel). The first measurement of WZ cross section in leptonic modes in CMS was measured using 2011 data corresponding to an integrated luminosity of 815 pb^{-1}. The cross section was measured over the full acceptance and for 60 < m_Z < 120 GeV/c^2 for each leptonic channel and found to be (Adiguzel et al., 2011):

Table 2.4. NLO cross section for WZ production at in pp and $p\bar{p}$ (Campbell et al., 2011).

	Tevatron $p\bar{p}$ (1.96 TeV)	LHC pp (7 TeV)	(14 TeV)
$\sigma_{NLO}(W^{+}Z)$[pb]	1.73 ± 0.20	$11.88^{+0.65}_{-0.5}$	$31.50^{+1.23}_{-0.95}$
$\sigma_{NLO}(W^{-}Z)$[pb]	1.73 ± 0.20	$6.69^{+0.37}_{-0.29}$	$20.32^{+0.79}_{-0.63}$
$\sigma_{NLO}(W^{\pm}Z)$[pb]	3.46 ± 0.30	$18.57^{+0.75}_{-0.58}$	$51.82^{+1.46}_{-0.14}$

$$\sigma_{WZ \rightarrow \ell\ell\ell\nu} = 0.062(\text{stat.}) \pm 0.004(\text{syst.}) \pm 0.004(\text{lumi})\ \text{pb}.$$

The inclusive WZ cross section, using respective W and Z boson branching ratios for leptonic decay modes is measured to be (Adiguzel et al., 2011):

$$\sigma_{WZ} = 17.0 \pm 2.4(\text{stat.}) \pm 1.1(\text{syst.}) \pm 1.0(\text{lumi})\ \text{pb}.$$

Up to now we discussed SM, its unanswered questions and the gauge principle, the spontaneous symmetry breaking, the electroweak interaction and the

Higgs mechanism. Then we have looked at the *WZ* production mechanism in SM and its experimental signature. Eventhough the SM is a very successful theory to explain most of the experimental results with very good agreement so far, it doesn't answer all the questions. Therefore it is not the ultimate theory of the particle physics. In order to head towards some answers to today's open questions in this field and beyond the SM, it is very important to search for new physics. So in the next section such possible extensions to the SM that predict existence of heavy charged gauge bosons that particular focus of this thesis will be discussed.

2.3. Beyond the Standard Model and New Physics Possibilities

New, heavy W' bosons that decay into a pair of W and Z bosons is predicted by many extensions of the SM. These extensions include models with extended gauge sectors designed to achieve unification and models with extra dimensions. In many W' models coupling to the leptons is suppressed, leading to a relative enhancement in triple gauge couplings that could lead to a WZ final state. Some of W' models will be introduced briefly in the following subsections.

2.3.1 Sequential Standard Model (SSM)

In the Sequential Standard Model (SSM) the coupling of the W' to fermions is the same as that of the SM W with the main production mechanism in *pp* collisions. The quark annihilation process with the associated Feynman diagram is given by Figure 2.6. The W' couplings to WZ are set to zero in this model.
In this formalism the decay width for $W' \to \ell\nu$ can be written as:

$$\Gamma(W' \to \ell\nu) = \frac{\alpha}{12} \frac{M_{W'}}{\sin^2\theta_W}, \tag{2.62}$$

where $\alpha = \frac{1}{128}$, $\sin^2\theta_W = 0.23$, $M_{W'}$ is the mass of the W' and $\ell = e, \mu, \tau$.

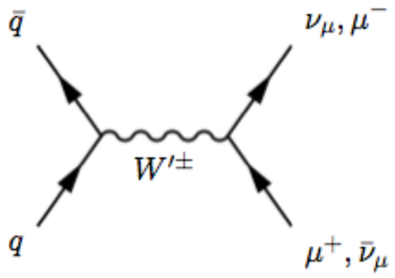

Figure 2.6 Tree level Feynman diagrams for $W'^+ \to \mu^+ \nu_\mu$ $W'^- \to \mu^- \bar{\nu}_\mu$.

It can be seen that the decay width is linear in W', with a leptonic branching ratio of 8.5% from Eq. (2.62). The braching ratio for $W' \to q\bar{q}$ is actually three times larger than that for leptons. On the other hand this channel suffers from significant multi-jet background whereas the leptonic channel is cleaner and has better signal to background separation. So this is the main reason that SSM W' is most easily searched for in the leptonic channel (Altarelli et al., 1989).

2.3.2. The Left-Right-Symmetric Models (LRSM)

The origin of parity violation in weak interactions stays unexplained in the SM. A priori the multiplets are explicitly designed to break parity in the weak sector. In this model, the left-handed particles are assigned to doublets, while the right-handed particles do not participate in weak interactions because they are $SU(2)_L$ singlets. The introduction of parity violation within the SM has nothing to do with spontaneous symmetry breaking of the gauge groups or other mechanism, but it has been included by hand.

The Left-Right-Symmetric Models (LRSM) can solve this problem and provide an extension of the SM. It is based on the gauge group $SU(2)_L \otimes SU(2)_R \otimes U(1)$. The general feature of these models is the main exact parity symmetry of the Lagrangian and an additional $SU(2)$ gauge group, resulting in an observable W' (and Z'). The symmetry is spontaneously broken by a scalar Higgs field to match the low-energy behaviour of maximum parity violation in weak interactions. Additionally, LRSM incorporate full quark-lepton symmetry and turn the quantum number of the $U(1)$ from hypercharge Y to the value of baryon-minus-lepton number B-L. Finally the theory gives natural explanation for the smallness of the neutrino masses in choosing an appropriate Higgs sector and by relating it to the observed suppression of V + A currents (Pati and Salam, 1974; Mohapatra and Pati, 1975; Mohapatra and Senjavonic, 1980).

2.3.3. The Little Higgs Models

Little Higgs Models also predict a W' heavy gauge boson at LHC energies. They provide a relatively new formulation of the physics of electroweak symmetry breaking. The key features of these models are summarized as following:

- The Higgs fields are Goldstone bosons, which are associated with some global symmetry breaking at a higher scale.
- The Higgs fields acquire a mass and become pseudo Goldstone bosons via symmetry breaking at the electroweak scale.
- The Higgs fields remain light since they are protected by the global symmetry and free from a one-loop quadratic sensitivity to the cutoff scale.

When we look at the motivation of new gauge bosons within these models briefly, in addition to the SM gauge bosons, a set of heavy gauge bosons which have the same quantum numbers are included in Little Higgs models. The Higgs boson quadratic divergences, induced by SM gauge boson loops, are canceled by quadratic divergences of the new gauge bosons by the choice of the gauge coupling constant. These new particle are expected to appear at the TeV-scale and should be detected at the LHC (Han et al., 2003).

2.3.4. Technicolor Models

Technicolor Models represent the last class of theories which imply the existence of new heavy charged boson (Anderson et al., 2011). They provide an alternative electroweak symmetry breaking (EWSM) mechanism to the Higgs procedure. They predict multiple extra $W'^{\pm}$ (and Z') bosons. It can be recent phenomelogical study can be found in reference (Anderson et al., 2012).

Experimental searches for a W'-boson are usually interpreted in the context of benchmark scenario (Altarelli et al., 1989) at Tevatron and LHC. This model only includes one extra charged vector boson with couplings to fermions identical to those of the corresponding SM *W*-boson, and no mixing with the EW SM bosons (Accomando and Becciolini, 2012).

Technicolor predicts a variety of new bound states of techniquarks which can decay to *WZ*. In fact, the existence of new particles coupling to the massive vector bosons is one of the primary properties. The availability of new particles is very attractive to provide modifications sufficient to control the WZ scattering divergences above 1 TeV. The technihadrons are called $\boldsymbol{\pi}_T$, $\boldsymbol{\rho}_T$ and a_T in analogy with QCD. A long standing problem with walking Technicolor has been very large for the precision-electroweak *S*-parameter. The *S*-parameter is a quantity used to provide generic constraints on physics beyond the SM. Recent models incorporate the idea that the *S*-parameter can be naturally suppressed if the lightest vector technihadron, ρ_T, and its axial vector partner, a_T, are nearly mass degenerate (Lane and Mrenna, 2003). These technihadrons are expected to have masses below 700 GeV/c^2 and their decays have distinctive signatures with narrow resonant peaks.

2.4. New Heavy Vector Bosons (W')

The W' boson is a hypothetical massive particle of electric charge ±1 and spin1, which is predicted in various extensions of the SM. A W' always couples to different flavors of fermions, similar to the W boson. In particular, if a W' couples quarks to leptons it is a leptoquark gauge boson (Babu and Kolda, 2005).

The Lagrangian terms describing couplings of a W' boson to fermions are given by

$$W'_\mu\left[\overline{u}_i\left(C^R_{q_{ij}}P_R + C^L_{q_{ij}}P_L\right)\gamma_\mu d_j + \overline{v}_i\left(C^R_{l_{ij}}P_R + C^L_{l_{ij}}P_L\right)\gamma^\mu e_j\right] + h.c. \tag{2.63}$$

where u, d, v and e are the SM fermions in the mass eigenstate basis, $i, j = 1, 2, 3$ label the fermion generation, and $P_{R,L} = (1 \pm \gamma_5)/2$. The coefficients $C^L_{q_{ij}}$, $C^R_{q_{ij}}$, $C^L_{l_{ij}}$, $C^R_{l_{ij}}$ are complex dimensionless paramaters. If $C^R_{l_{ij}} \neq 0$, then the ith generation includes a right-handed neutrino (Chen and Dobrescu, 2009). It is often assumed that there are correlations between the left- and right-handed couplings (Langacker and Sankar, 1989). Although this is true in some of the original models that include a W' (Mohapatra and Pati, 1975), there exist theories where all the left- and right-handed couplings are free parameters.

In this context, the W' gauge bosons (as exotic WZ rezonances) in pp collisions at a centre-of-mass energy of 7 TeV will be searched via trilepton signal in the CMS experiment for my thesis study. The main process is given by:

$$pp \to W' \to W(\to \ell_1 v_{\ell_1})Z(\to \ell_2^+ \ell_2^-)$$

where ℓ_1 and ℓ_2 can belong to identical or distinct families of leptons. The missing energy is carried away by the neutrinos. In the scattering process above, v_{ℓ_1} represent missing energy in the experiment. The Feynman diagram is shown in Figure 2.7 for this process. The background comes from the W and Z bosons and it is expected to be small. However, the focus will be on a search for an excess in the WZ invariant mass spectrum in this work.

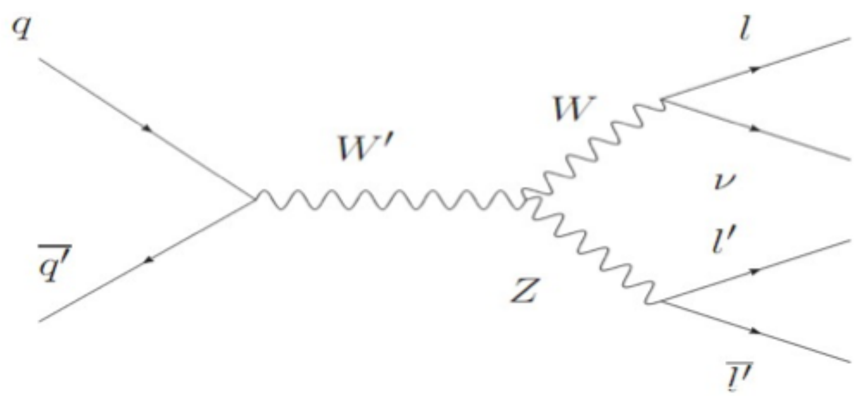

Figure 2.7 The Feynman diagram for W' to WZ decay mode.

The current limits on W' searches in leptonic channels in the context of the SSM exclude W' bosons with masses < 2.27 TeV at the 95% confidence level (C.L) (Chatrchyan, 2011a). Those searches assume that the $W' \rightarrow WZ$ decay mode is suppressed.

The recent results from the searches for new exotic particles decaying to the WZ final state with electrons and muons using 4.98 fb^{-1} of $\sqrt{s}$ = 7 TeV data collected by the CMS experiment at the LHC in 2011 show no significant excess in the mass distribution of the WZ candidates compared to the background expectation from SM process. Lower bounds at the 95% confidence level are set on the mass of hypothetical particles decaying to the WZ final state in several theoretical models. For technicolor model, ρ_T hadrons with masses between 167 and 687 GeV have been excluded in the parameter space $M(\pi_{TC}) = \frac{3}{4}M(\rho_{TC}) - 25$ GeV. Under the alternative assumption $M(\rho_{TC}) < M(\pi_{TC}) + M_W$, ρ_T hadrons with masses between 180 and 938 GeV have been excluded (Briglejevic et al., 2012).

3. EXPRIMENTAL SETUP

Hadron colliders are proper machines to extend the energy frontier for collision experiments. The Large Hadron Collider (LHC) was designed to provide parton-parton collisions up to energies of about 1 TeV.

In this chapter, first the general information about CERN will be given, then overview of both the LHC accelerator and the CMS detector will be presented with the aim of setting the context of the work.

3.1. CERN

The European Organization for Nuclear Research known as CERN is currently the largest particle physics laboratory of the world. It was founded on September 29, 1954 and situated on the France-Switzerland border near Geneva. The experiments at CERN shed light on the understanding of fundamental particles and their interactions. Some of its historical highlights are: the discovery of neutral currents in 1973, the discovery of the W and Z bosons in 1983, the high precision measurements of weak interactions at the LEP experiments and the exploration of a new state of matter known as the quark-gluon plasma. In addition it is also known for its social and cultural relevance. The half of the world's particle physicist, nearly 8000 visiting scientist, come to CERN for their research. It includes 580 universities and 85 nationalities.

3.2. The Large Hadron Collider

The Standard Model of Particle Physics has been well established as our best description of subatomic nature in the past decades. Its predictions have been tested and they are consistent with the many precision measurements. Most of these precision measurements were done by the Large Electron-Positron (LEP) collider at CERN. Its operation was taken from middle 1989 till the end of 2000. The center of mass energies were between 90 and 206 GeV. Z and $W^{\pm}$ bosons were produced by

LEP in large quantities so their properties could be measured precisely and compared with the predictions of the SM.

The LHC was designed to collide beams at the center-of-mass energy of $\sqrt{s}=14$ TeV, with a luminosity of 10^{34} $s^{-1}cm^{-2}$. 2808 bunches of $1.15\cdot10^{11}$ protons each will be accelerated in the 27 km long former LEP tunnel about 100 m below surface and will collide every 25 ns. It is the world's largest and most powerful proton-proton (pp) machine. The LHC is also a heavy ion *Pb-Pb* collider with a total energy up to 2.76 TeV per nucleon. Its purpose is to investigate the quark-gluon plasma. It produces collisions with a centre of mass energy 30 times higher than those in previous heavy ion accelerators. This property allows the LHC to have a complete program in heavy-ion collisions to include studies about the hot nuclear matter. The design parameters for the *pp* LHC operation are shown Table 3.1.

Overview of the accelerator chain is shown in Figure 3.1. There are several steps to obtain the protons and accelerate them to the injection energy: at first protons are obtained by ionising gaseous hydrogen and then accelerated in bunches to the LINAC 2 (linear accelerator) to an energy of 50 MeV. Then they are injected into the Proton Synchrotron Booster (PSB) and boosted to an energy of 1.4 GeV before being accelareted in the Proton Synchrotron (PS) to 26 GeV. Finally the beams are pushed up to 450 GeV injection energy in the Super Proton Synchrotron (SPS). The injected protons in LHC are accelerated up to collision energy, during the early running phase, 2010-2012 $\sqrt{s}=7$ TeV, nominal $\sqrt{s}=14$ TeV. The LHC has total number of 1232 superconducting dipole magnets, which provide a magnetic field of 8.33 Tesla. They are needed to keep protons on orbit during the acceleration. There are additional 392 quadrupole magnets, which are used to keep the beams focused. In order to obtain this high magnetic field, the superconducting magnets are operated at a temperature of 1.9 K (-271.3 °C) using liquid helium. Then the proton beams are injected into the rings in groups which are called bunches and the machine circulates and collides them at four interaction points.

Table 3.1. Design parameters of the Large Hadron Collider (Bruning et al., 2004).

Parameter	Value	Unit
Momentum at Collision	7	TeV
Dipole field at 7 TeV	8.33	T
Quadrupole gradient	220	T/m
Circumference	26659	m
Design Luminosity	10^{34}	$cm^{-2}s^{-1}$
Number of bunches	2808	
Particles per bunch	$1.15 \cdot 10^{11}$	
DC beam current	0.56	A
Stored energy per beam	362	MJ
Ultimate Dipole Field	9	T
Injection Dipole Field	0.4	T
Ramp Time	20	min
Magnet Coil inner diameter	56	mm
Distance between beams	194	mm

There are four different main detectors installed in the caverns along the ring: two of which are high luminosity experiments ATLAS (A Toroidal LHC Apparatus) and CMS (Compact Muon Solenoid). They are general-purpose detectors and their main goal is to search Higgs boson that is predicted to be responsible for the electroweak symmetry breaking mechanism. Besides, CMS and ATLAS search new physics phenomena such as supersymmetric particles, new massive vector bosons, extra dimensions, quark compositeness etc. at the TeV scale. The LHCb (Large Hadron Collider beauty) studies B physics (b-quark physics) and CP violation, and ALICE (A Large Ion Collider Experiment) is designed to study heavy ion collisions in order to observe quark-gluon plasma that is the state of hot nuclear matter. There are also two smaller experiments: LHCf (Large Hadron Collider forward) and TOTEM (TOTAL Elastic and diffractive cross-section Measurement). They are located in the tunnel, near ATLAS and CMS respectively and focus on forward physics.

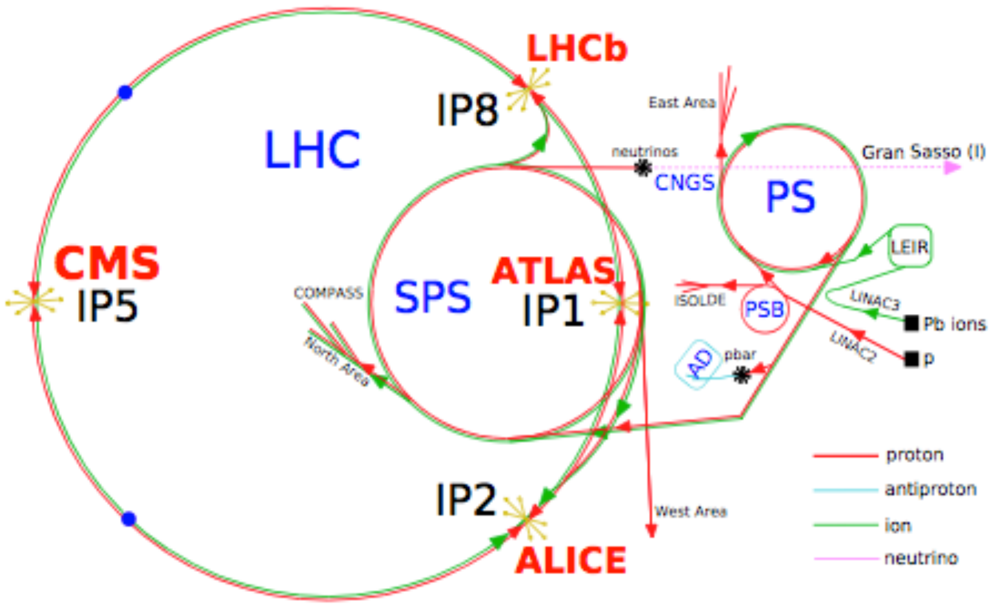

Figure 3.1. A schematic view of the CERN accelerator complex (Martelli, 2012).

3.2.1. LHC Operation and Physics at Proton-Proton Collider

The physics program at the LHC began operation in late 2009 with pp collisions at a center of mass energy of 7 TeV. By the end of 2011, CMS collected a data sample with integrated luminosity of $6fb^{-1}$. The center of mass energy was increased to 8 TeV. At the time of August 2012 a further 11 fb^{-1} integrated luminosity had been delivered. In this period, the LHC operated with bunch trains with a 50 ns bunch spacing. Current planning for the LHC and injector chain foresees a series of three long shutdowns. In the period 2013-2014, the center of mass energy will be increased to 14 TeV (or slightly lower). The plan for the LHC operators is to double the collision energy by 2015 (Chatrchyan et al., 2011b).

Proton-proton collisions phenomenology is very different from lepton collisions, because protons are not elementary particles and have a sub-structure. A proton composes of a number of point-like constituents, called "partons" (gluons and quarks). The constituent partons carrying a fraction of total proton energy interacts with each other in a collision and a fraction of total proton energy is exchanged.

There are two main topologies of events in *pp* collisions, depending on the energy transfer of the interacting partons: Large-distance collisions between the two incoming protons lead to a small momentum transfer and a suppression of particles scattering at large angle. These are known as “soft collisions”. The particles produced in final state of such interactions have large longitudinal momenta but small transverse momenta (p_T) relative to the beam line and most of the collisions energy escapes down to the beam pipe. The products of these soft interactions are called “minimum bias” events. They are not interesting for physics research purposes. In case of head-on collisions occurring between two partons of the incoming protons, interacting at small distances, a large momentum can be transferred. It is called as “hard scattering”. In these cases, final states particles can be produced at large angles with respect to beam line (high p_T) with creation of massive particles.

The constituents of protons, namely quarks and gluons, interact with only a fraction of the proton energy is given by

$$\sqrt{\hat{s}} = \sqrt{x_1 x_2 s} \tag{3.1}$$

In here x_1 and x_2 refer to the energy-fractions carried by the interacting partons, respectively. Whereas $\sqrt{\hat{s}}$ is the effective center-of-mass energy of the colliding partons (hard scattering), $\sqrt{s}$ is center-of-mass energy of the proton beams. Thus, the center of mass energy has to be larger compared to an electron-electron machine. Each collision will lead to a different type of event determined by the cross section of possible interactions. Because the fraction of momentum carried by interacting partons will be different. The cross section and the event rate at the LHC design luminosity for different processes as a function of the center of mass energy $\sqrt{s}$ is shown in Figure 3.2.

In order to discover new particles, it is not sufficient to achieve a high amount of energy but it is necessary to produce collisions at a significant rate. The number of events for a special process at a collider is given by

$$N_{event} = L\sigma_{event} \tag{3.2}$$

where σ_{event} is the cross section for the physics process under study and L is the luminosity of collider and depends only on the beam parameters. The luminosity of collider can be written for a Gaussian transverse beam profile distribution as:

$$L = f\,\frac{n_b N_b^2}{4\pi\sigma_x\sigma_y} \tag{3.3}$$

where σ_x and σ_y characterise the Gaussian widths of the transverse beam profiles in *x*- and *y*-direction, respectively; f is a frequency of the collision; N_b yields the number of particles per bunch and n_b the number of bunches per beam. In order to achieve the highest possible luminosity, all these parameters have to be tuned so the best capability for new discoveries can be reached. The total integrated luminosity delivered over the course of 2011 can be seen in Figure 3.3. In order to reach LHC design luminosity, a small transverse beam profile, a high bunch collision frequency and a large number of particles per bunch are required. At the LHC the nominal number of protons per bunch is about 10^{11}. Since this number is large, the average number of inelastic *pp* collisions ("minimum bias" events) per bunch crossing is high and it is up to 20 for design luminosity. This causes more difficult experimental conditions. Because the rare interesting events in a bunch crossing are superposed (pile-up) on top of these 20 minimum bias events.

In contrast to most hadron colliders in the past, it was decided to produce *pp* collisions instead of $p\bar{p}$ collisions in the LHC, because it's very difficult to produce sufficient number of antiprotons. The most active components of the protons are gluons rather than quarks and the distribution of gluons in protons and antiprotons is the same. This decision has important consequences for the design of the collider. Since e^+ and e^- move in opposite directions for a given electromagnetic field configuration, the LEP collider could use a single beam pipe where electrons and positrons could circulate next to each other. Since the LHC uses protons, two beam pipes and two different (opposite) magnetic field configurations are necessary.

The cross section of a special partonic process (like $q\bar{q} \rightarrow W' \rightarrow \ell\nu$) depends on the cross section $\hat{\sigma}$ of the proton partons (known as partonic cross section) which is modeled by Feynman graphs. Since only two partons interact directly with in a *pp* collision, the cross section is also dependent on the partons densities given as parton density functions (PDF) inside the proton. So that the cross section is given by

$$\sigma = \int dx_1 \int dx_2\, f_1\left(x_1, Q^2\right) f_2\left(x_2, Q^2\right)\, \hat{\sigma} \tag{3.4}$$

The PDF $f_i\left(x_i, Q^2\right)$ is defined as the probability to find a parton inside the proton carrying the momentum fraction x_i at the energy scale Q.

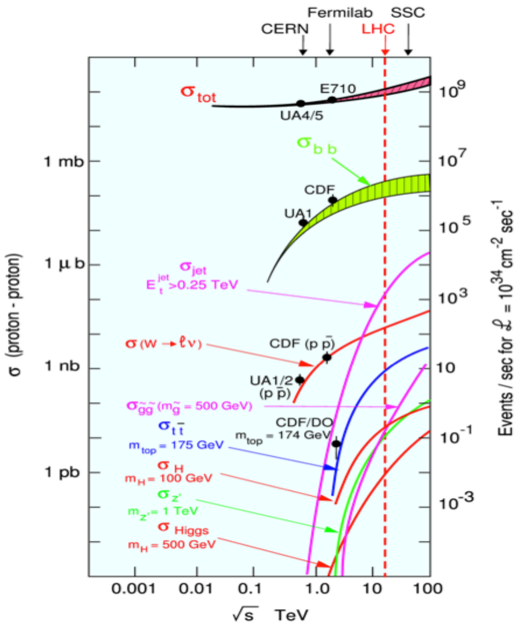

Figure 3.2. Hadronic cross sections and event rates for different physics processes as a function of the centre-of-mass energy $\sqrt{s}$ at proton-proton colliders (Bayatian et al., 2000).

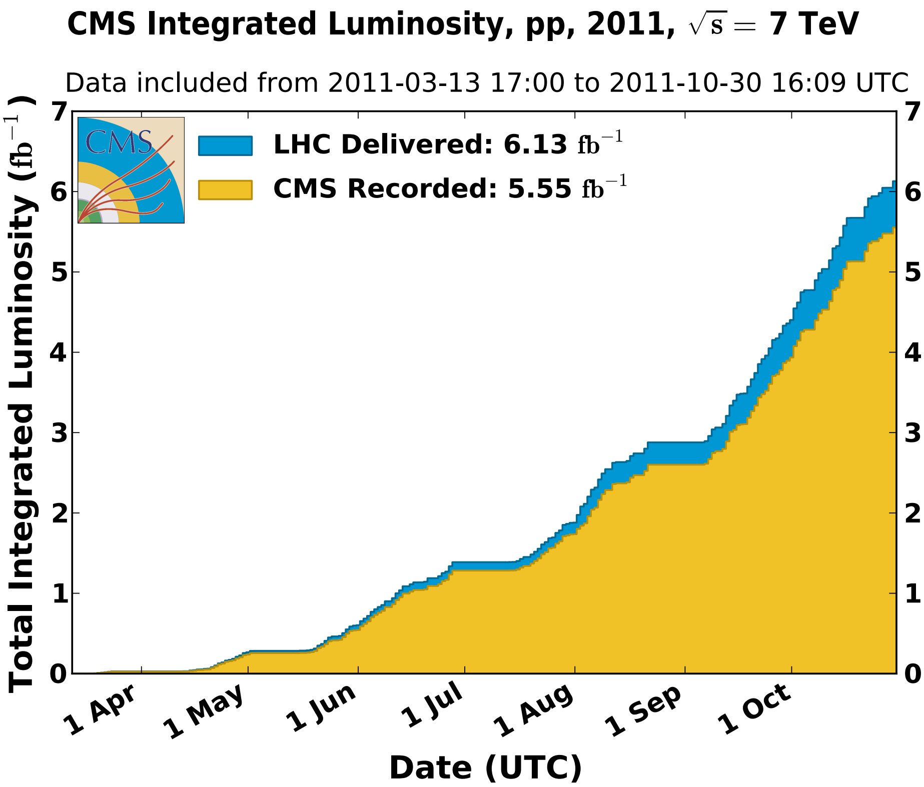

Figure 3.3. The total integrated luminosity both delivered by the LHC to CMS and recorded by CMS in 2011. There is less than 10 % difference between delivered and recorded luminosities for the CMS detector during the 2011 runs (http://cms.web.cern.ch/tags/luminosity).

In the following, a description of the CMS detector is given with focus on those subsystems of main importance for the work.

3.3. The Compact Muon Solenoid (CMS) Experiment

The Compact Muon Solenoid (CMS) is a general-purpose detector of the LHC. It is installed 100 m underground at the LHC interaction point 5 (P5) near the village of Cessy in France. It is built from various sub-components to measure the particles, which are directly or indirectly created within a *pp* collision. It is designed to measure the energy and momentum of photons, electrons, muons and other charged particles with high precision, resulting in an excellent mass resolution for many new particles ranging from the Higgs boson up to a possible heavy W' and Z' in the multi-TeV mass range (Bayatian et al., 1997). The detector requirements of the CMS experiment to meet the goals of the LHC physics programme can be summarized as follows:

- Good muon identification and momentum resolution over a wide range of momenta in the region $|\eta| < 2.5$, good dimuon mass resolution,
- Good charged particle momentum resolution and reconstruction efficiency in the inner tracker,
- Good electromagnetic energy resolution, good diphoton and dielectron mass resolution,
- Good E_T^{miss} and dijet mass resolution (Chatrchyan et al., 2008a).

In order to detect all particles produced from the collision, it was designed as a perfect sphere around the collision point. It performs the best coverage of the solid angle at the interaction point. The whole structure of the CMS is shown in figure 3.4. It consists of several sub-detectors. Each of them measure and identify different types of particles. Figure 3.5 shows a slice through CMS showing particles incident on the different sub-detectors. It looks like the structure of an onion.

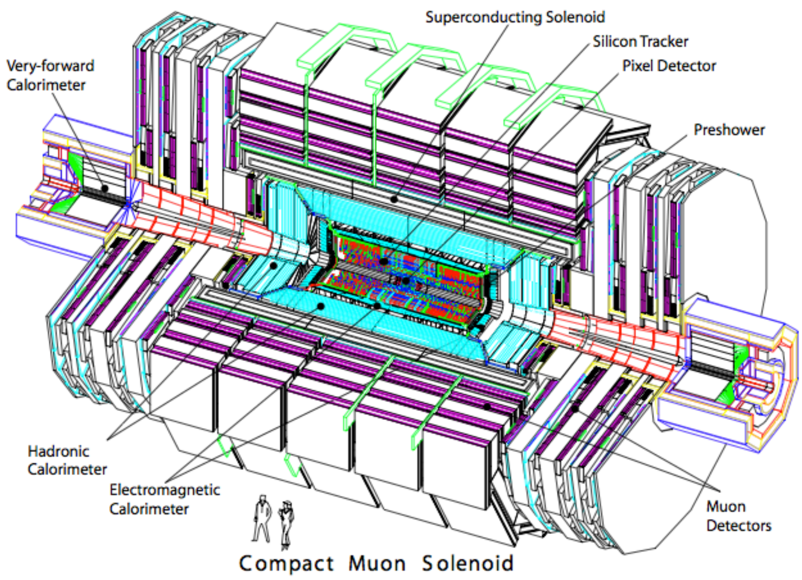

Figure 3.4. The whole view of the CMS detector (Chatrchyan et al., 2008a).

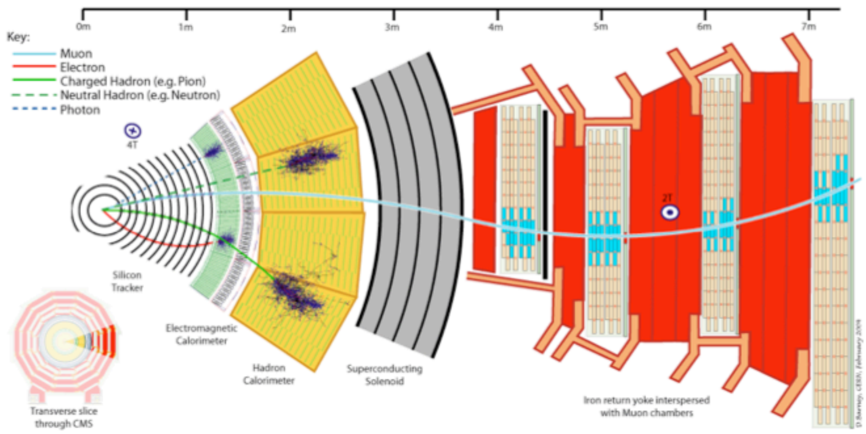

Figure 3.5. Slice through CMS showing particles incident on the different sub detectors (Sikler, 2005).

The structure of the CMS is the typical one for experiments at a collider. The detector has a cylindrical shape with the whole structure of 21.6 m length, a diameter of 14.6 m and a total weight of 14000 ton. It has almost 4π solid angle coverage and it can be subdivided into three major parts: there is a cylindirical central section (the barrel) around the beam line closed at its edges by two caps (the endcaps). It consists of a silicon tracking system, an electromagnetic and a hadronic calorimeter and a muon system. A high magnetic field of 3.8 T parallel to the beam axis is provided by a superconducting solenoid magnet.

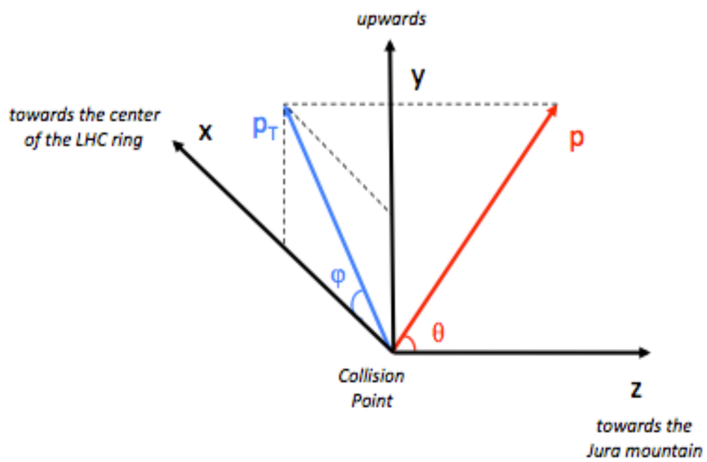

Figure 3.6. The CMS coordinate system (Martelli, 2012).

The LHC uses a right handed cartesian system as natural reference frame and it's origin is fixed in the average interaction vertex. The x axis points towards at the LHC centre, the z axis is parallel to the beam line and y axis is upward. The CMS coordinate system is shown in Figure 3.6. The coordinate triplet (r,ϕ,η) is a convenient and commonly used coordinate system. It is better to suit the cylindric geometry. Here r is the distance from the z axis, ϕ is the azimuthal angle in the transverse plane and η is the pseudo-rapidity and defined as $\eta = -\ln(\tan(\theta/2))$, where θ is the angle measured from the z axis in the 0, π range.

In order to calculate kinematic variables, such as the Missing Transverse Energy (*MET*) or the transverse momentum (p_T), the second reference frame is usually chosen. Because the energy balance of the events is only known in the transverse plane at hadron colliders. The projections in the transverse plane of momentum and energy are commonly used instead of momentum *p* and energy *E*. They are given by:

$$p_T = p.\sin\theta = \sqrt{p_x^2 + p_y^2}$$
$$E_T = \sqrt{E_x^2 + E_y^2} \tag{3.5}$$

Since the magnetic field curves the trajectory in that plane, E_z cannot be measured due to the energy losses in the region of the beam pipe. In the following sections the sub-detectors will be described in more detail.

3.3.1. The tracking system

The CMS inner tracking system is designed to provide a precise and efficient measurement of charged particles trajectories from the LHC collisions and also precise reconstruction of secondary vertices. It is a cylindric structure that surrounds the interaction point. It has a length of 5.8 m and a diameter of 2.5 m. The CMS solenoid provides a homogeneous magnetic field of $\sim$ 4T over the full volume of the tracker. Moreover, it is expected to play an important role in jet flavour tagging, especially for b and τ -jets by accurate secondary vertex reconstruction.

At the LHC design luminosity of $10^{34}cm^{-2}s^{-1}$ there are on average about 1000 particles from more than 20 overlapping proton-proton interactions in the acceptance of the tracker for each bunch crossing, i.e. every 25 ns. Therefore a detector technology featuring high granularity to identify the different trajectories and fast response to assign them to the correct bunch crossing are required. However, these features imply a high power density of the on-detector electronics, which in turn requires efficient cooling. This is in direct conflict with the aim of keeping to the minimum the amount of material in order to limit multiple scattering, bremsstrahlung, photon conversion and nuclear interactions. In addition, the intense particle flux also causes radiation damage to the tracking system. The main challenge in the design of the tracking system is to operate in the harsh LHC environment for an expected lifetime of 10 years. These requirements on granularity, speed and radiation hardness lead to a tracker entirely based on silicon detector technology. The tracking within a strong magnetic field is a very powerful tool for the identification and reconstruction of muons, electrons, photons and jets (Chatrchyan et al., 2008a).

A schematic drawing of the CMS tracker is shown in Figure 3.7. The total tracker system covers the pseudorapidity region $|\eta| < 2.5$. It consists of two main sub-detectors: the pixel tracker, as innermost structure and slicon strip tracker around. 3 pixel layers and 10 silicon strip layers are installed in the barrel and 2 pixel layers, 3 inner and 9 outer forward disks of silicon detectors are placed in each endcap. The total length is approximately 540 cm and the outer radius extends up to 107-110 cm.

The **pixel tracker** is the closest part of the tracking system to the interaction region. High resolution 3D space points are provided by this detector and it is required for accurate reconstruction of the charged track. Since it has high position resolution, it can determine the impact parameter of charged partices. It also allows secondary vertices reconstruction in 3D so it gives efficient identification of b and τ -jets. It consists of three-barrel layers (BPix) and two end-cap disks (FPix) on the each side. The BPix layers with 53 cm long are located at mean radii of 4.4 cm, 7.3

cm and 10.2 cm respectively. The FPix disks are extending from 6 to 15 cm in radius and are placed on each side at z =34.5 cm and 46.5 cm from the interaction point. The spatial resolution is $\approx 10\ \mu m$ for measurements in the $r-\phi$ plane and about 15-20 μm for the z direction and each pixel is $125 \times 125\ \mu m^2$. The pixel detector covers a pseudorapitiy range $-2.5 < \eta < 2.5$, matching the acceptance of the central tracker. The whole pixel system consists of about 1440 segmented silicon modules with a total of 66 million readout channels. The geometrical layouts of the CMS pixel detector and hit coverage as a function of pseudo-rapidity are shown in Figure 3.8 (Chatrchyan et al., 2008a).

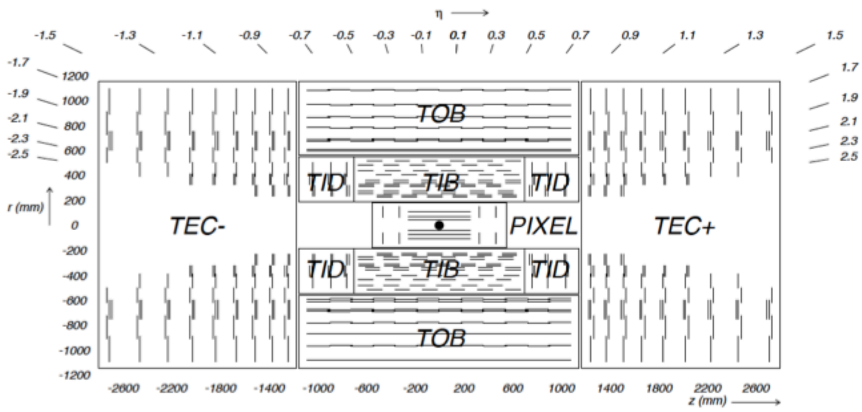

Figure 3.7. Schematic cross section through the CMS tracker. Each line represents a detector module. Double lines indicate back-to-back modules (Chatrchyan et al., 2008a).

The **silicon strip tracker** is the outermost region of the tracking system. Its radial region is between 20 cm and 116 cm. The sensor elements in the strip tracker are single sided *p*-on-*n* type silicon micro-strip sensors. It is composed of different subsystems: there are 4 inner layers (Tracker Inner Barrel, TIB) and 6 outer layers (Tracker Outer Barrel, TOB). On the each side of TIB, there are 3 mini disks (Tracker Inner Disks, TID). TIB/TID is surrounded by TOB. Each end cap region is composed of 9 disks (Tracker End Cap, TEC). There are 15 148 modules in total. They provide a measurement of the position of the particle in two dimensions. It is performed by calculating centre of the charge distribution in the different strips and detected through the ionisation produced by the particles traversing the detector. The single point resolution is of the order of about 300 μm for the z direction and 30 μm in the $r-\phi$ plane (Chatrchyan et al., 2008a). The longitutial view of silicon strip tracker is shown in Figure 3.9.

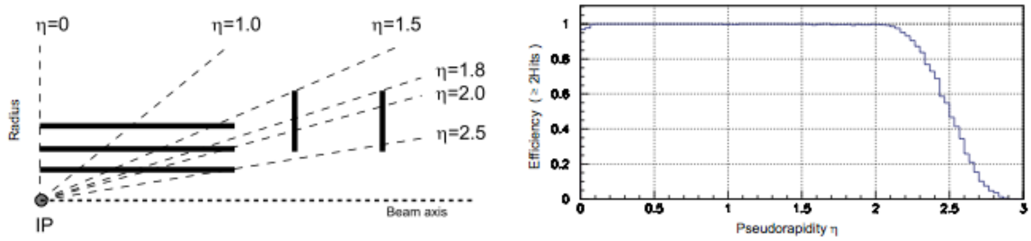

Figure 3.8. Geometrical layout of the pixel detector and hit coverage as a function of pseudo-rapidity (Chatrchyan et al., 2008a).

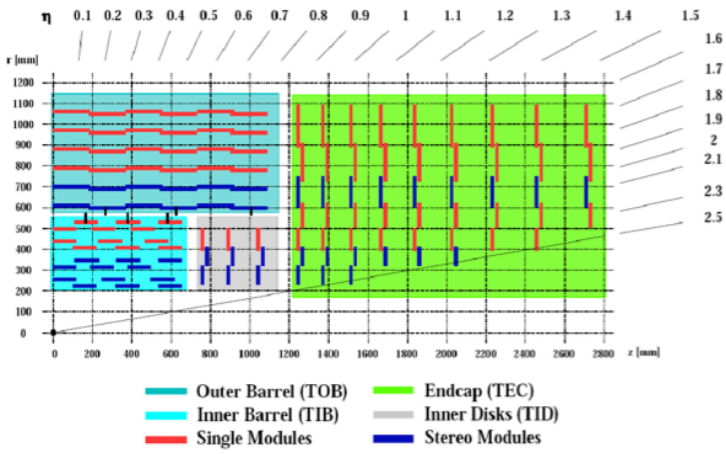

Figure 3.9. Longitudinal view of one quarter of the silicon strip tracker (Bayatian et al., 1994).

3.3.2. The Calorimeters

The calorimeters of the CMS play a significant role in exploiting the physics potential. The CMS calorimeters are designed to identify and measure the energy of photons, electrons and jets precisely and to provide hermetic coverage for measuring missing transverse energy. Additional requirements for the calorimeters are good efficiency for electron and photon identification, excellent background rejection against hadrons and jets, and good separation of τ-hadronic decays from normal QCD jets. The CMS calorimeter system is composed of two layers as electromagnetic calorimeter and hadronic calorimeter (Bayatian et al., 1997).

3.3.2.1. The Electromagnetic Calorimeter (ECAL)

The electromagnetic calorimeter (ECAL) is an important detector element for a large variety of SM and other physics processes. It plays an essential role in the study of the physics of electroweak symmetry breaking, especially through the Higgs sector's exploration. The search for the Higgs boson strongly relies on information from the ECAL at the LHC: by measuring the two-photon decay mode from $H \rightarrow \gamma\gamma$ for $m_H \leq 150$ GeV, and by measuring the electrons and positrons from the decay of Ws and Zs originating from the $H \rightarrow ZZ^*$ and $H \rightarrow WW$ for $140 \text{ GeV} \leq m_H \leq 700 \text{ GeV}$. It is designed to provide the cleanest signal and best energy resolution. It is also critical for other measurements from cascade decays of gluinos and squarks, where the lepton pair mass provides information about the supersymmetric particle spectrum, or the leptonic decay of new heavy vector bosons (W', Z') in the multi-TeV mass range (Bayatian et al., 1997).

The ECAL surrounds the Tracker. It measures the energy and the direction of electromagnetically interacting particles like electrons and photons and, together with the hadron calorimeter measures jets with high precision. It is a hermitic homogenous calorimeter. It is made of 61200 lead tungstate ($PbWO_4$) crystals mounted in the central barrel part, closed by 7324 crystals in each of the two endcaps. The characteristics of the $PbWO_4$ crystals make them a suitable choice for LHC operation. $PbWO_4$ crystals have a short radiation length (0.89 cm) and small Moliere radius (2.2 cm) and high density (8.28 g/cm^3) (Chatrchyan et al., 2008a). It is a fast scintillator, and radiation resistant, and relatively easy to produce from readily available materials, and substantial experience and production capacity. All these features allow designing a fine granularity and a compact calorimeter inside the solenoid (Bayatian et al., 1997).

The pseudorapidity coverage of geometrical crystal extends to $|\eta| < 3$. The transverse granularity of $\Delta\eta \times \Delta\phi = 0.0175 \times 0.0175$, corresponding to a crystal front face of about 22×22 mm^2, matches the $PbWO_4$ Moliere radius of 21.9 mm. By reducing the area over which the energy is summed, the small Moliere radius reduces the effect of pileup contributions to the energy measurement. Although the crystal front section does not change, the granularity in the endcaps $(1.48 < |\eta| < 3.0)$ increases progressively to a maximum value of $\Delta\eta \times \Delta\phi \approx 0.05 \times 0.05$. In order to limit the longitudinal shower leakage of high-energy electromagnetic showers to an acceptable level, a total thickness of about 26 radiation lengths at $|\eta| = 0$ is desired. In the barrel region, this corresponds to a crystal length of 23 cm. In the endcap region the existence of a preshower (a total of 3 X_0 of lead) allows the use of slightly shorter crystals (22 cm) (Bayatian et al., 1997).

The ECAL composes of two sub-detectors: ECAL barrel (EB) and ECAL endcaps (EE). The EB has an inner radius of 129 cm and a volume of 8.14 m^3. Its structure consists of 36 identical "supermodules". Each of them covers half the barrel length corresponding to a pseudorapidity range of $0 < |\eta| < 1.479$. The two ECAL endcaps (EE) cover a pseudorapidity range of $1.479 < |\eta| < 3.0$ and they are located at a longitudinal distance of 3.15 m from the interaction point. They are each structured as 2 "Dees", consisting of semi-circular aluminum plates that are cantilevered structural units of 5×5 crystals. They are known as "super-crystals" (Chatrchyan et al., 2008a). The endcap preshower covers a pseudorapidity range of $1.65 < |\eta| < 2.61$. The preshower detectors are placed in front of the ECAL crystals, and are designed to provide $\pi^0 - \gamma$ separation. The layout of the CMS electromagnetic calorimeter is shown in Figure 3.10.

For the energy of about from 25 GeV to 500 GeV, appropriate for photons from the $H \rightarrow \gamma\gamma$ decay, the energy resolution of the ECAL can be parametrized as (Chatrchyan et al., 2008a)

$$\left(\frac{\sigma}{E}\right)^2 = \left(\frac{a}{\sqrt{E}}\right)^2 + \left(\frac{\sigma_N}{E}\right)^2 + c^2 \qquad (E \text{ in GeV}) \qquad (3.5)$$

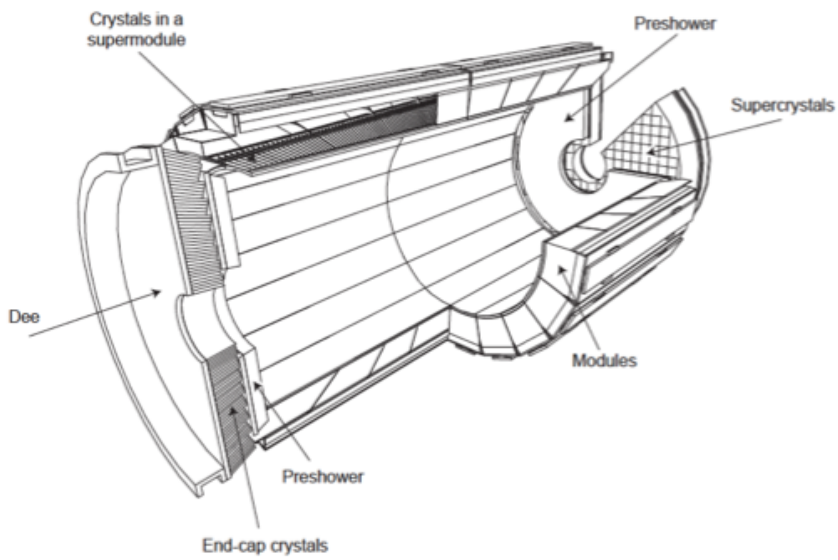

Figure 3.10. Layout of the CMS electromagnetic calorimeter showing the arrangement of crystal modules, super modules and endcaps, with the preshower in front (Chatrchyan et al., 2008).

where a is the stochastic term, σ_N is the noise and c is the constant term. The stochastic term includes fluctuations in the shower containment as well as contribution from photostatistics. The different contributions expected for the energy resolution are summarized in Figure 3.11. Terms representing the degradation of the energy resolution at extremely high energies have not been included. The noise term contains the contributions from electronic noise and pile-up energy; the former is quite important at low energy, the latter is negligible at low luminosity. The coefficients a and c are determined by the active detector material. The curve labeled as "intrinsic" includes the shower containment and a constant term of 0.55%. The constant term is kept down to this level in order to profit from the excellent stochastic term of $PbWO_4$ in the energy range relevant for the Higgs search. In order to achieve a good energy resolution, all the contributing terms are kept small and at the same order as the relevant photon energies (Chatrchyan et al., 2008a).

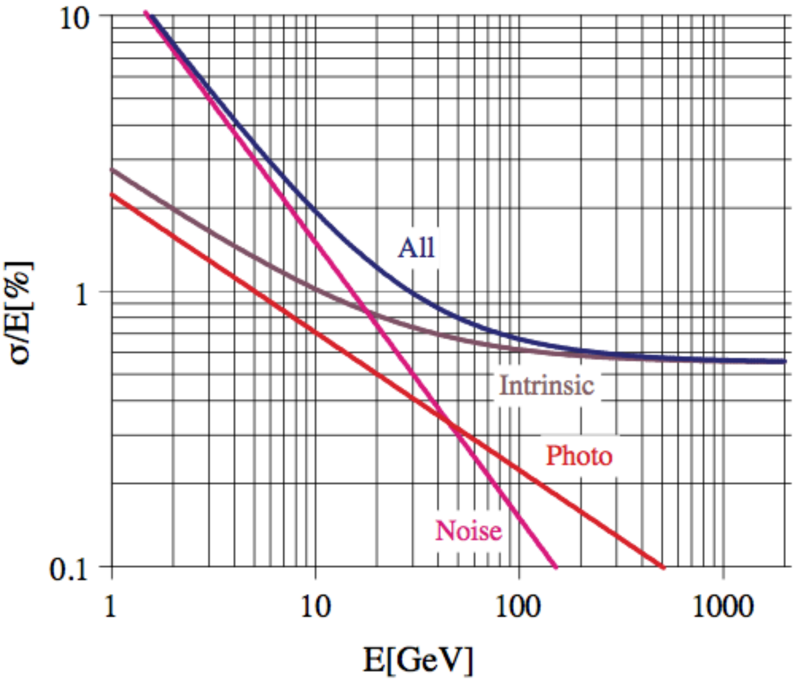

Figure 3.11. Different contributions to the energy resolution of the $PbWO_4$ calorimeter (Bayatian et al., 1997).

3.3.2.2. The Hadronic Calorimeter (HCAL)

In this part, the hadronic calorimeter (HCAL) and its sub-detectors will be described in detail. Then we will discuss the HCAL analysis in Chapter 7.

The HCAL is designed to measure the energies and directions of hadron jets and missing transverse energy due to neutrinos or exotic particles as they require a hermitic coverage. It also helps in the identification of electrons, photons and muons. It surrounds the electromagnetic calorimeter. The HCAL is a sampling calorimeter with alternating layers of brass and scintillator. Brass has been chosen as absorber material because it has a short interaction length, is a non-magnetic material and is easy to machine. The active material of the calorimeter consists of plastic scintillator tiles, which are readout by wave length-shifting (WLS) fibers. In order to provide good dijet separation and mass resolution, the tiles are arranged in projective towers with good granularity (Bayatian et al., 2006).

The HCAL composes of four sub-detectors: Hadronic Barrel (HB), Hadronic Endcap (HB), Hadronic Outer (HO) and Hadronic Forward (HB). The longitudinal view of the CMS hadronic calorimeter is shown in Figure 3.12. The hadron calorimeter barrel and endcaps are placed behind the tracker and the electromagnetic calorimeter as seen from the interaction point. The calorimeter between the outer extent of the ECAL (R = 1.77 m) and the inner extent of the magnet coil (R = 2.95 m) is hadronic barrel. Since this constrains the total amount of the material that can be put in to absorb the hadronic shower, the hadronic outer calorimeter (*or tail catcher*) is placed outside of the solenoid to complement the barrel calorimeter. Beyond $|\eta| = 3$, the forward hadron calorimeter is placed at 11.2 m from the interaction point. It extends the pseudorapidity coverage up to $|\eta| = 5.2$ using a Cherenkov-based and radiation hard technology (Chatrchyan et al., 2008a).

The hadronic calorimeter is read out in a tower-like structure. It is segmented into individual calorimeter cells along with three coordinates: η , ϕ and depth. The ϕ coordinate refers to the azimuthal angle and η is the pseudorapidity. The depth is an integer coordinate that enumerates the segmentation longitudinally, along the direction from the center of the nominal interaction region.

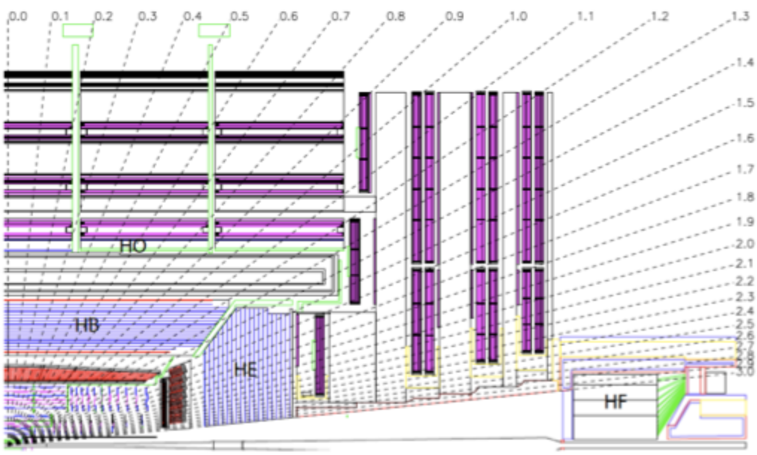

Figure 3.12. Longitudinal view of the CMS detector showing the locations of the hadronic barrel (HB), endcap (HE), outer (HO) and forward (HF) calorimeters (Chatrchyan et al., 2008a).

The layout of the barrel, endcap and outer calorimeter cells is shown in Figure 3.13. Most cells include several scintillator layers; for example, in most of the barrel all 17 scintillator layers are combined into a single depth segment. In this figure, the right end of the beam line is the interaction point. FEE represents the location of the Front End Electronics for the barrel and the endcap. In the diagram, the numbers on the top and left refer to segments in η , and the numbers on the right and the bottom refer to scintillator layers. Colors/shades indicate the combinations of layers that form the different depth segments, which are numbered sequentially starting at 1, moving outward from the interaction point. The outer calorimeter is assigned depth 4. Segmentation along ϕ is not shown. The tower structure for HCAL is summarized in Table 3.2. While HO has 15 (1–15) and HE has 14 (16–29), HB has 16 segmentations (1–16) on both sides of the $z = 0$ plane. All the layers in HB, belonging to a given η and ϕ slice, are grouped into one tower, excepting for the η indices of 15 and 16. For η index of 15, layers 13(14) to 16 belong to the second depth index. For η index of 16, layers 3 onwards belong to depth index 2. For HE, the first 2 η indices (16, 17) have only one depth slice, the next 9 η indices (18–26) have two depth slices and the remaining ones have 3 depth slices. The third depth slices corresponding to the last two η indices (28 and 29) belong to the same readout tower. The granularity in ϕ changes as a function of the η index. The tower size along ϕ is 5° for the first 20 η indices ($|\eta| < 1.740$), 10° for η indices 21 to 39 and 20° for the last two indices (40 and 41) (Banarjee, 2005). In total the HCAL contains 9072 readout channels: there are 2592 channels in HB, 2592 channels in HE, 2160 channels in HO and 1728 channels in HF (Baiatian, 2006).

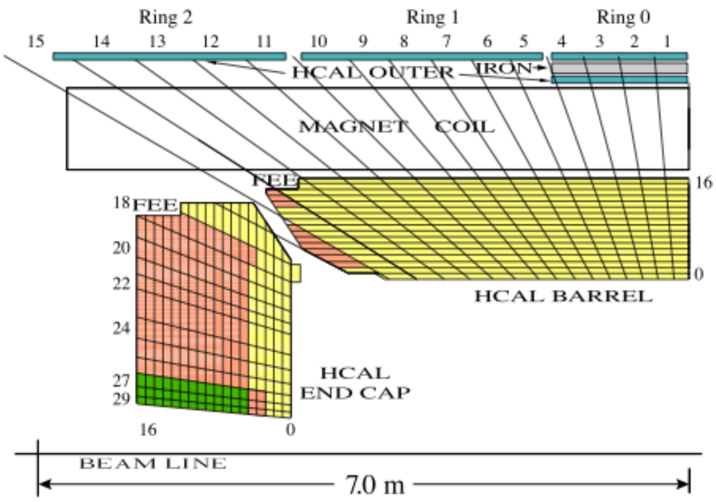

Figure 3.13. The HCAL tower segmentation in the *r, z* plane for one-fourth of the HB, HO and HE detectors (Chatrchyan et al., 2008a).

3.3.2.2.(1). Hadronic Barrel (HB)

The hadronic barrel (HB) covers the pseudorapidity range $|\eta| < 1.3$. It is divided into two half-barrel sections (HB+ and HB−). Each half-barrel composes of 18 identical azimuthal wedges ($\Delta\phi = 20^{\circ}$) and is inserted from either end of the cryostat of the superconducting solenoid. Each wedge is further segmented into four azimuthal angle ($\Delta\phi = 5^{\circ}$) sectors. Figure 3.14 shows the numbering scheme of the wedges. The plastic scintillator is divided into 16 η sectors, resulting in a segmentation $(\Delta\eta, \Delta\phi) = (0.087, 0.087)$ (Chatrchyan et al., 2008a).

Energy depositions result in scintillator light in the HB/HE. This light is carried by optical fibers to the hybrid photodiodes (HPDs). Then HPDs convert the light into an electrical output. Each HPD contains signals from 18 different channels. These channels correspond to 16 consecutive towers aligned with the same i_{ϕ}, from i_{η} = ±1 to ±16. i_{ϕ} and i_{η} indicate index of the projective towers. HB towers at i_{η} = ±15 and ±16 have two separate depths, giving a total of 18 channels. Since the HB is segmented into 72 slices in ϕ, there are 2 × 72 = 144 HPDs in the HB: 72 each for the HB+ and HB−. The readout boxes (RBXs) each contain four HPDs consecutive in ϕ-slice, for a total of 36 RBXs in the HB. The HE contains the same number of

HPDs/RBXs as the HB, but the geometry is more complicated due to the ϕ merging of towers and additional depth segmentation (Chou, 2010).

Table 3.2. Sizes of the HCAL readout towers in η and ϕ as well as the segmentation in depth. HF does not have pointing geometry and the η ranges provided here correspond to of $z \cong 1122.2$ cm. *The first two depth segmentations have finer η segmentation, namely 2.650-2.868 and 2.868-3.000 are referred to tower indices 28 and 29 (Banarjee, 2005).

Tower index	η range		Detector	Size		Depth segments
	Low	High		η	ϕ	
1	0.000	0.087	HB, HO	0.087	5^o	HB=1, HO=1
2	0.087	0.174	HB, HO	0.087	5^o	HB=1, HO=1
4	0.174	0.261	HB, HO	0.087	5^o	HB=1, HO=1
5	0.261	0.348	HB, HO	0.087	5^o	HB=1, HO=1
6	0.348	0.435	HB, HO	0.087	5^o	HB=1, HO=1
7	0.435	0.522	HB, HO	0.087	5^o	HB=1, HO=1
8	0.522	0.609	HB, HO	0.087	5^o	HB=1, HO=1
9	0.609	0.696	HB, HO	0.087	5^o	HB=1, HO=1
10	0.696	0.783	HB, HO	0.087	5^o	HB=1, HO=1
11	0.783	0.879	HB, HO	0.087	5^o	HB=1, HO=1
12	0.879	0.957	HB, HO	0.087	5^o	HB=1, HO=1
13	0.957	1.044	HB, HO	0.087	5^o	HB=1, HO=1
14	1.044	1.131	HB, HO	0.087	5^o	HB=1, HO=1
15	1.131	1.218	HB, HO	0.087	5^o	HB=2, HO=1
16	1.218	1.305	HB, HE	0.087	5^o	HB=2, HE=1
17	1.305	1.392	HE	0.087	5^o	HE=1
18	1.392	1.479	HE	0.087	5^o	HE=2
19	1.479	1.653	HE	0.087	5^o	HE=2
20	1.653	1.740	HE	0.087	5^o	HE=2
21	1.740	1.830	HE	0.090	10^o	HE=2
22	1.830	1.930	HE	0.100	10^o	HE=2
23	1.930	2.043	HE	0.113	10^o	HE=2
24	2.043	2.172	HE	0.129	10^o	HE=2
25	2.172	2.322	HE	0.150	10^o	HE=2
26	2.322	2.500	HE	0.178	10^o	HE=2
27	2.500	2.650	HE	0.150	10^o	HE=3
*28	2.650	2.853	HE	0.350	10^o	HE=3
29	2.853	2.964	HF	0.111	10^o	HF=2
30	2.964	3.139	HF	0.175	10^o	HF=2
31	3.139	3.314	HF	0.175	10^o	HF=2
32	3.314	3.489	HF	0.175	10^o	HF=2
33	3.489	3.664	HF	0.175	10^o	HF=2
34	3.664	3.839	HF	0.175	10^o	HF=2
35	3.839	4.013	HF	0.174	10^o	HF=2
36	4.013	4.191	HF	0.178	10^o	HF=2
37	4.191	4.363	HF	0.172	10^o	HF=2
38	4.363	4.538	HF	0.175	10^o	HF=2
39	4.538	4.716	HF	0.178	10^o	HF=2
40	4.716	4.889	HF	0.173	10^o	HF=2
41	4.889	5.191	HF	0.302	10^o	HF=2

3.3.2.2.(2). Hadronic Endcap (HE)

The hadronic endcap (HE) is a sampling calorimeter similar to HB. It covers the pseudorapidity range $1.3 < |\eta| < 3$. It is formed of two half-endcaps (HE+ and HE−) which are composed of 18 identical azimuthal wedges ($\Delta\phi = 20^{\circ}$). The HE consists of 14 η towers with 5° ϕ segmentation. The ϕ segmentation is 5° and the η segmentation is 0.087 for the 5 outermost towers (at the smaller η). The ϕ segmentation is 10° for the 8 innermost towers, while the η segmentation varies from 0.09 to 0.35 at the highest η. The HE has 2304 towers in total.

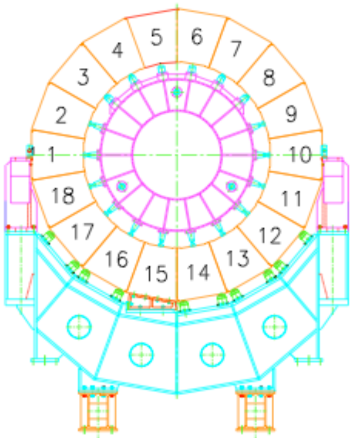

Figure 3.14. Numbering scheme for the HB wedges. Wedge 1 is on the inside (+*x* direction) of the LHC ring (Chatrchyan et al., 2008a).

While the numbering scheme in η is shown in Figure 3.15 (a), the CMS convention for ϕ as applied to HE is shown in Figure 3.15 (b). Two endcaps are about 1.8 thick with an inner radius of 40 cm and an outer radius of about 3 m. The granularity of the calorimeters is identical. It is $(\Delta\eta,\Delta\phi) = (0.087,0.087)$ for $|\eta| < 1.6$ and $(\Delta\eta,\Delta\phi) \approx (0.17,0.17)$ for $|\eta| \geq 1.6$. There are 19 layers of scintillator. While the HB has a minimum depth of 5.8 nuclear interaction lenghts λ_I, the HE including electromagnetic crystals, is about 10 interaction lenghts λ_I (Chatrchyan et al., 2008a).

3.3.2.2.(3). Hadronic Outer (HO)

In order to improve the hadronic shower containment, two layers of scintillators known as hadronic outer (HO) are placed outside of the solenoid but in front of the first muon station. This extends the total depth of the calorimeter to minimum 11.8 λ_I except at the barrel-endcap boundry region with an improvement in linearity and resolution. So that it is possible to identify and quantify and to measure the contribution from the late starting showers after HB. The HO also improves the E_T^{miss} resolution of the calorimeter.

The HO covers the pseudorapidity range $|\eta| < 1.26$. It is divided into 5 rings in η conforming to the muon ring structure. The rings are identified by the numbers -2, -1, 0, +1, +2 with increasing η. The numbering increases with *z*.

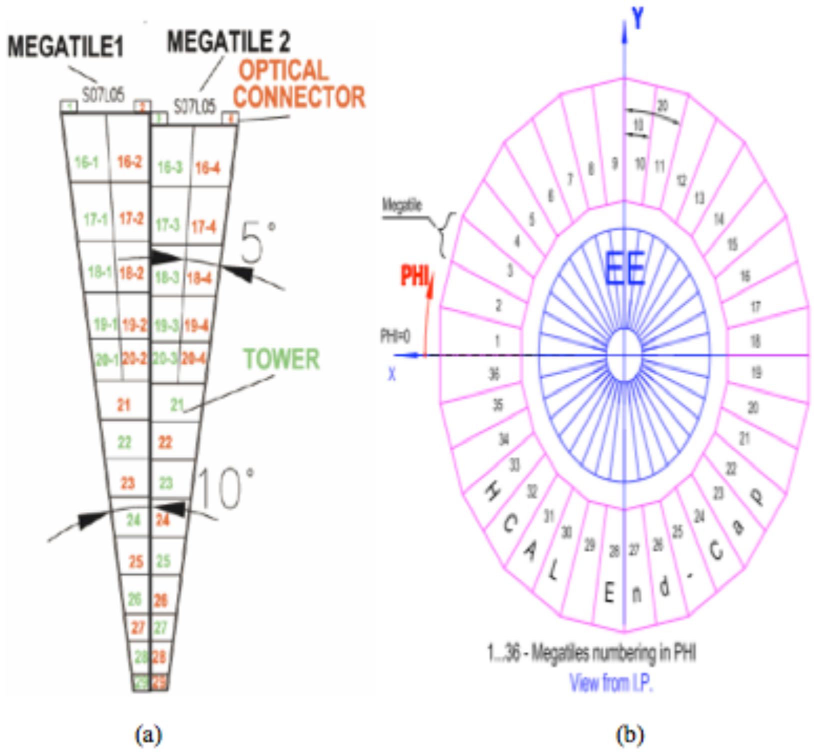

Figure 3.15. (a) Numbering scheme for the tiles in adjacent scintillator trays. (b) Numbering scheme for the HE wedges as viewed from the interaction point. The $+x$ direction points to the center of the LHC ring (Chatrchyan et al., 2008a).

The nominal central z position of the 5 rings are -5.342 m, -2.686 m, +2.686 m and +5.342m, respectively. The position of HO layers in the rings of the muon stations in the overall CMS setup is shown in Figure 3.16. Each ring of the HO is divided into 12 identical ϕ sectors (numbered 1 to 12 counting clockwise starting from 9 o'clock position). The 12 sectors are separated by 75-mm-thick stainless steel beams, which hold the successive layers of iron of return yoke. Each sector has 6 slices in ϕ. They are numbered 1 to 6 counting clockwise. For a layer, the ϕ slices are identical in all sectors. There is a further division along η in each ϕ slice, The smallest scintillator unit in HO is called a tile. The scintillator tiles in each ϕ sector belong to a plane. While the central ring has two layers, the others have one layer. Both layers of ring 0 have 8 η-divisions: -4, -3, -2, -1, 0, +1, +2, +3, +4. Ring 1 has 6 divisions: 5….10 and ring 2 has 5 divisions: 11...15. Ring -1 and ring -2 have the same number of divisions as rings 1 and 2 but '-' indices. In HO some sections use Silicon Photo Multipliers (SiPMs) rather than HPDs. They are installed in HO2P12 and HO1P10.

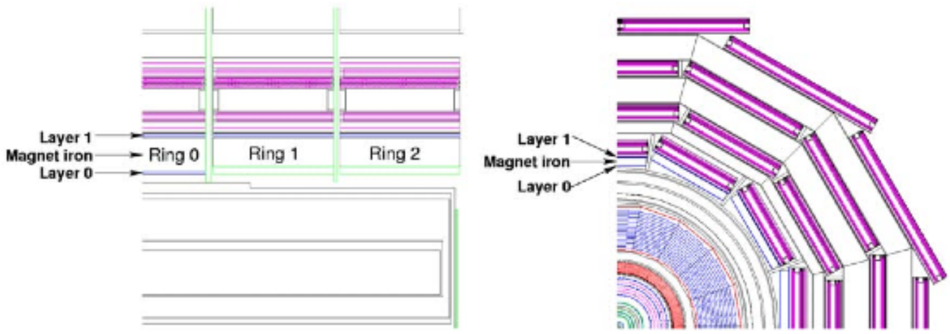

Figure 3.16. Longitudinal and transverse views of the CMS detector showing the position of HO layers (Chatrchyan et al., 2008a).

3.3.2.2.(4). Hadronic Forward (HF)

The hadronic forward calorimeter (HF) is placed 11.2 m away from the interaction point and on either side of the CMS detector. The HF has a radius of 12.5 cm from the center of the beam line and length of about 3 m. It covers the pseudorapidity range $3 < |\eta| <$ 5.2, sits in a very high radiation area. It is made of iron and quartz fibres. Each HF module (HF + or HF $-$) is constructed from 18 wedges. Its structure is azimuthally subdivided into 20° modular wedges. The two HF modules are shown in Figure 3.17. The fibres run parallel to the beam line and are bundled to form $(\Delta\eta,\Delta\phi) = (0.175,0.175)$ towers (Chatrchyan et al., 2008a).

The HF plays an important role for improving measurement of missing transverse energy, and identification and reconstruction of very forward jets. Besides ensuring good hermeticity, it has a crucial role in the determination of luminosity. The signal originates from Cerenkov light emitted in the quartz fibers. This light is read out and detected by photomultipliers (PMTs). The Cerenkov radiation occurs when a charged particle transverses a quartz fiber with a velocity greater than the speed of light. The quartz fibers, which run parallel to the beam line, have two different lengths to differentiate between shower processes. While the light from EM and hadronic showers in the absorber are provided by longer fibers (namely 1.65 m), the hadronic showers are contained by shorter fibers (namely 1.43 m) (Chatrchyan et al., 2008a). The long and shorts fibers are placed alternately with a separation of 5 mm.

Figure 3.17. A fully assembled and a partially assembled structure of the forward hadron calorimeter (Banarjee, 2005).

3.3.2.2.(5). HCAL Readout Electronics

The analogue signal from the HPD or photomultiplier (PMT) is converted to a digital signal by QIE (Charge-Integrator and Encoder). The QIE consists of four capacitors, which are connected in turn to the input, one during each 25 ns period. The integrated charge from the QIE capacitors is converted to a seven-bit word in a non-linear scale to cover the large dynamic range of the detector. The digital outputs of three QIE channels are combined with some monitoring information to create a 32-bit data word which is then transferred via the Gigabit Optical Link (GOL) at a rate of 40 MHz and transmitted to the counting house (service cavern). In the service cavern (USC55), the data is received by the HCAL Trigger/Readout (HTR) board. This board contains the Level-1 pipeline and also constructs the trigger primitives for HCAL. The trigger primitives are sent to the Regional Calorimeter Trigger (RCT) via Serial Link Board mezzanine cards. When the L1A is received by the HTR through the Timing Trigger Control (TTC) system, it prepares a packet of data for the Data Acquisition (DAQ). These packets of data (each covering 24 channels) are transmitted by LVDS (Channel link) to HCAL Data Concentrator Card (DCC). The DCC is the HCAL Front-End Driver (FED) and concentrates the data from up to 360 channels for transmission into DAQ (Chatrchyan et al., 2008a). The HCAL data flow review is simply shown in figure 3.18.

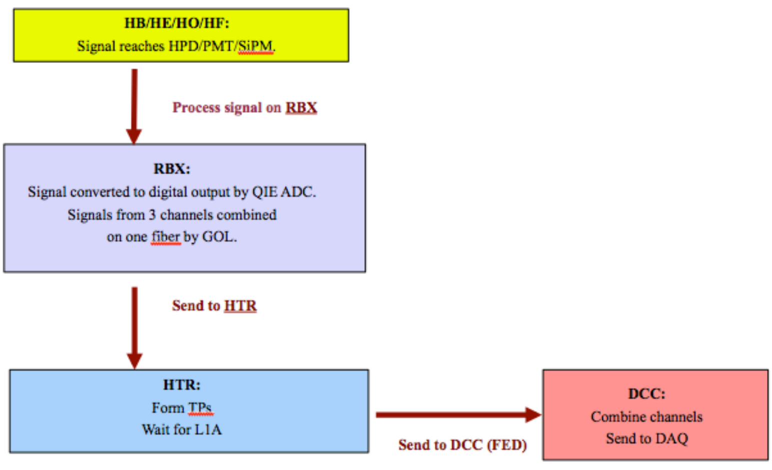

Figure 3.18. The data flow review of HCAL.

3.3.3. The Superconducting Magnet

The superconducting magnet for the CMS detector has been designed to reach a 4-T magnetic field with the capacity of stored energy of 2.6 GJ at full current. This magnetic field provides a large bending of the tracks of the charged particles. Thus it makes possible to measure their transverse momenta. The superconducting coil has a diameter of 6 m and a length of 12.5 m. It is located inside the barrel wheels. The magnetic flux generated by the superconducting coil is returned via a 1.5 m thick saturated iron yoke. The yoke is instrumented with muon stations. The magnet is cooled by liquid helium. The general parameters of the CMS superconducting solenoid are given in Table 3.3. The main features of the CMS solenoid are the use of high-purity aluminium-stabilised conductor and indirect cooling (Chatrchyan et al., 2008a).

Table 3.3. General parameters of the CMS magnet.

General parameters	
Magnetic length	12.5 m
Cold bore diameter	6.3 m
Central magnetic induction	4 T
Total Ampere-turns	41.7 MA-turns
Nominal current	19.14 kA
Inductance	14.2 H
Stored energy	2.6 GJ

3.3.4. The Muon System

The muon detection is a powerful tool for detecting signatures of interesting processes, like the "golden channel" for SM Higgs searches $\mathrm{H} \rightarrow \mathrm{ZZ} \rightarrow 4\mu$ or decay of the new heavy gauge bosons $Z' \rightarrow \mu\mu$ and $W' \rightarrow \mu\nu$. As can be understood from the name of the experiment, the detection of muons is of central importance for CMS. It is specially focused on triggering and reconstruction of muons at highest luminosities. Therefore, the CMS muon system is designed to have the capability of reconstructing the momentum and charge of muons over the entire kinematic range of the LHC (Chatrchyan, 2008a). It is the outermost group of CMS sub-detectors, and covers the pseudorapidity region $|\eta| < 2.4$. It is located inside the magnet iron return yoke. It has 3 functions: muon identification, momentum measurement and triggering. The muon system is composed of four stations. Due to the shape of the solenoid magnet, the muon system was naturally driven to have a cylindrical shape. It is divided into a barrel region ($|\eta| < 1.2$) and two endcaps ($0.9 < |\eta| < 2.4$). Before the last muon station, the total thickness of the absorber amounts to 16 interaction lengths allowing good muon identification.

The CMS uses three different types of gaseous particle detectors for muon identification: drift tubes (DT) are installed in the barrel region, cathode strip chambers (CSC) are installed in the endcap region, and resistive plate chambers (RPC) are installed in both the barrel and the endcap. Figure 3.19 shows the layout of one quarter of the CMS muon system.

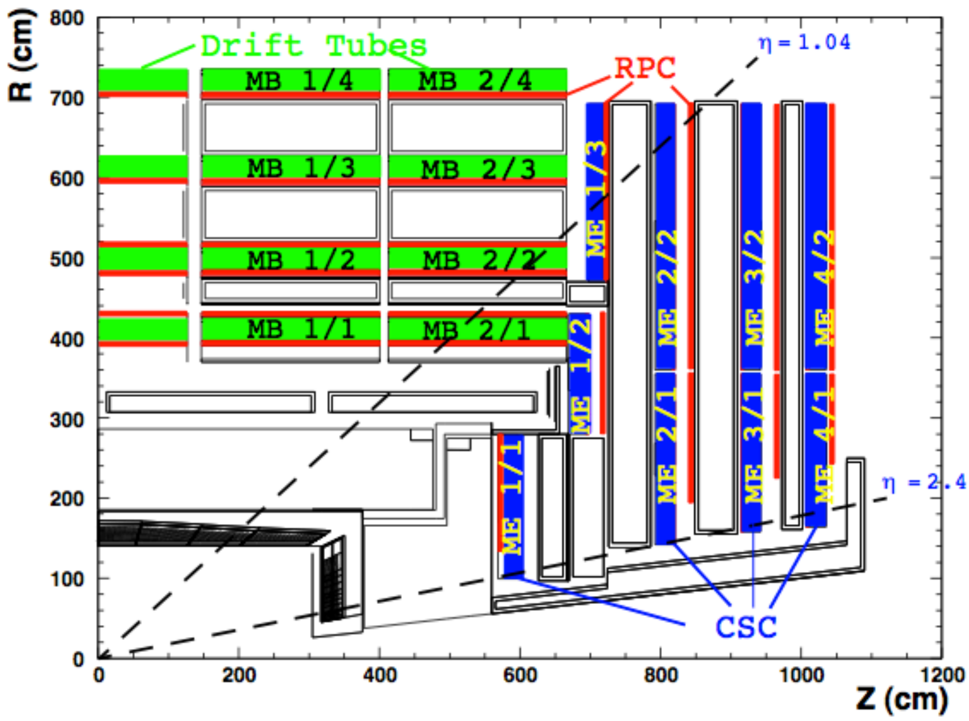

Figure 3.19. Layout of one quarter of the CMS muon system for initial low luminosity running (Martelli, 2012).

Drift tubes (DT) cover the pseudorapidity range $|\eta| < 1.2$ where, the occupancy, the background noise is small, the muon rate and the resudial magnetic field are relatively low compared to the endcaps. The barel drift tube (DT) chambers are organized into 4 stations interspersed among the layers of the flux return plates. The first 3 stations contain 8 chambers each, in 2 groups of 4, which measure the muon coordinate in the $r-\phi$ bending plane and 4 chambers provide a measurement in the z direction, along the beam line. The fourth station does not contain the z-measuring planes. In each station the 2 sets of 4 chambers are separated as much as possible to achieve the best angular resolution. In order to eliminate dead spots in the efficiency, the drift cells of each chamber are offset by a half-cell with respect to their neighbor. The muon time measurement with excellent time resolution is provided by this arrangement.

Cathode strip chambers (CSC) are used by the muon system in the 2 endcap regions of CMS where, the muon rates and background levels are high and the magnetic field is large and non-uniform. The CSCs identify muons in the $|\eta|$ range between 0.9 and 2.4 with their fast response time, fine segmentation, and radiation resistance. Each endcap has 4 stations of CSCs with chambers positioned perpendicular to the beam line and interspersed between the flux return plates. In each chamber, a precision measurement in the $r-\phi$ bending plane is provided by the cathode strips, which run radially outward. In order to measure η and beam-crossing time of a muon, the anode wires run approximately perpendicular to the strips. The DT and CSC subsystems can each trigger on the p_T of muons with good efficiency and high background rejection, independently from the rest of the detector.

Resistive plate chambers (RPC) are complementary to the other muon detectors. A dedicated trigger system consisting of RPCs was added in both the barrel and endcap regions. The RPCs provide a fast, independent, and highly-segmented trigger with a sharp p_T threshold over a large portion of the rapidity $(|\eta| < 1.6)$ of the muon system. The CMS RPC basic double-gap module consists of 2 gaps which are refered as up and down gaps, operated in avalanche mode to ensure good operation at high rates. They produce a fast response, with good time resolution but coarser resolution than the DTs or CSCs. They also help to resolve ambiguities in attempting to make tracks from multiple hits in a chamber (Chatrchyan et al., 2008a).

3.3.5. The Trigger and Data Acquisition (DAQ)

The proton-proton and heavy-ion collisions are provided by the LHC at high interaction rates. At the nominal design luminosity of 10^{34} $cm^{-2}s^{-1}$, the bunch crossing rate of 40 MHz and an average of 20 interactions per bunch crossing is expected every 25 ns (the beam crossing interval for protons). The CMS has more than 10^8 readout channels resulting in a data rate of the order of 10^{15} bits per second so ~1 MegaByte (MB) of data is still recorded for one bunch crossing after zero-suppression. Since it is impossible to store and process the large amount of data associated with the resulting high number of events, a drastic rate reduction has to be achieved. The CMS Trigger system performs this task and it is the start of the physics event selection process. The maximum rate can be archieved for offline processing and analysis by the DAQ system. The CMS Trigger system reduces the event rate in two steps called Level-1 (L1) Trigger (Bayatian et. al., 2000) and High-Level Trigger (HLT) (Bayatian et. al., 2002), respectively.

The L1 Trigger is designed to achieve a maximum output rate of 100 kHz and consists of custom-designed hardware processors, largely programmable electronics. It uses coarsely segmented data from the calorimeters and the muon system, while holding the high resolution data pipelined memories in the detector front-end electronics waiting for the L1 decision. The L1 trigger has to analyze every buch crossing. The L1 Trigger latency between a given bunch crossing and the distribution of the trigger decision to detector front-end electronics is 3.2 μs. The L1 trigger is based on the decision of local, regional and global components. The Local Triggers are based on energy deposits in the calorimeter trigger towers and track segments or hit patterns in muon chambers, respectively. Their information are combined by the Regional Triggers. The Regional Triggers use pattern logic to determine ranked and sorted trigger objects, for instance electron, photon, jets or muon candidates in limited spatial regions. The rank is determined as a function of energy or momentum or quality. The highest-rank calorimeter and muon objects across the entire experiment are determined by the Global Calorimeter and Global Muon Triggers. Then they are transfered to the Global Trigger. The latter takes the decision to reject or accept an event and distributes it to the subdetectors. The decision is based on algorithm calculations and on the readiness of the sub-detectors and the DAQ, which is determined by The Trigger Control System (TCS). The architecture of the L1 Trigger is displayed in Figure 3.20.

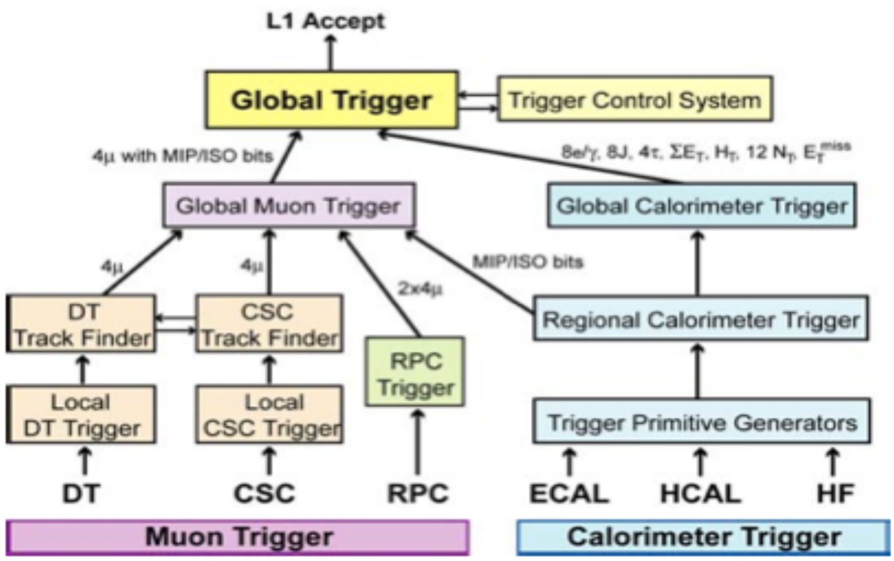

Figure 3.20. Architecture of the L1 Trigger (Chatrchyan et al., 2008a).

The HLT Trigger is a software system running on a large cluster of commercial processors in a filter farm. The HLT has access to the complete readout data and can perform highly complex calculations and algorithms, which are used to reconstruct the event. If an event is accepted by the L1, full detector information is read out by the Data Acquisition (DAQ) system at a rate of up to 100 kHz, passed to the event filter farm and used as input for HLT trigger. The HLT receives one event 10 μs on average. If events include ‘interesting’ physics, they are written to tape with a rate of 100 Hz. The HLT algorithms are implemented in the same software as used for offline reconstruction and analysis. It consists of subsequent reconstruction and selection steps. The HLT algorithms are improved with time and experience. The framework uses a modular architecture and the modules are defined at runtime by means of configuration files. The HLT menu consists of a set of trigger paths and each path addresses a specific physics object selection.

3.3.6. The Software and Computing

The CMS software and computing systems need to cover a large range of activities including the design, evaluation, construction, and calibration of the detector. It has to support the storage, transfer and manipulation of the recorded data for the lifetime of the experiment. The system accepts real-time detector information from the DAQ system: ensures safe curation of the raw data; performs pattern recognition, event filtering, and data reduction; supports the physics analysis activities of the collaboration. It also supports production and distribution of simulated data, and access to conditions and calibration information and other non-event data.

The *Event* is the central concept of the CMS data model. It provides access to the recorded data. Events are physically stored as persistent ROOT files. The event is used by a variety of physics modules, which may read data from it, or add new data with provenance information automatically include. Each module performs a well-defined function relating to the selection, reconstruction or analysis of the Event.

Modules are insulated from the computing environment and execute independently from one another. A complete CMS application is built by specifying to the Framework one or more ordered sequences of modules. Modules within the CMS Application Framework are shown in Figure 3.21. The Framework configures the modules, schedules their execution and provides access to global services and utilities (Chatrchyan et al., 2008a).

The CMS has several event formats like RAW, RECO and AOD with differing levels of detail and precision to achieve the required level of data reduction. The **RAW** Events contain the full-recorded information from the detector and a record of the trigger decision.

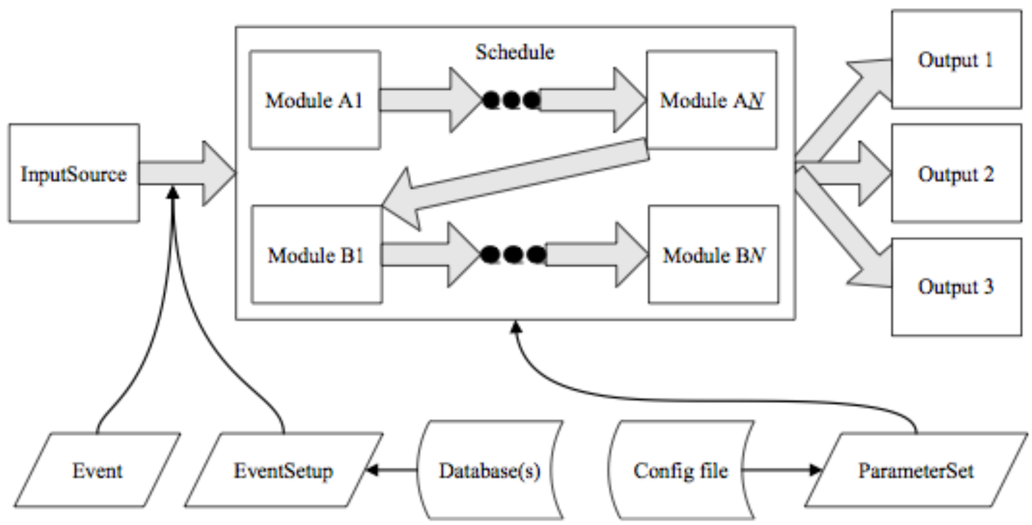

Figure 3.21. Modules within the CMS Application Framework (Chatrchyan et al., 2008a).

The RAW data is progressively archieved in safe storage, and designed to occupy ~1.5 MB/event while 2 MB/event for simulated data. The online system classifies the RAW data into several distintc primary datasets, based upon the trigger signature. **RECO (Reconstructed)** data is produced by applying several levels of pattern recognition and compression algorithms to the RAW data. These algorithms contain detector-specific filtering and correction of the digitized data; cluster- and track-finding; primary and secondary vertex reconstruction; and particle ID. The RECO events include high-level physics objects such as jets, muons, electrons, b-jets and a full record of the reconstructed hits and clusters used to produce them. The RECO events foreseen occupy ~ 0.5 MB/Event. **AOD (Analysis Object Data)** is the compact analysis format. By filtering of RECO data, the AOD data is produced. The AOD format requires ~100 kB/event. Besides the parameters of the high-level objects, AOD events include sufficient additional information to allow kinematic refitting. In order to analyze these data, the CMS offline computing system is arranged in four tiers: Tier-0, Tier-1, Tier-2 and Tier-3. While a single Tier-0 is located at CERN, a few Tier-1 centres at the national laboratories and several Tier-2 centres universities worldwide. The Tier-0 center accepts data from the online system and copy it to permanent mass storage. It carries out prompt reconstruction of the RAW data to produce first-pass RECO datasets. Then it distributes RAW and processed data to set of large Tier-1 centres. These centers provide services for data archiving and reconstruction, calibration, skimming and other data-intensive analysis tasks. The Tier-2 centres provide analysis activities and specialized activities such as offline calibration and alignment tasks, and detector studies and production of Monte Carlo simulation. Interactive resources for local groups are provided by the Tier-3 centers. It also provides additional best effort computing capacity for the collaboration. The data flow between CMS Computing Centers is displayed in Figure 3.22 (Chatrchyan et al., 2008a).

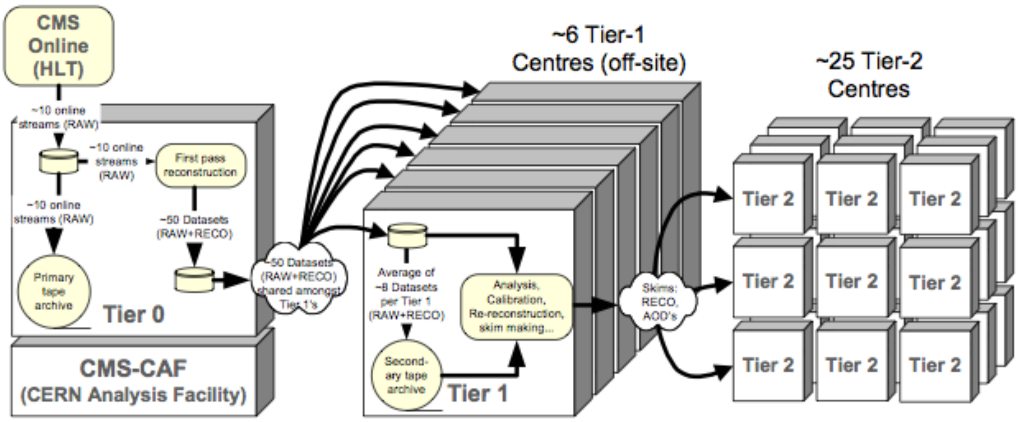

Figure 3.22. Dataflow between CMS Computing Centres (Chatrchyan et al., 2008a).

4. EVENT RECONSTRUCTION

Reconstruction is the process of constructing physics quantities from the raw data collected in the experiment. Therefore, it is the procedure of data reduction whose main client is the data analysis. The original particles that passed through, their momenta, directions and primary vertex of the event are defined in reconstruction algorithms. In order to combine measurements from the different sub-detectors, a flexible software reconstruction is designed. There are three kinds of reconstruction process; corresponding to local reconstruction within individual detector module, global reconstruction within a whole detector, and combination of these reconstructed objects to produce higher-level objects (Bayatian, 2006).

An overview of the reconstruction of the muons, electrons, jets and Missing Transverse Energy (*MET*) is respectively presented in this chapter with reference to the different algorithms used in CMS.

4.1. Muon Reconstruction

One of the CMS aims is to have an excellent muon reconstruction in a wide p_T range (where p_T is the component of the momentum in the transverse plane): low p_T momentum muons for b-physics studies (in this studies they peak at transverse momenta lower than 10 GeV/*c*), relatively energitic muons such as the ones coming from electroweak processes (p_T ~40 GeV/*c*) and very high momentum muons which are of the order of TeV/*c*, a distinctive signature expected by some new physics models as the heavy vector bosons W' decaying to a muon and a neutrino. In order to measure the momenta of those TeV muons, different algorithms are developed.

The muon reconstruction software performs reconstruction in the muon system and the silicon tracker. In order to allow its use in both the offline and the HLT (Bayatian, 2002), the software has been designed by using the concept of regional reconstruction. The muon reconstruction algorithm is seeded by the muon candidates that are found by the Level-1 muon trigger but didn't necessarily lead to a

Level-1 trigger accept. These seeds define a region of interest in the muon system. In this region, local reconstruction is performed. A different seed-generation algorithm has been developed for offline reconstruction. It performs local reconstruction in the entire muon system and uses patterns of segments reconstructed in the CSC and/or DT chambers as initial seeds (Bayatian, 2006). The reconstruction of a muon is performed in three steps in CMS:

- Local muon reconstruction (local-pattern recognition),
- Stand-alone muon reconstruction (using only the muons system, no tracker),
- Global muon reconstruction (including tracker).

The local muon reconstruction of hits within the muon system components is the first step. These hits are used to reconstruct linear track segments in each DT and CSC chamber.

The stand-alone muon reconstruction uses only measurements from the muon detectors. The silicon tracker is not used. Both tracking detectors (DT and CSC) and RPCs participate in the reconstruction**.**

The global muon reconstruction consists of extending the muon trajectories to include hits in the silicon tracker (silicon strip and silicon pixel detetors) (Bayatian, 2006).

Objects of different levels are defined with three stages of reconstruction. **Tracker muons** are reconstructed with the complementary approach of considering all the tracker tracks and identifying them as muon if a compatible signature is found in the calorimeters (energy deposition) and in the muon system (compatible hits and segments). Muons tracks that are reconstructed in the muon spectrometer are identified as **Standalone muons**. **Global muons** are reconstructed by fitting the standalone tracks to those selected in the tracker.

4.2. Electron Reconstruction

Electron reconstruction starts from the energy deposited in the ECAL so the ECAL energy deposit matched to a track in silicon tracker is a basic signature for an electron. Electron traversing the silicon layers of the pixel and inner tracker detectors radiate collections of bremsstrahlung photons and in presence of the 4 T solenoidal $\vec{B}$ field, the energy reaches the ECAL spread in ϕ due to charge particles only rotate in ϕ. The spread is p_T^e dependent. The amount of bremsstrahlung emitted when integrating along the electron trajectory can be very large. It depends on the average on the amount of tracker material traversed. The electron measurements can be complicated by the conversion of secondary electrons in the tracker material. It might lead to "showering" patterns and entail energy lost in the tracker material. Soft secondary electrons from e^+e^- pairs get partly trapped in the external $\vec{B}$ field and they loose most or all of their energy before reaching the ECAL. The photon conversion probability depends on the material budget and varies with η (Bayatian, 2006).

The standard CMS electron reconstruction algorithm (Adam et al., 2009; Chatrchyan et al., 2010c) is used for this analysis. Two complementary algorithms are used to efficiently isolate electrons in the p_T range of the W and Z decays. **The tracker-driven** algorithm is optimized for lower p_T electrons and those inside jets. It starts from a collection of the tracks and look for corresponding clusters of energy in the ECAL. **The ECAL-driven** algorithm is optimized for isolated electrons in the p_T range under consideration. The ECAL-driven electron reconstruction starts by the reconstruction of clusters of clusters (superclusters) in the ECAL. A group of one or more associated clusters of energy deposits in the ECAL is called as a 'supercluster (SC)'. It is constructed using an algorithm that takes into account the energy spread in ϕ due to the radiation in the tracker material and the bending of the electron trajectory in the 4T solenoidal magnetic fields. In order to initiate the electron track reconstruction, superclusters are used to select pairs or triplets of hits in the innermost tracker layers.

A tracker-driven approach which allows improvement of the reconstruction efficiency at low p_T, complements this seeding algorithms. Then electron seeds are used to initiate the reconstruction of electron tracks using a dedicated modeling of the energy loss and a Gaussian Sum Filter (GSF) to fit the trajectories. A cleaning is performed to resolve the ambiguity since several tracks are reconstructed due to the conversion of radiated photons in the tracker material. Electron candidates are built from the combinations of the ECAL superclusters and their associated GSF tracks by applying loose preselection cuts in order to preserve the highest possible efficiency while removing part of the QCD jet backgrounds. The electron four-momentum is obtained by taking angles from the associated Gaussian Sum Filter (GSF) track, and the energy from a combination of tracker and ECAL information. The information from the track is measured at the distance-of-closest approach to the nominal beam spot position (Adiguzel et al., 2011).

4.3. Jet Reconstruction

Quarks and gluons cannot be free due to their color charge. A jet is a narrow cone of hadrons and other particles produced by the hadronization of a quark or gluon. It is called as the experimental signature of a parton, materialized as a spray of energetic hadrons.

The huge QCD cross section ensures that jets will dominate high- p_T physics at the LHC. Jets will not only provide a benchmark for understanding the detector, but they also serve as an important tool in the search for physics beyond the SM. The accurate reconstruction and measurement of jets coming from high- p_T quarks and gluons are required by event signatures of SUSY, Higgs boson production, compositeness and other new physics processes. Jet energy resolution and linearity are key factors in separating signal events from backgrounds (Bayatian, 2006).

In the collider experiments, well-defined jet finding procedures are required to allow for accurate comparison between parton-level predictions from theory and hadron-level observations. A jet is reconstructed from energy deposition in calorimeter towers and from track momenta of charged particles. Jet reconstruction algorithms are used for jet reconstruction. These algorithms provide a set of rules for clustering particles or calorimeter towers based on proximity into jets (Salam, 2009). A fundamental requirement of jet algorithms is to have infrared and collinear (IRC) safety. **Infrared safety** is that adding a soft gluon (soft emissinons) should not change the results of the jet clustering. **Collinear safety** is that splitting one parton into two partons should not change the results of the jet clustering (Salam, 2009). Figure 4.1 shows the configurations of infrared and collinear safety separately.

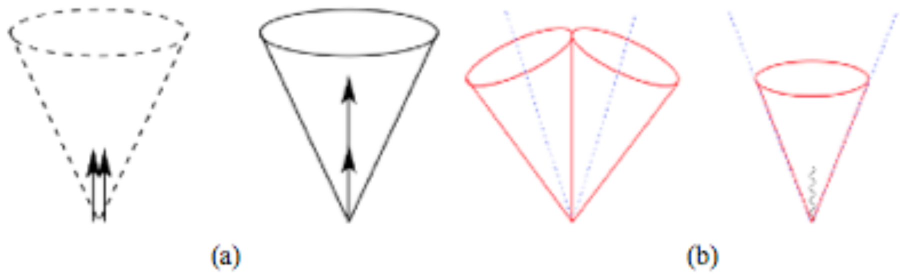

Figure 4.1. The configurations of infrared safety (a) and collinear safety (b).

There are two kinds of mainstream algorithms used by the CMS experiment:

- Cone-Type Algorithms:
  - Midpoint Cone (Blazey et al., 2000)
  - Iterative Cone (Bayatian, 2006)
  - Seedless Infrared Stable Cone (Salam, 2007)
- Sequential Clustering Algorithms:
  - k_T (Salam, 2007; Catani et al., 1993)
  - Cambridge/Aachen (Dokshitzer et al., 1997; Wobisch et al., 1999)
  - Anti- k_T (Cacciari et al., 2008)

The Cone Type algorithms are typically not infrared and collinear-safe except SISCone (Seedless Infrared Stable Cone). They are typically complex. Iterative cone is a simple cone-based algorithm. Due to its short execution time, it is used by CMS in the HLT. Current cone jet algorithms such as iterative cone, take all particles in the event as a seed and search for stable cones. A soft particle is added between the two hard particles, it behaves as a seed and then a third stable cone may be found. This problem is known as infrared unsafety. In order to solve this problem, a seedless search for stable cones is proposed and is named as Midpoint Cone Algorithm. This algorithm is also designed to facilitate the splitting and merging of jets. The final version of the seedless algorithm is SISCone. It is practical at parton, hadron and detector levels. It proposes combining a non-iterative approach with a moderate computational execution time. It doesn't work for the events with high pile-up activity and it is not CPU efficient. So it is not recommended as default jet finding algorithm in CMS. While CMS supports iterative cone algorithm with cone $R = 0.5$, supports SISCone algorithm with cone sizes $R = 0.5$ and $R = 0.7$.

The Sequential Clustering Algorithms are infrared and collinear-safe by construction. They are clean and simple algorithms and are based on pair-wise recombination of particles according to their reciprocal distances. Its measurement can be generalized as

$$d_{ij} = \min(p_{Ti}^{2p}, p_{Tj}^{2p})\frac{\Delta R_{ij}^2}{R^2} \tag{4.1}$$

where d_{ij} is the distance between particle (or calorimeter tower) i, j and p is a parameter. The anti-k_T is used by CMS as default jet reconstruction algorithm. It is a special form of the k_T algorithm. The parameter p is 1 for k_T algorithm. It means that soft particles are clustered firstly. If $p = -1$, anti-k_T algorithm is obtained and hard particles are clustered firstly rather than soft particles (Salam, 2010). If $p = 0$, Cambridge/Aachen algorithm is obtained. It is an energy dependent clustering algorithm. The best shape of jets is given by anti-k_T algorithm. Very demanding

CPU requirements are the major faults of these algorithms. While CMS supports k_T algorithm with cone sizes $R = 0.4$ and $R = 0.6$, supports anti-k_T algorithm with cone sizes $R = 0.5$ and $R = 0.7$.

4.4. Missing Transverse Energy (MET) Reconstruction

One of the main physics quantities at hadron colliders is the Missing Transverse Energy. It enables us to understand the existence of particles invisible to the detector. All major detectors at hadron colliders have been designed to cover as much solid angle as possible. The primary motivation for this is to provide a complete picture of an event as possible, including the presence of one or more energetic neutrinos or other weekly-interacting stable particles though apparent missing energy. Energetic particles, which are produced in the direction of the beam pipe, make it impossible to directly measure missing energy longitudinal to the beam direction. However, transverse energy balance can be measured with accuracy good enough to help establish a physics signature involving one or more non-interacting particles (Bayatian, 2006).

Since the discovery of W boson, measurement of missing energy has been a major tool in the search of new phenomena at hadron colliders. The existence of the neutrino from W boson decay will result in a significant E_T^{miss}. The missing transverse energy (E_T^{miss}) measurement is necessary for distinguishing a W signal from QCD background. There are three kinds of algorithms to reconstruct MET as Calorimetric MET (*caloMET*), Track-Corrected MET (*tcMET*) and Particle-Flow MET (*pfMET*) in CMS.

In *caloMET* algorithm, MET is constructed as the negative vector sum of the transverse energy deposited in calorimeter towers.

In *tcMET* algorithm, the MET as measured in the calorimeters is further corrected using the information from other sub-detectors. Especially measurements from CMS tracker are exploited when possible**.**

The *pfMET* algorithm that is used in this analysis provides the best performance for the CMS detector. The algorithm combines information from all CMS sub-systems: the inner tracker, the muon chambers, and all the calorimetry to classify reconstructed objects according to particle type (electron, muon, photon, charges or neutral hadron). The E_T^{miss} is computed as the negative vector sum of all PF objects as following

$$pf\overrightarrow{MET} = -\sum_{pfParticles} \vec{p}_T \tag{4.2}$$

5. MEASUREMENT OF WZ INVARIANT MASS SPECTRUM

Goal of this study is to search for W' gauge bosons via trilepton signal in the CMS experiment. Main process is given as

$$
\begin{aligned}
& pp \rightarrow \mathrm{W}' + \mathrm{X} \\
& \quad\downarrow \\
& \mathrm{W}' \rightarrow \mathrm{W}(\ell_1 \boldsymbol{\nu}_{\ell_1})\mathrm{Z}(\ell_2^+ \ell_2^-)
\end{aligned}
$$

In the scattering process above ν_{ℓ_1} represents missing energy carried away by neutrinos in the event and, ℓ_1 and ℓ_2 can belong to identical or distinct families of leptons. The background comes from W and Z bosons and it is expected to be small. The Feynman diagram of the process is shown in Figure 5.1.

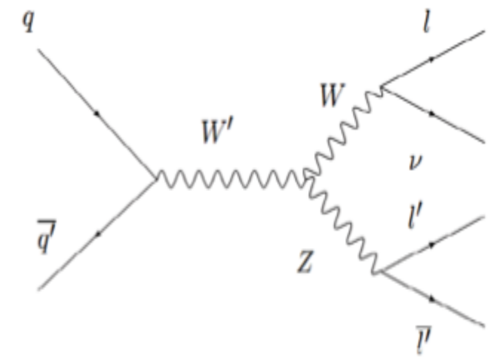

Figure 5.1. The representative Feynman diagram for W' production.

The $W^{\pm}Z \rightarrow \ell^{\pm}\nu_{\ell}\ell'^{+}\ell'^{-}$ decay is characterized by:

- a pair of same-flavor, opposite-charge, high-p_T isolated leptons with an invariant mass corresponding to a Z boson.
- a third, high p_T isolated lepton from W boson.
- a significant amount of missing transverse energy E_T^{miss}, associated with the escaping neutrino.

In this analysis, it is considered that the WZ pair originates from a massive resonance (W'), so first we will look for a bump in the WZ invariant mass spectrum to observe the massive gauge bosons. But we cannot define the invariant mass perfectly, because of the unknown longitudinal momentum (p_z^{ν}) of the neutrino. We will discuss this point in Chap.5.4.6. The background events for this process can be grouped as irreducible and reducible processes. The irreducible processes produce the same final state as our signal. The reducible processes produce different physics, but similar signal in the detector. In order to reject significant fraction of background events with similar signatures, the selection criteria aim to identify the WZ events with as high efficiency as possible. To search for a resonance in the WZ spectrum, these criteria will be applied.

In this chapter, measurement of WZ invariant mass spectrum will be discussed. Then the observed WZ invariant mass spectrum will be compared with the MC prediction to test the smoothness of data.

5.1. Data Samples

This analysis is based on data recorded by the CMS experiment in 2011 corresponding to 4.8 fb^{-1} of the total integrated luminosity. The events must fire each type of trigger looking for a pair of electrons or a pair of muons, respectively. Since they are generally independent, data is sorted into following DoubleElectron and DoubleMu primary datasets (PDs) based on trigger type:

- /DoubleElectron/Run2011A-May10ReReco-v1/AOD (runs 160404–163869)
- /DoubleElectron/Run2011A-PromptReco-v4/AOD (runs 165071–168437)
- /DoubleElectron/Run2011A-05Aug2011-v1/AOD (runs 170053–172619)
- /DoubleElectron/Run2011A-PromptReco-v6/AOD (runs 172620–175770)
- /DoubleElectron/Run2011B-PromptReco-v1/AOD (runs 175832–180296)
- /DoubleMu/Run2011A-May10ReReco-v1/AOD (runs 160404–163869)
- /DoubleMu/Run2011A-PromptReco-v4/AOD (runs 165071–168437)

- /DoubleMu/Run2011A-05Aug2011-v1/AOD (runs 170053–172619)
- /DoubleMu/Run2011A-PromptReco-v6/AOD (runs 172620–175770)
- /DoubleMu/Run2011B-PromptReco-v1/AOD (runs 175832–180296)

The standard CMS selection of good runs and luminosity sections was applied based on official CMS files. These dataset was reconstructed with CMS software version CMSSW_4_2_X. The integrated luminosities for each data set are shown in Appendix A.

5.2. Monte Carlo Samples

All simulated signal and background samples were taken from the official CMS Fall11 production cycle with digitization and reconstruction done with CMSSW_4_2_X.

5.2.1. Backgrounds and Signal

Background processes were produced using MADGRAPH (Allwall et al., 2007), PYTHIA (Sjostrand et al., 2006) and POWHEG (Frixione et al., 2007) generators. These backgrounds include irreducible and reducible processes. While irreducible processes produce the same final state as our signal, reducible processes produce different physics, but similar signal in the detector. Therefore these backgrounds can be grouped as physics and instrumental backgrounds. The SM WZ production is our primary background for a resonant search as physics background and it is dominant. The SM WZ sample is produced by the MC event generator MADGRAPH (Allwall et al., 2007). The physics background also includes ZZ production where one of the leptons is either outside the detector acceptance or mis-reconstructed. It has a small production cross-section and an irreducible background. The instrumental backgrounds are due to mis-identified lepton candidates from jets and photons. These background processes include $Z + jets$, $W + jets$ $t\bar{t}$, $Z\gamma$ and QCD multi-jet events. The background from QCD multi-jet events was also studied in the simulation and found to be negligible after the Z-candidate selection. The full list of background samples, including their datasets name and cross-sections are shown Table 5.1.

Table 5.1. Background processes considered in this analysis with leading order (LO) and higher-order cross-sections. All datasets are from official production using either MAGRAPH or PYHTIA for the matrix element calculation. The W+Jets cross section (marked with *) is next-to-next-leading order while all others are next-to-leading order (NLO).

Sample	Dataset Name	σ_{LO} (pb)	$\sigma_{(N)NLO}$ (pb)
$WZ \to \ell\nu\ell\ell$	WZJetsTo3LNu_TuneZ2_7TeV-madgraph-tauola	0.7192	0.879
$Z(\to \ell\ell) + jets$	DYJetsToLL_TuneZ2_M-50_7TeV-madgraph-tauola	2474.0	3048
$t\bar{t}$	TTJets_TuneZ2_7TeV-madgraph-tauola	94.76	157.5
$W(\to \ell\nu) + jets$	WJetsToLNu_TuneZ2_7TeV-madgraph-tauola	27770.0	31314.0*
$WW \to 2\ell 2\nu$	WWJetsTo2L2Nu_TuneZ2_7TeV-madgraph-tauola	3.783	4.882
$V\gamma + jets$	GVJets_7TeV_madgraph	56.64	65
$ZZ \to 4e$	ZZTo4e_7TeV-powheg-pythia6	---	0.0154
$ZZ \to 4\mu$	ZZTo4mu_7TeV-powheg-pythia6	---	0.0154
$ZZ \to 4\tau$	ZZTo4tau_7TeV-powheg-pythia6	---	0.0154
$ZZ \to 2e2\mu$	ZZTo2e2mu_7TeV-powheg-pythia6	---	0.0308
$ZZ \to 2e2\tau$	ZZTo2e2tau_7TeV-powheg-pythia6	---	0.0308
$ZZ \to 2\mu 2\tau$	ZZTo2mu2tau_7TeV-powheg-pythia6	---	0.0308

The full list of W' signal samples are shown in Table 5.2. These samples were generated with PHYTIA 6.4 (Sjostrand et al., 2006). The leptonic decays of the vector bosons ($W \to \ell\nu$ and $Z \to \ell^+\ell^-$) with $\ell = e, \mu, \tau$ are only considered by these samples. The *k*-factors are listed in Table 5.3 and they were taken from Ref. (Kim et al., 2011). The *k*-factor is used to normalize the LO calculations. The theoretical *k*-factor is conventionally defined as the ratio between the NLO and LO cross sections (Vogt, 2002).

Table 5.2. An overview of the $W' \rightarrow WZ \rightarrow \ell\nu\ell\ell$ signal samples giving the W' mass along with the associated leading order (LO) and next-to-next-to-leading order (NNLO) cross sections in the SSM. The cross sections include the branching ratios for the bosonic decays into charged leptons $\ell = e,\mu,\tau$ (Brigljevic et al., 2011).

W' Mass	σ_{LO} (pb)	σ_{NLO} (pb)
200	1.324	1.797
250	1.118	1.517
300	0.6337	0.8599
400	0.204	0.2768
500	0.07915	0.1074
600	0.0362	0.0489
700	0.01806	0.0244
800	0.009857	0.01328
900	0.005551	0.00744
1000	0.003322	0.00442
1100	0.002041	0.002704
1200	0.001289	0.001690
1300	0.0008333	0.001082
1400	0.0005395	0.000690
1500	0.0003606	0.000456

Due to high luminosity provided by LHC, there is an order of 20 minimum bias pp interactions at each bunch crossing. These interactions pollute any interesting hard events with many soft particles. In most events of interest, there is only one hard scattering interaction. The other proton collisions are typically soft, leading to significant jet activity, particularly in forward regions of the detector. These kinds of collisions are known as *pile-up* (Cacciari and Salam, 2008). The parton showers originate from the hard interaction and from partons radiated in the initial or final state. Besides, the soft radiation from the remaining partons must be considered for a full picture of the event. As a result of the radiation, we have a large number of low energy hadrons distributed between the proton remnant and the hard jets that resulted from the final state partons. This additional activity is known as the *underlying event*. It can deposit significant energy in the detector.

Table 5.3. *k* factors used for W' signal samples by mass point (Kim et al., 2011).

Mass(GeV)	k_{NNLO} factor
200	1.357
250	1.357
300	1.357
400	1.357
500	1.357
600	1.351
700	1.352
800	1.347
900	1.341
1000	1.332
1100	1.325
1200	1.311
1300	1.298
1400	1.279
1500	1.265

The production MC samples are generated with distributions for the number of pile-up interactions. These distributions do not exactly match the conditions expected for each data-taking period. The primary vertex reconstruction of CMS has been shown to be efficient and well behaved up to relatively high levels of pile-up. But the final distribution for the number of reconstructed primary vertices is still sensitive to the details of the primary vertex reconstruction. It is also sensitive to differences in the underlying event in data vs. Monte Carlo. In addition, there is a potentially larger effect that the distribution for the number of reconstructed vertices can be biased by the offline event selection criteria and even by the trigger. In order to factorize these effects, pileup reweighting is applied using the 3D method and the input data distribution, which corresponds to the 73.5 mb minimum bias cross section. The pileup is modeled by reweighting the MC simulation to match the number of reconstructed vertices found in data. The individual event weight is calculated using 3D histograms. These weight histograms are created using MC distribution used in the sample generation process and the data distribution as the input (Brigljevic et al. 2011).

5.3. Triggers

Most of events or processes produced at a high-energy hadron colliders are not interesting. Since it is impossible to store and process the large amount of data, we have to avoid running the offline code on millions of uninteresting events. As discussed in Chapter 3.3.5, High Level Trigger (HLT) takes events accepted by the L1 (first level of the CMS Trigger), then the HLT algorithms and filters decide whether the event should be kept for an offline analysis. Therefore, it is a crucial part of the CMS data flow. The offline analysis depends on the outcome of HLT so the triggers are defined as path blocks according to the offline analysis.

In this analysis, the events triggered by HLT paths of interest are considered. We use the double HLT listed here below and require that our signal events have to satisfy at least one HLT path (double lepton triggers). In order to control the recorded event rate, each of these triggers imposes energy thresholds on the candidate object. The thresholds corresponding to various run ranges are shown in Table 5.4. We use some HLT path only for those runs for which it is unprescaled. Since we don't know that whether the interesting events are passing at the same rate, we require one HLT muon leg to satisfy the $p_T > 17\,\mathrm{GeV}$ and the other leg the $p_T > 8\,\mathrm{GeV}$ requirement.

Here double HLT lepton triggers names are listed:

- For the $Z \rightarrow ee$ channel:

- HLT_Ele_17_CaloIdT_CaloIsoVL_TrkIdVL_TrkIsoVL_Ele8_CaloIdT_CaloIsoVL_TrkIdVL_TrkIsoVL_v*

• For the $Z \rightarrow \mu\mu$ channel:

Because of the changes in the HLT menu during data taking in 2011, three different paths are applied as following:

- HLT_Double_Mu7_v*
- HLT_Mu13_Mu8_v*
- HLT_Mu17_Mu8_v*

Table 5.4. Thresholds for the double electron and double muon triggers used in this analysis. The Level-1 seed for the electron triggers initially requires only one object with $E_T > 12$ GeV, but later requires an additional deposit with $E_T > 5$ GeV.

	$E_T(e^{\pm})/(GeV)$		$P_T(\mu^{\pm})/(GeV/c)$	
Run Range	L_1	HLT	L_1	HLT
160329-164236	12 --	17 8	3 3	7 7
165088-170759	12 --	17 8	3 3	13 8
170826-178380	12 5	17 8	3 3	13 8
178420-180296	12 5	17 8	3 3	17 8

The early 2011 MC samples didn't include all the luminosity-dependent trigger configurations as used in data. In this case, we require the HLT objects to match the leptons coming from the Z decay and reproduce the HLT requirements by applying the corresponding p_T thresholds.

5.4. Event Selection

The aim of the event selection is to identify the signal region where the background contribution is small. It is performed in six steps:

5.4.1. PreSelection

Analysis is done separately for all four e and μ channel combinations. The preselection looks for events:

- which contain at least three reconstructed leptons, electrons or muons with $p_T > 10$ GeV/c
- which satisfy at least one HLT path (double lepton triggers) which is described above.

The preselection strongly reduces the instrumental backgrounds. In particular QCD backgrounds with $WW + jets$ or $W + jets$ are strongly reduced by three leptons requirement.

5.4.2. Lepton Selection

The lepton identification strategy from a recent analysis of SM WZ production is followed for this analysis (Chatrchyan, 2011c).

5.4.2.1. Electron Identification and Isolation

All electrons within the detector acceptance ($|\eta| < 2.5$) are used for this analysis. In order to define selection working points (WP) of different efficiency on the signal and rejection on the backgrounds (Adam et al., 2010), threshold cuts on the Table 5.5 have been tuned together.

These kinds of selections are referred as simple cuts. To select electrons among the basic collection of GSF electrons, simple cuts are used on few discriminating variables. These variables can be categorized into three groups: electron ID variables, conversion rejection variables and isolation variables. Two different working points are used in this analysis. A loose selection (WP95) is required for electrons from the Z decays where the background is low and a tighter one (WP80) for electrons from W decays where the background from multi-jet events is higher. The variables and cut values used for two selections are given in Table 5.5.

The energy deposited in the electromagnetic calorimeter is measured in clusters of clusters (SC) which collect bremsstrahlung photons emitted along the electron trajectory in the tracker volume. Several tests of the compatibility of the electromagnetic shower shape with the isolated electron criteria must also be performed on all electrons. The shower is evaluated for the following variables: The variable $\sigma_{i\eta i\eta}$ is width of the electromagnetic cluster in terms of pseudorapidity where the measurement is taken from cluster shape covariance. The variables $\Delta\phi$ and $\Delta\eta$ refer the difference in the measured position of the ECAL supercluster vs. the associated track, and E_{HCAL} / E_{ECAL} is the ratio of energy deposited in ECAL and HCAL. Since the calorimeter response differs significantly between the barrel and endcap, the values for these criteria are determined separately for Ecal Barrel (EB) and Ecal Endcap (EE).

Photons that arise from a hard interaction have a high probability to convert into an $e^{+}e^{-}$ pair within the tracker. Those tracks appear as missing hits in the innermost regions. In order to discriminate against them, the electron tracks have no missing hits. Electrons coming from W decay are also checked for extra tracks in their immediate vicinity. If any fall within a distance d of 0.2 mm between conversion tracks or are not sufficiently separated to satisfy $\Delta\cot(\theta) < 0.02$, they are rejected. This criteria is called as ‘conversion rejection’.

Table 5.5. The definition of simpe cuts for the electron candidates in the barrel (EB) and in the endcaps (EE). The loose selection is used for electrons from Z decay, and tight one for W decays.

	loose selection (WP95)		tight selection (WP80)	
Electron ID	EB	EE	EB	EE
σ_{inin}	0.012	0.031	0.01	0.031
$\lvert\Delta\eta_{in}\rvert$	0.007	0.011	0.005	0.006
$\lvert\Delta\phi_{in}\rvert$	0.8	0.7	0.027	0.021
Conversion rejection	EB	EE	EB	EE
Expected missing inner hits	0	0	0	0
Dist	NA	NA	0.02	0.02
Dcot	NA	NA	0.02	0.02
Isolation	EB	EE	EB	EE
Combined Relative Isolaton	0.15	0.1	0.07	0.06

A combined relative isolation is used and built from the sum of the transverse energy of all tracks and calorimeter (ECAL and HCAL) deposits. The values of the isolation variable are drawn by considering only the objects, which fall within a cone ($\Delta R = \sqrt{\Delta\phi^2 + \Delta\eta^2} < 0.3$) around the electron track direction for the track contribution, and around the direction defined by the SC position and the nominal beam spot position for the calorimetric contributions. It is given with the following formula:

$$Comb\mathrm{Re}lIso = \left(\sum p_T(tracks) + \sum E_T(ECAL) + \sum E_T(HCAL)\right) \Big/ p_T^{ele} \tag{5.1}$$

In this equation, the tracks and calorimetry deposits associated with the electron footprint are removed in the track and ECAL contributions. We set a requirement on the ratio of the isolation sum to the electron's transverse momentum in order to allow a high acceptance for energetic electrons.

The isolation variables are sensitive to pileup effect and also contribute to underlying event. An average pile-up of roughly five collisions was expected in 2011 run conditions of the LHC. Pile-up causes to increase the mean energy deposited in the detector so it leads to the rise of the mean isolation values. Therefore the efficiency of a cut on isolation variables strongly depends on pile-up conditions. Mostly, due to the requirement that the tracks contributing to the isolation cone originate from a common vertex, the effect is to be strong in calorimeters (ECAL, HCAL) and quite weak in the tracking system. In order to make selection as non-sensitive as possible and have a pile-up robust analysis, the isolation variable has to be corrected. Among the several correction methods, FastJet (Cacciari and Salam, 2008; Cacciari, Salam and Soyez, 2008b) has been chosen to estimate the mean pile-up contribution within the isolation cone of lepton. A ρ variable (energy density) is defined for each jet in a given event and the median of the ρ distribution is taken for each event. The correction to the isolation variable is given by following formula

$$\sum Iso_{corrected} = \sum Iso - \rho.A \tag{5.2}$$

where A is the area of the cone in the (η,ϕ) space. Since ρ is given in $1/(\Delta\eta\Delta\phi)$ units, it has the dimension of an angle. An effective area is used rather than computing geometrical area in order to avoid dealing with different thresholds in the isolation and FastJet algorithms. The effective area is defined as the ratio of the slope obtained from linearly fitting $\sum Iso(N_{vtx})$ to the one from linearly fitting FastJet $\rho(N_{vtx})$. The isolation cut efficiencies are made stable with respect to changing pile-up conditions in this way. Distributions of criteria used to select barrel and endcap electrons are shown in Appendix B.

5.4.2.2. Muon Identification and Isolation

A pseudorapidity cut is selected as $|\eta| < 2.4$ because of the CMS muon system instrumentation. The muons are required to be reconstructed with the Global Muon algorithm and to fulfill various track quality requirements. In order to perform a quality measurement, the global track has to be built up with more than 10 hits in the inner tracker, including one or more hits in the pixel detector and at least one hit in the muon system. In addition, the muon must be matched to track segments in two different muon stations. In order to reject muons from hadrons decaying in flight and from kaons punching-trough the calorimeter, a $\chi^2/ndof < 10$ cut is applied on the muon global fit. The overall quality of the global muon fit must be high as measured by a requirement on the normalized χ^2 (meaning that we divide the χ^2 value by the number of degrees of freedom in the fit). For rejection of cosmic muons, which do not originate from a collision, the transverse impact parameter of the global fit from the beam spot position must be less than 2 mm. The muon identification and isolation requirements are shown in Table 5.6.

In order to reject muons arising from jets, muon isolation criteria is applied. The isolation variable is defined as the sum of tracker tracks and ECAL and HCAL transverse deposits, divided by the muon transverse momentum. The values of the isolation variable are drawn by considering only the objects, which fall within a cone of $\Delta R = \sqrt{\Delta\phi^2 + \Delta\eta^2} < 0.3$ around the muon track. It is called as relative combined isolation and given as follows:

$$CombRelIso = \left(\sum p_T(tracks) + \sum E_T(ECAL) + \sum E_T(HCAL)\right) \Big/ p_T^{\mu} \quad (5.3)$$

In this equation, the tracks and calorimetry deposits associated with the muon track are not considered. The same pile up correction is applied. It depends on the number of reconstructed vertices in the event and on the region of the detector in which the muon is found. It is based on the FASTJET determination of the energy density ρ and using effective areas. While the isolation variable is lower than 0.15 for the loose (Z) selection, it is lower than 0.1 for the tight (W) selection.

Due to photons from internal bremsstrahlung in W and Z decays, which can produce a fake electron aligned with the muon, electron/muon ambiguities appear. Electrons are rejected if they are within a cone $\Delta R < 0.01$ around a muon for removing such ambiguities. Distributions of criteria used to select muons are given in

Appendix B.

Table 5.6. Muon identification and isolation requirements. While the loose selection is used for muons from Z candidates, tight one is used for those from W candidates.

Description	cut
Number of pixel hits	> 0
Number of tracker hits	> 10
Normalized Chi2	< 10
Number of muon hits	> 0
Number of chambers with matched segments	> 1
Vertex d0	< 0.2 cm
comb.rel.isolation (loose selection)	< 0.15
comb.rel.isolation (tight selection)	< 0.1

5.4.3. Z Candidate Selection

In this analysis, the first selection is to require a Z candidate which is built from a pair of opposite-sign, same flavor leptons with the leading and second leptons having $p_T > 20\ GeV$ and $p_T > 10\ GeV$ for both $Z \rightarrow ee$ and $Z \rightarrow \mu\mu$. The leptons should pass loose ID and loose isolation cuts defined above. They also have to match to trigger objects from the selected HLT paths. The invariant mass of pair of μ / e should lie between 60 and 120 GeV/c^2. If several matching combinations (two candidates constructed from a common lepton) are found, the best candidate is chosen as the closest to the nominal Z mass. If a second, independent Z candidate using two different leptons is found, the event is rejected to reduce ZZ background. After these requirements, the reconstructed mass distributions of the Z boson candidates for $Z \rightarrow \mu\mu$ and $Z \rightarrow ee$ channels are shown in Figure 5.2.

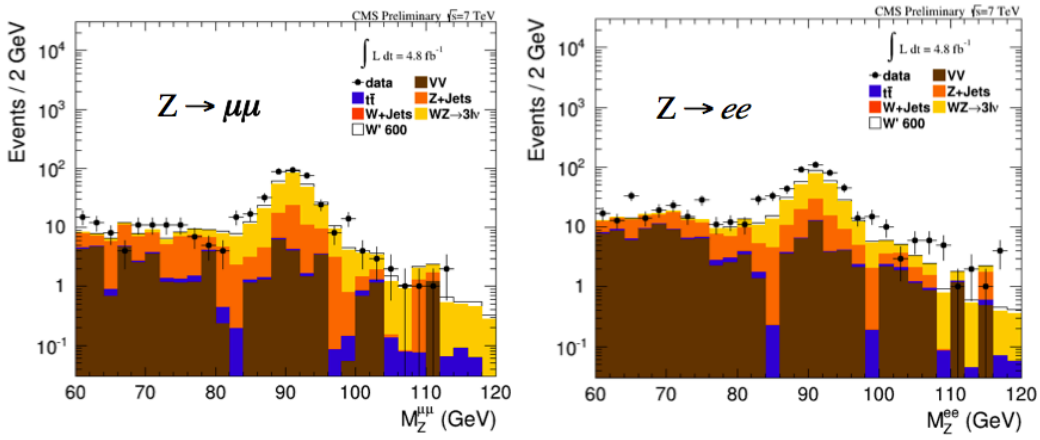

Figure 5.2. Distribution of reconstructed mass of the Z boson candidate for $Z \to \mu\mu$ (left) and $Z \to ee$ (right) channels.

5.4.4. W. Candidate Selection

We assign the highest-p_T candidate from the remaining leptons requiring $p_T > 20$ GeV/c to the W boson decay. The tight (WP80) criteria is applied on both its identification and isolation. The W candidate selection is finalized looking for the high missing transverse energy produced by a high p_T neutrino. The transverse mass of the W boson candidate $M_T(W)$ is given by:

$$M_T(W) \equiv \sqrt{2.E_T^{miss}.p_T^{\ell}.\Delta\phi} \tag{5.4}$$

where p_T^{ℓ} is the transverse momentum of the lepton assigned to the W, E_T^{miss} is the missing transverse energy of the event assigned to neutrino and $\Delta\phi$ is the angle between that lepton and E_T^{miss} in the transverse plane. If several W candidates are found, the one with highest p_T lepton is chosen in order to reduce backgrounds with fake third lepton and soft p_T spectrum. The transverse mass of the W boson candidate for $W \to \mu\nu$ and $W \to e\nu$ channels is shown figure 5.3.

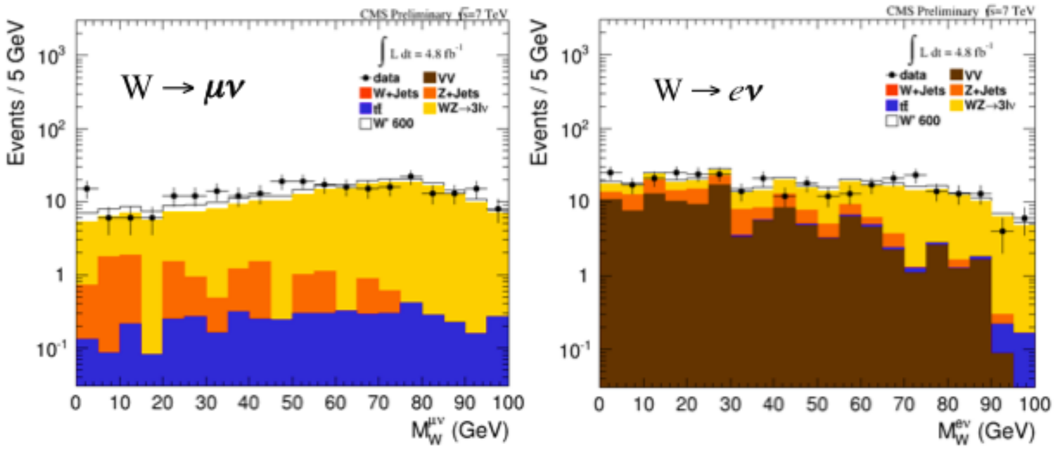

Figure 5.3. Distribution of transverse mass of the W boson candidate for $W \rightarrow \mu\nu$ (left) and $W \rightarrow e\nu$ (right) channels.

5.4.5. MET Selection

The missing transverse energy is calculated by using the Particle Flow Algorithm, which is discussed in Section 4.4. In this analysis, E_T^{miss} is required to be larger than 30 GeV to select W boson decays and reject a large fraction of events without a genuine W decay. This requirement discriminates against high-p_T jets mis-identified as leptons or photon conversions from $Z + jets$ or $Z\gamma$ events, respectively. After a valid selection of Z and W candidates in the event, the E_T^{miss} distributions are shown for $\mu\mu$ and ee channels separately and also combined in Figure 5.4.

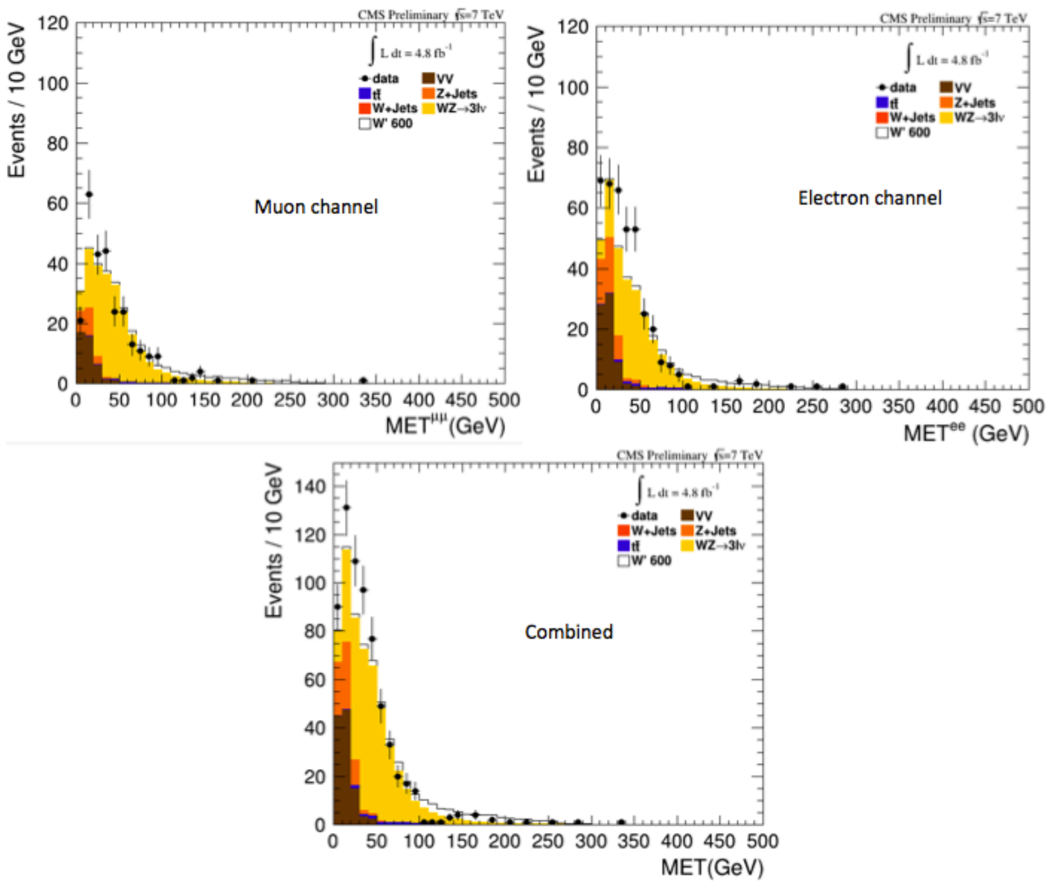

Figure 5.4. Missing transverse energy (E_T^{miss}) for MC background, signal (W' at 600 GeV) and data after the valid Z and W candidates selection for muon and electron channels separately (top) and combined (bottom).

5.4.6. WZ Candidate Selection

If WZ candidates come from massive exotic particles, there is a narrow width in the spectrum of the reconstructed mass $M(WZ)$. Therefore, the massive exotic particles decaying via WZ should be most easily distinguished from the SM WZ background. After both W and Z candidates are chosen, the two are combined into a WZ candidate as final step. Since the longitudinal momentum (p_z^{ν}) of the neutrino is unknown, the invariant mass of this candidate can't be identified uniquely. We estimate the invariant mass of the WZ candidate by making two assumptions. We reduce the longitudinal momentum of p_z^{ν} to a quadratic equation by assuming the mass of the W. It is found that the less energetic of the two neutrino solutions gives the correct value nearly 75% of the time according simulation. If there is no real solution to this quadratic equation, we change our assumption of the W invariant mass. When the transverse mass is greater than the invariant mass, imaginary solutions arise. While this cannot happen physically, detector resolution effects can cause the transverse mass to be reconstructed greater than the nominal mass. In these cases, the assumption that led to the imaginary solution is changed. We assume the invariant mass to be equal to the reconstructed transverse mass. This causes the discriminant to vanish and two identical real solutions are left. Since real part of the solution depends on our assumption for the invariant mass, this method differs from setting the discriminant to 0 by hand. This method results in no events being discarded at this stage (Brigljevic et al., 2011).

After applying the selection criteria, the event yields in the data and as expected from MC for the signal and the backgrounds are presented in Table 5.7. After the MET selection at the end of the event selection, the event yield for four channels is presented in Table 5.8. The event yields for all expected signals are shown in Appendix C. Possible differences between data and simulation can bring to important biases in the events selection. A major issue is the pile-up increase. As we discussed in Chap. 5.2.1, a pile-up reweighting procedure is applied to all variables used in the analysis in order to make sure to deal with simulated events reproducing data well.

We expect that WZ events, which originate from the decay of a massive particle, should be more energetic than the events expected from the SM. In order to further suppress SM background events and to achieve further separation between resonant particles and SM WZ production, two additional selection requirements are applied. The first cut is on the scalar sum of the charged leptons' transverse momenta (H_T). It is given as:

$$H_T = \sum_i p_T^{(\ell_i)} \tag{5.4}$$

In this equation, i runs over the three charged leptons associated with $Z \rightarrow \ell^+ + \ell^-$

and $W^{\pm} \rightarrow \ell^{\pm} + \nu_{\ell}$ decays. All crosschecks distributions are shown in Appendix B after H_T cut is applied.

Table 5.7. Observed and expected signal and background yields after the main steps of the event selection. The numbers correspond to an integrated luminosity of 4.8 fb^{-1}.

Sample	Preselection	Z selection	W Selection	E_T^{miss}
Z+jets	273048.91 ± 326.11	99379.91 ± 194.9	65.23 ± 5.36	3.48 ± 1.22
$t\bar{t}$	28869.59 ± 18.84	1985.205 ± 4.95	10.51 ± 0.38	8.75 ± 0.34
ZZ	450.34 ± 0.32	114.11 ± 0.16	60.15 ± 0.12	14.61 ± 0.06
Vγ	17654.4 ± 115.42	3553.61 ± 51.91	113.16 ± 9.76	5.73 ± 2.1
W+jets	10133.01 ± 134.83	32.74 ± 8.89	0 ± 0	0 ± 0
WW	475.34 ± 2.99	65.01 ± 0.89	0.36 ± 0.1	0.26 ± 0.08
WZ	1990.43 ± 2.57	629.82 ± 1.45	385.19 ± 1.13	275.73 ± 0.96
Total Background	332622.04 ± 371.17	105760.43 ± 201.96	634.62 ± 11.2	308.58 ± 2.63
Data	652881 ± 808.01	95123 ± 308.42	610 ± 24.69	309 ± 17.57
$W' \rightarrow WZ \rightarrow 3\ell\nu$				
W' 600	235.64 ± 1.63	88.08 ± 1.0003	66.05 ± 0.86	62.78 ± 0.84

The second cut is on the mass of the WZ system. The thresholds for these selections have been optimized for each mass point separately. In order to maximize signal over background, these mass windows and minimum H_T cuts values were found by simultaneously varying the cuts.

Figure 5.5 shows the H_T distributions for the SM background, the data and a hypothetical W' signal with a mass of 600 GeV. The cuts are listed in Table 5.9 for each W' mass. We require increasing values of H_T for higher masses. Due to decreasing background statistics, all mass points above 800 GeV have the same cut.

Table 5.8. Observed and expected signal and background yields for four channels after the main steps of the event selection. The numbers correspond to an integrated luminosity of 4.8 fb^{-1}.

Sample	3μ	$2\mu 1e$	$3e$	$1\mu 2e$
Z+jets	0.063 ± 0.034	0.344 ± 0.211	2.642 ± 1.141	0.431 ± 0.377
$t\bar{t}$	1.5 ± 0.108	1.47 ± 0.108	1.956 ± 0.183	3.82 ± 0.252
ZZ	5.042 ± 0.024	2.336 ± 0.021	2.022 ± 0.024	5.225 ± 0.044
Vγ	0 ± 0	2.66 ± 1.12	3.071 ± 1.779	0 ± 0
W+jets	0 ± 0	0 ± 0	0 ± 0	0 ± 0
WW	0 ± 0	0 ± 0	0.057 ± 0.04	0.204 ± 0.077
WZ	83.74 ± 0.43	56.45 ± 0.353	57.74 ± 0.512	77.79 ± 0.592
Total Background	90.35 ± 0.445	63.27 ± 1.19	67.49 ± 2.183	87.48 ± 0.75
Data	85 ± 9.21	60 ± 7.74	82 ± 9.05	82 ± 9.05
$W' \to WZ \to 3\ell\nu$				
W'600	17.31 ± 0.358	14.92 ± 0.33	13.76 ± 0.459	16.78 ± 0.507

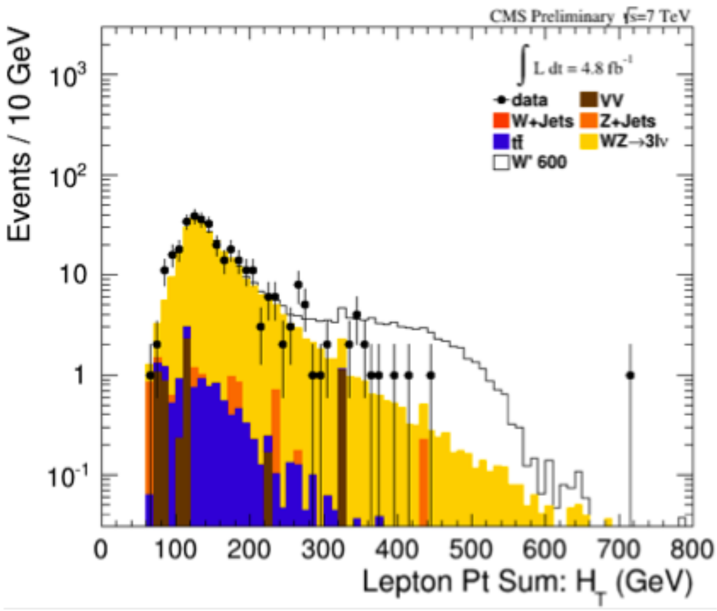

Figure 5.5. Scalar sum of charged lepton transverse momenta after the WZ candidate selection.

The detailed breakdown for all MC processes contributing to the expected background is listed in Table 5.9. As seen from this table, the SM WZ background is dominant. The combined expected MC background, expected signal and observed event yields for all mass points are listed in Table 5.10. As can be seen from this table, there is a good agreement between data and background but efficiency is high for the signal. Figure 5.6 shows the invariant mass distribution of the WZ candidates for the selected events before and after H_T cut corresponding to W$'$ with a mass of 600 GeV. As can be seen from the figure, though we lose the signal, we could suppress most of the SM background events after the H_T cut is applied. The invariant mass of the three leptons after all selection criteria is shown in Figure 5.7. The tri-lepton mass is not consistent with the Z mass. It indicates that there is no background contribution from final state radiation with photon conversion. The mass window cuts, the individual and total background contributions for each of the search windows for each W' mass point are shown in Table 5.11. The mass window cuts are directly taken from reference (Brigljevic et al., 2011). Expected backgrounds for $Z+jets$, $V\gamma$, $W+jets$ and WW are negligible so they are not shown in this table.

Table 5.9. Breakdown of the number of expected background events after H_T cut has been applied for the full WZ mass spectrum.

Mass Point	$N_{t\bar{t}}$	N_{zz}	N_{wz}	N_{BkgMC}
W' 200	8.754 ± 0.347	14.622 ± 0.058	275.738 ± 0.961	299.116 ± 1.024
W' 250	3.819 ± 0.226	6.108 ± 0.067	123.306 ± 0.643	133.235 ± 0.685
W' 300	2.913 ± 0.198	4.96 ± 0.035	102.423 ± 0.586	111.297 ± 0.62
W' 400	0.847 ± 0.107	1.689 ± 0.02	38.701 ± 0.36	41.238 ± 0.376
W' 500	0.772 ± 0.103	1.504 ± 0.021	33.341 ± 0.334	35.619 ± 0.35
W' 600	0.221 ± 0.055	0.662 ± 0.012	14.862 ± 0.224	15.746 ± 0.231
W' 700	0.027 ± 0.019	0.303 ± 0.008	6.38 ± 0.145	6.711 ± 0.147
W' 800	0.008 ± 0.005	0.206 ± 0.007	4.092 ± 0.117	4.307 ± 0.117
W' 900	0.008 ± 0.005	0.206 ± 0.007	4.092 ± 0.117	4.307 ± 0.117
W' 1000	0.008 ± 0.005	0.206 ± 0.007	4.092 ± 0.117	4.307 ± 0.117
W' 1100	0.008 ± 0.005	0.206 ± 0.007	4.092 ± 0.117	4.307 ± 0.117
W' 1200	0.008 ± 0.005	0.206 ± 0.007	4.092 ± 0.117	4.307 ± 0.117
W' 1300	0.008 ± 0.005	0.206 ± 0.007	4.092 ± 0.117	4.307 ± 0.117
W' 1400	0.008 ± 0.005	0.206 ± 0.007	4.092 ± 0.117	4.307 ± 0.117
W' 1500	0.008 ± 0.005	0.206 ± 0.007	4.092 ± 0.117	4.307 ± 0.117

Table 5.10. Number of expected background (N_{Bkg}), observed (Data) and signal (N_{sig}) events after H_T cut has been applied for the full WZ mass spectrum. The optimized cut value is listed for each W' mass considered. The numbers correspond to an integrated luminosity of 4.8 fb^{-1}.

Mass Point	H_T Cut (GeV)	N_{BkgMC}	Data	N_{sig}
W' 200	0	299.116 ± 1.024	309 ± 17.578	784.473 ± 18.001
W' 250	150	133.235 ± 0.685	130 ± 11.4	525.618 ± 13.644
W' 300	160	111.297 ± 0.62	109 ± 10.44	499.180 ± 10.051
W' 400	220	41.238 ± 0.376	42 ± 6.48	197.346 ± 3.574
W' 500	230	35.619 ± 0.35	40 ± 6.324	108.017 ± 1.642
W' 600	290	15.746 ± 0.231	16 ± 4	53.525 ± 0.777
W' 700	360	6.711 ± 0.147	5 ± 2.236	26.395 ± 0.381
W' 800	400	4.307 ± 0.117	3 ± 1.732	15.731 ± 0.219
W' 900	400	4.307 ± 0.117	3 ± 1.732	9.794 ± 0.131
W' 1000	400	4.307 ± 0.117	3 ± 1.732	6.000 ± 0.078
W' 1100	400	4.307 ± 0.117	3 ± 1.732	3.624 ± 0.048
W' 1200	400	4.307 ± 0.117	3 ± 1.732	2.049 ± 0.028
W' 1300	400	4.307 ± 0.117	3 ± 1.732	1.167 ± 0.017
W' 1400	400	4.307 ± 0.117	3 ± 1.732	0.573 ± 0.009
W' 1500	400	4.307 ± 0.117	3 ± 1.732	0.326 ± 0.005

Table 5.11. Background contributions, total number of background events, number of observed events (Data) and the number of signal events for the search windows for each W' mass point. N_{BkgMC} is the total background contribution obtained from simulation.

Mass Point	Window (GeV)	$N_{t\bar{t}}$	N_{zz}	N_{wz}	N_{BkgMC}	Data	N_{sig}
W' 200	190-210	0.703 ± 0.095	1.657 ± 0.020	26.679 ± 0.270	29.041 ± 0.287	25 ± 5	221.06 ± 9.617
W' 250	230-270	0.303 ± 0.226	1.214 ± 0.015	15.664 ± 0.229	17.182 ± 0.323	25 ± 5	213.33 ± 8.705
W' 300	280-320	1.219 ± 0.054	0.739 ± 0.013	11.678 ± 0.199	12.637 ± 0.207	8 ± 2.828	208.11 ± 6.38
W' 400	360-440	0.121 ± 0.040	0.405 ± 0.010	6.776 ± 0.150	7.303 ± 0.156	2 ± 1.414	116.62 ± 2.772
W' 500	450-550	0.064 ± 0.030	0.142 ± 0.007	4.327 ± 0.120	4.535 ± 0.124	7 ± 2.645	64.443 ± 1.278
W' 600	540-660	0.0015 ± 0.001	0.088 ± 0.004	1.875 ± 0.078	1.964 ± 0.078	1 ± 1	34.26 ± 0.625
W' 700	620-780	0.0015 ± 0.001	0.046 ± 0.003	0.975 ± 0.058	1.023 ± 0.058	0 ± 0	18.807 ± 0.327
W' 800	710-890	0 ± 0	0.024 ± 0.002	0.575 ± 0.045	0.600 ± 0.045	0 ± 0	11.137 ± 0.186
W' 900	760-1040	0 ± 0	0.028 ± 0.002	0.568 ± 0.044	0.597 ± 0.044	0 ± 0	7.384 ± 0.114
W' 1000	820-1180	0 ± 0	0.022 ± 0.008	0.376 ± 0.037	0.398 ± 0.038	0 ± 0	4.624 ± 0.069
W' 1100	890-1310	0 ± 0	0.011 ± 0.001	0.310 ± 0.030	0.322 ± 0.030	0 ± 0	2.804 ± 0.042
W' 1200	940-1460	0 ± 0	0.007 ± 0.001	0.231 ± 0.025	0.238 ± 0.025	0 ± 0	1.600 ± 0.025
W' 1300	1020-1580	0 ± 0	0.004 ± 0.001	0.163 ± 0.021	0.168 ± 0.022	0 ± 0	0.881 ± 0.014
W' 1400	1100-1690	0 ± 0	0.003 ± 0.0009	0.093 ± 0.017	0.096 ± 0.017	0 ± 0	0.402 ± 0.008
W' 1500	1200-1800	0 ± 0	0.002 ± 0.0008	0.064 ± 0.014	0.066 ± 0.014	0 ± 0	0.222 ± 0.004

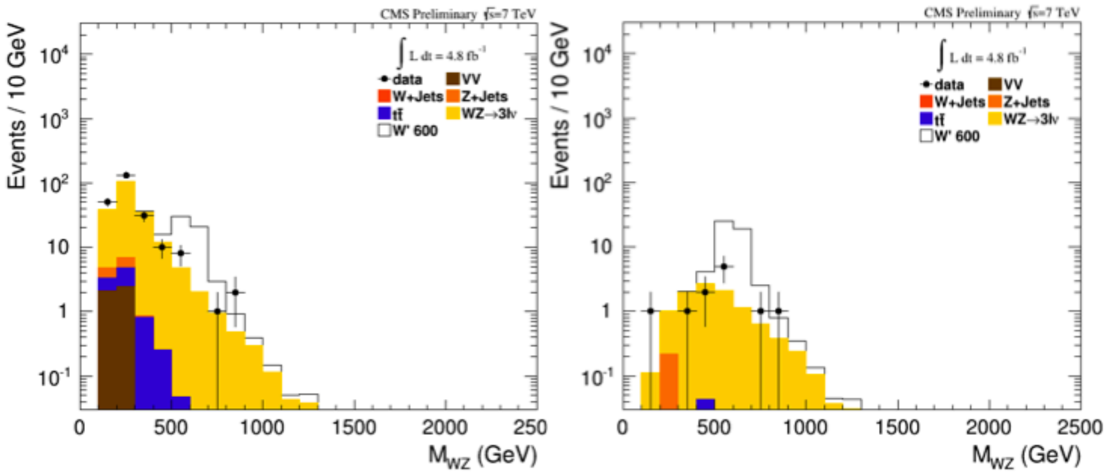

Figure 5.6. WZ invariant mass after the WZ candidate selection (left) and after all selection criteria have been applied (right), optimized for the search for W' with mass of 600 GeV.

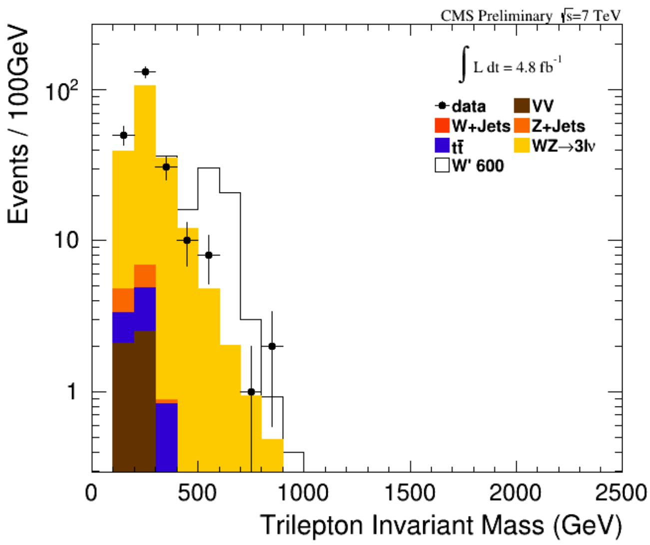

Figure 5.7. Invariant mass of the charged three leptons after all selection criteria have been applied.

Many experimental signatures, both SM and beyond, involve leptons in the final state at CMS. Accurate and reliable lepton efficiency measurements are needed for the evaluation of cross sections and signal yields. Therefore, selection effects for the signal count and background subtraction should be investigated. In the following chapter, this point will discussed and the efficiency results will be compared for data and simulation.

5.5. Lepton Selection Efficiency

We determine the efficiency of electron and muon selection criteria by applying a 'tag and probe' method (Daskalakis et al., 2007; Adam et al., 2009) to each stage of the selection in the same way for data and simulation, and the uncertainty on the ratio of efficiencies is taken as the systematic uncertainty.

The tag and probe tool is used for this calculation. It is a generic tool and developed to measure any user defined object efficiency from data at CMS by exploiting di-object resonances like Z, J/ψ. In general, the 'tag' is object that passes a set of very tight selection criteria. The tight selection is applied to one leg in order to ensure sufficient purity. The 'probe' is object that passes very loose selection criteria. The resonances are constructed as pairs with one tag and one probe. The invariant mass of the combination is consistent with the mass of the resonance. Then passing probes are defined according to whatever is the efficiency to measure. For a given measurement, probes are defined as the object passing the previous step. The 'tag + passing probe' and 'tag + failing probe' line shapes are fit separately with signal and background in order to extract the efficiency for signal events. Different shapes are used in order to fit the signal and background. A Voigtian convoluted with a Crystal Ball function is used for $Z \rightarrow e^+e^-$ events and a Gauss convoluted with a Crystal Ball function is used for $Z \rightarrow \mu^+\mu^-$ events. An exponential function is used for background. The corresponding parameters are defined in Appendix D. The efficiency is computed from the ratio of the signal yields in the line shapes above. The procedure is repeated in bins of the probe variables (e.g. p_T, η ...) to compute efficiency histograms as a function of those variables. Special HLT paths are used to select data and MC for tag and probe fits. Selection used for electrons and muons requires following HLT paths, respectively:

- HLT_Ele17_CaloIdVT_CaloIsoVT_TrkIdT_TrkIsoVT_SC8_Mass30_v*
- HLT_Mu30_v* and HLT_Mu40_v*.

The total efficiency is considered as the product of reconstruction, identification, isolation and trigger efficiencies for electrons and muons. It is given as following equation for electrons and muons, respectively:

$$\varepsilon_{\text{total}} = \varepsilon_{\text{reconstruction}} \cdot \varepsilon_{\text{ID}} \cdot \varepsilon_{\text{isolation}} \cdot \varepsilon_{\text{HLT}} \tag{5.6}$$

$$\varepsilon_{\text{total}} = \varepsilon_{\text{track}} \cdot \varepsilon_{\text{stand-alone}} \varepsilon_{\text{ID}} \cdot \varepsilon_{\text{isolation}} \cdot \varepsilon_{\text{HLT}} \tag{5.7}$$

Electron and muon selection efficiency will be discussed in following chapters for each stage of the selection. All efficiencies are calculated in different p_T **(**or E_T**)** and pseudorapidity bins (η) for each dataset, separately to look whether the efficiencies are changing according to bins. Since the value of efficiency is not changing as a function of bins, then the average efficiency is calculated.

5.5.1. Electron Selection Efficiency

The Tag and Probe software package is used to derive efficiency for each of the above steps: Super Cluster → GsfElectron → Electron ID → Isolation → HLT Trigger Matching. A WP60 selection is applied on the tag. The probe is a supercluster (SC) for the reconstruction efficiency. The reconstruction efficiency is defined as the fraction of probe SC that are matched to a reconstructed GSF electron (see in section 4.2). This efficiency is given as $\varepsilon_{\text{reconstruction}}$ in the equation 5.6. The results are shown in Table 5.12 for different supercluster E_T bins and in Table 5.13 for different pseudorapidity bins for SC with $E_T > 20$ GeV. A very good agreement is found between data and MC.

Following the same procedure, efficiencies are determined for the electron identification and isolation. The probes are respectively reconstructed GSF, and reconstructed GSF electrons passing identification criteria. Efficiencies are defined for both the loose (WP95) and the tight (WP80) selection used in this analysis. The loose selection is used for Z candidates selection together with a p_T threshold of p_T

> 10 GeV/*c*. In this case, the efficiencies are determined for $p_T > 10$ GeV/*c*. The efficiencies are determined for $p_T > 20$ GeV/*c* for the case of tight selection. The electron identification and isolation efficiencies are given as $\varepsilon_{\mathrm{ID}}$ and $\varepsilon_{\mathrm{isolation}}$ in equation 5.6, respectively. These efficiencies are given in Table 5.12 and 5.13. An example of the fit of the $M_{\ell\ell}$ distribution for passing and failing probes is shown in Figure 5.8 for the case of the electron ISO efficiency for WP80.

The efficiency for an isolated electron to be identified in the trigger is given as ε_{HLT}. It is calculated separately for each leg of the trigger since these are independent. The results for these measurements are given in Table 5.14 and 5.15. The all average efficiencies are given in Table 5.16 and 5.17. Results cover the lepton E_T and pseudorapidity ranges for each data set and a MC sample are shown in Appendix E.

Table 5.12. Electron Reconstruction, ID and Isolation Efficiency for different E_T bins.

E_T Bins	SCToGSF	WP95ID	WP80ID	WP95Iso	WP80Iso
20 < E_T < 30	0.96 ± 0.001	0.952 ± 0.001	0.725 ± 0.002	0.876 ± 0.001	0.577 ± 0.0024
30 < E_T < 40	0.969 ± 0.0006	0.971 ± 0.002	0.791 ± 0.001	0.948 ± 0.0006	0.759 ± 0.001
40 < E_T < 50	0.973 ± 0.0004	0.979 ± 0.0005	0.831 ± 0.001	0.98 ± 0.001	0.857 ± 0.003
50 < E_T < 60	0.973 ± 0.001	0.98 ± 0.001	0.842 ± 0.002	0.988 ± 0.0007	0.90 ± 0.002
60 < E_T < 70	0.984 ± 0.002	0.981 ± 0.002	0.857 ± 0.005	0.99 ± 0.001	0.941 ± 0.003
70 < E_T < 80	0.986 ± 0.003	0.981 ± 0.003	0.86 ± 0.008	0.992 ± 0.002	0.957 ± 0.004
80 < E_T < 100	0.985 ± 0.004	0.98 ± 0.004	0.861 ± 0.008	0.993 ± 0.002	0.963 ± 0.004
100 < E_T < 200	0.986 ± 0.004	0.984 ± 0.004	0.871 ± 0.01	0.994 ± 0.002	0.980 ± 0.004

Table 5.13. Electron Reconstruction ID and Isolation Efficiency for different pseudorapidity bins.

$\|\eta\|$ Bins	SCToGSF	WP95 ID	WP80 ID	WP95 Iso	WP80 Iso
$0 < \|\eta\| \leq 0.78$	0.979 ± 0.0005	0.9792 ± 0.0005	0.855 ± 0.0066	0.963 ± 0.0005	0.7919 ± 0.0011
$0.78 < \|\eta\| \leq 1.444$	0.975 ± 0.0006	0.9763 ± 0.022	0.84 ± 0.0013	0.9657 ± 0.0006	0.7939 ± 0.0013
$1.444 < \|\eta\| \leq 1.566$	0.966 ± 0.0357	0.9734 ± 0.0354	0.8124 ± 0.065	0.969 ± 0.032	0.8482 ± 0.059
$1.566 < \|\eta\| \leq 2.0$	0.962 ± 0.001	0.9648 ± 0.0008	0.687 ± 0.0025	0.9405 ± 0.0011	0.8348 ± 0.0022
$2.0 < \|\eta\| \leq 2.5$	0.939 ± 0.001	0.963 ± 0.001	0.7046 ± 0.0031	0.9025 ± 0.0036	0.8384 ± 0.0016

Table 5.14. Electron HLT Efficiency for different E_T bins.

E_T Bins	WP95ToHLT17	WP95ToHLT8
$20 < E_T < 30$	0.964 ± 0.001	0.978 ± 0.001
$30 < E_T < 40$	0.974 ± 0.0004	0.976 ± 0.0006
$40 < E_T < 50$	0.977 ± 0.0003	0.978 ± 0.0003
$50 < E_T < 60$	0.978 ± 0.001	0.979 ± 0.001
$60 < E_T < 70$	0.979 ± 0.002	0.98 ± 0.002
$70 < E_T < 80$	0.978 ± 0.003	0.979 ± 0.003
$80 < E_T < 100$	0.981 ± 0.003	0.981 ± 0.003
$100 < E_T < 200$	0.981 ± 0.004	0.982 ± 0.004

Table 5.15. Electron HLT Efficiency for different pseudorapidity bins.

$\|\eta\|$ Bins	WP95ToHLT17	WP95ToHLT8
$0 < \|\eta\| \leq 0.78$	0.975 ± 0.001	0.977 ± 0.0006
$0.78 < \|\eta\| \leq 1.444$	0.978 ± 0.0006	0.979 ± 0.0006
$1.444 < \|\eta\| \leq 1.566$	1 ± 0.03	1 ± 0.03
$1.566 < \|\eta\| \leq 2.0$	0.977 ± 0.001	0.979 ± 0.001
$2.0 < \|\eta\| \leq 2.5$	0.963 ± 0.001	0.972 ± 0.002

Table 5.16. Average Efficiencies over E_T bins.

Efficiency	data	MC	data/MC
ScToGsf	0.969 ± 0.0008	0.979 ± 0.003	0.989 ± 0.0038
WP95 ID	0.971 ± 0.001	0.976 ± 0.003	0.994 ± 0.0039
WP80 ID	0.802 ± 0.001	0.808 ± 0.008	0.992 ± 0.009
WP95 Iso	0.954 ± 0.0008	0.953 ± 0.004	1 ± 0.03
WP80 Iso	0.795 ± 0.002	0.791 ± 0.006	1 ± 0.009
WP95 HLT17	0.974 ± 0.0007	0.985 ± 0.002	0.98 ± 0.002
WP95 HLT8	0.977 ± 0.0008	0.986 ± 0.002	0.98 ± 0.002

Table 5.17. Average Efficiencies over pseudorapidity bins.

Efficiency	data	MC	data/MC
ScToGsf	0.970 ± 0.004	0.972 ± 0.09	0.997 ± 0.09
WP95 ID	0.973 ± 0.01	0.977 ± 0.09	0.995 ± 0.09
WP80 ID	0.805 ± 0.009	0.814 ± 0.09	0.988 ± 0.1
WP95 Iso	0.952 ± 0.004	0.957 ± 0.09	0.994 ± 0.09
WP80 Iso	0.803 ± 0.006	0.800 ± 0.09	1 ± 0.1
WP95 HLT17	0.975 ± 0.004	0.986 ± 0.09	0.988 ± 0.09
WP95 HLT8	0.977 ± 0.004	0.986 ± 0.09	0.99 ± 0.09

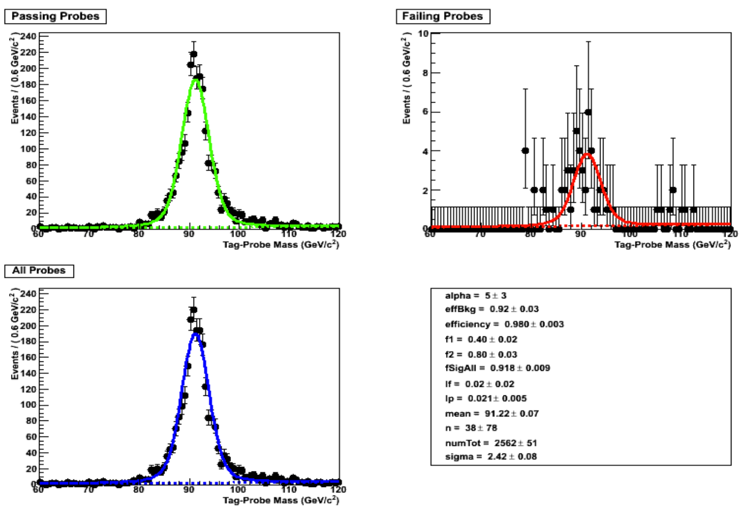

Figure 5.8. $M_{\ell\ell}$ distribution for passing and failing probes used for the measurements of the electron ISO efficiency for WP80 for an E_T bin for a dataset.

5.5.2. Muon Selection Efficiency

The same efficiencies for muons are considered as above. $\varepsilon_{\text{track}}$ and $\varepsilon_{\text{stand-alone}}$ are the efficiencies to reconstruct a track in the tracker given a stand-alone and to reconstruct a stand-alone muon given a track in the tracker, respectively. Two measurements are assumed to be completely independent. The efficiency of passing all identification requirements given a muon identified both in the tracker and the muon system is described as ε_{ID}. The efficiency of passing isolation requirements given a muon, which satisfies the identification requirements, is defined as $\varepsilon_{\text{isolation}}$. The efficiency of finding an HLT muon given an isolated muon is given as ε_{HLT}. In order to avoid a bias due to trigger, it is also required that this tag muon is matched to an HLT object passing an unprescaled single muon trigger. The results for each efficiency measurement are given in Table 5.18 and 5.19 for each pseudorapidity and P_T bin. The all average efficiencies are given in Table 5.20 and 5.21. Results cover the lepton P_T and pseudorapidity ranges for each data set and a MC sample are shown in Appendix E.

Table 5.18. Muon ID, Isolation and Trigger Efficiency for different P_T bins.

P_T bins	ε_{Trk}	ε_{Std}	ε_{ID}	$\varepsilon_{Isolation}$	ε_{HLT_17}	ε_{HLT_8}
$10 < P_T < 20$	0.991 ± 0.0018	0.973 ± 0.0071	0.971 ± 0.008	0.845 ± 0.007	0.676 ± 0.0089	0.69 ± 0.0087
$20 < P_T < 30$	0.99 ± 0.00073	0.974 ± 0.0016	0.987 ± 0.0017	0.918 ± 0.0019	0.967 ± 0.001	0.967 ± 0.001
$30 < P_T < 40$	0.990 ± 0.00036	0.98 ± 0.00059	0.966 ± 0.0007	0.967 ± 0.0007	0.970 ± 0.0004	0.970 ± 0.0004
$40 < P_T < 50$	0.990 ± 0.00029	0.979 ± 0.00049	0.965 ± 0.0006	0.989 ± 0.00035	0.970 ± 0.0004	0.970 ± 0.0004
$50 < P_T < 60$	0.991 ± 0.00073	0.978 ± 0.0009	0.963 ± 0.0016	0.994 ± 0.0006	0.970 ± 0.0009	0.970 ± 0.0009
$60 < P_T < 100$	0.991 ± 0.001	0.979 ± 0.00017	0.963 ± 0.0027	0.993 ± 0.001	0.971 ± 0.0015	0.971 ± 0.0015

Table 5.19. Muon ID, Isolation and Trigger Efficiency for different η bins.

$\|\eta\|$ Bins	ε_{Trk}	ε_{Std}	ε_{ID}	$\varepsilon_{Isolation}$	ε_{HLT_17}	ε_{HLT_8}
0 < $\|\eta\|$<0.5	0.991 ± 0.00038	0.984 ± 0.0007	0.972 ± 0.0022	0.966 ± 0.0008	0.971 ± 0.0041	0.971 ± 0.0041
0.5 < $\|\eta\|$ < 1	0.993 ± 0.00035	0.984 ± 0.0007	0.975 ± 0.0008	0.973 ± 0.0008	0.969 ± 0.0005	0.97 ± 0.0005
1 < $\|\eta\|$ <1.5	0.987 ± 0.00055	0.989 ± 0.0006	0.957 ± 0.0009	0.981 ± 0.0007	0.966 ± 0.0006	0.966 ± 0.00059
1.5 < $\|\eta\|$ <2	0.994 ± 0.00043	0.981 ± 0.0009	0.951 ± 0.00029	0.981 ± 0.0008	0.962 ± 0.0007	0.963 ± 0.0007
2 < $\|\eta\|$ < 2.5	0.984 ± 0.0009	0.989 ± 0.001	0.962 ± 0.0017	0.979 ± 0.0009	0.960 ± 0.001	0.953 ± 0.001

Table 5.20. The Average Efficiencies over P_T bins.

Efficiency	data	MC	Ratio (data/MC)
ε_{Std}	0.99 ± 0.0004	0.993 ± 0.00008	0.996 ± 0.0004
ε_{Trk}	0.978 ± 0.001	0.983 ± 0.0002	0.994 ± 0.001
ε_{ID}	0.964 ± 0.001	0.973 ± 0.001	0.99 ± 0.001
$\varepsilon_{Isolation}$	0.97 ± 0.001	0.96 ± 0.003	1.01 ± 0.001
ε_{HLT_17}	0.964 ± 0.001	0.986 ± 0.002	0.977 ± 0.001
ε_{HLT_8}	0.964 ± 0.001	0.994 ± 0.00007	0.969 ± 0.001

Table 5.21. The Average Efficiencies over η bins.

Efficiency	data	MC	Ratio (data/MC)
ε_{Std}	0.99 ± 0.0004	0.992 ± 0.00007	0.997 ± 0.0004
ε_{Trk}	0.98 ± 0.0008	0.98 ± 0.0001	0.996 ± 0.001
ε_{ID}	0.965 ± 0.001	0.974 ± 0.0001	0.99 ± 0.001
$\varepsilon_{Isolation}$	0.974 ± 0.0007	0.964 ± 0.0008	1.01 ± 0.001
ε_{HLT_17}	0.966 ± 0.002	0.987 ± 0.0001	0.978 ± 0.001
ε_{HLT_8}	0.967 ± 0.002	0.987 ± 0.0001	0.979 ± 0.001

5.6. Data-driven Cross-check of the Background Estimation

The background processes are expected to contribute to the three-lepton final state as discussed in Sec. 5.2.1. They consist of genuine $W^{\pm} \rightarrow \ell^{\pm} + \nu_{\ell}$ or $Z \rightarrow \ell^{+} + \ell^{-}$ decays along with some number of additional jets misidentified as leptons. The probability of a jet to satisfy the lepton identification criteria is low. Therefore, the expected contribution from a given process decreases as the number of jets. Similarly, only one misidentified lepton is sufficient to cause contamination in Z+jets events. Data-driven methods are used to estimate background contributions from these processes. This method also measures a part of the $t\bar{t}$ background. Other background processes are estimated from MC simulation. It is possible to obtain agreement between data and simulation in this way. All backgrounds can be taken from simulation for the resonance search. These samples represent di-boson processes with extra jets (WW, WZ, ZZ, $Z\gamma$, and $W\gamma$) along with $Z + jets$, $W + jets$, and $t\bar{t}$. The contributions from $t\bar{t}$ and WW processes may be small (Adiguzel, 2011).

5.6.1. $Z + jets$ Background Estimation

The 'matrix method' is used to perform a data-driven estimation of the contribution to the signal region from backgrounds where a misidentified jet gets together with a Z candidate formed from real leptons. This will be composed of $Z + jets$ events. This background is one of the largest background contributions to this analysis. The results from estimation are used to check on the simulated yields for the resonance search. The matrix method requires the definition of two samples:

- **Tight cut sample:** events passing all selection criteria for W and Z candidate events.
- **Loose cut sample:** events passing all the selection criteria except for the isolation requirement on the W daughter lepton.

The observables are the total number of events in these two samples. The loose-cut sample (N_{loose}) contains events with the W candidates reconstructed from true isolated leptons (N_{lep}) or from fake ones from misidentified jets (N_{jet}). These numbers are not directly observable in collision data, so we instead count the number N_{tight} and compare with the superset of events N_{loose} . The number of events for the loose-cut and tight-cut samples can be expressed as:

$$N_{loose} = N_{lep} + N_{jet} \tag{5.8}$$

$$N_{tight} = \varepsilon_{tight} N_{lep} + P_{fake} N_{jet} \tag{5.9}$$

In the equation (5.9), ε_{tight} is the efficiency of true leptons to pass isolation cuts, and P_{fake} is the efficiency of fake leptons (misidentified jets) and can be also referred as " fake rate" from another perspective. The tag and probe method is applied to obtain the ε_{tight} and P_{fake} values in independent samples of collision data (Adiguzel, 2011). These values are given in Table 5.22 for electrons and muons. The final background estimate is determined separately for each mass window, with the data driven results compared to generator-level information in MC samples in Table 5.23.

Table 5.22. Isolation Efficiencies for true and fake leptons.

Measurement	Efficiency%
$\varepsilon_{tight}(e)$	93.4 ± 0.04
$\varepsilon_{tight}(\mu)$	97.11 ± 0.02
$P_{fake}(e)$	7 ± 1
$P_{fake}(\mu)$	6 ± 1

Table 5.23. Expected numbers of true- and fake-lepton events calculated using 4.8 fb^{-1} of data. The measured number of true leptons $\varepsilon_{tight} N_{lep}$ may be compared with the expected number of tight leptons from signal-like events with isolated leptons based on MC information in the final column, "$MC\ N_{lep}^{tight}$".

SAMPLE	$\varepsilon_{tight}.N_{Lep}$	$P_{fake}.N_{Jet}$	MCN_{Lep}^{tight}
W'200	23.7 ± 4.6	1.2 ± 0.1	26.5 ± 0.07
W'250	25.6 ± 4.8	1.1 ± 0.1	14.6 ± 0.06
W'300	8.1 ± 2.7	0.8 ± 0.1	11,09 ± 0.4
W'400	2.8 ± 1.6	0.6 ± 0.2	6.3 ± 0.2
W'500	6.6 ± 2.6	0.2 ± 0.07	4 ± 0.1
W'600	0.9 ± 0.9	0.07 ± 0.4	1.7 ± 1.3
W'700	0 ± 0	0 ± 0	0.9 ± 0.004
W'800	0 ± 0	0 ± 0	0.3 ± 0.03
W'900	0 ± 0	0 ± 0	0.5 ± 0.03
W'1000	0 ± 0	0 ± 0	0.39 ± 0.2
W'1100	0 ± 0	0 ± 0	0.3 ± 0.03
W'1200	0 ± 0	0 ± 0	0.2 ± 0.02
W'1300	0 ± 0	0 ± 0	0.17 ± 0.02
W'1400	0 ± 0	0 ± 0	0.1 ± 0.01
W'1500	0 ± 0	0 ± 0	0.04 ± 0.08

5.6.1.1. Measurement of Isolation Efficiency for True Leptons

The efficiency for the true leptons to pass the isolation requirement is measured using collision data. We define some collection of lepton candidates. The collection has a high purity of true leptons without using any isolation criteria that would bias our ε_{tight} measurement. The same tag and probe method is applied in the measurement of the lepton selection efficiencies in section 5.5. A Z-enriched sample is defined by requiring two opposite-charge leptons with the same flavor and invariant mass between 60 GeV/c^2 and 120 GeV/c^2. The leptons are required to have $p_T > 10$ GeV and both leptons must pass the identification criteria which is used on candidates for the W decay and at least one must pass the associated isolation requirement which is called as the tag object. The remaining lepton candidate is the probe. Only one Z candidate per event is allowed in the above mass window. The efficiency is obtained as following equation:

$$\varepsilon_{tight} = \frac{2(N_{TT} - B_{TT})}{(N_{TF-}B_{TF}) + 2(N_{TT} - B_{TT})} \tag{5.9}$$

Where, N is the total number of events in the Z-candidate mass window, B is the combinatorial background from W events. The $Z + jets$ events are dominant in the resulting dataset, but some $t\bar{t}$, WZ and $W + jets$ events are also included. While the $t\bar{t}$ and $W + jets$ contributions tend to be distributed across the invariant mass range, the processes with a true $Z \rightarrow \ell^+\ell^-$ decay contribute to a peak in the invariant mass distribution. So that in order to estimate background events and subtract the non-peaking events, a linear fit on events outside of the Z mass window (sideband region from [70-80 GeV] and [100-110 GeV]) is applied. In equation 5.9, TT indicates that both leptons pass the isolation cuts and TF indicates that exactly one of the leptons fails the isolation cut.

5.6.1.2. Measurement of Isolation Efficiency for Fake Leptons

The interaction topologies of the charged and neutral vector boson are very similar at the LHC. We expect a similar spectrum of jets events with a W compared to events with a Z. We need to use a W-enriched sample from collision data to perform measurement of the rate (P_{fake}). We select $W + jet$ candidate events by requiring the event to have a very good quality W lepton candidate satisfying tight lepton identification and isolation requirements. The W lepton candidate is referred to as a tag lepton. Then we require the event to have only one additional lepton candidate (passes the identification criteria without isolation) with opposite flavor and the same charge (since Z decays can never give one electron and one muon) to reject Z, WW and $t\bar{t}$ processes. The P_{fake} is defined as the ratio of the event count with the probe passing isolation to the total number of selected events in the W-enriched region.

5.6.2. QCD Background Estimation

The major source of this background comes from QCD multi-jet events. Most multi-jet events come from soft interactions. These interactions generate little transverse momentum such that the p_T requirements significantly reduce relevant QCD cross-section. Beyond this, tight constraints on the kinematics of the event are provided by the Z mass window and requirement of significant E_T^{miss}. The pure multi-jet interactions are unlikely to replicate in the event.

The other source of this background comes from $W + jets$ events. These events contain a real $W^{\pm} \rightarrow \ell^{\pm} + \nu_{\ell}$ decay. This decay process should have a similar E_T^{miss} distribution to genuine WZ events and two jets are misidentified as leptons so in order to avoid misidentification of leptons, we use constraint on Z mass along with lepton selection requirements. $W + jets$ events have the highest cross section among MC background samples in this analysis but its contribution is negligible in the final sample.

In consideration of the above arguments through a direct MC investigation of the expected QCD contribution is not feasible. Because simulated QCD data has extremely large statistics. Early studies of the CMS detectors show that a multi-jet event would yield a Z candidate, a W candidate or high H_T. In these studies the probabilities to find a Z or a W are independent and employing selection criteria are very similar to this analysis. So they conservatively estimate a contribution of less than 0.5 events/fb^{-1} passing all selection criteria in the lowest-mass search windows and a level corresponding to less than 10% of the total yield from other background processes.

6. SEARCH FOR WZ RESONANCES

This chapter will start describing briefly the WZ cross-section measurement technique that leads to limit setting. Then the systematic uncertainties that contribute to errors of these measurements will be introduced. The results displayed in transverse invariant mass spectrum (see Figure 5.6) have to be investigated using a statistical method to decide up to which W' masses a signal for new physics can be detected if present or excluded if absent. This mass limit will be obtained at certain significance: typically a deviation of 5σ from background expectations states a discovery, while a 95% exclusion level is specified if there is no signal.

This chapter will describe the CLs-method (Read, 2000-2002; Gross and Read, 2000) to obtain a limit at certain significance. Finally limit results will be given.

6.1. Cross Section Measurement Technique

The cross section is calculated using Eq. 6.1:

$$\boldsymbol{\sigma} = \frac{N_{signal}}{A.\,\boldsymbol{\varepsilon}.\,\mathrm{L}} \tag{6.1}$$

where, N_{signal} is the number of observed signal event, A refers to the fiducial and kinematic acceptance, ε is the selection efficiency for events in the acceptance and $\mathrm{L}=\int L\,dt$ is the integrated luminosity.

The cross section $\sigma(pp \rightarrow W + Z \rightarrow \ell + \nu_{\ell} + \ell'^{+} + \ell'^{-})$ is determined separately for each of the four channels ($eee,\ ee\mu,\ \mu\mu e,\ \mu\mu\mu$) since $A.\varepsilon$ is different for these channels and then combined for a final result.

The choice of PDF and other theoretical uncertainties affect the value of A. The value of ε is susceptible to errors from triggering and reconstruction as well as uncertainties that effect A. In order to eliminate the uncertainties associated with the model, the efficiencies obtained from the simulation (ε_{sim}) are corrected with correction factors (ρ). These correction factors are computed as the efficiency ratios $\rho = \varepsilon / \varepsilon_{sim}$, derived by measuring ε and ε_{sim} in the same way on data and simulation, respectively. In equation 6.1, $A.\varepsilon$ can be replaced by $A.\ \varepsilon_{sim}.\ \rho$, where $A.\ \varepsilon_{sim}$ is the fraction of generated WZ events (decaying into only electron and muon final states) with dilepton mass between 60 GeV/c^2 and 120 GeV/c^2 selected in the simulation. In addition, N_{signal} (number of signal events) is not directly measured, but it is obtained by subtracting the estimated number of background events N_{bkg} from the observed number of selected WZ candidates events N_{obs}. Therefore the equation 6.1 can be written as

$$\sigma = \frac{(N_{obs} - N_{back})\ .\ (1 - f_\tau)}{A.\ \varepsilon_{sim} . \rho .\ \mathrm{L}} \tag{6.2}$$

WZ to taus background is also taken into account and subtracted as a fraction of N_{signal} itself, where f_τ is the fraction of reconstructed WZ events containing a tau lepton estimated from simulation. The yields estimated from both MC simulation and data driven methods are used for N_{backg}. It is given as

$$N_{backg} = p_{fake} . N_{Jet} + N_{bkg}^{ZZ} + N_{bkg}^{Z\gamma} \tag{6.3}$$

where, N_{bkg}^{ZZ} and $N_{bkg}^{Z\gamma}$ are ZZ, $Z\gamma$ yields, respectively. Both backgrounds include a real Z. While one of the leptons is either outside the detector acceptance or mis-reconstructed in ZZ production, mis-identified lepton candidates come from jets and photons in $Z\gamma$. They are obtained from simulated samples and expected to be small. In this equation, $p_{Fake} . N_{Jet}$ gives the matrix method estimate (Sec. 5.6.1) for backgrounds consisting of a real lepton pair accompanied by a misidentified jet (dominated by $Z + \text{jets}$, but also accounting for $t\bar{t}$ and WW contributions).

In high energy physics, if difference between number of observed events and number of background events is not equal to zero, we can only mention about a measurement of cross section. So, how to calculate the cross section assuming signal events are seen will be explained in this part.

The interpretation of search results for new particles near the sensitivity limit of an experiment is a common problem in particle physics. The loss of sensitivity may be due to a combination of small signal rates, the presence of background comparable to the expected signal, and the loss of discrimination between two models due to insufficient experimental resolution (Read, 2000). So the next part will explain how the lower bound is derived with the so-called CL_s method, why this method is used, and how to interpret the result.

6.2. The Statistical Technique for Setting a Limit

The Large Hadron Collider (LHC) started to take data at the end of 2009. It is expected to produce an unprecedented amount of data to be analyzed. These data offer the largest potential for the discovery of new physics and introduce many challenges to the statistical techniques used in High Energy Physics. Different statistical approaches will be used for statistical inference of the data. That implies different techniques to be considered. Each technique answers different questions and using specific treatment of systematic uncertainties.

There are three major types of statistical techniques:

- **Classical /Frequentist:** this technique of statistics restricts itself to making statements of the form "probability of the data given the hypothesis". The definition of the probability in this context is based on a limit of frequencies of various outcomes. In that sense it is objective.
- **Bayesian:** this technique of statistics allows one to make statements of the form "probability of the hypothesis given the data", which requires a prior probability of the hypothesis. Often the definition of probability in this context is a "degree of belief".

- **Likelihood-based:** this intermediate approach also uses a frequentist notion of probability (i.e does not require a priori the hypothesis), but it does not guarantee to have the properties (i.e coverage) that frequentists methods aim to achieve (or achieve by construction). This approach does "obey the likelihood principle" (as do Bayesian methods), while frequentist methods do not (Moneta et al., 2011).

The goal of a search is to exclude as strongly as possible the existence of signal in its absence or to confirm the existence of a true signal as strongly as possible while holding the probabilities of falsely excluding a true signal or falsely discovering a non-existent signal at or below specified levels.

The analysis of search results can be formulated in terms of a hypothesis test. The signal is absent in the null hypothesis and it exists in the alternate hypothesis. An analysis of search results is simply a formal definition of the procedure. The procedure quantifies the degree to which the hypotheses are favored or excluded by an experimental observation (Read, 2000).

In defining an analysis of search results, the first step is to identify the observables in the experiment, which comprise the search results. The simplest observable is the number of candidates satisfying a certain set of criteria. More advanced observables may be some feature of the candidates for instance reconstructed invariant mass, b-quark tagging probability, or even composite properties (such as the output of a multi-dimensional discriminant or artificial neural-network analysis). The next step is to define a test-statistic or function of the observables and the model parameters (particle mass, production rate, etc.) of the known background and hypothetical signal, which ranks experiments from the least to most signal-like (most to least background-like). The last step is to define the rules for exclusion and discovery i.e. specify ranges of values of the test statistic in which observations will lead to one conclusion or the other. In practice one often wishes to specify the significance of the exclusion or discovery, and not simply give a true or false answer. In other words a *confidence level* for the exclusion will be quoted. A *confidence limit* for exclusion is defined as the value of a population parameter, which is excluded at specified confidence level. A particle mass or a production rate are given as population parameter. A confidence limit is a lower (upper) limit if the exclusion confidence is greater (less) than the specified confidence level for all values of the population parameter below (above) the confidence limit. It should be noted that confidence intervals obtained in this way do not have the same interpretation as traditional frequentist confidence intervals nor as Bayesian credible intervals (Read, 2000).

Looking at the binned transverse invariant mass distribution for a certain W' mass with N bins in total, one can interpret every single bin as a result of an independent Poisson counting experiment with the probability distribution given as:

$$P(\mu,n) = \frac{\mu^n}{n!}.e^{-\mu} \tag{6.4}$$

For a given mean value μ, $P(\mu,n)$ gives the probability to obtain the result n in a counting experiment if μ is the expected value. There are two different "per bin counting experiments" looking at the final variable (the transverse invariant mass). One of them can use as mean value μ the number of *signal plus background* events ($\mu = s + b$). The other experiment takes the number of background events ($\mu = b$) as mean. Therefore, we have two probabilities: $P(\mu = s + b; n)$ and $P(\mu = b; n)$. These probabilities can be used to construct a discrimination variable for the significance of the signal. The likelihood ratio Q_i is the ratio of the probability densities for the signal plus background hypothesis to background hypothesis. For each bin i

$$Q_i(m_{W'}) = \frac{P(\boldsymbol{\mu} = s_i(m_{W'}) + b_i; n_i)}{P(\boldsymbol{\mu} = b_i; n_i)} \tag{6.5}$$

where, $s_i(m_{W'})$ is the number of signal events in bin i, which is a function of the W' mass $m_{W'}$, and b_i is the number of background events in bin i.

For a given signal and background prediction (for example given by a MC simulation), the likelihood ratio Q_i can be calculated for having n_i events in this bin. The number of signal events in a single bin depends on the mass of the W' in this study. So it is a parameter of the likelihood. The overall combination of the N "per bin counting experiments" can be written by the multiplication of each probability ratio:

$$Q(m_{W'}) = \prod_{i=1}^{N} Q_i(m_{W'}) \tag{6.6}$$

Instead of using the variable Q, it is convenient and practical to work with $-2\ln Q(m_{W'})$. A simple straightforward calculation using equation (6.4) and (6.5) leads to

$$-2\ln Q(m_{W'}) = 2s_{tot} - 2\sum_{i=1}^{N} n_i \ln(1+\frac{s_i}{b_i}) \tag{6.7}$$

In this equation, s_{tot} is the sum of total measured signal events. The likelihood ratio can be thought of as a generalization of the change in χ^2 for a fit to a distribution including signal plus background relative to fit to pure background distribution. The distributions of $-2\ln Q(m_{W'})$ are expected to converge to $\Delta\chi^2$ distributions in the high-statistics limit ($\mu \to \infty$).

The determination of signal significance is performed by generating numerous so-called "pseudo-experiments": Poisson distributed random numbers are generated once using the mean value $\mu = s_i + b_i$ and once $\mu = b_i$ to generate different n_i (see equation 6.7) for each bin in the transverse invariant mass. The resulting transverse invariant mass distribution is within statistical considerations equal to the obtained MC distribution. This generation of the "pseudo-experiments" is repeated numerously. For each experiment $-2\ln Q$ using formula (6.7) is calculated and filled in a histogram. As a result one obtains two Gaussian shaped distributions centered at $-2\ln Q$ of $\mu = s_i + b_i$ and $\mu = b_i$, respectively (Read, 2000). Typical distribution of the $-2\ln Q$ for different signals is given in Figure 6.1.

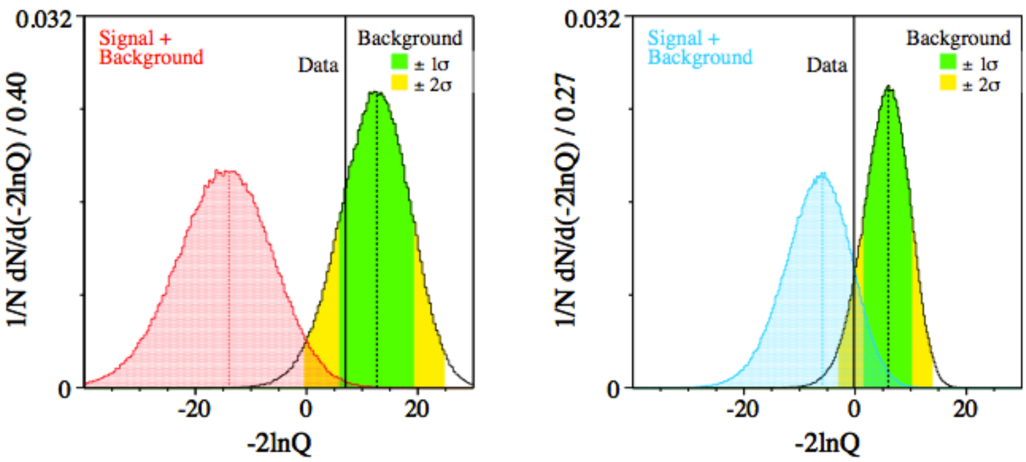

Figure 6.1. Typical distribution of $-2\ln Q$ for different signals (Read, 2000).

The distributions of the achieved pseudo-statistic are integral-normalized for the determination of the different confidence level (CL) for each hypothesis. They are defined as $\mathrm{P}_{s+b}(x)$ and $\mathrm{P}_b(x)$ using $x := -2\ln Q$, respectively. While $\mathrm{P}_{s+b}(x)$ is the probability distribution function of the test statistic for signal plus background experiments, $\mathrm{P}_b(x)$ is the probability distribution function of the test statistic for background-only experiments. If the hypothesis of having measured background only is true, the integral

$$CL_b = \int_{x_0}^{\infty} \mathrm{P}_b(x)\,dx \tag{6.8}$$

is investigated. In the same way, the significance for having signal plus background measured can be tested using,

$$CL_{s+b} = \int_{X_0}^{\infty} \mathrm{P}_{s+b}(x)\,dx \tag{6.9}$$

where, X_o is the value of $-2\ln Q$ from the experiment (real data) or from MC simulation.

The calculation of the CL_b gives a measure in how the experimental data are in coincidence with the background only expectation. If the X_o is smaller than the mean value of $\mathrm{P}_b(x)$, the data contain more than just background. So, the probability of a signal on top of the expected background is larger and the CL_b holds values larger than 0.5. If X_o is larger than the mean value of $\mathrm{P}_b(x)$ the data do not even match with the background expectation and CL_b is less than 0.5 (lack of background). As a summary, CL_b results in values around 0.5, when the data match with background expectation, while CL_b holds larger values for data containing background plus additional signal.

For equation (6.9), the integral is less than 0.5 if an experiment has only measured background. When the measured data exceed the signal plus background expectation, the integral is larger than 0.5. If the measurement is in coincidence with the $-2\ln Q$ MC expectation for signal plus background, it is identical to 0.5 (see figure 6.1).

A discovery is defined as excess in the measured data of more than 5σ assuming a Gaussian character for both $\mathrm{P}_{s+b}(x)$ and $\mathrm{P}_b(x)$:

$$1 - CL_b \leq 5.7 \times 10^{-7} \tag{6.10}$$

The $1 - CL_b$ indicates the overlap of both distributions $\mathrm{P}_{s+b}(x)$ and $\mathrm{P}_b(x)$, so the sensitivity is correlated to the separation of the distributions. If a discovery is not possible, an exclusion limit can be calculated by convention with 95% confidence. Hence, the probability for excluding an existing signal is less than 5%. It can be mathematically described by

$$CL_{s+b} < 0.05 \tag{6.11}$$

In other words, the probability to find signal-like fluctuation of the background is excluded with 95% confidence.

The use of CL_{s+b} has drawbacks. It might result in unphysical effects (Carsten76-78). In order to avoid this, the ratio CL_{s+b} is normalised to CL_b:

$$CL_s = \frac{CL_{s+b}}{CL_b} \tag{6.12}$$

Then 95% exclusion level is given by

$$CL_s < 0.05 \tag{6.13}$$

The error for the different confidence levels (i.e.the σ-deviation) can be extracted from the σ-bands of $\mathrm{P}_{s+b}(x)$ and $\mathrm{P}_b(x)$. A change of the integration limit X_o in the CL_b-integral of $\pm\sigma$ directly results in the upper and lower errors on the confidence level CL. The narrower the distributions of the pseudo-statistics, the smaller the error on the discovery or exclusion limit (Read, 2000).

6.3. Systematic Uncertainties

A group of particle physics experiment involves the search for a new signal or measuring a small signal at the circumstances with significant background. A limit on, or a measurement of, a physical quantity at a given confidence level is usually set by comparing a number of detected events with the expected number of background events in the 'signal' region where the signal events (if exist) should reside. This comparison can made for the observed events and the expected background depends strongly on the systematic uncertainties existing in the measurement. Therefore, systematic uncertainties must be taken into consideration in the limit or confidence belt calculation (Zhu, 2007). In this part, systematic uncertainties will be given in six categories.

6.3.1. Background Uncertainties

This category comprises uncertainties on the background yields. The major contribution comes from uncertainties in the NLO *k*-factor (Sec. 5.2.1) corrections for WZ for the resonance search. Since the MAGRAPH generator used for simulating the WZ process contains explicit production of additional jets at matrix element level, it is expected to give correct kinematic description of the process which includes higher order corrections, and the prediction is only rescaled with a global factor to the total NLO cross section computed with MCFM (Campbell and Ellis, 2010). In order to estimate uncertainties from remaining differences between the spectra predicted by MAGRAPH and true NLO predictions, several kinematic distributions for WZ between MADGRAPH and MCFM are compared. It is found that they are agreement in all cases within 10%. In order to account for these differences, a uncertainty of 10% on the *k*-factor is taken. Uncertainties on the ZZ, $Z\gamma$ and WZ cross sections of 7.5% (Campbell, Ellis and Williams, 2011), 13 % (Chatrchyan, 2011d) and 17% (Chatrchyan, 2011c) are also considered. The results were taken from reference (Brigljevic et al. 2011).

6.3.2. MET resolution and Scale, Electron Energy Scale, Muon Energy Scale

In this category, we combine the uncertainties that affect product of the acceptance, reconstruction, and identification efficiencies of the final state objects, as determined from simulation.

The impact of the E_T^{miss} scale and resolution uncertainties are estimated by varying the relevant parameter and measuring the effects on the yield of signal and background in MC for each mass point under consideration. The reconstruction of the WZ invariant mass also includes E_T^{miss} variation.

The electron momentum scale can be controlled using Z boson decays to electrons. The Z-line shape selecting electrons with E_T > 25 GeV are fitted. It shows differences in scale between data and MC of 0.1% (0.2%) in the ECAL barrel (ECAL endcaps), thus significantly improved with respect to previous 2010 results (Nourbakhsh et al., 2011). The electron momentum scale uncertainty also receives other contributions that come from the ECAL laser corrections and linearity. Overall, the ECAL energy scale is known to 0.6 % in EB and to 1.5 % in EE. We consider a 2% electron momentum scale uncertainty and propagate through the analysis chain (Adiguzel et al., 2011).

The errors on absolute muon momentum scale are measured within 1% in both data and MC on J/ψ and Z resonances studies from 2010 (CMS collaboration, 2010)

All uncertainty results are directly taken from reference (Brigljevic et al., 2011) and given in Table 6.1.

6.3.3. Pile-up Uncertainty

In order to take into account of mismeasurement of pile-up, we consider variations on vertex multiplicity distribution. All simulated events are weighted based on the number of reconstructed vertices to match the distribution for collision events. The distribution reflects the 73.5 mb minimum bias cross section. In order to estimate the pile-up uncertainty on this reweighting process, the poisson mean for the number of vertices in the data distribution is varied by $N_{vtx} \pm 1$ and the difference in yield is calculated in these cases. For each mass point, the largest absolute values of these uncertainties is selected as the estimate of pile-up uncertainty. The pile-up uncertainties are summarized in Table 6.2.

Table 6.1. Summary of systematic uncertainties associated with E_T^{miss} scale, E_T^{miss} resolution, muon momentum scale, and electron scale for each mass point. The values show the maximum expected variation in event yield for sum of MC background samples and for the W′ signal.

	E_T^{miss} Scale		E_T^{miss} Resolution		Muon p_T Scale		Electron Energy scale	
M(W′)	Bckg (%)	Signal (%)	Bckg (%)	Signal (%)	Bckg (%)	Signal (%)	Bckg (%)	Signal (%)
200	0.99	0.01	0.52	1.9	0.45	3.1	1.0	1.9
250	0.24	0.90	0.59	1.3	2.5	1.6	3.1	2.5
300	1.1	0.49	0.72	0.97	2.2	0.51	4.3	1.3
400	1.7	0.43	0.77	0.53	1.9	1.0	4.2	2.2
500	1.8	0.38	0.91	0.36	1.7	0.71	3.6	1.5
600	1.3	0.10	1.4	0.30	3.1	0.55	4.8	1.6
700	2.4	0.15	1.7	0.23	5.3	0.91	4.2	1.7
800	3.9	0.28	1.9	0.20	3.9	0.87	4.3	1.7
900	2.3	0.24	1.9	0.13	3.0	0.72	6.4	0.94
1000	2.7	0.03	2.4	0.12	5.0	0.37	8.7	0.49
1100	1.1	0.16	2.2	0.13	2.6	0.15	6.7	0.51
1200	0.16	0.13	2.6	0.12	2.8	0.34	13	0.54
1300	0.70	0.10	2.9	0.12	4.7	0.12	5.7	0.38
1400	4.7	0.10	3.7	0.14	4.2	0.46	8.2	0.85
1500	0.01	0.02	4.2	0.19	0.72	0.37	11	1.3

6.3.4. Theoretical Uncertainties

Due to the choice of the parton distribution functions (PDFs), we include uncertainties on the theoretical side. In this analysis, the CTEQ6 (Pumplin et al., 2002) was used as PDF, and the uncertainties were determined according to the method described in Ref (Campbell, Huston and Stirling, 2007). The uncertainty for the WZ background at the high masses is much larger than the others. The higher mass regions correspond to higher values of the parton center of mass energy ($\hat{s}$). The regions are sensitive to momentum fractions and PDF uncertainty is larger. Particularly, the PDF uncertainties for the $q\bar{q}$ and gg processes become significantly larger for values of $\hat{s}/s$ (or large WZ mass). This effect leads to significantly larger errors on the WZ background simulation for higher-mass search windows. The PDF uncertainties are summarized in Table 6.2.

Table 6.2. Pile-up and PDF uncertainties for the various W′ masses. The values show the maximum expected variation in event yield for MC background samples and for the W′ signal. For PDF uncertainties, the values for the signal were available only down to 300 GeV, so they are assumed to be the same for two lowest mass points.

	Pile up		PDF	
M(W′)	Bckg (%)	Signal (%)	WZ Bckg (%)	Signal (%)
200	1.7	0.31	3.2	2.370
250	2.2	0.58	3.4	2.370
300	1.9	2.0	3.3	2.370
400	2.2	0.71	3.2	2.764
500	2.6	2.3	3.6	3.181
600	1.7	1.6	4.0	3.704
700	3.0	0.82	4.7	4.198
800	4.0	1.4	4.8	4.624
900	3.6	1.6	6.3	5.135
1000	0.36	1.4	8.9	5.695
1100	0.83	1.1	7.8	6.088
1200	1.3	1.2	12.0	6.516
1300	1.3	1.9	28.0	7.349
1400	2.3	1.4	7.8	7.760
1500	0.02	2.6	0.0	8.471

6.3.5. Electron and Muon Reconstruction, identification

This group includes the systematic uncertainties affecting the data vs. simulation correction factors for the efficiencies of the trigger, reconstruction and identification requirements. The lepton efficiencies are determined using a tag and probe method (Daskalakis et al., 2007) in the same way for simulation and collision data and the uncertainty on the ratio of the efficiencies is taken as the systematic uncertainty as described in Sec. 5.5. In this analysis, results cover the lepton p_T and pseudorapidity ranges. The reconstruction efficiency for electrons is also a necessary measurement which must be considered for matching of ECAL superclusters to tracks. So the values are taken from a previous analysis aimed specifically at measuring electron reconstruction efficiencies (Baffioni et al., 2010). The results are given in Table 6.3.

6.3.6. Luminosity

The uncertainty on the luminosity measurement is estimated at %2.2 (Brigljevic et al., 2011).

6.3.7. Systematic Uncertainties Summary

The systematic uncertainties contribute to the limit results. The systematics are added to the statistic uncertainty in quad and that value is used for the background uncertainty. The systematic uncertainties summary is given in Table 6.3. These values were directly taken from reference (Brigljevic et al., 2011).

6.4. Limit Results

The upper limit on the cross section for the production of a boson W' is calculated as a function of the mass, using the CL95 implementation of CL_s statistics in the RooStats (Moneta et al., 2010) package and it is later on translated into a lower limit in the mass. Where the CL_s, statistic falls below %5. The exclusion limits on the production cross section are calculated by comparing the numbers of observed events with the numbers of expected signal and background events from the MC simulation. A scale factor is applied to each event based on the data/MC ratios obtained for the electron and muon efficiencies. Then the events are counted in the MC sample. The value of the scale factor is chosen based on the decay channels of the reconstructed W and Z. Systematic uncertainties are incorporated in the limit setting procedure by treating them as nuisance parameters. They are the measured luminosity and the product of detector acceptance and efficiency. Each of these is modeled with a Gaussian distribution using the measured value as the mean and the systematic uncertainty as the width.

Table 6.3. Summary of the Systematic Uncertainties. For the first two groups of uncertainties, signal impact and background impact show the maximum expected variation event yields for MC W' samples and for combined background samples, respectively. Only those background which contributed to the final yield are listed. For the third group (the efficiencies), the yield columns correspond the maximum expected variation in the ratio of data to MC based on tag and probe studies.

Sys. Uncertainty	Signal Impact (%)	Background Impact (%)
E_T^{miss} resolution & scale	see Table 6.1	
Muon p_T scale	see Table 6.1	
Electron energy scale	see Table 6.1	
Pile-up	see Table 6.2	
PDF	see Table 6.2	
Electron trigger efficiency	0.6	0.6
Electron reconstruction efficiency	0.9	0.6
Electron ID and isolation efficiencies	1.0	0.8
Muon trigger efficiency	0.5	0.5
Muon reconstruction efficiency	0.4	0.5
Muon ID and isolation efficiencies	0.7	0.7
$Z\gamma$		13
ZZ		7.5
WZ cross section		17
WZ NLO k-factors		10
Luminosity	2.2	2.2

The numbers of expected and observed events, including all the background sources discussed are detailed in Table 6.4 along with the search window and the expected and observed limit. The expected limit is obtained as the average limit of a large number of background-only pseudo-experiments. In other words, it is taken as the median value derived from 1000 MC pseudo-experiments where, all the parameters (efficiencies, number of estimated background events, luminosity) take random values with their uncertainties. The expected limit (with the one and two sigma bands showing its variation), the observed limit and the theoretical cross-section for the production of a W' boson decaying into tri-lepton plus neutrino as a function of $M_{W'}$ are given in Figure 6.2. The theoretical cross sections are calculated using by PYTHIA event generator. Its values are shown in Appendix F. The intersection between the observed limit and the theoretical cross section determines the lower limit on W' mass. Then, the existence of a W' boson with SM couplings with a mass below 800 GeV/c^2 can be excluded at a %95-confidence level.

The calculation of the limit was repeated without including the systematic uncertainty. The limit results were unaffected, because the expected background is a fraction of an event in the search windows for the W' signals close to mass where the limit is set, and no events are observed.

Table 6.4. Search windows for each W′ mass point giving the number of expected background events from MC, number of observed events, number of expected signal events from MC, signal efficiency, and the expected and observed exclusion limits on the $\sigma \times \mathrm{BR}(W' \rightarrow 3\ell\nu)$ at 95% C.L.

Mass point	Window (GeV)	N_{BkgMC}	N_{DATA}	N_{Sig}	ε_{Sig} (%)	Exp.Limit (pb)	Obs.Limit (pb)
W′ 200	190-210	29.49 ± 7.75	25 ± 5	288.7 ± 9.6	3.3 ± 0.11	0.098	0.0884
W′ 250	230-270	17.48 ± 4.71	25 ± 5	217.6 ± 8.7	2.9 ± 0.11	0.094	0.1383
W′ 300	280-320	12.84 ± 3.49	8 ± 2.82	212 ± 6.5	5 ± 0.15	0.037	0.0295
W′ 400	360-440	7.45 ± 2.95	2 ± 1.41	118.4 ± 2.77	8.7 ± 0.20	0.0119	0.0123
W′ 500	450-550	4.62 ± 1.31	7 ± 2.64	65.6 ± 1.27	12 ± 0.24	0.0117	0.0155
W′ 600	540-660	2.0 ± 0.53	1 ± 1	34.9 ± 0.62	14 ± 0.27	0.0068	0.0055
W′ 700	620-780	1.03 ± 0.33	0 ± 0	19.1 ± 0.32	16 ± 0.28	0.0044	0.0038
W′ 800	710-890	0.6 ± 0.2	0 ± 0	11.3 ± 0.18	17 ± 0.29	0.0041	0.0041
W′ 900	760-1040	0.605 ± 0.207	0 ± 0	7.5 ± 0.11	20 ± 0.32	0.0035	0.0034
W′ 1000	820-1180	0.41 ± 0.15	0 ± 0	4.7 ± 0.06	21 ± 0.33	0.0032	0.0033
W′ 1100	890-1310	0.33 ± 0.12	0 ± 0	2.84 ± 0.04	21 ± 0.33	0.0033	0.0033
W′ 1200	940-1460	0.25 ± 0.11	0 ± 0	1.61 ± 0.02	19 ± 0.31	0.0036	0.0036
W′ 1300	1020-1580	0.17 ± 0.08	0 ± 0	0.89 ± 0.01	16.9 ± 0.29	0.0041	0.0040
W′ 1400	1110-1690	0.09 ± 0.04	0 ± 0	0.4 ± 0.008	11.8 ± 0.24	0.0057	0.0058
W′ 1500	1200-1800	0.06 ± 0,03	0 ± 0	0.22 ± 0.004	9.9 ± 0.22	0.0067	0.0069

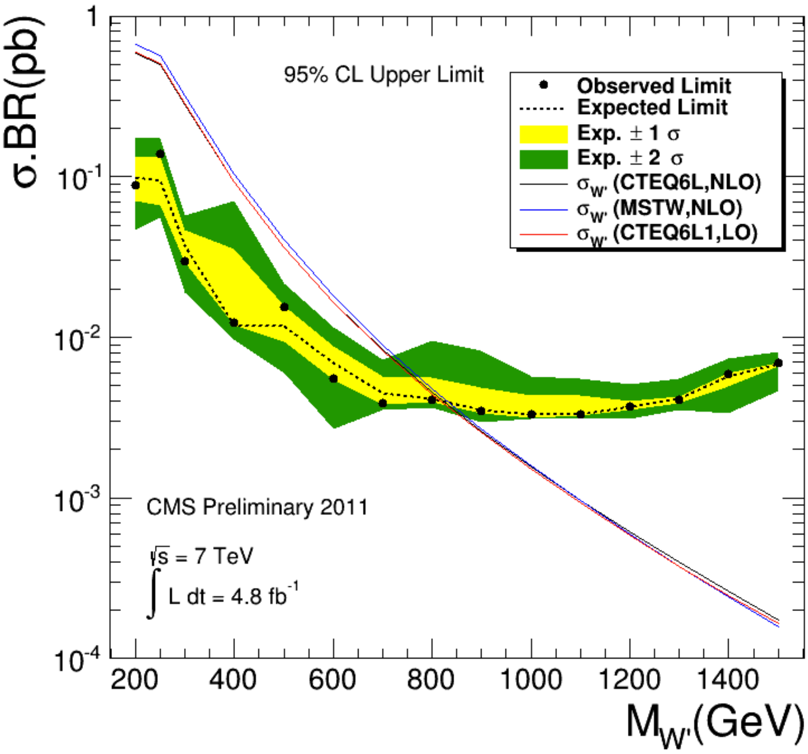

Figure 6.2. Expected and observed 95 %C.L upper limits on cross section as function of resonance mass for W' along with the combined statistical and systematic uncertainties depicted with light yellow (1σ) and dark green (2σ) bands. The theory curves for W' are also provided.

7. LASER STABILITY OF HF AND HB CALORIMETER

7.1. Introduction

A hadronic calorimeter (HCAL) measures the energy and the position of particles from the hadronizing quarks and gluons in the collisions as discussed in Sec. 3.3.2.2. The HCAL is a sampling calorimeter that contains brass plates interleaved with plastic scintillators (Bayatian, 2006). The scintillation light is collected by embedded plastic fibers. Then it is routed to photodetectors, which measure the intensity of the light. A laser calibration system is used to validate the measurement of this light. It measures the linearity of the electronics. It is also used to measure time-of-flight differences across the detector. It monitors the stability of the energy measurements and control optical system (fibers, splices, optical connectors etc.) and stability and linearity of response for each channel (photodetectors, preamplifiers, ADC, HV supply), timing of each channel.

In this part, the mechanical set up of the laser calibration system will be reviewed; then how the system distributes the laser light into the HCAL and how the system calibrates the HCAL will be described. Finally, the stability of its readouts will be evaluated and the response of Hadronic Forward (HF) and Hadronic Barrel (HB) calorimeter using global laser and local laser runs in 2010 will be analyzed.

7.2. Laser Calibration System

The HCAL laser calibration system examines the calorimeter's performance. This is provided in part by exciting the scintillators using an ultraviolet (UV) nitrogen laser with a wavelength of 337 nm. The light is distributed to various HCAL readouts using a collection of fiber optic cables by the laser calibration system. A selection device directs the light into multiple regions of the detector. The individual elements of the detector cannot be singly addressed given the substantial amount of channels involved. The laser pulse has a known time structure and filters vary its intensity. These two properties combine to provide a versatile calibration and monitoring system.

7.2.1. Laser Setup

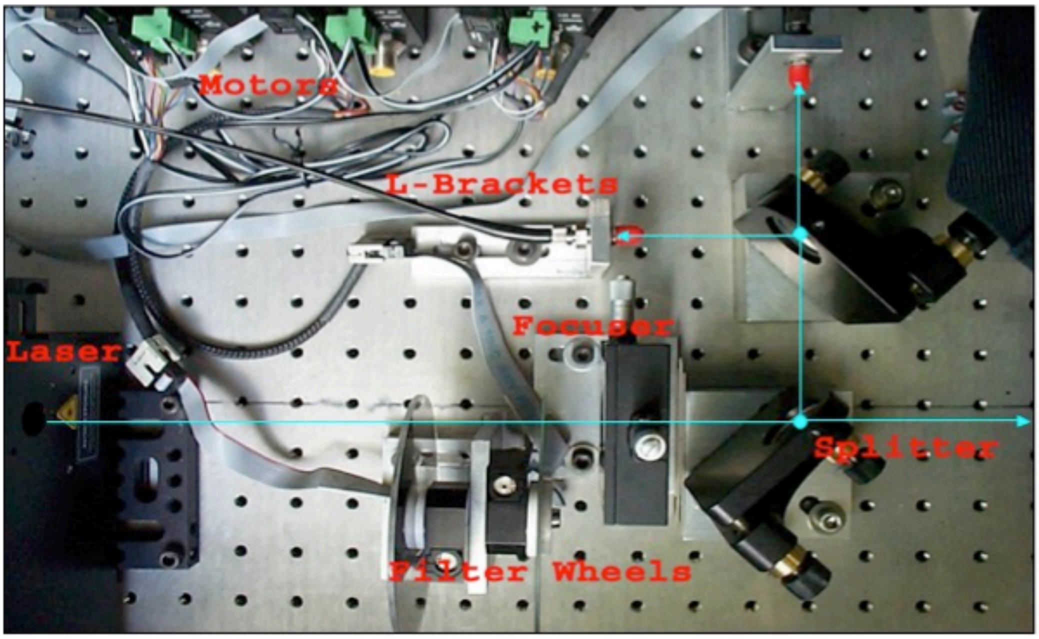

Figure 7.1. Top view of schematic of laser system and associated components. The blue line represents the laser beam.

The laser system is shown in Figure 7.1. It is along with associated optical components. The placement of all optical components must be accurate to within 10 μm in order to maximize the amount of light transmitted. As small vibrations or tensions in the table are detrimental, the laser calibration system is constructed on an optical breadboard that dampens vibrations and prevents warping under heavy loads.

The laser emits 4 ns pulses of 260 μJ where the pulse-to-pulse energy variations are specified to be 4% within the beam spot size that is originally 8 x 8 mm^2 (Spectra-Physics, 2007). In order to control the intensity of the pulse, the laser beam is incident upon two continuously varying neutral density (ND) filter wheels, which contain an ND coating. It attenuates the light passing through it. The attenuation wouldn't be uniform across the beam-spot because of the large beam-spot size. Since the beam-spot shifts slightly from pulse to pulse, this becomes more significant. Therefore, two anti-correlated filter wheels –facing in opposite directions- are utilized. A rotary stepping motor controls each filter wheel. Each wheel is specified to be linear (within 5%) in optical density as the wheel is changed by equal angles. The optical density is given as $\log_{10}\left[S/S_0\right]$, where S (S_0) is the optical density at an arbitrary (reference) position. The level of attenuation (i.e. the amount of ND coating) increases with rotational angle.

Afterwards, the beam passes through a focusing lens with a focal length of 20 cm. In order to get better match the outgoing quartz fibers (200 μm) that finally route the light to the HCAL, this focuses the beam-spot down to several hundred micrometers in diameter. Then the beam incident upon the first of two beam samplers, which are held by a mirror gimbal. In order to achieve various laser beams with diverse intensities, two samplers are used. Each of them picks off 5% of the incoming pulse energy (Thor Labs). Thus the laser light is sampled regardless of attenuation setting. The two samplers are held by the mirror gimbals, which allow the angle of incidence to be controlled. Then the beam is reflected, transmitted and split to three destinations, which are the fiber harness and two pin diodes. The fiber harness is controlled with a linear stepping motor and can be moved. Two L-brackets hold quartz fiber optic cables, which route the light to pin diodes. The pin diodes allow us to measure the intensity of the light – independently from the HCAL detector – via an oscilloscope or data acquisition system (DAQ). Each pin diode's signal is electrically split in to three channels, where each successive channel is electrically attenuated by approximately 64x. The signal is then readout by a Charge Analog-to-Digital-Converter (QADC). Therefore, if a QADC channel is saturated, we simply readout the next channel and correct for the attenuation.

7.3. Stability of Response of HF and HB Calorimeters

During 2010, the stability of response of HF and HB calorimeters had been studied. Since it was a long period, some of the results will be introduced in here.

Over 400 global runs (from collisions), which included laser calibration sequence (abort gap events) were analyzed between July-September, 2010. In this period, the run '141791' was taken as first and the run '146728' as last on 27th of October 2010. No laser runs were taken beyond that date.

In this analysis, root files created by online Detector Diagnostic package were used. Firstly average laser amplitude was plotted in linear ADC count for each channel. Then run-to-run relative RMS (root mean square) of laser amplitude was checked. Average and RMS are calculated over all events for each run.

In the first part of this analysis, HF and HB laser energy distributions were checked for a specific run (r146728). This distribution is shown in Figure 7.2 (a) for HF and in Figure 7.3 (a) for HB. In these distributions, each entry corresponds to an average of response of a single channel to laser. Average is done over all events. The eta-phi distribution of average response (linear ADC) to laser is given in Figure 7.2 (b) for single run (r146728) for HF and in Figure 7.3 (b) for HB. In HB no signal is reaching HPD for 2 RBXes and 1 RBX has very low signal.

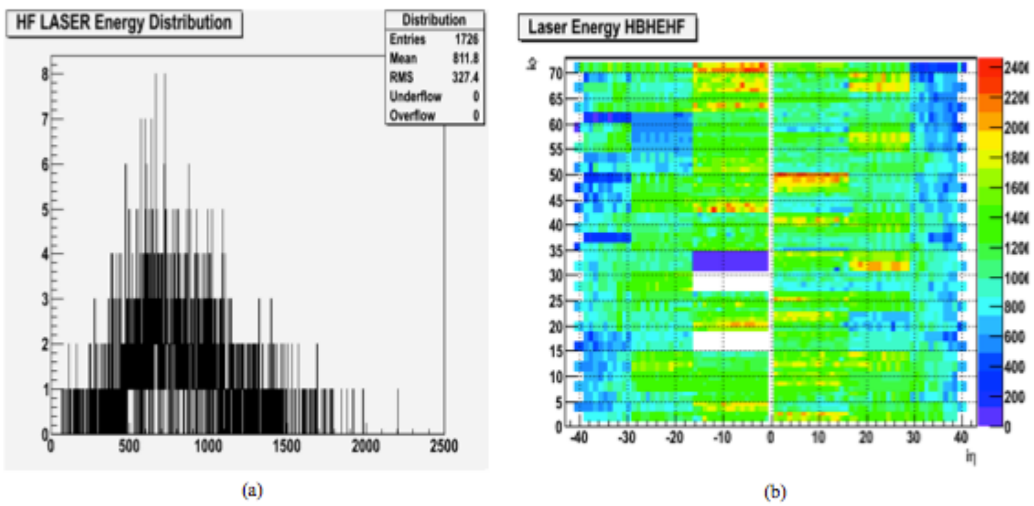

Figure 7.2. (a) HF laser energy distribution for r146728 **(**b) Eta-phi distribution of average response to laser for r146728. The response is given in linear ADC.

Then normalized distribution was calculated via RMS of energy divided by average energy. The distribution of 'laser RMS of energy/average energy' is shown in Figure 7.4 (a) for HF and 'laser RMS of energy/average energy' versus average energy for HF in Figure 7.4 (b). Typically event-to-event RMS of energy distribution is 13 % and channels with low value of energy response have larger RMS for HF.

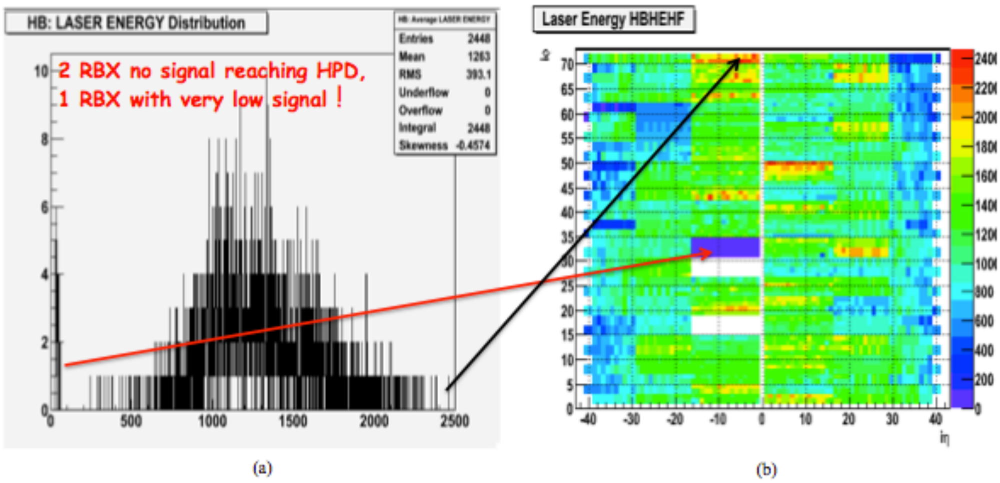

Figure 7.3. (a) HB laser energy distribution for r146728 (b) Eta-phi distribution of average response to laser for r146728. The response is given in linear ADC.

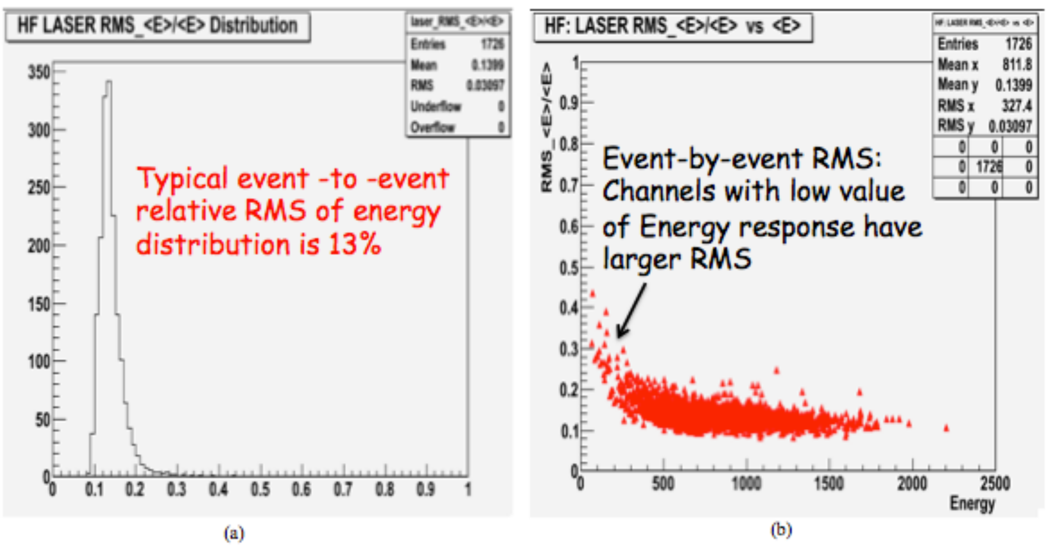

Figure 7.4. (a). The distribution of 'laser RMS of energy divided by average energy' (b). 'Laser RMS of energy/average energy' versus average energy for HF.

In the second part of this analysis, laser average signal was calculated, and then it was plotted versus run number. Those plots are shown in Figure 7.5 and 7.6 for HF and HB, respectively. The Figure 7.5 (a) shows laser average signal versus run number for all HF, (b) for HFM, (d) for HFP. The Figure 7.5 (c) shows laser average energy ratio for HFM/HFP. The Figure 7.6 (a) shows laser average signal versus run number for all HB, (b) for HBM, (d) for HBP. The Figure 7.6 (c) shows the ratio for HBM/HBP. According to those plots, the laser intensity changes as a function of run. Run-to-run fluctuations are at the level of ~4% (3.3%) for HF (HB).

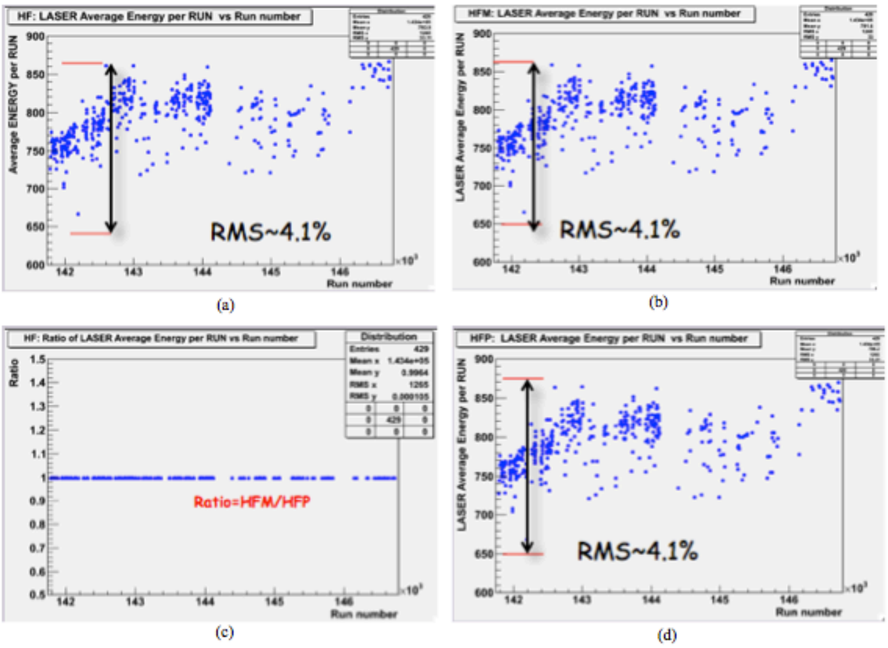

Figure 7.5. The laser average signal versus run number. (a) For all HF (b) for HFM (c) Laser average energy ratio (HFM/HFP) (d) for HFP.

In the third part of this analysis, it was decided to apply normalization, in order to eliminate common shifts in specific channels. So laser energy was corrected by dividing to laser average signal for laser fluctuations. Then run-to-run mean energy response and relative RMS of mean energy response were calculated for before and after laser intensity correction. The Figure 7.7 (a) and 7.8 (a) shows run-to-run relative RMS of mean energy response versus mean energy response before laser intensity correction for HF and HB, respectively. The Figure 7.7 (b) and 7.8 (b) shows the same distribution after laser intensity correction for HF and HB, respectively.

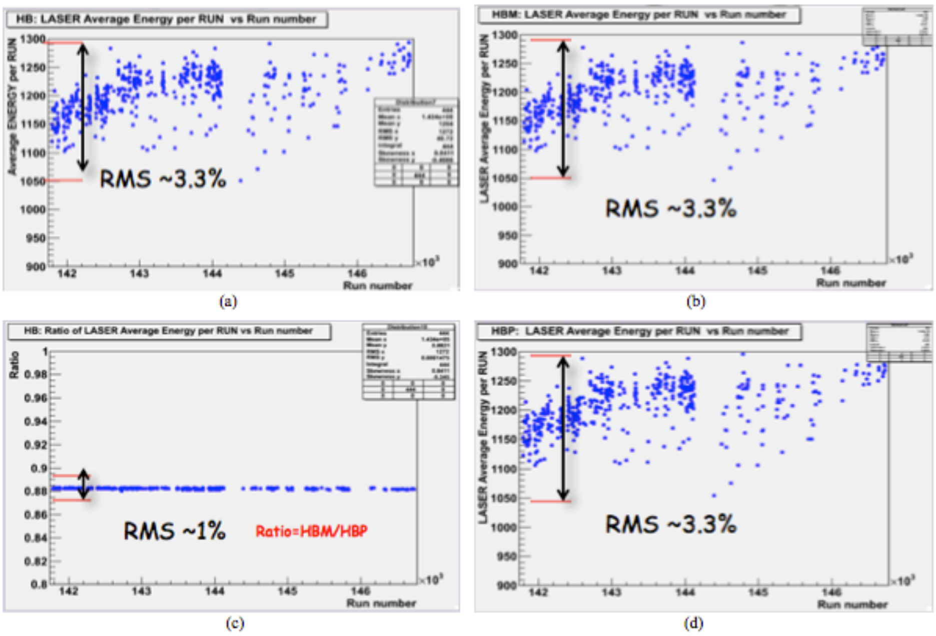

Figure 7.6. The laser average signal versus run number. (a) For all HB (b) for HBM (c) Laser average energy ratio (HBM/HBP) (d) for HBP.

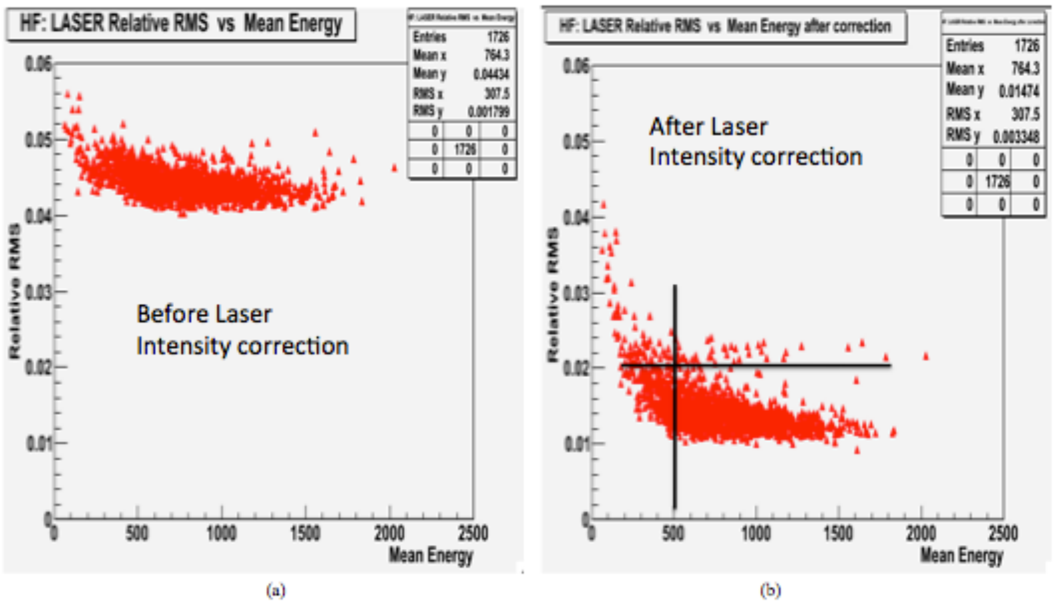

Figure 7.7. Run-to-run relative RMS of mean energy response versus mean energy response before (a) and after laser intensity correction (b) for HF.

For a good channel (ieta=38, phi=29, depth=2), HF laser signal after correction versus run number is shown in Figure 7.9. For this channel relative RMS is ~ 1.1% and same distribution is obtained for some channels. It is shown in Figure 7.10. It was realized that some of them are problematic channels because of two runs that have only 250 events. The channels list was summarized if they have run-to-run relative RMS bigger than %2.2 of Mean Energy Response and Mean Energy bigger than 500 ADC. These channels are given in Table 7.1. For HB, it is clarified that if the channels have run-to-run relative RMS bigger than 1.5%. These channels are given in Table 7.2

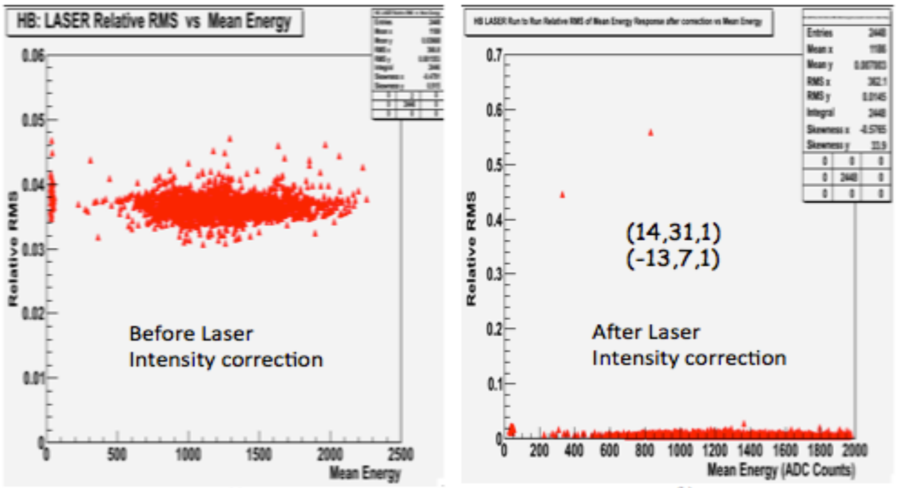

(a) (b)

Figure 7.8. Run-to-run relative RMS of mean energy response versus mean energy response before (a) and after laser intensity correction (b) for HB.

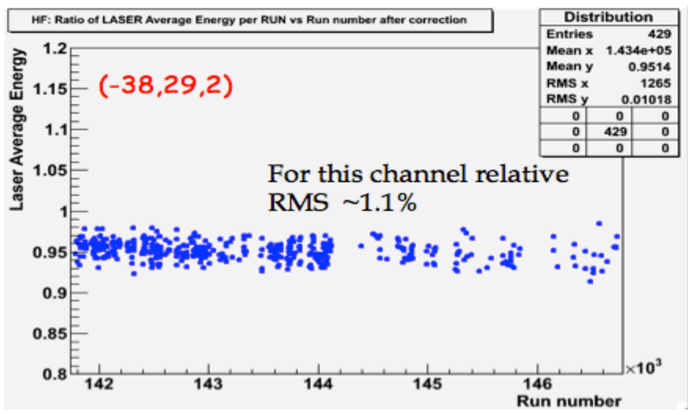

Figure 7.9. HF laser signal after correction versus run number for a good channel (ieta=38, phi=29, depth=2).

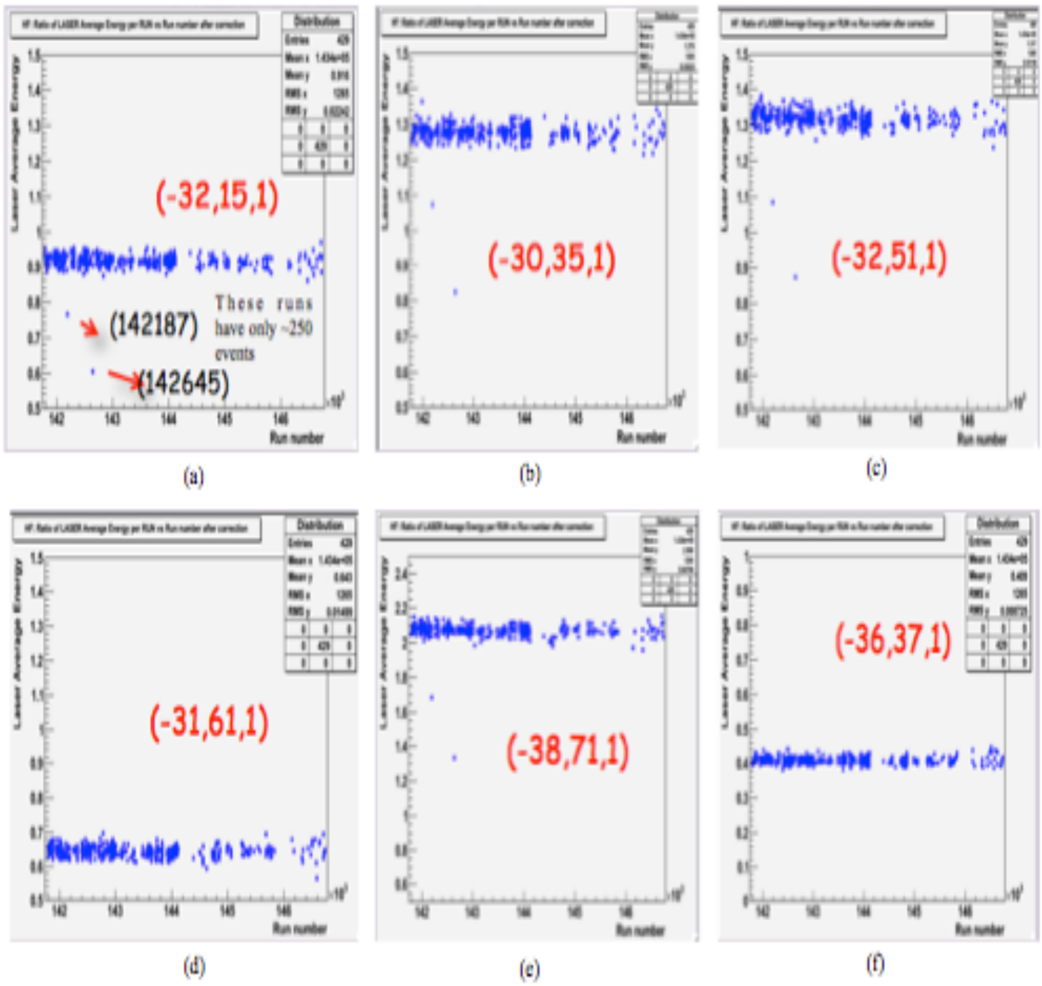

Figure 7.10. HF laser signal after correction versus run number for different channels.

Table 7.1. The channels list if they have run-to-run relative RMS bigger than %2.2 of Mean energy Response and Mean Energy bigger than 500 ADC for HF.

Channel (Ieta, Iphi, Depth)	Value (%)
-32, 15, 1	2.4
-30, 35, 1	2.3
-36, 37, 1	2.3
-32, 51, 1	2.39
-31, 61, 1	2.3
-38, 71, 1	2.31

Table 7.2. The channels list if they have run-to-run relative RMS bigger than %1 for HB.

Channel (Ieta, Iphi, Depth)	Value (%)
13, 1, 1	2.1
-15, 7, 1	2.7
-13, 7, 1	5.5
-14, 31, 1	4.45
-16, 35, 1	1.54
-2, 39, 1	1.51
3, 42, 1	1.51
7, 42, 1	1.75
15, 42, 2	1.79
16, 42, 1	1.96
-16, 43, 1	1.74
15, 42, 2	1.77
-13, 43, 1	1.60
-8, 43,1	1.79
-1,43,1	1.52
-6, 68, 1	1.51

7.4. Results

Stability of responses of HF and HB had been studied using global laser runs between July–August-September 2010. Laser data provides a good tool to monitor stability of energy response of HF and HB.

Amplitude of laser response varies channel by channel from 100 ADC/ch to 2200 ADC/ch for HF and it is varies from 200 ADC/ch to 2000 ADC/ch for HB. However HBM phi: 31-32-33-34 have lower laser signal and 2 RBXes no signal reaching HPDs. Since end of September, no laser data has been taken (problem with Laser Trigger board). Channels with low laser intensity have significantly larger event-by-event RMS of response, above 30%, while for high intensity channels RMS is around 10% for HF and 6% for HB. Laser intensity changes as a function of run. Run-to-run fluctuations are at the level of ~4% (3.3%) for HF (HB). Run-to-run RMS of mean laser response of individual channels is checked after correction for overall laser intensity for HF and HB. Most of channels have relative signal run-to-run RMS < 1% for HF and for HB < 1.5%. Channel HB (-13,7,1) shows large instability in response to laser with RMS > 5.5%. Channel HB (14,31,1) has a stable response to laser.

8. CONCLUSION

In summary, this thesis consists of two parts: One of them is the measurement of WZ mass spectrum and the search for new particles. The other is HCAL laser stability analysis.

In first part, the WZ mass spectrum is measured. Then it is compared with the MC prediction. Later, the measured WZ mass spectrum is searched for resonance signals. If there is no evidence for WZ resonances, model independent cross section upper limit is calculated and compared with the cross section prediction of SSM model. Then the excluded mass limits for the WZ resonance model are set. As a conclusion, a search for new exotic particles decaying to the WZ final state with electrons and muons is performed using 4.8 fb^{-1} of data collected by CMS experiment at $\sqrt{s} = 7$ TeV . No significant excess is found in the mass distribution of the WZ candidates compared to the background expectation from SM processes. The results are interpreted in the context of different theoretical models and lower bounds are set at the 95% C.L. on the masses of hypothetical particles decaying to the WZ tri-leptonic final state. Assuming the SSM, W' bosons with masses below 800 GeV are excluded.

In the second part, the stability of responses of HF and HB have been studied using global laser runs between July-August-September 2010. Laser data provide a good tool to monitor stability of energy response of HF and HB. The results show that amplitude of laser response varies channel by channel from 100 ADC/ch to 2200 ADC/ch (200 ADC/ch to 2000 ADC/ch) for HF (HB). However HBM phi: 31-32-33-34 have lower laser signals and in 2 RBXes no signal is reaching HPDs. Channels with low laser intensity have significantly larger event-by-event RMS of response, above 30%, while for high intensity channels RMS is around 10% for HF and 6% for HB. Laser intensity changes as a function of the run. Run-to-run fluctuations are at the level of ~4% (3.3%) for HF (HB). Most of the channels have relative signal run-to-run RMS < 1% for HF and for HB < 1.5%. Channel HB (-13,7,1) shows large instability in response to laser with RMS > 5.5%. Channel HB (14,31,1) has stable response to laser.

REFERENCES

ABERS, E.S., and LEE, B.W., 1973, "Gauge Theories", Phys. Rep. 9, 1-141.

ABULENCIA, A., et al., 2007, "Observation of WZ Production", CDF Collaboration, Phys. Rev. Lett. 98, 161801 and arXiv:hep-ex/0702027v1.

ACCOMANDO, E., and BECCIOLINI, D., 2012, "Interference effects in heavy W' - boson searches at the LHC", arxiv:1110.0713v2.

ADAM, N., et al., 2009, "Generic Tag and Probe Tool for Measuring Efficiency at CMS with Early Data", CMS AN-2009/111.

_________, 2010, "Measurements of Inclusive W and Z Cross Sections in pp Collisions at $\sqrt{s}$ = 7 TeV ", CMS AN-2010/116.

ADAM, W., et al., 2009, "Electron Reconstruction in CMS", CMS AN-2009/164.

ADIGUZEL, A., et al., 2011, "Measurement of the WZ cross section at the CMS Experiment", CMS AN-2011/259.

AITCHISON, I. J. R., and HEY, A. J. G., 1960. "Gauge Theories in Particle Physics: A Practical Introduction", A. Hilger, Bristol.

ALTARELLI, G., MELE B., and RUIZ-ALTABA M., 1989, "Searching for New Heavy Vector Bosons in $p\bar{p}$ Colliders", Z.Phys. C45 (1989) 109.

ALWALL, J., et al., 2007, "MadGraph/MadEvent v4: The New Web Generation", JHEP 09 (2007) 028 and arXiv:0706.2334.

ANDERSEN, J.R., et al., 2011, "Discovering Technicolor", Eur.Phys.J.Plus 126 (2011) 81 and arXiv: hep-ph/1104.1255v2.

_________, 1989, " W' and Z' Limits for Minimal Walking Technicolor", Phys.Rev. D85 (2012) 055017 and arXiv: hep-ph /1105.1433.

AMBROSIO, M., et al., 2001, "Matter Effects in Upward Going Muons and Sterile Neutrino Oscillations", MACRO Collaboration, Phys.Lett.B517:59- 66.

ARNISON, G., et al., 1983a, "Experimental Observation of Isolated Large Transverse Energy Electrons with Associated Missing Energy at $\sqrt{s}$=540", UA1 Collaboration, Phys. Lett., B122 103-116.

_________,1983b, “Experimental Observation of Lepton Pairs of Invariant Mass Around 95-GeV/c^2 at the CERN SPS Collider”, UA1 Collaboration, Phys. Lett., B126 398-410.

BABU, K.S., and KOLDA, C., 2005, “The W′ Searches”, http://pdg.lbl.gov/2006/reviews/wprime_s056210.pdf.

BAFFIONI, S., et al., “Electron Efficiency Measurement from 7 TeV Data”, CMS AN-2010/471.

BAGNAIA, P., et al., 1983, “Evidence for Z0 ---> e+ e- at the CERN anti-p p Collider”, UA2 Collaboration, Phys.Lett. B129 130-140.

BAIATIAN, G., et al., 2006, “Design, Performance, and Calibration of CMS Hadron-Barrel Calorimeter Wedges”, CMS-NOTE/2006-138.

BANARJEE, S., 2005, “Simulation Geometry for the CMS HCAL”, CMS-NOTE/2005-016.

BARNER, M., et al., 1983, “Observation of Single Isolated Electron with High Transverse Momentum in Events with Missing Transverse Energy at the Cern Anti-pp Collider”, UA2 Collaboration, Phys. Lett., B122 476-485.

BAYATIAN, G., et al., 1994, CMS Collaboration Technical Proposal, CERN/LHCC 94–38, LHCC/P1.

_________, 1997, CMS Electromagnetic Calorimeter Project Technical Design Report, CMS TDR 4, CERN/LHCC 97–33.

_________, 2000, CMS TriDAS Project Technical Design Report Volume I: The Trigger Systems, CMS TDR 6.1, CERN/LHCC 2000–38.

_________, 2002, CMS TriDAS Project Technical Design Report Volume II: Data Acquisition and High-Level-Trigger, CMS TDR 6.2, CERN/LHCC 2002-026.

_________, 2006, CMS Physics Tehcnical Design Report, Volume I: Detector Performance and Software, CMS TDR 8.1, CERN/LHCC 2006-001.

Beam Samplers – Beam Pick-Offs. Thor Labs Catalog. Thor Labs, Inc.

BLAZEY, G.C., 2000, “Run II Jet Physics: Proceedings of the Run II QCD and Weak Boson Physics Workshop”, arXiv:hep-ex/0005012v2.

BRIGLJEVIC, V. et al., 2011, "Search for exotic WZ resonances at CMS", CMS AN-2011/333.

BRUNING, O., et al., 2004, LHC Design Report. Vol. I: The LHC Main Ring, 10.5170/CERN-2004-003-V-1.

CACCIARI, M., and SALAM, G.P., 2008, "Pileup Subtraction Using Jet Areas", Phys.Lett. B 659 (2008) 119-126 and arXiv-hep-ph:0707.1378v1.

CACCIARI, M., SALAM, G.P., and SOYEZ, G., 2008a, "The Anti-kt Jet Clustering Algorithm", arXiv-hep-ph:0802.1189v2.

________, 2008b, "The Catchment Area of Jets", JHEP 04 (2008) 005 and arXiv-hep-ph:0802.1188v2.

CAMPBELL, J.M., HUSTON, J., and STIRLING W., 2007, "Hard Interactions of Quarks and Gluons: A Primer for LHC Physics", Rept.Prog.Phys.70:89 and arXiv:hep-ph/0611148v1.

CAMPBELL, J.M., and ELLIS, R.K., 2010, "MCFM for the Tevatron and the LHC", Nucl.Phys.Proc.Suppl.205-206:10-15 and arXiv-hep-ph:1007.3492v1.

CAMPBELL, J.M., ELLIS, R.K., and WILLIAMS, C., 2011, "Vector boson pair production at the LHC", JHEP 07 (2011) 018 and arXiv-hep-ph: 1105.0020v1.

CATANI, S., et al., 1993, "Longitudinally Invariant K_t Clustering Algorithms for Hadron Hadron Collisions", Nucl.Phys. B, 406:187–224.

CHANOWITZ, M. S., 1988, "Electroweak Symmetry Breaking", Ann. Rev. Nucl. Part. Sci. 1988.38: 323-420.

CHATRCHYAN, S., et al., 2008a, The CERN Large Hadron Collider: Accelerator and Experiments Volume2, The CMS Collabration JINST 3 S08004.

_________, 2008b, "Measuring Electron Efficiencies at CMS with Early Data", The CMS Collaboration CMS-PAS-EGM-07-001.

_________, 2010a, "Performance of Muon Identification in pp Collisions at sqrt(s) = 7 TeV", The CMS Collaboration CMS-PAS-MUO-10-002.

_________, 2010b, "Measurement of Momentum Scale and Resolution of the CMS Detector using Low-mass Resonances and Cosmic Ray Muons", The CMS Collaboration CMS-PAS-TRK-10-004.

_________, 2010c, “Electron reconstruction and identification at √s = 7”, The CMS Collaboration CMS PAS EGM-10-004.

_________, 2011a, “Search for W' in the leptonic channels in pp Collisions at sqrt(s) = 7 TeV”, CMS-PAS-EXO-11-024 and arXiv:hep-ex/1204.4764v2.

_________, 2011b, Technical proposal for the upgrade of the CMS detector through 2020, CERN-LHCC-2011-006.

_________, 2011c, “Measurement of the WW, WZ, and ZZ cross sections at CMS”, CMS-PAS-EWK-11-010.

_________, 2011d, “Measurement of the W-gamma and Z-gamma Ptoduction in pp Collisions at sqrt(s) = 7TeV”, Phys. Lett. B701, 535-555 (2011) and arXiv-hep-ex:1105.2758v2.

_________, 2012, “Search for a W' or Techni-ρ Decaying to WZ in pp Collisions at √s = 7 TeV”, Phys. Rev. Lett. 109, 141801 and CMS-PAS-EXO-11-041.

CHEN, M.C., and DOBRESCU, B.A., 2009, “ W′ Boson Searches”, http://pdg.lbl.gov/2009/reviews/rpp2009-rev-wprime-searches.pdf.

CHOU, J.P., et al., 2010, “Anomalous HB/HE Noise at Startup: Characteristics and Rejection Algorithms”, CMS IN-2010/006.

DASKALAKIS, G., et al., 2007, “Measuring Electron Efficiencies at CMS With Early Data”, CMS AN-2007/019.

DOKSHITZER, Y.L., et al., 1997, “Better jet clustering algorithms”, JHEP 08 (1997) 001 and arXiv:hepph/9707323v2.

ENGLERT, F., and BROUT, R., 1964, “Broken Symmetry and the Mass of Gauge Vector Mesons”, Phys. Rev. Lett. 13, 321.

FRIXIONE, S., et al., 2007, “Matching NLO QCD Computations with Parton Shower Simulations: the POWHEG Method”, JHEP 11 (2007) 070 and arXiv:0709.2092.

FUKUDA, S., et al., 2000, “Tau Neutrinos Favored over Sterile Neutrinos in Atmospheric Muon Neutrino Oscillations”, Super-Kamiokande Collaboration, Phys.Rev.Lett. 85, 3999.

GLASHOW, S.L., 1961, “Partial Symmetries of weak Interactions”, Nucl. Phys. 22.579-588.

GLASHOW, S.L., ILIOPOULOS, J., and MAIANI, L., 1970, "Weak Interactions with Lepton-Hadron Symmetry", Phys. Rev. D, 2(7):1285–1292.

GOLDSTONE, 1961, "Fields Theory with Superconductor Solution", N. Cimento, CERN Geneva, Volume 19, pp 154-164.

GROSS, E., and READ, A.L., 2000, "Prospects for the Standard Model Higgs Boson Search in the LEP 2000 Run", CERN-EP-2000-034.

GURALNIK, G. S., HAGEN, C. R., and KIBBLE T. W. B., 1964, "Global Conservation Laws and Massless Particles", Phys. Rev. Lett. 13, 585.

HAN, T., LOGAN, H.E., MCELRATH, B., and WANG, L.T., 2003, "Phenomenology of the Little Higgs Model", Phys. Rev. D67 (2003), p. 095004.

HEISENBERG W., 1932, "On the Structure of Atomic Nuclei", Z. Phys. 77, 1.

HIGGS, P. W., 1964a, "Broken Symmetries, Massless Particles and Gauge Fields", Phys. Rev. Lett. 12, 132-133.

_________, 1964b, "Broken Symmetries and the Masses of Gauge Bosons", Phys. Rev. Lett. 15, 508.

http://cms.web.cern.ch/tags/luminosity

KIM, D., et al., 2011, "PDF Uncertainties and K-factor for the W' Search", CMS AN-2011/273.

LANE, K., and MRENNA, S., 2003, "The Collider Phenomenology of Technihadrons in the Technicolor Straw Man Model", Phys. Rev. D 67(2003) 115011 and hep-ph/0210299.

LANGACKER, P., and Sankar, S.U., 1989, "Bounds on the Mass of WR and the WL - WR Mixing Angle zeta in General SU(2)L times SU(2)R times U(1) Models", Phys. Rev. D40, 1569 (1989).

MARTELLI, A., 2012, "First Measurement of the WZ Production cross section with the CMS Detector at the LHC", CERN-THESIS-2012-014.

MOHAPATRA, R.N., and PATI, J.C., 1975, "Left-Right Gauge Symmetry and an 'Isoconjugate' Model of CP Violation", Phys. Rev. D11 (1975), p. 566-571.

MOHAPATRA, R.N., and SENJAVONIC, G., 1980, "Neutrino Mass and Spontaneous Parity Nonconservation", Phys. Rev. Lett. 44 (1980), p. 912.

_________, 1975, "Exact Left-Right Symmetry and Spontaneous Violation of Parity", Phys.Rev. D12 (1975) 1502.

MONETA, L., et al., 2010, "The RooStats Project", arXiv:physics.data-an/1009.1003v1.

NAKAMURA, K. and PARTICLE DATA GROUP, 2010, "Review of Particle Physics", J. Phys. G: Nucl. Part. Phys. 37 075021.

NAMBU, Y., 1960, "Axial Vector Current Conservation in Weak Interactions", Phys. Rev. Lett. 4, 380.

NOURBAKHSH, S., 2011, "Energy Scale of CMS Electromagnetic Calorimeter with 2010 Data", CMS AN-2011/038.

NOVAES, S.F.,2000, "Standard Model: An Introduction", arXiv-hep-ph:0001283v1.

PATI, J.C., and SALAM, A., 1974, "Lepton Number as the Fourth Color", Phys. Prev/D10(1974), p.275 289.

PUMPLIN, J., et al., 2002, "New Generation of Parton Distributions with Uncertainties from Global QCD analysis", JHEP 0207:012 and arXiv:hep-ph/0201195v3.

READ, A.L, 2000, "Modified Frequentist Analysis of Search Results (The CLs Method)", 1st Workshop on Confidence Limits, CERN, Geneva, Switzerland, 17-18 Jan 2000, pp. 81-101, CERN-OPEN-2000-205.

________, 2002, "Presentation of Search Results; the CLs Technique", J.Phys.G28:2693-2704.

SALAM, A., and WARD, J.C., 1964, "Electromagnetic and Weak Interactions", Phys. Rev.Lett.13:168-171.

SALAM, A., 1968, "Weak and Electromagnetic Interactions", Proc. 8th Nobel Symposium, Stockholm.

SALAM, G.P., 2007, "A Practical Seedless Infrared Safe Cone Algorithm", arXiv:0705.2696v1 [hep-ph].

SALAM, G.P., and SOYEZ, G., 2007, "A Practical Seedless Infrared Safe Cone Algorithm", JHEP05 (2007) 086.

SALAM, G.P., 2010, “Towards Jetography”, arXiv: hep-ph /0906.1833v2.

SIKLER, F., 2005, “Hadronic physics with the CMS experiment”, arXiv:hep-ph/0504259.

SJOSTRAND, S.M.T., and SKANDS, P.Z., 2006, “PYTHIA 6.4 Physics and Manual”, JHEP 0605 (2006) and arXiv:hep-ph/0603175.

Spectra-Physics. VSL Series Nitrogen Lasers. Newport Corporation, 2007.

UTIYAMA, R., 1956, “Invariant theoretical Interpretation of Interaction”, Phys. Rev. 101, 1597-1607.

VOGT, R., 2002, “What is the Real K factor?”, arXiv:hep-ph/0207359v1.

WEINBERG, S., 1967, “A Model Leptons”, Phy Rev. Lett, 19(21):1264-1266.

WILZECK, F., 1982, “Quantum Chromodynamics: The Modern Theory of the Strong Interaction”, Ann. Rev. Nucl. Part. Sci.32:177-209.

WOBISCH, M., and Wengler, T., 1999, “Hadronization Corrections to Jet Cross Sections in Deep-Inelastic Scattering”, arXiv:hep-ph/9907280v1.

YANG, C.N., and MILLS R.L., 1954, “Conservation of Isotopic Spin and Isotopic Gauge Invariance”, Phys. Rev. 96, 191.

ZHU, Y., 2007, “Upper Limit for Poisson variable incorporating systematic uncertainties by Bayesian approach”, Nucl.Instrum.Meth. A578 (2007) 322-328, POS (ACAT) 059.

CURRICULUM VITAE

She was born on October 10, 1981, in Adana, Turkey. She finished her high school education in Adana, 1999. She graduated with the highest cumulative grade point average in the Physics Department in 2003 at Niğde University. She got her master degree in High Energy Physics from Çukurova University in 2007 and she started her PhD. study at the same year. She has been studying in Çukurova University since 2007.

APPENDIX

A. INTEGRATED LUMINOSITIES

Table A.1. The total integrated luminosities for DoubleMu data sets.

Data Set	HLT Path	Selected LS	Recorded (/pb)	Effective (/pb)
/DoubleMu/Run2011A-May10ReReco-v1/AOD	HLT_DoubleMu7_v1	10746	46.966	46.966
	HLT_DoubleMu7_v2	16572	168.581	46.966
/DoubleMu/Run2011A-PromptReco-v4/AOD	HLT_Mu13_Mu8_v2	35024	697.040	697.040
	HLT_Mu13_Mu8_v3	163	4.415	4.415
	HLT_Mu13_Mu8_v4	1690	253.757	253.757
/DoubleMu/Run2011A-05Aug2011-v1/AOD	HLT_Mu13_Mu8_v6	12365	389.876	389.876
/DoubleMu/Run2011A-PromptReco-v6/AOD	HLT_Mu13_Mu8_v6	13949	441.387	441.387
	HLT_Mu13_Mu8_v7	6893	265.313	265.313
/DoubleMu/Run2011B-PromptReco-v1/AOD	HLT_Mu17_Mu8_v10	12936	756.508	756.508
	HLT_Mu17_Mu8_v11	1808	128.945	128.945
	HLT_Mu17_Mu8_v7	34705	1.816 (/fb)	1.816 (/fb)

Table A.2. The total integrated luminosities for DoubleElectron data sets.

Data Set	HLT Path	Selected LS	Recorded (/pb)	Effective (/pb)
/DoubleElectron/Run2011A -May10ReReco-v1/AOD	HLT_Ele_17_CaloIdT_ TrkIdVL_ CaloIsoVL_ TrkIsoVL_Ele8_CaloIdT_ TrkIdVL_CaloIsoVL_TrkIsoVL_v2	7414	40.685	40.685
	HLT_Ele_17_CaloIdT_ TrkIdVL_ CaloIsoVL_ TrkIsoVL_Ele8_CaloIdT_ TrkIdVL_CaloIsoVL_TrkIsoVL_v3	16572	168.529	168.529
/DoubleElectron/Run2011A -PromptReco-v4/AOD	HLT_Ele_17_CaloIdT_ TrkIdVL_ CaloIsoVL_ TrkIsoVL_Ele8_CaloIdT_ TrkIdVL_CaloIsoVL_TrkIsoVL_v4	9337	136.382	136.382
	HLT_Ele_17_CaloIdT_ TrkIdVL_ CaloIsoVL_ TrkIsoVL_Ele8_CaloIdT_ TrkIdVL_CaloIsoVL_TrkIsoVL_v5	24770	541.531	541.531
/DoubleElectron/Run2011A -05Aug2011-v1/AOD	HLT_Ele_17_CaloIdT_ CaloIsoVL_TrkIsoVL_Ele8_ CaloIdT_CaloIsoVL_TrkIdVL_TrkIsoVL_v7	12365	389.876	341.459

Table A.3. The total integrated luminosities for DoubleElectron data sets.

Data Set	HLT Path	Selected LS	Recorded (/pb)	Effective (/pb)
/DoubleElectronRun2011A -PromptReco-v6/AOD	HLT_Ele_17_CaloIdT_ CaloIsoVL_TrkIsoVL_Ele8_ CaloIdT_CaloIsoVL_TrkId VL_TrkIsoVL_v7	13949	441.387	441.387
	HLT_Ele_17_CaloIdT_ CaloIsoVL_TrkIsoVL_Ele8_ CaloIdT_CaloIsoVL_TrkId VL_TrkIsoVL_v8	6892	265.313	265.313
/DoubleElectron/Run201B -PromptReco-v1/AOD	HLT_Ele_17_CaloIdT_ CaloIsoVL_TrkIsoVL_Ele8_ CaloIdT_CaloIsoVL_TrkId VL_TrkIsoVL_v10	12936	756.508	756.508
	HLT_Ele_17_CaloIdT_ CaloIsoVL_TrkIsoVL_Ele8_ CaloIdT_CaloIsoVL_TrkId VL_TrkIsoVL_v8	1808	128.945	128.945
	HLT_Ele_17_CaloIdT_ CaloIsoVL_TrkIsoVL_Ele8_ CaloIdT_CaloIsoVL_TrkId VL_TrkIsoVL_v9	34901	1.829 (/fb)	1.829 (/fb)

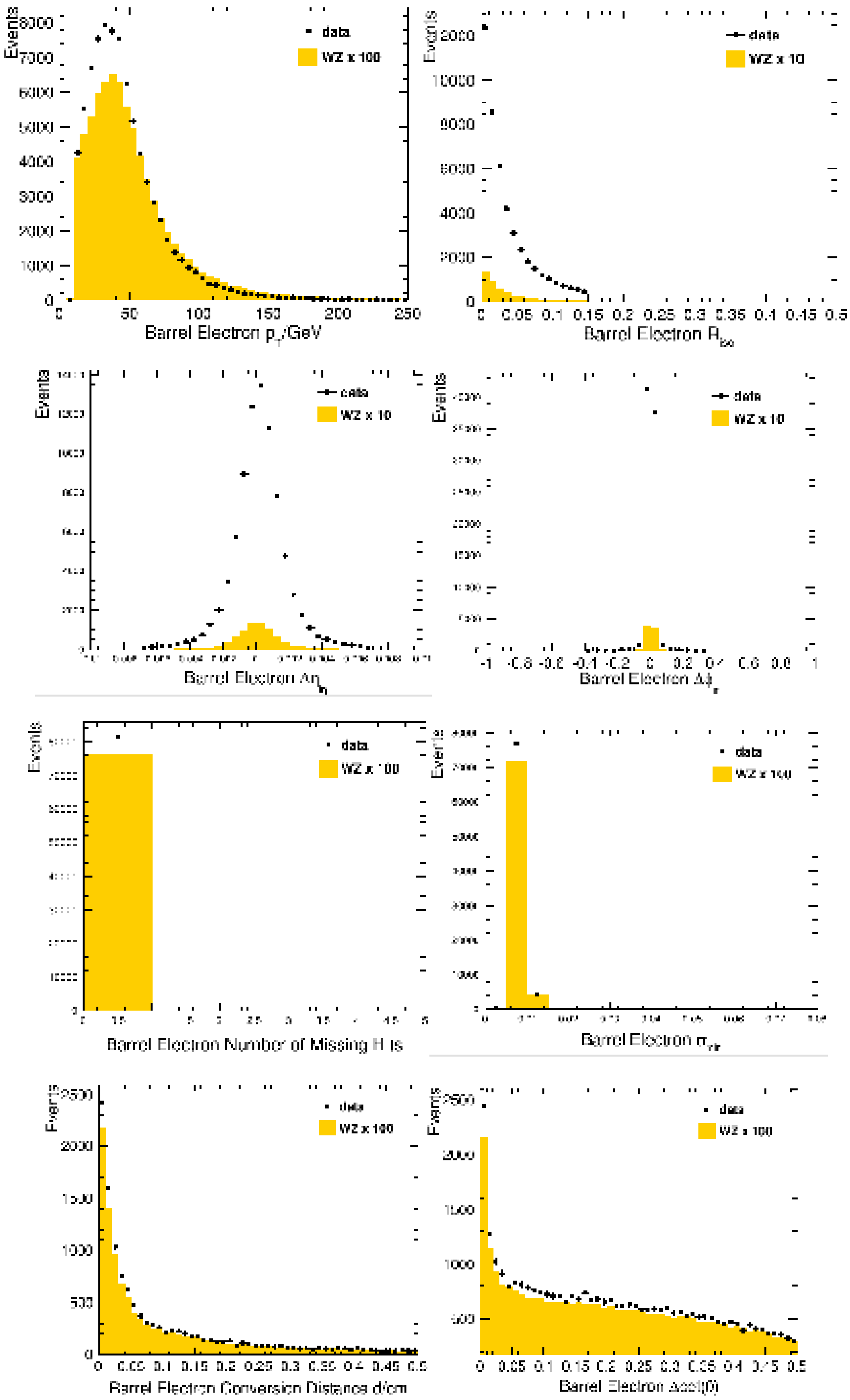

Figure B.1. Distributions of criteria used to select barrel electrons, considering all remaining candidates with E_T > 15 GeV/c after Z ® $\mathbf{l}^+\mathbf{l}^-$ decay is defined.

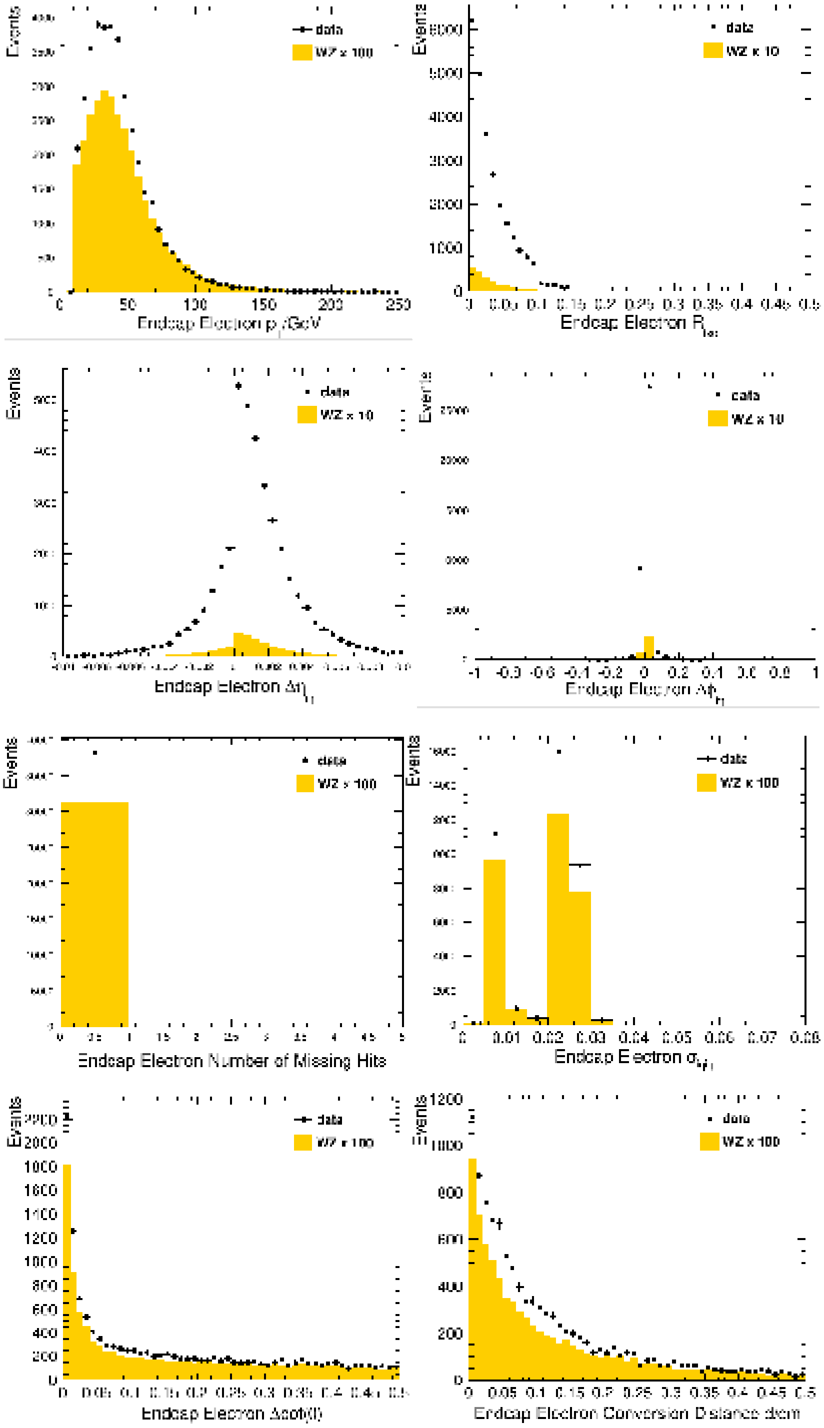

Figure B.2. Distributions of criteria used to select endcap electrons, considering all remaining candidates with E_T > 15 GeV/c after Z ® $\mathbf{l}^+\mathbf{l}^-$ decay is defined.

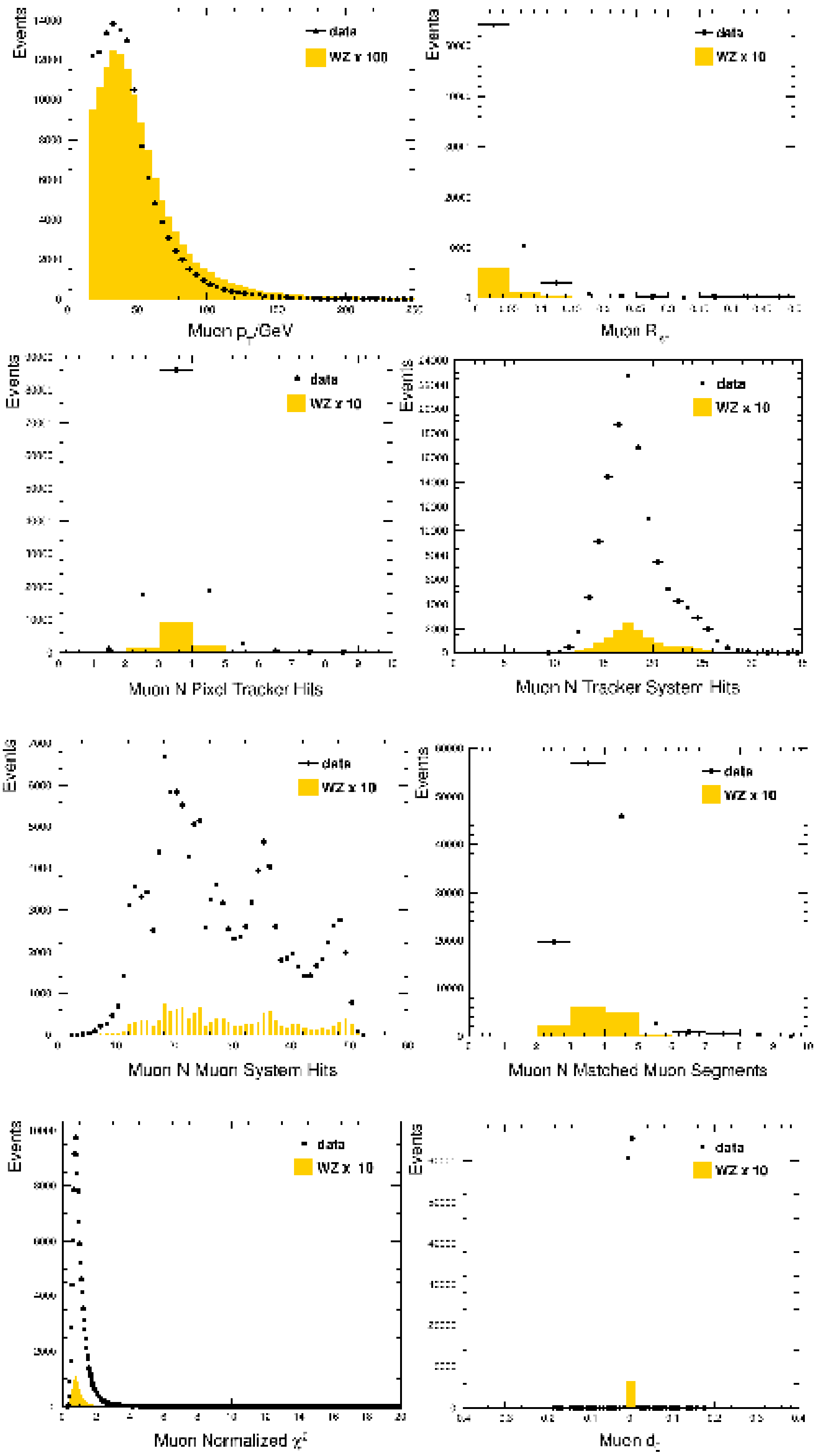

Figure B.3. Distributions of criteria used to select muons, considering all remaining candidates with $p_T > 15$ GeV/c after Z ® $\mathbf{l}^{+}\mathbf{l}^{-}$ decay is defined.

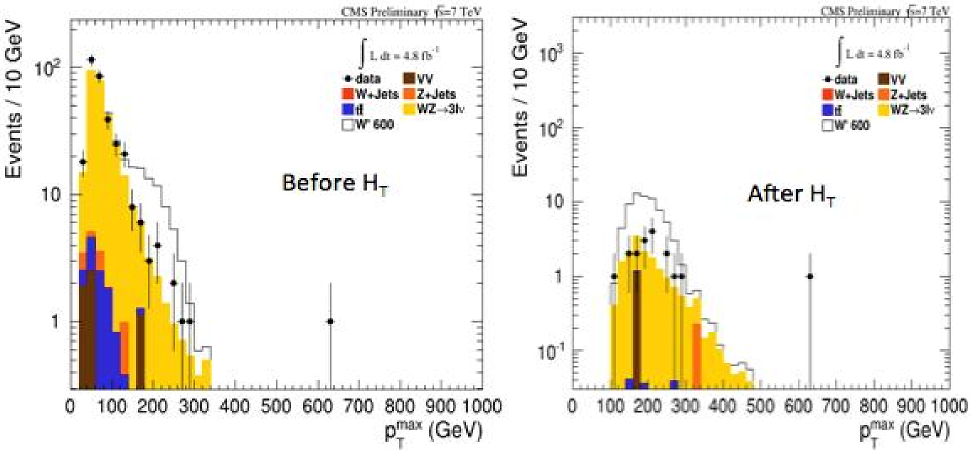

Figure B.4. Leading lepton p_T distributions before H_T cut (left) and after H_T cut (right).

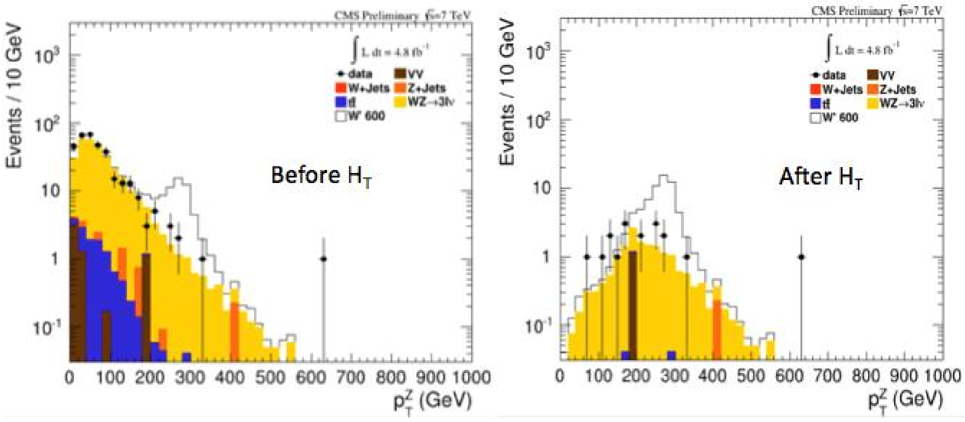

Figure B.5. p_T^Z distributions before H_T cut (left) and after H_T cut (right).

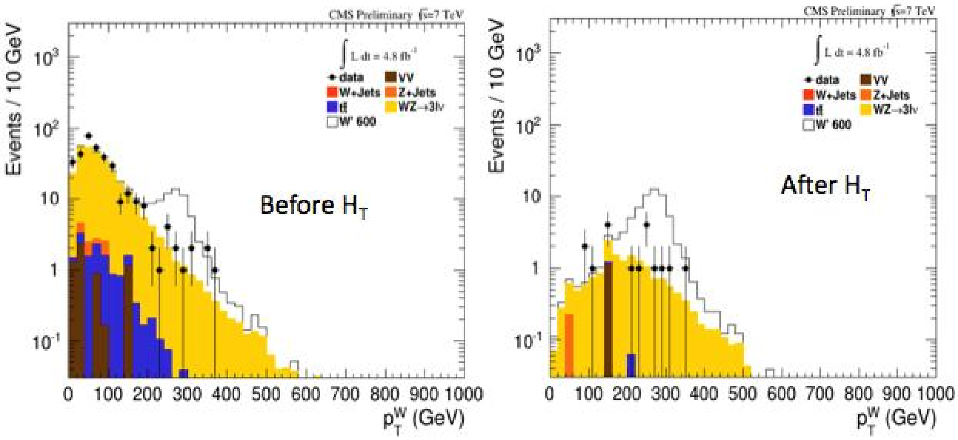

Figure B.6. p_T^W distributions before H_T cut (left) and after H_T cut (right).

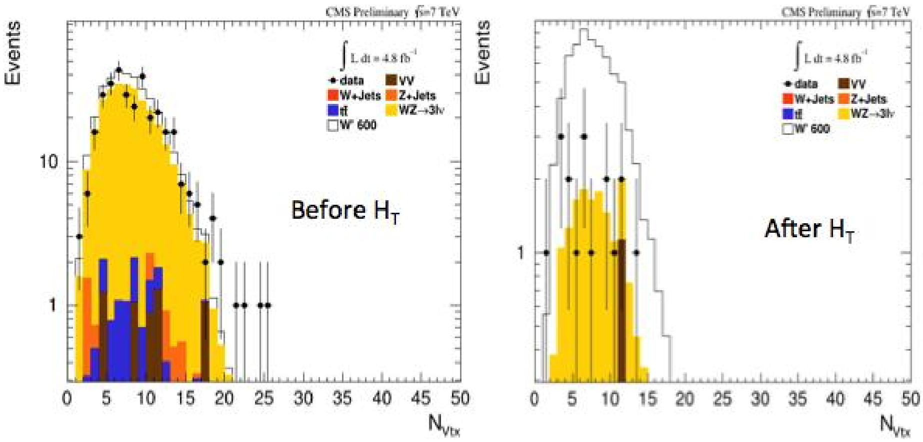

Figure B.7. Number of primary vertex distributions before H_T cut (left) and after H_T cut (right).

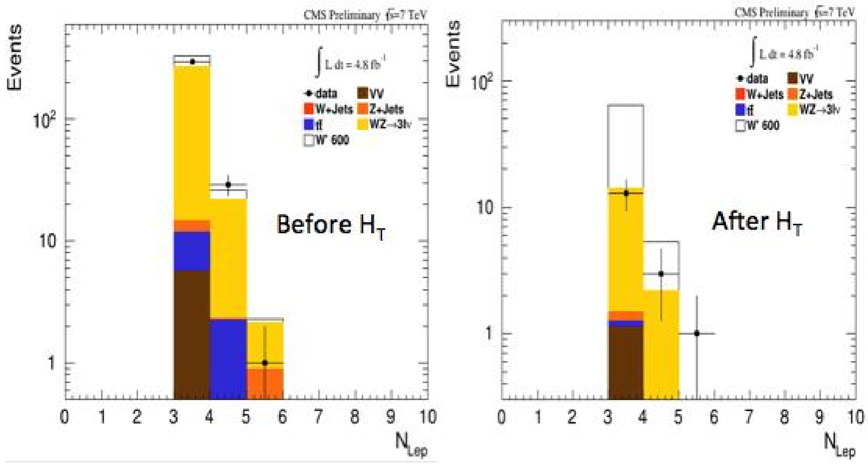

Figure B.8. Number of leptons distributions before H_T cut (left) and after H_T cut (right).

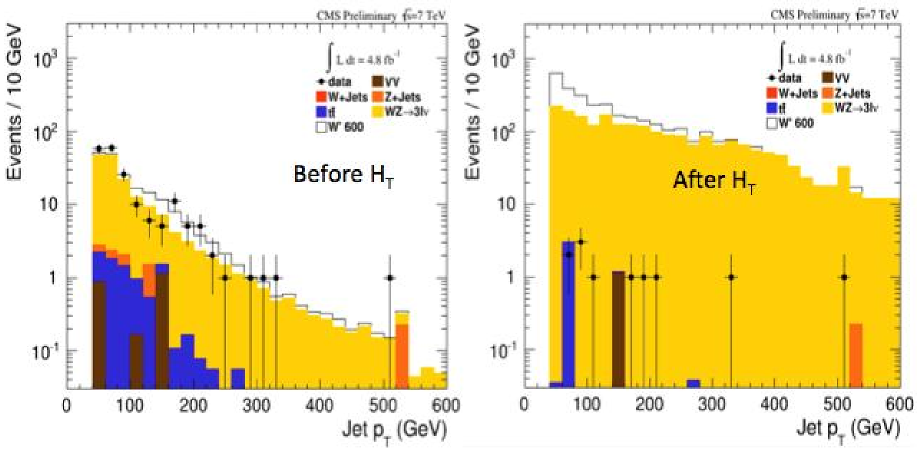

Figure B.9. Leading jet p_T before H_T cut (left) and after H_T cut (right), considering calorimeter jets with $p_T > 40$ and $|\eta| < 2.5$.

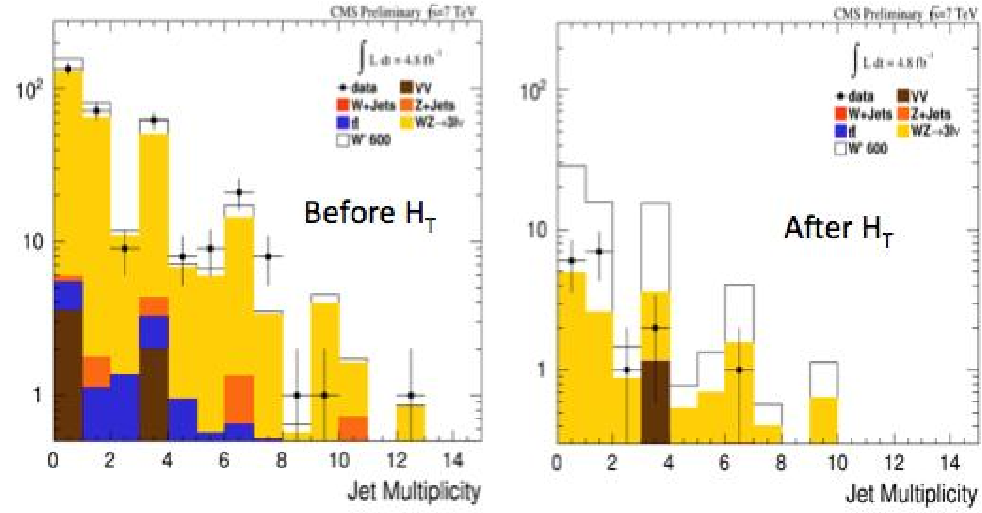

Figure B.10. Jet multiplicity before H_T cut (left) and after H_T cut (right), considering calorimeter jets with $p_T > 40$ and $|\eta| < 2.5$.

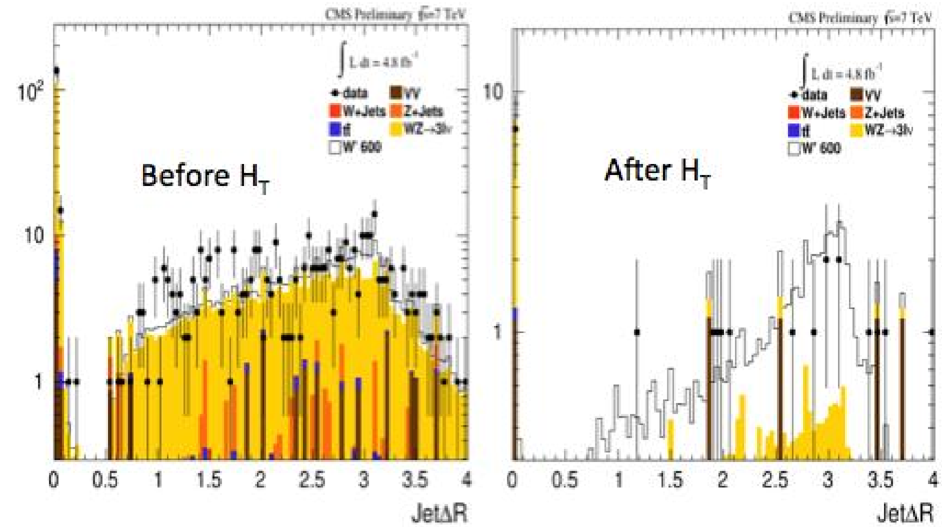

Figure B.11. ΔR (jet, lepton) before H_T cut (left) and after H_T cut (right).

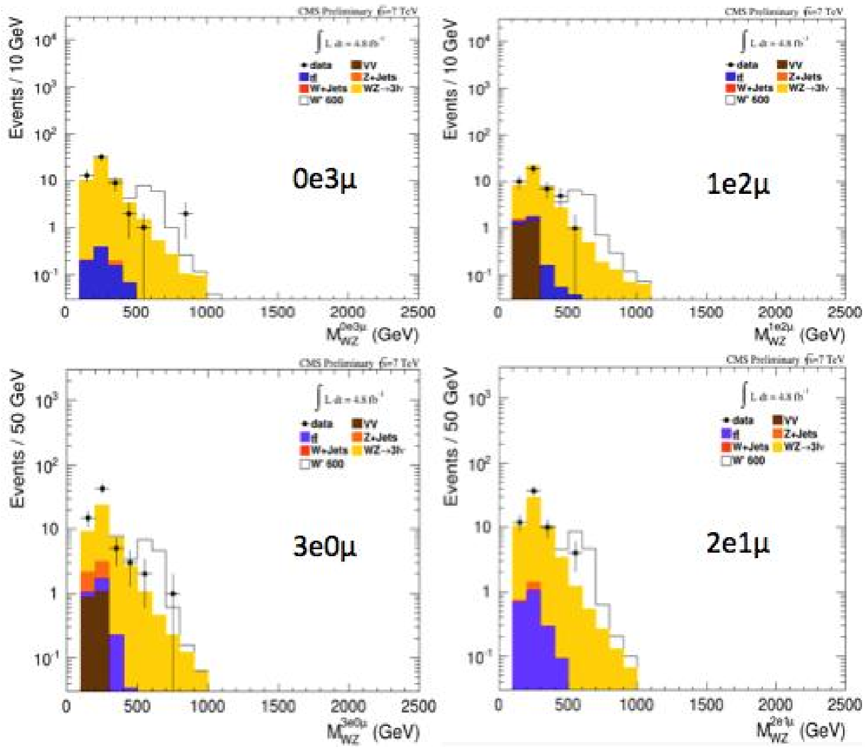

Figure B.12. WZ Mass distributions by channel before H_T cut.

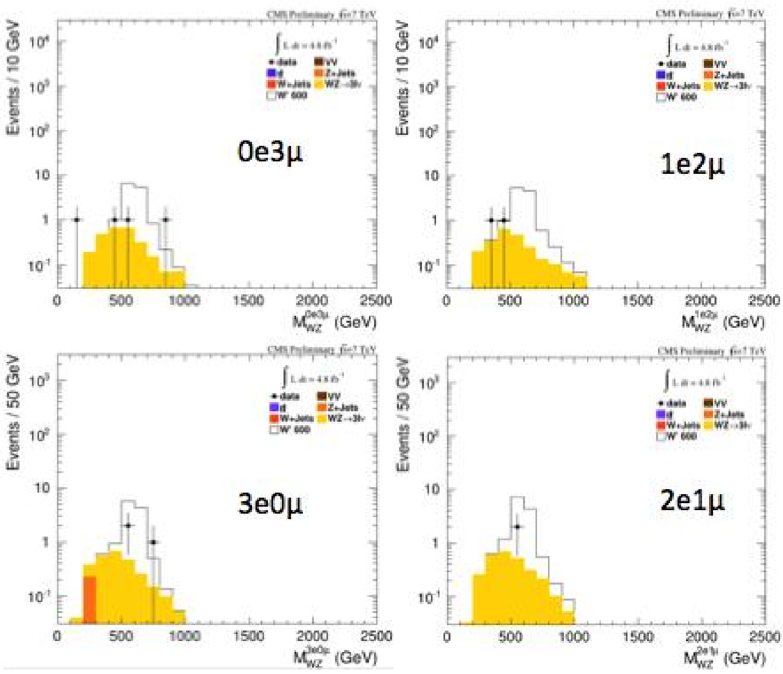

Figure B.13. WZ Mass distributions by channel after H_T cut.

C. EVENT YIELDS FOR W¢SIGNAL SAMPLES

Table C.1. Expected signal yields after the main steps of the event selection. The numbers correspond to an integrated luminosity of 4.8 fb^{-1}.

Sample	Preselection	Z selection	W Selection	E_T^{miss}
W¢200	5045.637 ± 45.730	1878.361 ± 27.891	1216.229 ± 22.385	784.473 ± 18.001
W¢250	4889.348 ± 41.509	1847.596 ± 26.647	1231.395 ± 20.918	906.492 ± 17.795
W¢300	3026.208 ± 24.613	1145.058 ± 15.212	800.23 ± 12.753	647.764 ± 11.444
W¢400	1136.182 ± 8.547	428.712 ± 5.290	310.547 ± 4.502	271.709 ± 4.208
W¢500	478.049 ± 3.454	175.562 ± 2.093	132.165 ± 1.819	121.952 ± 1.748
W¢600	235.648 ± 1.635	88.08 ± 1.000	66.061 ± 0.864	62.785 ± 0.842
W¢700	121.550 ± 0.829	45.436 ± 0.507	35.876 ± 0.446	33.635 ± 0.436
W¢800	69.428 ± 0.462	25.698 ± 0.280	19.999 ± 0.247	19.332 ± 0.243
W¢900	39.973 ± 0.262	14.698 ± 0.160	11.458 ± 0.141	11.186 ± 1.124
W¢1000	24 ± 0.157	8.629 ± 0.094	6.759 ± 0.083	6.593 ± 0.082
W¢1100	14.504 ± 0.104	5.035 ± 0.056	3.997 ± 0.050	3.887 ± 0.049
W¢1200	9.022 ± 0.059	2.881 ± 0.033	2.269 ± 0.030	2.214 ± 0.029
W¢1300	5.861 ± 0.038	1.6 ± 0.02	1.281 ± 0.018	1.251 ± 0.017
W¢1400	3.67 ± 0.024	0.824 ± 0.011	0.647 ± 0.010	0.629 ± 0.010
W¢1500	2.43 ± 0.016	1.327 ± 0.007	0.382 ± 0.006	0.371 ± 0.006

Table C.2. Expected signal yields for four channels after the main steps of the event selection. The numbers correspond to an integrated luminosity of 4.8 fb^{-1}.

Sample	3m	2m1e	3e	1m2e
W¢200	227.877 ± 7.877	177.922 ± 7.004	161.244 ± 9.58	217.441 ± 11.008
W¢250	269.017 ± 7.933	184.668 ± 20.426	201.251 ± 11.006	251.545 ± 14.728
W¢300	183.777 ± 4.934	140.947 ± 4.349	142.042 ± 6.225	180.997 ± 6.995
W¢400	74.994 ± 1.777	58.409 ± 1.574	61.356 ± 2.307	76.95 ± 2.597
W¢500	34.086 ± 0.75	27.417 ± 0.673	28.493 ± 0.985	31.955 ± 1.034
W¢600	17.31 ± 0.358	14.928 ± 0.335	12.763 ± 0.459	16.783 ± 0.507
W¢700	9.174 ± 0.185	7.924 ± 0.171	7.966 ± 0.247	8.569 ± 0.256
W¢800	5.318 ± 0.104	4.675 ± 0.098	4.327 ± 0.134	5.011 ± 0.143
W¢900	2.902 ± 0.337	2.621 ± 0.054	2.595 ± 0.078	3.067 ± 0.084
W¢1000	1.766 ± 0.034	1.508 ± 0.032	1.588 ± 0.047	1.73 ± 0.049
W¢1100	0.998 ± 0.02	0.896 ± 0.019	0.937 ± 0.028	1.054 ± 0.029
W¢1200	0.54 ± 0.011	0.508 ± 0.029	0.535 ± 0.016	0.630 ± 0.018
W¢1300	0.32 ± 0.007	0.295 ± 0.007	0.302 ± 0.01	0.332 ± 0.01
W¢1400	0.164 ± 0.004	0.14 ± 0.003	0.152 ± 0.005	0.172 ± 0.006
W¢1500	0.097 ± 0.002	0.081 ± 0.002	0.090 ± 0.003	0.102 ± 0.003

D. Template Shape Definition for the Fits

A Voigtian (Breit-Wigner convulated with a Gaussian) convoluted with a Crystal Ball function is used for $Z \rightarrow e^+e^-$ events, a Gauss convoluted with a Crystal Ball function is used for $Z \rightarrow \mu^+\mu^-$ events and an exponential function is used for background as template for the fits. The fitted paramaters are defined as follows:

- Parameters of the Voigtian
  - sv (sigma) (sv$_{pp}$, this paramater is constrained to be the same for the failing probe sample)
  - mv (mean) (mv$_{pp}$, this paramater is constrained to be the same for the failing probe sample)
  - width (width$_{pp}$, this paramater is constrained to be the same for the failing probe sample)
- Parameters of the Crystal Ball

  The function is defined as:

$$f(x;\alpha,n,\bar{x},\sigma) = \exp\left(-\frac{\left(x-\bar{x}\right)^2}{2\sigma}\right) \text{ for } \frac{x-\bar{x}}{\sigma} \geq -|\alpha| \tag{1}$$

and

$$f(x;\alpha,n,\bar{x},\sigma) = A \times \left(B - \frac{\left(x-\bar{x}\right)}{\sigma}\right)^{-n} \text{ for } \frac{x-\bar{x}}{\sigma} < -|\alpha| \tag{2}$$

with

$$A = \left(\frac{n}{|\alpha|}\right)^n \times \exp(-|\alpha|^2 / 2) \tag{3}$$

and

$$B = \frac{n}{|\alpha|} - |\alpha| \tag{4}$$

and the fitted parameters are:

- alpha (alpha$_{pp}$ for the passing probe sample and alpha$_{\mathrm{fp}}$ for the failing probe sample)
- n (n_{pp} for the passing probe sample and n_{fp} for the failing probe sample)
- mean $\bar{x}$ is fixed to $\bar{x} = 0$.
- sigma (sigma$_{pp}$ for the passing probe sample and sigma$_{\mathrm{fp}}$ for the failing probe sample)

· Parameters of the Gaussian

The function is defined as:

$$\mathrm{g}(x;\mu,\sigma) = \frac{1}{\sqrt{2\pi\sigma}} e^{-\frac{(x-\mu)^2}{2\sigma^2}} \tag{5}$$

and the fitted paramaters are:

- μ (the mean or expectation of the distribution)
- σ (its standard deviation; its variance is therefore σ^2)

· and for the background shape a exponential is used with a single slope parameter:

- c1(slope)

E. EFFICIENCIES

Table E.1. Muon ID, Iso and HLT efficiencies for different P_T bins for DoubleMu_Run2011A_May10ReReco_v1 data set.

/DoubleMu/Run2011A-May10ReReco-v1/AOD						
P_T Bins	e_{Trk}	e_{Std}	e_{ID}	$e_{Isolation}$	e_{HLT_17}	e_{HLT_8}
$10 < P_T < 20$	0.994 ± 0.002	0.985 ± 0.009	0.98 ± 0.01	0.855 ± 0.009	0.69 ± 0.01	0.998 ± 0.001
$20 < P_T < 30$	0.989 ± 0.001	0.985 ± 0.002	0.971 ± 0.002	0.934 ± 0.003	0.9992 ± 0.0003	0.9992 ± 0.0003
$30 < P_T < 40$	0.9896 ± 0.0005	0.9889 ± 0.0006	0.9745 ± 0.0009	0.9732 ± 0.0009	0.9986 ± 0.0002	0.9986 ± 0.0002
$40 < P_T < 50$	0.991 ± 0.0004	0.9886 ± 0.0005	0.9749 ± 0.0007	0.9927 ± 0.0004	0.9986 ± 0.0002	0.9986 ± 0.0002
$50 < P_T < 60$	0.99 ± 0.001	0.989 ± 0.001	0.974 ± 0.002	0.9954 ± 0.0008	0.9989 ± 0.0004	0.9989 ± 0.0004
$60 < P_T < 100$	0.988 ± 0.002	0.989 ± 0.002	0.973 ± 0.003	0.993 ± 0.002	0.9985 ± 0.0008	0.9985 ± 0.0008

Table E.2. Muon ID, Iso and HLT efficiencies for different pseudorapidity bins for DoubleMu_Run2011A_MayReReco_v1 data set.

DoubleMu/Run2011A-May10ReReco-v1/AOD						
$\|h\|$ Bins	e_{Trk}	e_{Std}	e_{ID}	$e_{Isolation}$	e_{HLT_17}	e_{HLT_8}
$0 < \|h\| < 0.5$	0.9881 ± 0.0006	0.9853 ± 0.0009	0.970 ± 0.01	0.974 ± 0.001	0.996 ± 0.0004	0.9995 ± 0.0001
$0.5 < \|h\| < 1$	0.9929 ± 0.0005	0.9872 ± 0.0008	0.976 ± 0.001	0.9776 ± 0.001	0.9952 ± 0.0004	0.9993 ± 0.0002
$1 < \|h\| < 1.5$	0.9884 ± 0.0007	0.9929 ± 0.0008	0.979 ± 0.001	0.9836 ± 0.0009	0.9938 ± 0.0005	0.9978 ± 0.0003
$1.5 < \|h\| < 2$	0.9957 ± 0.0005	0.9894 ± 0.001	0.979 ± 0.001	0.984 ± 0.001	0.9932 ± 0.0006	0.9984 ± 0.0003
$2 < \|h\| < 2.5$	0.985 ± 0.001	0.99 ± 0.001	0.965 ± 0.002	0.983 ± 0.001	0.9902 ± 0.0009	0.9976 ± 0.0005

Table E.3. Muon ID, Iso and HLT efficiencies for different P_T bins for DoubleMu_Run2011A_PromtReco_v4 data set.

/DoubleMu/Run2011A-PromptReco-v4/AOD						
P_T Bins	e_{Trk}	e_{Std}	e_{ID}	$e_{Isolation}$	e_{HLT_17}	e_{HLT_8}
$10 < P_T < 20$	0.992 ± 0.001	0.983 ± 0.004	0.975 ± 0.005	0.866 ± 0.004	0.595 ± 0.006	0.595 ± 0.006
$20 < P_T < 30$	0.9905 ± 0.0005	0.9844 ± 0.0009	0.972 ± 0.001	0.930 ± 0.001	0.848 ± 0.002	0.848 ± 0.002
$30 < P_T < 40$	0.991 ± 0.002	0.9873 ± 0.0003	0.974 ± 0.0004	0.9729 ± 0.0004	0.85 ± 0.0009	0.85 ± 0.0009
$40 < P_T < 50$	0.9909 ± 0.0002	0.9873 ± 0.0002	0.9727 ± 0.0003	0.9919 ± 0.0002	0.8483 ± 0.0008	0.8483 ± 0.0008
$50 < P_T < 60$	0.991 ± 0.0005	0.987 ± 0.0006	0.9719 ± 0.0009	0.9942 ± 0.0004	0.851 ± 0.002	0.851 ± 0.002
$60 < P_T < 100$	0.9941 ± 0.0007	0.984 ± 0.001	0.970 ± 0.002	0.9943 ± 0.0007	0.857 ± 0.003	0.857 ± 0.003

Table E.4. Muon ID, Iso and HLT efficiencies for different pseudorapidity bins for DoubleMu_Run2011A_PromptReco_v4 data set.

/DoubleMu/Run2011A-PromptReco-v4/AOD						
h Bins	e_{Trk}	e_{Std}	e_{ID}	$e_{Isolation}$	e_{HLT_17}	e_{HLT_8}
$0 < \|h\| < 0.5$	0.9914 ± 0.0003	0.9854 ± 0.0004	0.9727 ± 0.0005	0.9726 ± 0.0005	0.85 ± 0.010	0.9854 ± 0.0004
$0.5 < \|h\| < 1$	0.9938 ± 0.0002	0.9861 ± 0.0004	0.9757 ± 0.0005	0.9769 ± 0.0005	0.848 ± 0.001	0.9861 ± 0.0004
$1 < \|h\| < 1.5$	0.9883 ± 0.0003	0.99 ± 0.0004	0.9753 ± 0.0006	0.9832 ± 0.0004	0.848 ± 0.001	0.99 ± 0.0004
$1.5 < \|h\| < 2$	0.9945 ± 0.0003	0.985 ± 0.0005	0.9732 ± 0.006	0.9848 ± 0.0005	0.844 ± 0.001	0.985 ± 0.0005
$2 < \|h\| < 2.5$	0.9842 ± 0.0006	0.9904 ± 0.0006	0.966 ± 0.0010	0.9834 ± 0.0006	0.827 ± 0.002	0.9904 ± 0.0006

Table E.5. Muon ID, Iso and HLT efficiencies for different P_T bins for DoubleMu_Run2011A_05Aug2011_v1 data set.

/DoubleMu/Run2011A-05Aug2011-v1/AOD						
P_T Bins	ε_{Trk}	ε_{Std}	ε_{ID}	$\varepsilon_{Isolation}$	ε_{HLT_17}	ε_{HLT_8}
$10 < P_T < 20$	0.991 ± 0.002	0.974 ± 0.007	0.959 ± 0.009	0.850 ± 0.007	0.68 ± 0.009	0.68 ± 0.009
$20 < P_T < 30$	0.991 ± 0.0007	0.983 ± 0.001	0.970 ± 0.002	0.923 ± 0.002	0.9913 ± 0.0007	0.9913 ± 0.0007
$30 < P_T < 40$	0.9906 ± 0.0004	0.9859 ± 0.0005	0.9722 ± 0.0007	0.9698 ± 0.0007	0.9942 ± 0.0003	0.9942 ± 0.0003
$40 < P_T < 50$	0.9916 ± 0.0003	0.9857 ± 0.0004	0.9717 ± 0.0006	0.9909 ± 0.0003	0.9952 ± 0.0002	0.9952 ± 0.0002
$50 < P_T < 60$	0.9932 ± 0.0007	0.985 ± 0.001	0.971 ± 0.001	0.9950 ± 0.0006	0.9952 ± 0.0006	0.9952 ± 0.0006
$60 < P_T < 100$	0.994 ± 0.001	0.986 ± 0.002	0.971 ± 0.003	0.989 ± 0.001	0.993 ± 0.001	0.993 ± 0.001

Table E.6. Muon ID, Iso and HLT efficiencies for different pseudorapidity bins for DoubleMu_Run2011A_05Aug2011_v1 data set.

/DoubleMu/Run2011A-05Aug2011-v1/AOD						
η Bins	ε_{Trk}	ε_{Std}	ε_{ID}	$\varepsilon_{Isolation}$	ε_{HLT_17}	ε_{HLT_8}
$0 < \|\eta\| < 0.5$	0.993 ± 0.0004	0.9844 ± 0.0007	0.9739 ± 0.0008	0.9697 ± 0.0008	0.9954 ± 0.0003	0.9954 ± 0.0003
$0.5 < \|\eta\| < 1$	0.9947 ± 0.0003	0.9842 ± 0.0007	0.9741 ± 0.0009	0.975 ± 0.0008	0.9946 ± 0.0003	0.9946 ± 0.0003
$1 < \|\eta\| < 1.5$	0.986 ± 0.0006	0.9894 ± 0.0006	0.9713 ± 0.0010	0.9814 ± 0.0007	0.9905 ± 0.0005	0.9905 ± 0.0005
$1.5 < \|\eta\| < 2$	0.9952 ± 0.0004	0.9816 ± 0.0009	0.970 ± 0.001	0.983 ± 0.0008	0.9865 ± 0.0007	0.9865 ± 0.0007
$2 < \|\eta\| < 2.5$	0.9852 ± 0.001	0.989 ± 0.001	0.963 ± 0.002	0.979 ± 0.001	0.965 ± 0.001	0.965 ± 0.001

Table E.7. Muon ID, Iso and HLT efficiencies for different P_T bins for DoubleMu_Run2011A_PromtReco_v6 data set.

/DoubleMu/Run2011A-PromptReco-v6/AOD						
P_T Bins	e_{Trk}	e_{Std}	e_{ID}	$e_{Isolation}$	e_{HLT_17}	e_{HLT_8}
$10 < P_T < 20$	0.987 ± 0.002	0.971 ± 0.006	0.96 ± 0.007	0.848 ± 0.006	0.694 ± 0.007	0.694 ± 0.007
$20 < P_T < 30$	0.99 ± 0.0006	0.982 ± 0.001	0.969 ± 0.001	0.925 ± 0.002	0.9922 ± 0.0005	0.9922 ± 0.0005
$30 < P_T < 40$	0.9899 ± 0.0003	0.9854 ± 0.0004	0.9708 ± 0.0006	0.9702 ± 0.0006	0.9940 ± 0.0002	0.9940 ± 0.0002
$40 < P_T < 50$	0.9907 ± 0.0003	0.9849 ± 0.0003	0.9707 ± 0.0005	0.9907 ± 0.0003	0.9950 ± 0.0002	0.9950 ± 0.0002
$50 < P_T < 60$	0.9909 ± 0.0006	0.9859 ± 0.0008	0.970 ± 0.001	0.9942 ± 0.0005	0.9952 ± 0.0004	0.9952 ± 0.0004
$60 < P_T < 100$	0.9917 ± 0.001	0.986 ± 0.001	0.970 ± 0.002	0.9946 ± 0.0009	0.9962 ± 0.0007	0.9962 ± 0.0007

Table E.8. Muon ID, Iso and HLT efficiencies for different pseudorapidity bins for DoubleMu_Run2011A_PromptReco_v6 data set.

/DoubleMu/Run2011A-PromptReco-v6/AOD						
h Bins	e_{Trk}	e_{Std}	e_{ID}	$e_{Isolation}$	e_{HLT_17}	e_{HLT_8}
$0 < \|h\| < 0.5$	0.9916 ± 0.0003	0.9845 ± 0.0005	0.9724 ± 0.0007	0.9692 ± 0.0006	0.9963 ± 0.0002	0.9963 ± 0.0002
$0.5 < \|h\| < 1$	0.9939 ± 0.0003	0.985 ± 0.0005	0.9745 ± 0.0007	0.9755 ± 0.0006	0.9940 ± 0.0003	0.9940 ± 0.0003
$1 < \|h\| < 1.5$	0.9856 ± 0.0005	0.9883 ± 0.0005	0.9709 ± 0.0007	0.9822 ± 0.0006	0.9904 ± 0.0004	0.9904 ± 0.0004
$1.5 < \|h\| < 2$	0.9939 ± 0.0003	0.9786 ± 0.0007	0.9671 ± 0.0009	0.9839 ± 0.0006	0.9872 ± 0.0005	0.9872 ± 0.0005
$2 < \|h\| < 2.5$	0.9831 ± 0.0008	0.9885 ± 0.0008	0.964 ± 0.001	0.9805 ± 0.0009	0.968 ± 0.001	0.968 ± 0.001

Table E.9. Muon ID, Iso and HLT efficiencies for different P_T bins for DoubleMu_Run2011B_PromptReco_v1 data set.

/DoubleMu/Run2011B-PromptReco-v1/AOD						
P_T Bins	e_{Trk}	e_{Std}	e_{ID}	$e_{Isolation}$	e_{HLT_17}	e_{HLT_8}
$10 < P_T < 20$	0.992 ± 0.002	0.971 ± 0.008	0.966 ± 0.009	0.836 ± 0.008	0.695 ± 0.010	0.695 ± 0.010
$20 < P_T < 30$	0.9897 ± 0.0008	0.968 ± 0.002	0.955 ± 0.002	0.911 ± 0.002	0.9920 ± 0.0007	0.9920 ± 0.0007
$30 < P_T < 40$	0.9904 ± 0.0004	0.9748 ± 0.0007	0.9615 ± 0.0008	0.9636 ± 0.0008	0.9944 ± 0.0003	0.9944 ± 0.0003
$40 < P_T < 50$	0.9906 ± 0.0003	0.9745 ± 0.0006	0.9599 ± 0.0007	0.9883 ± 0.0004	0.9946 ± 0.0003	0.9946 ± 0.0003
$50 < P_T < 60$	0.9921 ± 0.0008	0.972 ± 0.001	0.958 ± 0.002	0.9941 ± 0.0007	0.9946 ± 0.0006	0.9946 ± 0.0006
$60 < P_T < 100$	0.991 ± 0.001	0.974 ± 0.002	0.958 ± 0.003	0.993 ± 0.001	0.995 ± 0.001	0.995 ± 0.001

Table E.10. Muon ID, Iso and HLT efficiencies for different pseudorapidity bins for DoubleMu_Run2011B_PromptReco_v1 data set.

/DoubleMu/Run2011B-PromptReco-v1/AOD						
h Bins	e_{Trk}	e_{Std}	e_{ID}	$e_{Isolation}$	e_{HLT_17}	e_{HLT_8}
$0 < \|h\| < 0.5$	0.9909 ± 0.0004	0.9854 ± 0.0007	0.9728 ± 0.0009	0.9624 ± 0.0009	0.9958 ± 0.0003	0.9958 ± 0.0003
$0.5 < \|h\| < 1$	0.9933 ± 0.0004	0.9857 ± 0.0007	0.9750 ± 0.0009	0.9719 ± 0.0009	0.9947 ± 0.0004	0.9947 ± 0.0004
$1 < \|h\| < 1.5$	0.9872 ± 0.0006	0.9861 ± 0.001	0.945 ± 0.001	0.9798 ± 0.0008	0.9903 ± 0.0005	0.9903 ± 0.0005
$1.5 < \|h\| < 2$	0.9939 ± 0.0005	0.948 ± 0.001	0.936 ± 0.002	0.9798 ± 0.0009	0.9864 ± 0.0007	0.9864 ± 0.0007
$2 < \|h\| < 2.5$	0.985 ± 0.001	0.983 ± 0.001	0.960 ± 0.002	0.978 ± 0.001	0.966 ± 0.001	0.966 ± 0.001

Table E.11. Muon ID, Iso and HLT efficiencies for different P_T bins for a MC Sample.

MC: DYJetsToLL_TuneZ2_M-50_7TeV-madgraph-tauola						
P_T Bins	e_{Trk}	e_{Std}	ε_{ID}	$\varepsilon_{Isolation}$	ε_{HLT_17}	ε_{HLT_8}
$10 < P_T < 20$	0.9937 ± 0.0003	0.977 ± 0.001	0.971 ± 0.002	0.791 ± 0.001	0.694 ± 0.002	0.9953 ± 0.0003
$20 < P_T < 30$	0.9936 ± 0.0001	0.9815 ± 0.0003	0.9738 ± 0.003	0.8868 ± 0.0004	0.9902 ± 0.0001	0.9951 ± 0.0001
$30 < P_T < 40$	0.9931 ± 0.00006	0.9846 ± 0.00009	0.9746 ± 0.0001	0.9542 ± 0.0003	0.99181 ± 0.00007	0.99514 ± 0.00005
$40 < P_T < 50$	0.9936 ± 0.00005	0.9849 ± 0.00007	0.97467 ± 0.0001	0.98473 ± 0.00008	0.99257 ± 0.00005	0.99515 ± 0.00004
$50 < P_T < 60$	0.9941 ± 0.0001	0.9849 ± 0.0002	0.9738 ± 0.0003	0.9914 ± 0.001	0.9928 ± 0.0001	0.9952 ± 0.0001
$60 < P_T < 100$	0.995 ± 0.0002	0.984 ± 0.0003	0.9724 ± 0.0005	0.9924 ± 0.0002	0.9924 ± 0.0002	0.9946 ± 0.0002

Table E.12. Muon ID, Iso and HLT efficiencies for different pseudorapidity bins for a MC Sample.

MC: DYJetsToLL_TuneZ2_M-50_7TeV-madgraph-tauola						
h Bins	e_{Trk}	e_{Std}	ε_{ID}	$\varepsilon_{Isolation}$	ε_{HLT_17}	ε_{HLT_8}
$0 < \|h\| < 0.5$	0.9936 ± 0.00006	0.9827 ± 0.0001	0.9735 ± 0.0001	0.9556 ± 0.0002	0.99394 ± 0.00006	0.99394 ± 0.00006
$0.5 < \|h\| < 1$	0.9949 ± 0.00006	0.9839 ± 0.0001	0.9761 ± 0.0001	0.9636 ± 0.0002	0.98968 ± 0.00009	0.98968 ± 0.00009
$1 < \|h\| < 1.5$	0.99198 ± 0.00008	0.9876 ± 0.0001	0.9776 ± 0.0002	0.9721 ± 0.0002	0.99007 ± 0.00009	0.99007 ± 0.00009
$1.5 < \|h\| < 2$	0.9956 ± 0.00007	0.9821 ± 0.0001	0.9730 ± 0.0002	0.9744 ± 0.002	0.9881 ± 0.0001	0.9881 ± 0.0001
$2 < \|h\| < 2.5$	0.9901 ± 0.0001	0.9894 ± 0.0002	0.9724 ± 0.0003	0.9604 ± 0.0003	0.9657 ± 0.0002	0.9657 ± 0.0002

Table E.13. Electron ID, Iso and HLT efficiencies for different E_T bins for DoubleElectron_Run2011A_May10ReReco_v1 data set.

/DoubleElectron/Run2011A-May10ReReco-v1/AOD							
E_T Bins	SCTo GSF	GsfTo WP95ID	GsfTo WP80ID	WP95ID ToIso	WP80ID ToIso	WP95 ToHLT17	WP95 ToHLT8
$20 < E_T < 30$	0.944 ± 0.004	0.958 ± 0.003	0.739 ± 0.005	0.913 ± 0.003	0.724 ± 0.004	0.938 ± 0.003	0.955 ± 0.002
$30 < E_T < 40$	0.962 ± 0.001	0.974 ± 0.001	0.802 ± 0.003	0.964 ± 0.001	0.846 ± 0.002	0.951 ± 0.001	0.958 ± 0.001
$40 < E_T < 50$	0.971 ± 0.001	0.981 ± 0.0008	0.841 ± 0.002	0.986 ± 0.0007	0.913 ± 0.002	0.9549 ± 0.0001	0.957 ± 0.000005
$50 < E_T < 60$	0.976 ± 0.002	0.979 ± 0.002	0.852 ± 0.005	0.995 ± 0.001	0.949 ± 0.003	0.959 ± 0.003	0.962 ± 0.003
$60 < E_T < 70$	0.98 ± 0.005	0.98 ± 0.005	0.871 ± 0.009	0.997 ± 0.002	0.969 ± 0.005	0.957 ± 0.005	0.962 ± 0.005
$70 < E_T < 80$	0.966 ± 0.008	0.982 ± 0.007	0.85 ± 0.02	0.998 ± 0.003	0.976 ± 0.007	0.954 ± 0.009	0.956 ± 0.009
$80 < E_T < 100$	0.986 ± 0.008	0.982 ± 0.009	0.85 ± 0.02	0.992 ± 0.005	0.978 ± 0.009	0.978 ± 0.007	0.978 ± 0.007
$100 < E_T < 200$	0.98 ± 0.002	0.97 ± 0.001	0.87 ± 0.02	1 ± 0.002	0.992 ± 0.006	0.96 ± 0.01	0.96 ± 0.01

Table E.14. Electron ID, Iso and HLT efficiencies for different pseudorapidity bins for DoubleElectron_Run2011A_MayReReco_v1 data set.

/DoubleElectron/Run2011A-May10ReReco-v1/AOD							
$\|\eta\|$ Bins	SCTo GSF	GsfTo WP95ID	GsfTo WP80ID	WP95ID ToIso	WP80ID ToIso	WP95 ToHLT17	WP95 ToHLT8
$0 < \|\eta\| \le 0.78$	0.976 ± 0.001	0.981 ± 0.001	0.864 ± 0.002	0.974 ± 0.001	0.884 ± 0.002	0.951 ± 0.001	0.957 ± 0.001
$0.78 < \|\eta\| \le 0.1444$	0.973 ± 0.001	0.978 ± 0.001	0.843 ± 0.003	0.976 ± 0.001	0.886 ± 0.002	0.953 ± 0.001	0.959 ± 0.001
$1.444 < \|\eta\| \le 1.566$	1 ± 0.05	0.8 ± 0.1	0.8 ± 0.1	1 ± 0.07	1 ± 0.1	1 ± 0.07	1 ± 0.07
$1.566 < \|\eta\| \le 2.0$	0.956 ± 0.002	0.965 ± 0.002	0.703 ± 0.005	0.959 ± 0.002	0.891 ± 0.004	0.953 ± 0.002	0.959 ± 0.002
$2.0 < \|\eta\| \le 2.5$	0.934 ± 0.003	0.97 ± 0.002	0.737 ± 0.005	0.971 ± 0.002	0.917 ± 0.003	0.952 ± 0.002	0.957 ± 0.002

Table E.15. Electron ID, Iso and HLT efficiencies for different E_T bins for DoubleElectron_Run2011A_PromtReco_v4 data set.

/DoubleElectron/Run2011A-PromptReco-v4/AOD							
E_T Bins	SCTo GSF	GsfTo WP95ID	GsfTo WP80ID	WP95ID ToIso	WP80ID ToIso	WP95 ToHLT17	WP95 ToHLT8
$20 < E_T < 30$	0.957 ± 0.002	0.959 ± 0.001	0.746 ± 0.002	0.917 ± 0.001	0.73 ± 0.002	0.972 ± 0.0009	0.990 ± 0.0005
$30 < E_T < 40$	0.965 ± 0.0006	0.974 ± 0.005	0.805 ± 0.001	0.965 ± 0.0006	0.841 ± 0.001	0.985 ± 0.0003	0.991 ± 0.0003
$40 < E_T < 50$	0.972 ± 0.0005	0.982 ± 0.0004	0.845 ± 0.001	0.987 ± 0.003	0.911 ± 0.008	0.989 ± 0.0003	0.992 ± 0.0002
$50 < E_T < 60$	0.979 ± 0.001	0.983 ± 0.001	0.856 ± 0.002	0.991 ± 0.0007	0.941 ± 0.002	0.990 ± 0.0006	0.993 ± 0.0005
$60 < E_T < 70$	0.984 ± 0.002	0.985 ± 0.002	0.863 ± 0.005	0.994 ± 0.001	0.963 ± 0.003	0.991 ± 0.001	0.993 ± 0.001
$70 < E_T < 80$	0.989 ± 0.003	0.981 ± 0.003	0.857 ± 0.007	0.992 ± 0.002	0.973 ± 0.004	0.994 ± 0.001	0.995 ± 0.001
$80 < E_T < 100$	0.988 ± 0.004	0.984 ± 0.004	0.868 ± 0.008	0.993 ± 0.002	0.975 ± 0.004	0.996 ± 0.002	0.997 ± 0.001
$100 < E_T < 200$	0.987 ± 0.004	0.987 ± 0.005	0.89 ± 0.01	0.997 ± 0.003	0.98 ± 0.005	0.992 ± 0.003	0.992 ± 0.003

Table E.16. Electron ID, Iso and HLT efficiencies for different pseudorapidity bins for DoubleElectron_Run2011A_PromptReco_v4 data set.

/DoubleElectron/Run2011A-PromptReco-v4/AOD							
$\|\eta\|$ Bins	SCTo GSF	GsfTo WP95ID	GsfTo WP80ID	WP95ID ToIso	WP80ID ToIso	WP95 ToHLT17	WP80 ToHLT8
$0 < \|\eta\| \le 0.78$	0.979 ± 0.0005	0.982 ± 0.0005	0.864 ± 0.001	0.974 ± 0.0005	0.858 ± 0.001	0.984 ± 0.0003	0.990 ± 0.0003
$0.78 < \|\eta\| \le 0.1444$	0.973 ± 0.0007	0.978 ± 0.0006	0.849 ± 0.001	0.976 ± 0.0006	0.863 ± 0.001	0.988 ± 0.0004	0.993 ± 0.0003
$1.444 < \|\eta\| \le 1.566$	0.93 ± 0.05	1 ± 0.02	0.88 ± 0.08	0.96 ± 0.03	0.96 ± 0.04	1.00 ± 0.02	1.00 ± 0.02
$1.566 < \|\eta\| \le 2.0$	0.961 ± 0.001	0.968 ± 0.001	0.707 ± 0.002	0.968 ± 0.001	0.887 ± 0.002	0.985 ± 0.0006	0.992 ± 0.0004
$2.0 < \|\eta\| \le 2.5$	0.94 ± 0.001	0.967 ± 0.001	0.736 ± 0.005	0.968 ± 0.009	0.918 ± 0.002	0.988 ± 0.0006	0.993 ± 0.0004

Table E.17. Electron ID, Iso and HLT efficiencies for different E_T bins for DoubleElectron_Run2011A_05Aug2011_v1 data set.

/DoubleElectron/Run2011A-05Aug2011-v1/AOD							
E_T Bins	SCTo GSF	GsfTo WP95ID	GsfTo WP80ID	WP95ID ToIso	WP80ID ToIso	WP95 ToHLT17	WP80 ToHLT8
$20 < E_T < 30$	0.96 ± 0.002	0.958 ± 0.003	0.739 ± 0.004	0.901 ± 0.002	0.683 ± 0.004	0.897 ± 0.003	0.902 ± 0.003
$30 < E_T < 40$	0.967 ± 0.001	0.9732 ± 0.001	0.801 ± 0.002	0.961 ± 0.001	0.82 ± 0.002	0.871 ± 0.001	0.872 ± 0.002
$40 < E_T < 50$	0.9718 ± 0.0008	0.9823 ± 0.0006	0.839 ± 0.002	0.9857 ± 0.0006	0.897 ± 0.001	0.869 ± 0.001	0.869 ± 0.001
$50 < E_T < 60$	0.978 ± 0.002	0.984 ± 0.002	0.857 ± 0.004	0.991 ± 0.001	0.935 ± 0.003	0.865 ± 0.004	0.866 ± 0.004
$60 < E_T < 70$	0.984 ± 0.004	0.985 ± 0.003	0.863 ± 0.008	0.997 ± 0.002	0.965 ± 0.005	0.868 ± 0.007	0.868 ± 0.007
$70 < E_T < 80$	0.993 ± 0.004	0.99 ± 0.005	0.87 ± 0.01	0.991 ± 0.004	0.983 ± 0.005	0.87 ± 0.01	0.87 ± 0.01
$80 < E_T < 100$	0.981 ± 0.006	0.99 ±0 .005	0.86 ± 0.01	0.988 ± 0.004	0.963 ± 0.007	0.86 ± 0.01	0.86 ± 0.01
$100 < E_T < 200$	0.985 ± 0.007	0.978 ± 0.008	0.88 ± 0.02	0.988 ± 0.005	0.974 ± 0.008	0.9 ± 0.01	0.91 ± 0.01

Table E.18. Electron ID, Iso and HLT efficiencies for different pseudorapidity bins for DoubleElectron_Run2011A_05Aug2011_v1 data set.

DoubleElectron_05Aug_v1							
|h| Bins	SCTo GSF	GsfTo WP95ID	GsfTo WP80ID	WP95ID ToIso	WP80ID ToIso	WP95 ToHLT17	WP80 ToHLT8
0 < |h| £ 0.78	0.979 ± 0.0009	0.981 ± 0.0008	0.86 ± 0.002	0.971 ± 0.0008	0.844 ± 0.002	0.872 ± 0.002	0.872 ± 0.002
0.78 < |h| £ 0.1444	0.976 ± 0.001	0.979 ± 0.001	0.846 ± 0.002	0.973 ± 0.001	0.843 ± 0.002	0.874 ± 0.002	0.875 ± 0.002
1.444 < |h| £ 1.566	0.94 ± 0.05	1 ± 0.03	0.87 ± 0.09	1 ± 0.03	0.93 ± 0.07	1.00 ± 0.03	1.00 ± 0.03
1.566 < |h| £ 2.0	0.964 ± 0.002	0.971 ± 0.002	0.704 ± 0.004	0.955 ± 0.002	0.874 ± 0.003	0.878 ± 0.003	0.878 ± 0.003
2.0 < |h| £ 2.5	0.938 ± 0.002	0.967 ± 0.002	0.732 ± 0.004	0.963 ± 0.002	0.905 ± 0.003	0.867 ± 0.003	0.87 ± 0.003

Table E.19. Electron ID, Iso and HLT efficiencies for different E_T bins for DoubleElectron_Run2011A_PromtReco_v6 data set.

/DoubleElectron/Run2011A-PromptReco-v6/AOD							
E_T Bins	SCTo GSF	GsfTo WP95ID	GsfTo WP80ID	WP95ID ToIso	WP80ID ToIso	WP95 ToHLT17	WP80 ToHLT8
$20 < E_T < 30$	0.96 ± 0.002	0.954 ± 0.002	0.739 ± 0.003	0.9 ± 0.002	0.665 ± 0.003	0.975 ± 0.001	0.9848 ± 0.0009
$30 < E_T < 40$	0.968 ± 0.0008	0.973 ± 0.007	0.801 ± 0.002	0.958 ± 0.0007	0.8 ± 0.002	0.9837 ± 0.0005	0.9841 ± 0.0005
$40 < E_T < 50$	0.971 ± 0.0006	0.98 ± 0.00005	0.838 ± 0.001	0.9838 ± 0.0005	0.887 ± 0.001	0.9867 ± 0.0004	0.987 ± 0.0004
$50 < E_T < 60$	0.978 ± 0.001	0.984 ± 0.001	0.842 ± 0.003	0.9905 ± 0.0009	0.934 ± 0.002	0.9885 ± 0.0009	0.9888 ± 0.0009
$60 < E_T < 70$	0.987 ± 0.002	0.984 ± 0.003	0.861 ± 0.006	0.994 ± 0.002	0.959 ± 0.004	0.987 ± 0.002	0.988 ± 0.002
$70 < E_T < 80$	0.991 ± 0.004	0.982 ± 0.004	0.862 ± 0.009	0.992 ± 0.003	0.967 ± 0.005	0.989 ± 0.003	0.989 ± 0.003
$80 < E_T < 100$	0.984 ± 0.005	0.977 ± 0.005	0.84 ± 0.01	0.991 ± 0.003	0.976 ± 0.005	0.988 ± 0.003	0.988 ± 0.003
$100 < E_T < 200$	0.98 ± 0.006	0.987 ± 0.006	0.89 ± 0.01	0.995 ± 0.003	0.983 ± 0.005	0.988 ± 0.004	0.991 ± 0.003

Table E.20. Electron ID, Iso and HLT efficiencies for different pseudorapidity bins for DoubleElectron_Run2011A_PromptReco_v6 data set.

/DoubleElectron/Run2011A-PromptReco-v6/AOD							
$\|\eta\|$ Bins	SCTo GSF	GsfTo WP95ID	GsfTo WP80ID	WP95ID ToIso	WP80ID ToIso	WP95 ToHLT17	WP95 ToHLT8
$0 < \|\eta\| \le 0.78$	0.979 ± 0.0007	0.981 ± 0.0006	0.861 ± 0.01	0.969 ± 0.0006	0.828 ± 0.001	0.985 ± 0.0004	0.986 ± 0.0004
$0.78 < \|\eta\| \le 0.1444$	0.975 ± 0.0008	0.977 ± 0.0008	0.846 ± 0.002	0.973 ± 0.0007	0.83 ± 0.002	0.988 ± 0.0005	0.988 ± 0.0005
$1.444 < \|\eta\| \le 1.566$	0.95 ± 0.05	1 ± 0.03	0.81 ± 0.03	0.95 ± 0.05	0.88 ± 0.08	1 ± 0.03	1 ± 0.03
$1.566 < \|\eta\| \le 2.0$	0.961 ± 0.001	0.967 ± 0.001	0.699 ± 0.003	0.951 ± 0.001	0.864 ± 0.002	0.985 ± 0.0007	0.986 ± 0.0007
$2.0 < \|\eta\| \le 2.5$	0.941 ± 0.002	0.967 ± 0.001	0.727 ± 0.003	0.959 ± 0.001	0.893 ± 0.002	0.97 ± 0.001	0.977 ± 0.001

Table E.21. Electron ID, Iso and HLT efficiencies for different E_T bins for DoubleElectron_Run2011B_PromtReco_v1 data set.

DoubleElectron_2011B_v1							
E_T Bins	SCTo GSF	GsfTo WP95ID	GsfTo WP80ID	WP95ID ToIso	WP80ID ToIso	WP95 ToHLT17	WP95 ToHLT8
$20 < E_T < 30$	0.963 ± 0.001	0.949 ± 0.001	0.714 ± 0.002	0.854 ± 0.001	0.548 ± 0.002	0.970 ± 0.0007	0.984 ± 0.0005
$30 < E_T < 40$	0.971 ± 0.0004	0.969 ± 0.0004	0.784 ± 0.001	0.938 ± 0.0005	0.715 ± 0.001	0.984 ± 0.0003	0.984 ± 0.0003
$40 < E_T < 50$	0.974 ± 0.0003	0.978 ± 0.0003	0.825 ± 0.0008	0.977 ± 0.0003	0.826 ± 0.0008	0.987 ± 0.0002	0.987 ± 0.0002
$50 < E_T < 60$	0.979 ± 0.0008	0.979 ± 0.0008	0.837 ± 0.002	0.985 ± 0.0006	0.885 ± 0.002	0.988 ± 0.0005	0.988 ± 0.0005
$60 < E_T < 70$	0.984 ± 0.002	0.979 ± 0.002	0.853 ± 0.004	0.987 ± 0.001	0.927 ± 0.003	0.990 ± 0.001	0.991 ± 0.001
$70 < E_T < 80$	0.986 ± 0.002	0.98 ± 0.003	0.861 ± 0.006	0.993 ± 0.002	0.946 ± 0.004	0.988 ± 0.002	0.989 ± 0.002
$80 < E_T < 100$	0.986 ± 0.003	0.979 ± 0.003	0.866 ± 0.006	0.995 ± 0.002	0.956 ± 0.004	0.991 ± 0.002	0.992 ± 0.002
$100 < E_T < 200$	0.989 ± 0.003	0.985 ± 0.003	0.861 ± 0.007	0.994 ± 0.002	0.98 ± 0.003	0.988 ± 0.002	0.989 ± 0.002

Table E.22. Electron ID, Iso and HLT efficiencies for different pseudorapidity bins for DoubleElectron_Run2011B_PromptReco_v1 data set.

DoubleElectron_2011B_v1							
|h| Bins	SCTo GSF	GsfTo WP95ID	GsfTo WP80ID	WP95ID ToIso	WP80ID ToIso	WP95 ToHLT17	W95 ToHLT8
0 < |h| £ 0.78	0.981 ± 0.0004	0.977 ± 0.0004	0.849 ± 0.007	0.956 ± 0.0004	0.752 ± 0.0009	0.985 ± 0.0002	0.986 ± 0.0002
0.78 < |h| £ 0.1444	0.976 ± 0.0005	0.975 ± 0.03	0.835 ± 0.0009	0.959 ± 0.0005	0.754 ± 0.001	0.988 ± 0.0003	0.988 ± 0.0003
1.444 < |h| £ 1.566	0.98 ± 0.02	0.97 ± 0.03	0.79 ± 0.06	0.97 ± 0.02	0.79 ± 0.05	1 ± 0.04	1 ± 0.04
1.566 < |h| £ 2.0	0.964 ± 0.0008	0.962 ± 0.00008	0.676 ± 0.002	0.927 ± 0.0009	0.805 ± 0.002	0.987 ± 0.0004	0.988 ± 0.0004
2.0 < |h| £ 2.5	0.950 ± 0.0009	0.960 ± 0.0008	0.685 ± 0.002	0.933 ± 0.001	0.79 ± 0.001	0.968 ± 0.0007	0.980 ± 0.0005

Table E.23. Electron ID, Iso and HLT efficiencies for different E_T bins for a MC Sample

MC:DYJetsToLL_TuneZ2_M-50_7TeV-madgraph-tauola							
E_T Bins	SCTo GSF	GsfTo WP95ID	GsfTo WP80ID	WP95ID ToIso	WP80ID ToIso	WP95 ToHLT17	WP80 ToHLT8
$20 < E_T < 30$	0.971 ± 0.006	0.95 ± 0.006	0.73 ± 0.01	0.86 ± 0.009	0.6 ± 0.001	0.971 ± 0.005	0.974 ± 0.004
$30 < E_T < 40$	0.985 ± 0.003	0.975 ± 0.002	0.797 ± 0.006	0.947 ± 0.003	0.749 ± 0.006	0.984 ± 0.002	0.984 ± 0.0007
$40 < E_T < 50$	0.975 ± 0.002	0.983 ± 0.002	0.832 ± 0.005	0.98 ± 0.002	0.856 ± 0.004	0.99 ± 0.001	0.99 ± 0.001
$50 < E_T < 60$	0.989 ± 0.004	0.993 ± 0.003	0.85 ± 0.01	0.997 ± 0.002	0.914 ± 0.009	0.988 ± 0.003	0.988 ± 0.003
$60 < E_T < 70$	0.986 ± 0.007	0.988 ± 0.008	0.88 ± 0.02	0.997 ± 0.003	0.96 ± 0.01	0.997 ± 0.003	0.997 ± 0.003
$70 < E_T < 80$	0.98 ± 0.01	0.98 ± 0.01	0.86 ± 0.03	0.993 ± 0.009	0.96 ± 0.02	1 ± 0.004	1 ± 0.004
$80 < E_T < 100$	0.99 ± 0.01	0.98 ± 0.01	0.82 ± 0.04	0.98 ± 0.01	0.96 ± 0.02	0.99 ± 0.01	0.99 ± 0.01
$100 < E_T < 200$	0.973 ± 0.02	0.99 ± 0.01	0.9 ± 0.05	1 ± 0.007	1 ± 0.007	1 ± 0.007	1 ± 0.007

Table E.24. Electron ID, Iso and HLT efficiencies for different pseudorapidity bins for a MC Sample.

MC:DYJetsToLL_TuneZ2_M-50_7TeV-madgraph-tauola							
$\|\eta\|$ Bins	SCTo GSF	GsfTo WP95ID	GsfTo WP80ID	WP95ID ToIso	WP80ID ToIso	WP95 ToHLT17	WP80 ToHLT8
$0 < \|\eta\| \le 0.78$	0.981 ± 0.002	0.987 ± 0.002	0.864 ± 0.004	0.963 ± 0.003	0.778 ± 0.005	0.991 ± 0.001	0.991 ± 0.001
$0.78 < \|\eta\| \le 0.1444$	0.978 ± 0.002	0.982 ± 0.002	0.846 ± 0.006	0.968 ± 0.003	0.801 ± 0.006	0.9892 ± 0.0002	0.989 ± 0.0002
$1.444 < \|\eta\| \le 1.566$	1 ± 0.7	1 ± 0.7	1 ± 0.7	1 ± 0.7	1 ± 0.7	1 ± 0.7	1 ± 0.7
$1.566 < \|\eta\| \le 2.0$	0.97 ± 0.004	0.956 ± 0.005	0.691 ± 0.001	0.939 ± 0.005	0.818 ± 0.008	0.984 ± 0.003	0.985 ± 0.003
$2.0 < \|\eta\| \le 2.5$	0.932 ± 0.006	0.96 ± 0.005	0.7 ± 0.001	0.931 ± 0.006	0.822 ± 0.009	0.965 ± 0.004	0.965 ± 0.004

F. THEORETICAL CROSS SECTIONS

Table F.1. The Theoretical Cross Sections.

W' Samples	PDF: 6 (MSTW 2008 NLO)	PDF: 7 (CTEQ6L, NLO)	PDF: 8 (CTEQ6L1, LO)
W' 200	6.628×10^{-1}pb	5.815×10^{-1}pb	5.978×10^{-1}pb
W' 250	5.669×10^{-1}pb	4.954×10^{-1}pb	5.059×10^{-1}pb
W' 300	3.181×10^{-1}pb	2.808×10^{-1}pb	2.848×10^{-1}pb
W' 400	1.029×10^{-1}pb	9.235×10^{-2}pb	9.211×10^{-2}pb
W' 500	4.004×10^{-2}pb	3.629×10^{-2}pb	3.612×10^{-2}pb
W' 600	1.802×10^{-2}pb	1.651×10^{-2}pb	1.634×10^{-2}pb
W' 700	8.893×10^{-3}pb	8.371×10^{-3}pb	8.185×10^{-3}pb
W' 800	4.775×10^{-3}pb	4.542×10^{-3}pb	4.444×10^{-3}pb
W' 900	2.691×10^{-3}pb	2.620×10^{-3}pb	2.540×10^{-3}pb
W' 1000	1.586×10^{-3}pb	1.569×10^{-3}pb	1.518×10^{-3}pb
W' 1100	9.556×10^{-4}pb	9.71×10^{-4}pb	9.343×10^{-4}pb
W' 1200	5.934×10^{-4}pb	6.149×10^{-4}pb	5.88×10^{-4}pb
W' 1300	3.761×10^{-4}pb	3.977×10^{-4}pb	3.771×10^{-4}pb
W' 1400	2.411×10^{-4}pb	2.610×10^{-4}pb	2.47×10^{-4}pb
W' 1500	1.569×10^{-4}pb	1.741×10^{-4}pb	1.648×10^{-4}pb